

Syracuse University

**SURFACE**

---

Dissertations - ALL

SURFACE

---

December 2017

# Design, Synthesis and Study of Thermomechanically Active Polymer Networks Based on Latent Crosslinking of Semicrystalline Polymers

Wenbin Kuang  
*Syracuse University*

Follow this and additional works at: <https://surface.syr.edu/etd>



Part of the [Engineering Commons](#)

---

## Recommended Citation

Kuang, Wenbin, "Design, Synthesis and Study of Thermomechanically Active Polymer Networks Based on Latent Crosslinking of Semicrystalline Polymers" (2017). *Dissertations - ALL*. 813.

<https://surface.syr.edu/etd/813>

This Dissertation is brought to you for free and open access by the SURFACE at SURFACE. It has been accepted for inclusion in Dissertations - ALL by an authorized administrator of SURFACE. For more information, please contact [surface@syr.edu](mailto:surface@syr.edu).

## **Abstract**

Demand has arisen rapidly for smart materials in the world of the need to develop and understand new functional products like plastics, rubber, adhesives, fibers, and coatings. Such products are essentially composed of polymers, large molecules of high molecular weight with homogeneous or various repeating units, which researchers term “macromolecules” that engender specific structural, morphological, and physical and mechanical properties. Those polymers with the capacity to change their configuration in accordance with environmental alteration are specifically referred to as shape memory polymers (SMPs), attracting much interest of study both academically and industrially. Herein, this dissertation aims at design, fabrication, and characterization of novel crosslinkable semicrystalline polymeric materials utilizing different techniques and mechanisms in order to explore their special thermomechanical features as well as the possibilities for potential industrial application based on shape memory (SM) effects. Key aspects include use of modern polymer synthesis to tailor thermal and shape memory properties and the adoption of electrospinning processing techniques to form continuous, fine fibers that allow unique molecular modifications, study of enzymatic degradation behavior involving physical form and microstructural state, and unprecedented approaches of making new kinds of shape memory assisted self-healing (SMASH) materials and thermal-responsive self-reversible actuators that require no human intervention. In the following is described the dissertation scope and organization.

**Chapter 1** goes over background relating to material science within the scope of SM material, self-healing (SH) material, and actuators.



**Chapter 2** outlines research conducted to achieve new compositions of matter and post-synthesis process, along with supporting characterization for the development of novel SMP materials with featuring tunable reversible actuation capability under ambient stimulus. We prepared a family of crosslinkable (unsaturated), semicrystalline cyclooctene (CO)-based copolymers with varying second monomer and composition via ring opening metathesis polymerization (ROMP). The unsaturation enables covalent crosslinking of polymer chains, in the presence of select thermal initiator through compression molding, allowing subsequent formation of a temperature-responsive network that shows a reversible two-way shape memory (2WSM) effect, indicative of crystallization-induced elongation upon cooling and melting-induced contraction upon heating when a constant, external stress is applied. Molecular, thermomechanical, and SM experiments were performed to investigate and tune the reversible actuation of aforementioned copolymers for the purpose of yielding quantitative guidelines for tailoring material and actuation performance through variations in composition and process.

**Chapter 3** seeks a latent-crosslinkable, mechanically flexible, fully thermoplastic shape memory polymer. Towards this end, we have developed a simple but effective macromolecular design that includes pendent crosslinking sites via the chain extender of a polyurethane architecture bearing semicrystalline poly( $\epsilon$ -caprolactone) (PCL) soft segment. This new composition was used to prepare fibrous mats by electrospinning and films by solvent casting, each containing thermal initiators for chemical crosslinking. Relevant to medical applications, *in vitro* enzymatic degradation experiments were carried out to understand the effect of crosslinking state and crystalline structure on degradation behavior of the materials.

**Chapter 4** builds upon the results of **Chapter 3**, reporting on the design, fabrication and characterization of a novel, electrospun SMASH polymer blend that incorporates the

aforementioned latent-crosslinkable polyurethane. This unique blend system has been unprecedentedly developed by employing a solution in which crosslinkable polyurethane and linear polyurethane are mixed homogeneously for electrospinning. After preparing a family of blends with varying compositions, comprehensive characterizations and various healing tests were done to determine optimal healing performance. Further, the effect of different damage types and molecular anisotropy (nanofibers aligned in high speeds during electrospinning process) were studied for their effect on healing performance.

**Chapter 5** continues along the line of **Chapter 3**, presenting the fabrication and testing of novel, electrospun SMP composites that were designed to exploit molecular and geometric anisotropy in reversible actuation under external stress-free condition upon change in ambient temperature. More specifically, the SMP composites consist of two electrospinnable constituents, one being the aforementioned latent crosslinkable polyurethane that serves to shape fixing and recovery (SM properties), and the other being a thermoplastic elastomer known as Pellethane that provides the internal stress field needed for 2WSM to occur. Multiple designs were developed and investigated in this chapter, in particular, including uniaxial actuator, bending actuator, and twisting actuator along with their bench demonstration of self-reversible actuation.

**Chapter 6** discusses the overall dissertation conclusions, followed descriptions of suggestions for future work, some of which are sub-sectioned at the end of this dissertation.

**Design, Synthesis and Study of Thermomechanically Active Polymer  
Networks Based on Latent Crosslinking of Semicrystalline Polymers**

By  
Wenbin Kuang  
B.S., Tianjin University, 2012

DISSERTATION  
Submitted in partial fulfillment of the requirements for the degree of  
Doctor of Philosophy in Chemical Engineering

Syracuse University  
December 2017

Copyright © 2017 Wenbin Kuang

All Rights Reserved

*To my parents*

*Pingan and Ping*

*for their endless, unconditional love and support*

## **Acknowledgements**

First and foremost, I would like to thank my advisor, Dr. Patrick T. Mather for all of his guidance, inspiration, and support throughout my entire time at Syracuse University. Back in 2012 Dr. Mather gave me the opportunity to join his research group and to also be a part of Syracuse Biomaterials Institute (SBI), since which his intelligence and drive have become constant sources of inspiration and motivation for me. He has given me the tools and resources to reach my greatest potential both as a student and as a professional scientist. For this, I will forever be grateful, as it has profoundly shaped my academic and career paths. In addition, his great work ethics and persistent pursuit of knowledge have inspired me to be passionate in my every work and go beyond the limits to succeed in what I do. Dr. Mather has been a great advisor, mentor, and role model and it is because of him that I learned not only how to conduct research properly and effectively, but also how to think and look at things the way I never did. These values and all that I learned from him will carry on through my future career, directing me to set my standards higher. I am very thankful of him for having such an enlightening and rewarding experience as a member of Mather Research Group (MRG).

I would further like to thank my dissertation committee, Dr. Julie Hasenwinkel, Dr. James Henderson, Dr. Ian Hosein, Dr. Zhen Ma and Dr. Teng Zhang, for contributing to the quality of this work and in-depth understanding the science behind it. Their time and input are greatly appreciated.

I also would like to thank Dr. Amir Torbati, my first mentor who really opened the door and made my transition to SBI and MRG quite smooth. His great patience and passion for teaching has given me an extraordinary example of being an outstanding mentor and researcher. Everything

that I learned from him better prepared me for my own research paths. It's been a huge honor and pleasure to work with him in SBI.

I would also like to express my gratitude to Dr. Ryan Tappel, my second mentor who closely worked with me and guided me through the progress of my very first project (**Chapter 2**). His wealth of knowledge and attention to details have inspired my creativity and persistence. Additionally, I hereby would like to thank Brian Schwartz, my undergraduate mentee, whose efforts contributed to the work of SMASH material (**Chapter 4**). Particularly, I would like to thank Dr. Erika Rodriguez whose research findings and accomplishments I have followed and referenced in **Chapter 4**. I also would like to acknowledge all past and present research colleagues, Dr. Eric Finkelstein (SBI facility lab manager), Dr. Richard Baker, Dr. Hossein Nejad, Dr. Erin McMullin, Dr. Xinzhu Gu, Dr. Pine Yang, Dr. Eric Ouellette, Dr. Wenyang Pan, Dr. Ariel Ash-Shakoor, Melodie I. Lawton, Allen Osaheni, Matthew Ali, Julia Tumbic, and Jaimee Robertson. Thank you for your collaboration, knowledge, and brainstorming sections.

I also appreciate the support provided by the Physics Machine Shop at Syracuse University. Namely, Lou Buda, Charles Brown, Phil Arnold, and Lester Schmutzler provided excellent workmanship in designing and constructing engineering tools for my research experiments. I would like to thank Dr. Debroah Kerwood from NMR laboratory for her expertise and help in using NMR and analyzing the data.

I would like to thank Karen P. Low, Lynore de la Rosa, and Jason Markle for all their support and logistics through my Ph.D. studies. Moreover, I would like to recognize all the financial contributors, specifically Syracuse University teaching assistantship, Nike Inc., and National Science Foundation (NSF) EFRI award all whose support made all my achievements possible.

Last but not least, I would like to thank all of my friends and family for providing me endless love, support, and encouragement all which motivated me to keep going and to never give up.



# Table of Contents

<b>Acknowledgements</b> .....	<b>vii</b>
<b>Table of Contents</b> .....	<b>x</b>
<b>List of Tables</b> .....	<b>xv</b>
<b>List of Schemes</b> .....	<b>xvi</b>
<b>List of Figures</b> .....	<b>xx</b>
<b>List of Videos</b> .....	<b>xxxii</b>
<b>Chapter 1: Introduction</b> .....	<b>1</b>
1.1 Background.....	1
1.1.1 Polymer Basics .....	1
1.1.2 Polymer Classification.....	1
1.1.3 Thermal Transitions.....	3
1.1.4 Polymerization.....	4
1.1.5 Crosslinking.....	5
1.2 Polymer Mechanical Properties .....	7
1.3 Shape Memory Polymers.....	8
1.3.1 Shape Memory Effects .....	8
1.3.2 Two-way Shape Memory Polymers .....	10
1.3.3 Shape Memory Assisted Self-healing .....	13
1.4 Biodegradable Polymers .....	15
1.5 Electrospinning .....	17
1.6 Scope of Dissertation .....	19
1.6.1 2WSM Polymers .....	19
1.6.2 SMASH Materials .....	21
1.6.3 Self-reversible Polymeric Actuators .....	21
1.7 References.....	22

Tables, Schemes and Figures.....	36
<b>Chapter 2: Tuning of Reversible Actuation via ROMP-based Copolymerization of Semicrystalline Polymers .....</b>	<b>50</b>
2.1 Synopsis .....	50
2.2 Introduction.....	50
2.3 Experimental Section .....	54
2.3.1 Materials .....	54
2.3.2 ROMP Copolymerization.....	54
2.3.3 Molecular Characterization .....	56
2.3.4 Peroxide Curing and Gel Fraction Measurement.....	56
2.3.5 Wide-angle X-ray Scattering.....	57
2.3.6 Thermal and Dynamic Mechanical Analysis .....	58
2.3.7 Shape Memory Characterization.....	59
2.4 Results and Discussion .....	60
2.4.1 Sample Preparation.....	60
2.4.2 Thermal and Dynamic Mechanical Analysis .....	61
2.4.3 Shape Memory Analysis .....	63
2.4.4 WAXS Analysis .....	68
2.5 Conclusions.....	69
2.6 References.....	71
Tables, Schemes and Figures.....	76
<b>Chapter 3: A Latent-crosslinkable Poly(<math>\epsilon</math>-caprolactone) (PCL)-based Thermoplastic Polyurethane: Synthesis, Shape Memory, and Degradation .100</b>	
3.1 Synopsis .....	100
3.2 Introduction.....	100
3.3 Experimental Section.....	103
3.3.1 Materials .....	103

3.3.2 Polyurethane Synthesis.....	104
3.3.3 Molecular Characterization.....	105
3.3.4 Sample Preparation .....	106
3.3.5 Gel Fraction Measurement.....	107
3.3.6 Microstructural Characterization .....	108
3.3.7 Thermal and Dynamic Mechanical Analysis.....	108
3.3.8 Shape Memory Characterization .....	109
3.3.9 Enzymatic Degradation Study .....	111
3.4 Results and Discussion .....	112
3.4.1 Molecular Characterization .....	112
3.4.2 Microstructural Characterization.....	113
3.4.3 Thermal and Dynamic Mechanical Analysis .....	114
3.4.4 Shape Memory Characterization .....	115
3.4.5 Enzymatic Degradation Study.....	117
3.5 Conclusions.....	120
3.6 References.....	122
Tables, Schemes and Figures.....	128
<b>Chapter 4: Electrospun Polyurethane Blends Exhibiting Shape Memory and Self-healing Properties.....</b>	<b>147</b>
4.1 Synopsis .....	147
4.2 Introduction.....	147
4.3 Experimental Section .....	150
4.3.1 Materials .....	150
4.3.2 Synthesis of Polyurethanes.....	151
4.3.3 Molecular Analysis.....	152
4.3.4 Fabrication of x-PU:l-PU Blends .....	152
4.3.4.1 Electrospinning .....	153

4.3.4.2 Hot Compaction .....	153
4.3.5 Microstructural Characterization.....	154
4.3.6 Thermal and Dynamic Mechanical Analysis .....	155
4.3.7 Reversible Plasticity Shape Memory .....	156
4.3.8 Self-healing Experimentation.....	157
4.4 Results and Discussion .....	160
4.4.1 Blends Preparation.....	160
4.4.2 Thermal and Dynamic Mechanical Analysis .....	161
4.4.3 RPSM Analysis .....	162
4.4.4 SH Study .....	164
4.4.4.1 Effect of Composition.....	164
4.4.4.2 Effect of Damage Type.....	166
4.4.4.3 Effect of Molecular Anisotropy.....	168
4.5 Conclusions.....	170
4.6 References.....	172
Tables, Schemes and Figures.....	177
<b>Chapter 5: Design and Fabrication of Self-reversible Actuators via Electrospinning: Influence of Micro-geometry and Molecular Anisotropy ..</b>	<b>199</b>
5.1 Synopsis .....	208
5.2 Introduction.....	209
5.3 Experimental Section.....	213
5.3.1 Materials .....	213
5.3.2 Preparation of Electrospun Bilayers.....	214
5.3.3 Thermal, Dynamic Mechanical, and Shape Memory Analysis ..	216
5.3.4 Fabrication and Characterization of Actuators.....	218
5.4 Results and Discussion .....	220
5.4.1 Preparation of Electrospun Bilayers.....	220

5.4.2 Thermal, Dynamic Mechanical, and Shape Memory Analysis ..	222
5.4.3 Self-reversible Actuators .....	225
5.4.4 Actuation Mechanism.....	228
5.5 Conclusions.....	230
5.6 References.....	231
Tables, Schemes, Figures and Videos .....	236
<b>Chapter 6: Conclusions and Future Work.....</b>	<b>268</b>
6.1 Overall Summary.....	268
6.2 Latent-crosslinkable PCL-based Polyurethane.....	268
6.2.1 Conclusions .....	268
6.2.2 Future Work.....	269
6.3 Self-reversible Actuators .....	274
6.3.1 Conclusions .....	274
6.3.2 Future Work.....	275
6.4 References.....	279
Schemes and Figures .....	283
<b>Appendix.....</b>	<b>289</b>
A1. Poly(tetrahydrofuran)-based Polyurethane .....	289
A1.1. POSS-incorporating PU.....	289
A1.2. Saturated PU, Acylation, and Crosslinking.....	291
A1.3. Backbone-carrying Unsaturation .....	293
A2. PCL-diols and PCL-based PUs Bearing Unsaturation in Backbone.....	294
A3. Uniaxially Self-reversible Actuator.....	297
A4. References.....	300
Tables, Schemes, and Figures.....	302
<b>Vita .....</b>	<b>345</b>

## List of Tables

**Table 2-1.** Synthesis Summary of CO-based copolymers.

**Table 2-2.** Thermal and Microstructural Characteristics as A Function of DCP wt. %.

**Table 2-3.** 1WSM and 2WSM characteristics as A Function of composition and DCP wt. %.

**Table 3-1.** Synthesis Summary of CO-based copolymers

**Table 3-2.** Thermal and Structural properties of PCL<sub>3k</sub>-based Thermoplastic Polyurethanes

**Table 3-3.** 1WSM and 2WSM characteristics for Crosslinked PCL<sub>3k</sub>-TPUs in Different Forms

**Table 3-4.** Densities of PCL<sub>3k</sub>-TPU crosslinked cast film and crosslinked spun fiber mat

**Table 4-1.** Synthesis Summary of Polyurethanes

**Table 4-2.** RPSM Characteristics as A Function of 1-PU wt. %

**Table 4-3.** Self-healing Efficiency as A Function of 1-PU wt. %

**Table 4-4.** Preparation of Electrospinning Solutions for Various Compositions

**Table 4-5.** Thermal and Structural properties of Electrospun Fiber Mats and Linear Polymer

**Table 4-6.** Thermal and Structural properties of Hot Compacted Fiber Mats

**Table 4-7.** Self-healing Efficiency for Different Types of Damages

**Table 4-8.** Self-healing Efficiency as A Function of Anisotropy

**Table 5-1.** Solution Preparation for Electrospinning

**Table 5-2.** Fabrication of Bilayers via Electrospinning

**Table 5-3.** Composition Evaluation

**Table 5-4.** Thermal Characteristics of Cured Fibrous Bilayers

## List of Schemes

**Scheme 1-1.** Schematic Drawings of (a) monomer, (b) linear polymer, (c) thermoplastic, (d) crosslink, (e) elastomer, and (f) thermoset.

**Scheme 1-2.** Polymer molecular structure and morphology.

**Scheme 1-3.** Free radical polymerization divided into three distinct stages: (a) initiation, (b) propagation, and (c) termination.  $I$  represents the initiator,  $R_0^\cdot$  stands for active radical,  $M$  is the monomer,  $R_1^\cdot$  is the active polymer chain at early stage.  $R_n^\cdot$  is the extending chain with  $n$  number of monomers and  $R_{n+1}^\cdot$  is after the addition of one repeat unit.  $R_{n+m}$  is the resulting polymer terminated by recombination where  $P_n + P_m$  are by disproportionation.

**Scheme 1-4.** (A) Schematic of general thiol-ene coupling by (a) free radical and (b) Michael addition. (B) Common alkyl thiols. (C) Typical multifunctional thiols.

**Scheme 1-5.** Schematic detailing the bimorph actuator fabrication process. Step 1: the DCP-crosslinked PCO strip is programmed above its  $T_m$  and its shape is fixed by cooling below its  $T_m$ ; Step 2: the programmed strip is mounted inside the custom-made aluminum mold; Step 3: the matrix material is injected inside the mold and photo-cured; Step 4: the mold is further thermally cured and the pre-sectioned actuator is removed; Step 5: the actuator is sectioned to the required geometry.

**Scheme 1-6.** Schematic of electrospinning setup used for producing polymer fibers. Polymer fibers are formed during flight of polymer solution jet over electric field while solvent evaporates.

**Scheme 2-1.** Copolymerization of *cis*-cyclooctene (CO) with various second monomers: **a)** poly(cyclooctene-*co*-cyclooctadiene) (PCO-COD), **b)** poly(cyclooctene-*co*-norbornene) (PCO-NO), and **c)** poly(cyclooctene-*co*-cycloheptene) (PCO-CH) via ring opening polymerization in the presence of Grubbs catalyst 2<sup>nd</sup> generation. The reaction is held at room temperature (~22 °C) for 30 min under nitrogen

environment before terminated by ethyl vinyl ether, followed by addition of tris(hydroxymethyl)phosphine in 2-propanol to cleanse residual catalyst.

**Scheme 3-1.** Preparation of PCL-based thermoplastic polyurethanes (PCL-TPU) by reacting Polycaprolactone-diol (PCL-diol) and 3,4-Dihydroxy-1-butene (DHB) with Hexamethylene diisocyanate (HDI).

**Scheme 4-1. a)** Synthesis of linear PCL-based thermoplastic polyurethane (l-PU) using polycaprolactone-diol with number-average molecular weight of 3,000 Da (PCL) and hexamethylene diisocyanate (HDI); **b)** Latent crosslinkable PCL-based thermoplastic polyurethane (x-PU) synthesized by the previously developed approach.

**Scheme 4-2. a)** The schematic of the custom-made device used to create consistent puncture (“wound”). A size 17 pin highlighted in dashed rectangular is installed perpendicularly in the center between two wooden platens with smooth surfaces; **b)** side (cross-sectional) view of the custom-made device.

**Scheme 5-1.** A two-step approach of fabricating bilayers via electrospinning. Step 1: x-PU (red) is first spun into one layer; Step 2: x-PU was substituted by Pellethane (blue) that forms the other layer. Rotating speed of collecting mandrel is adjusted to create molecular and geometric anisotropy when switching solutions.

**Scheme 5-2.** Geometry of bending actuator from cured Bilayer01. Yellow arrow indicates the fiber orientation introduced during electrospinning. The x-PU layer in red while the Pellethane layer in blue. \* The average thickness of each layer was measured based on SEM image using ImageJ.

**Scheme 5-3.** Geometry of twisting actuator from cured Bilayer01. Yellow arrow indicates the fiber orientation introduced during electrospinning. The x-PU layer in red while the Pellethane layer in blue. \* The average thickness of each layer was measured based on SEM image using ImageJ.



**Scheme 5-4.** Geometry of flattening actuator from cured Bilayer02. Yellow arrow indicates the fiber orientation introduced during electrospinning. The x-PU layer in red while the Pellethane layer in blue. \* The average thickness of each layer was measured based on SEM image using ImageJ.

**Scheme 5-5.** Geometry of untwisting actuator from cured Bilayer02. Yellow arrow indicates the fiber orientation introduced during electrospinning. The x-PU layer in red while the Pellethane layer in blue. \* The average thickness of each layer was measured based on SEM image using ImageJ.

**Scheme 5-6.** Hypothetic actuation mechanism of bending actuator prepared from cured Bilayer01. The x-PU chains are in red while the Pellethane in blue. Originally, highly oriented Pellethane fibers are imposing compressive stress onto x-PU chains some of which formed crystallites align in cross-wise direction. Upon heating above  $T_m$  of x-PU but not high enough to relax Pellethane fibers, x-PU crystallites melt and become amorphous domain which occupies more space than in its fully crystallized state. Consequently, the actuator bends towards Pellethane side. Upon cooling, the shape transformation is reversed due to recrystallization process.

**Scheme 5-7.** Hypothetic actuation mechanism of flattening actuator prepared from cured Bilayer02. The x-PU chains are in red while the Pellethane in blue. Originally, x-PU fibers are highly oriented so that corresponding crystallites align along the direction of fiber axis. Meanwhile, Pellethane fibers are randomly distributed and applying a certain amount of compressive stress onto x-PU, yielding a naturally curled bilayer towards Pellethane side. Upon heating above  $T_m$  of x-PU but not high enough to relax Pellethane fibers, x-PU crystallites melt and contract to lower entropic energy. Consequently, the actuator becomes flat upon heating and the shape transformation is reversed due to recrystallization process upon cooling.

**Scheme 6-1.** Thermoreversible DA/retro-DA reactions of dynamically-crosslinked networks prepared from a reactive mixture containing PFu having pendent furfuryl groups and a bismaleimide model crosslinker.

**Scheme 6-2.** Example schematic of a POSS-incorporating polyurethane synthesis.

**Scheme 6-3.** Example schematic of fabrication process for the free-standing actuators which may exhibit reversible two-way actuation in tension. First is to dual-spin the x-PU containing an amount of crosslinker and the TPE at the same time. Hot compaction would be conducted to chemically crosslink the x-PU. Subsequently, the sample would be heated to ca. 15 °C above  $T_m$  of the POSS, then stretched uniaxially to a large extent, and finally cooled down to a low temperature below all  $T_c$ 's while the external stress is maintained.

## List of Figures

**Figure 1-1.** Idealized Young's Modulus profile of a polymer as a function of temperature.

**Figure 1-2.** Stress-strain behaviors of common fiber, rigid plastic, flexible plastic, and elastomer.

**Figure 1-3.** Demonstration of four classes of shape memory polymers in terms of their dynamic mechanical behavior: (I) chemically crosslinked glassy thermosets, (II) chemically crosslinked semicrystalline rubbers, (III) physically crosslinked thermoplastics, and (IV) physically crosslinked block copolymers.

**Figure 1-4.** (a) One-way shape memory (1WSM) cycles/loops for an example of a crosslinked poly(cyclooctene). (b) Two-way shape memory (2WSM) cycles/loops for an example of an end-linked polycaprolactone.

**Figure 1-5.** Two-way reversible actuation of an PCL-*co*-PEG SMP foam with (i) 10%, (ii) 20%, (iii) 30%, (iv) 40%, (v) 50%, and (vi) 60% initial applied strain.

**Figure 1-6.** Two-way shape memory behavior of the SMPU-EPU laminated composite.

**Figure 1-7.** (a) Force-displacement profiles for the virgin, damaged, and healed state of a 1-PCL:n-PCL blend. (b) Notched 1-PCL:n-PCL blend showing stereo micrographs of deformation and crack growth clamped in the Linkam tensile stage (scale bar: 500  $\mu\text{m}$ ). (c) Snapshots of crack closure and crack rebonding when the sample was unclamped from the Linkam tensile stage and heated to the temperature indicated above (stereo micrographs scale bar: 500  $\mu\text{m}$ ).

**Figure 1-8.** Experimental mass loss data for hydrogels synthesized from end-methacrylated PEG-PCL macromonomers and incubated in solutions with (a) 1.0 mg/ml, (b) 0.4 mg/ml, (c) 0.2 mg/ml, and (d) 0.1 mg/ml *pseudomonas lipase*.

**Figure 2-1.** Thermogravimetric analysis (TGA) graph of all synthesized polymers: PCO (black), 1COD (red), 3COD (blue), 5COD (pink), 10COD (dark green), 3NO (cyan), and 3CH (green).

**Figure 2-2.** Differential Scanning Calorimetry (DSC) analysis graph of **a)** pristine PCO-COD polymers with varying COD mol. % contents: (i) PCO, (ii) 1COD, (iii) 3COD, (iv) 5COD, and (v) 10COD; and of **b)** pristine PCO-based copolymers with different second monomers: (i) 3COD, (ii) 3NO, and (iii) 3CH. Heating rate is 10 °C/min.

**Figure 2-3.** 2D WAXS pattern **a)** of the PCO0.50 sample, **b)** of the 3NO0.50 sample and **c)** of the 3CH0.50 sample. The X-ray wavelength ( $\lambda$ ) is 1.5405 Å.

**Figure 2-4.** Differential Scanning Calorimetry (DSC) analysis graph of **a)** crosslinked PCO-COD polymers with DCP concentration of 0.25 wt. %: (i) PCO0.25, (ii) 1COD0.25, (iii) 3COD0.25, and (iv) 5COD0.25; and of **b)** crosslinked PCO-COD copolymers with DCP concentration of 0.50 wt. %: (i) PCO0.50, (ii) 1COD0.50, (iii) 3COD0.50, and (iv) 5COD0.50; and of **c)** crosslinked PCO-based copolymers with varying second monomers at a DCP concentration of 0.50 wt. %: (i) 3COD0.50, (ii) 3NO0.50, and (iii) 3CH0.50. Heating rate is 10 °C/min.

**Figure 2-5.** Storage modulus ( $E'$ ) vs temperatures for crosslinked copolymers with DCP concentration of **a)** 0.25 wt. % and **b)** 0.50 wt. %, respectively: PCO (black), 1COD (red), 3COD (blue), 5COD (pink), 3NO (cyan), and 3CH (green).  $E'$  was recorded at a heating rate of 3 °C/min with frequency of 1 Hz.

**Figure 2-6.** Tan  $\delta$  vs temperatures for crosslinked copolymers with DCP concentration of **a)** 0.25 wt. % and **b)** 0.50 wt. %, respectively: PCO (black), 1COD (red), 3COD (blue), 5COD (pink), 3NO (cyan), and 3CH (green).

**Figure 2-7.** One-way shape memory cycles for **a)** PCO0.25, **b)** 1COD0.25, **c)** 3COD0.25, and **d)** 5COD0.25, respectively. The sample is deformed by increasing stress at 70 °C. A temporary shape was fixed by cooling at a rate of 2 °C/min and unloading, and then the original shape was recovered by heating at 2 °C/min. “\*” indicates starting point.

**Figure 2-8.** One-way shape memory cycles for **a)** PCO0.50, **b)** 1COD0.50, **c)** 3COD0.50, **d)** 5COD0.50, **e)** 3NO0.50, and **f)** 3CH0.50, respectively. The sample is deformed by increasing stress at 70 °C. A

temporary shape was fixed by cooling at a rate of 2 °C/min and unloading, and then the original shape was recovered by heating at 2 °C/min. “\*” indicates starting point.

**Figure 2-9.** Two-way shape memory behavior of PCO-COD copolymers containing different COD contents cured with 0.25 wt. % DLP: (i) PCO0.25, (ii) 1COD0.25, (iii) 3COD0.25, and (iv) 5COD0.25. The samples were stretched under high temperature (70 °C) at a constant strain of 70%. The deformation step is followed by a cooling process at a rate of 2 °C/min, inducing an increase in strain. Then, the increased strain decreases by a heating process at a rate of 2 °C/min to 70 °C. Cycle: first (black), second (red), third (blue).

**Figure 2-10.** Two-way shape memory behavior of PCO-COD copolymers containing different COD contents cured with 0.50 wt. % DLP: (i) PCO0.50, (ii) 1COD0.50, (iii) 3COD0.50, and (iv) 5COD0.50. The samples were stretched under high temperature (70 °C) at a constant strain of 70%. The deformation step is followed by a cooling process at a rate of 2 °C/min, inducing an increase in strain. Then, the increased strain decreases by a heating process at a rate of 2 °C/min to 70 °C. Cycle: first (black), second (red), third (blue).

**Figure 2-11.** Two-way shape memory behavior of copolymers containing various second monomer cured with 0.50 wt. % DLP: (i) 3COD0.50, (ii) 3NO0.50, and (iii) 3CH0.50. The samples were stretched under high temperature (70 °C) at a constant strain of 70%. The deformation step is followed by a cooling process at a rate of 2 °C/min, inducing an increase in strain. Then, the increased strain decreases by a heating process at a rate of 2 °C/min to 70 °C. Cycle: first (black), second (red), third (blue).

**Figure 2-12.** Gel fraction value ( $G$ ) as a function of COD content cured with different DCP concentrations. (○) indicates 0.25 wt. % DLP and (●) 0.50 wt. % DLP.

**Figure 2-13. a)** Actuation magnitude ( $R_{a,m}$ ) and **b)** recovery magnitude ( $R_{r,m}$ ) as a function COD content at different DCP concentrations for PCO, 1COD, 3COD, and 5COD. (○) indicates 0.25 wt. % DCP and (●) 0.50 wt. % DCP.

**Figure 2-14.** Thermal strain hysteresis ( $\Delta T$ ) as a function of COD content cured with different DCP concentrations. Thermal strain hysteresis was calculated from the temperature difference at the half of strain loop generating during cooling and heating. ( $\circ$ ) indicates 0.25 wt. % DCP and ( $\bullet$ ) 0.50 wt. % DCP.

**Figure 2-15.** 2WSM characteristics of copolymers with varying second monomers in comparison in terms of actuation magnitude and recovery magnitude.

**Figure 2-16. a)** Two-way shape memory behavior for 3COD0.50 at different heating/cooling rates, 0.5 °C/min (pink), 1.0 °C/min (blue), 2.0 °C/min (red), and 3.0 °C/min (black). The sample was deformed under a tensile stress of 300 kPa at 70 °C; **b)** Actuation magnitude ( $R_{a,m}$ ) and strain hysteresis ( $\Delta T$ ) versus heating/cooling rate based on the two-way shape memory behavior of the 3COD0.50 sample, respectively. Maximum  $R_{a,m}$  ( $\bullet$ ) and  $\Delta T$  ( $\circ$ ). The strain hysteresis was calculated from the temperature difference ( $\Delta T$ ) at the half of strain loop in two-way shape memory cycles.

**Figure 2-17. a)** 3D two-way shape memory behavior for 3COD0.50 at different stresses, (i) 100 kPa, (ii) 200 kPa, and (iii) 300 kPa. The sample was deformed under each constant stress at 70 °C, followed by cooling and heating steps (2 °C/min), respectively; **b)** Maximum strain and strain hysteresis versus stress based on the two-way shape memory behavior of the 3COD0.50 sample, respectively. Maximum strain ( $\bullet$ ) and strain hysteresis ( $\circ$ ). The strain hysteresis was calculated from the temperature difference ( $\Delta T$ ) at the half of strain loop in two-way shape memory cycles.

**Figure 2-18.** 2D WAXS patterns of the 3COD0.50 sample with an increase of loading after cooling: (i) unstretched, (ii) 100 kPa, (iii) 200 kPa, and (iv) 300 kPa. Stretching direction is vertical. The X-ray wavelength ( $\lambda$ ) is 1.5405 Å.

**Figure 2-19.** WAXS plots of (i) 3COD0.50, (ii) 3NO0.50, (iii) 3CH0.50, and (iv) PCO0.50. The X-ray wavelength ( $\lambda$ ) is 1.5405 Å.

**Figure 2-20.** Azimuthal scanning profiles for the 3COD0.50 sample as a function of the applied stress: (i) 100 kPa, (ii) 200 kPa, and (iii) 300 kPa. The X-ray wavelength ( $\lambda$ ) is 1.5405 Å.

**Figure 3-1.** Differential Scanning Calorimetry (DSC) analysis graph of (i) PCL<sub>2k</sub>-TPU and (ii) PCL<sub>3k</sub>-TPU. Heating and cooling rates of 10 °C/min.

**Figure 3-2.** Scanning electron microscope (SEM) images of PCL<sub>3k</sub>-TPU: **a)** virgin cast film surface; **e)** crosslinked cast film surface; **b)** and **f)** virgin spun fiber mat surface (770 nm average diameter) at different magnifications; **c)** and **g)** crosslinked spun fiber mat at different magnifications; **d)** and **h)** cryofracture (cross-section) views of crosslinked spun fiber mat at different magnifications. Scale bar = 50 μm in **a), b), c), d),** and **e)**; 10 μm in **f), g),** and **h).**

**Figure 3-3.** 2D Wide-angle X-ray Scattering (WAXS) patterns of **a)** virgin cast film, **b)** crosslinked cast film, **c)** virgin spun fiber mat, and **d)** crosslinked spun fiber mat of PCL<sub>3k</sub>-TPU; **e)** WAXS profiles of (i) virgin cast film, (ii) crosslinked cast film, (iii) virgin spun fiber mat, and (iv) crosslinked spun fiber mat. The X-ray wavelength ( $\lambda$ ) is 1.5405 Å.

**Figure 3-4.** Differential Scanning Calorimetry (DSC) analysis graph of virgin cast film (i), crosslinked cast film (ii), virgin spun fiber mat (iii), and crosslinked spun fiber mat (iv) of PCL<sub>3k</sub>-TPU. Heating and cooling rates of 10 °C/min.

**Figure 3-5. a)** Storage modulus ( $E'$ ) vs temperatures for virgin cast film (black) and crosslinked cast film (red) of PCL<sub>3k</sub>-TPU.  $E'$  was recorded at a heating rate of 3 °C/min with frequency of 1 Hz; **b)** one-way and **c)** two-way shape memory cycles for crosslinked cast film of PCL<sub>3k</sub>-TPU. “\*” indicates starting point; **d)** two-way shape memory behavior for crosslinked cast film of PCL<sub>3k</sub>-TPU at different stresses, (i) 0.30 MPa, (ii) 0.50 Mpa, and (iii) 0.70 Mpa. The samples were deformed under each constant stress at 80 °C, followed by cooling and heating steps (2 °C/min), respectively.

**Figure 3-6. a)** Storage modulus ( $E'$ ) vs temperatures for virgin spun fiber mat (black) and crosslinked spun fiber mat (red) of PCL<sub>3k</sub>-TPU.  $E'$  was recorded at a heating rate of 3 °C/min with frequency of 1 Hz; **b)** one-way and **c)** two-way shape memory cycles for crosslinked spun fiber mat of PCL<sub>3k</sub>-TPU. “\*” indicates starting point; **d)** two-way shape memory behavior for crosslinked spun fiber mat of PCL<sub>3k</sub>-TPU at different

stresses, (i) 0.15 MPa, (ii) 0.30 Mpa, and (iii) 0.45 Mpa. The samples were deformed under each constant stress at 80 °C, followed by cooling and heating steps (2 °C/min), respectively.

**Figure 3-7.** Maximum strain and strain hysteresis versus stress based on the two-way shape memory behavior of **a)** crosslinked cast film and **b)** crosslinked spun fiber mat, respectively. Maximum strain (■) and strain hysteresis (□). The strain hysteresis was calculated from the temperature difference ( $\Delta T$ ) at the half of strain loop in two-way shape memory cycles.

**Figure 3-8.** Enzymatic degradation study of PCL<sub>3k</sub>-TPU: **a)** Mass remaining profiles, **b)** crystallinities profiles, **c)** normalized number-average molecular weight ( $M_n$ ) remaining profiles for virgin samples only, and **d)** evolution profiles of gel fraction value for crosslinked samples only during degradation by Lipase PS (0.4 mg/mL) in a pH 7.4 PBS solution at 37 °C. Virgin cast film (●), crosslinked cast film (○), virgin spun fiber mat (▲), and crosslinked spun fiber mat (Δ).

**Figure 3-9.** Photographs of PCL<sub>3k</sub>-TPU samples during enzymatic degradation: **a)** virgin cast film; **b)** crosslinked cast film; **c)** virgin spun fiber mat; **d)** crosslinked spun fiber mat. Columns from left to right refer to control, day 2, day 18, day 34, and day 66, respectively.

**Figure 3-10.** SEM images of PCL<sub>3k</sub>-TPU samples during enzymatic degradation: **a)** virgin cast film; **b)** crosslinked cast film; **c)** virgin spun fiber mat; **d)** crosslinked spun fiber mat. Columns from left to right refer to control, day 2, day 18, day 34, and day 66, respectively. Scale bar = 50  $\mu$ m.

**Figure 3-11.** Thermogravimetric analysis (TGA) graph of virgin cast film (i), crosslinked cast film (ii), virgin spun fiber mat (iii), and crosslinked spun fiber mat (iv) of PCL<sub>3k</sub>-TPU. Heating rate of 10 °C/min.

**Figure 3-12.** Thermogravimetric analysis (TGA) graph of virgin cast film (i), crosslinked cast film (ii), virgin spun fiber mat (iii), and crosslinked spun fiber mat (iv) of PCL<sub>3k</sub>-TPU. Heating rate of 10 °C/min.

**Figure 3-13.** 2D Small-angle X-ray Scattering (SAXS) patterns of **a)** virgin cast film, **b)** crosslinked cast film, **c)** virgin spun fiber mat, and **d)** crosslinked spun fiber mat of PCL<sub>3k</sub>-TPU; **e)** SAXS profiles of (i)



virgin cast film, (ii) crosslinked cast film, (iii) virgin spun fiber mat, and (iv) crosslinked spun fiber mat. The X-ray wavelength ( $\lambda$ ) is 1.5405 Å.

**Figure 3-14.** Water uptake profiles during degradation by Lipase PS (0.4 mg/mL) in a pH 7.4 PBS solution at 37 °C. Virgin cast film (●), crosslinked cast film (○), virgin spun fiber mat (▲), and crosslinked spun fiber mat (Δ).

**Figure 4-1.** Differential Scanning Calorimetry (DSC) analysis graph of **a)** electrospun fiber mats and linear polymer: **(i)** 100:0, **(ii)** 90:10, **(iii)** 80:20, **(iv)** 70:30, **(v)** 60:40, **(vi)** 50:50, and **(vii)** 0:100; and of **b)** hot compacted fiber mats: **(i)** 100:0, **(ii)** 90:10, **(iii)** 80:20, **(iv)** 70:30, **(v)** 60:40, and **(vi)** 50:50.

**Figure 4-2.** Scanning electron microscope (SEM) images of electrospun fiber mats: **a)** 90:10, **c)** 80:20, **e)** 70:30, **i)** 60:40, and **l)** 50:50; SEM images of hot compacted fiber mats: **b)** 90:10, **d)** 80:20, **f)** 70:30, **j)** 60:40, and **m)** 50:50. Cryofracture (cross-section) views of hot compacted **g)** 80:20 and **h)** 60:40 samples at high magnifications. The scale bar is 50 μm.

**Figure 4-3.** Storage modulus ( $E'$ ) vs temperatures for **a)** electrospun fiber mats and **b)** hot compacted fiber mats, respectively: 100:0 (black), 90:10 (red), 80:20 (green), 70:30 (blue), 60:40 (pink), and 50:50 (cyan).  $E'$  was recorded at a heating rate of 3 °C/min with frequency of 1 Hz.

**Figure 4-4.** Reversible plasticity shape memory (RPSM) cycle of **a)** 100:0, **b)** 90:10, **c)** 80:20, **d)** 70:30, **e)** 60:40, and **f)** 50:50, respectively, where each sample was deformed to 140% strain at room temperature and recovered at 80 °C. Strain vs temperature curve (blue) and stress vs strain curve (red) are plotted for each composition. “\*” indicates starting point.

**Figure 4-5.** Stress vs strain curves for the virgin, puncture damaged and healed states of **a)** 100:0, **b)** 90:10, **c)** 80:20, **d)** 70:30, **e)** 60:40, and **f)** 50:50, respectively. In particular, the healed 80:20 sample shows a profile highly identical to the virgin state, indicating complete restoration of mechanical properties.

**Figure 4-6. a)** Optical microscope images of a hot compacted 80:20 sample showing **(i)** the virgin state, **(ii)** puncture damaged and stretched (~40% strain) state at RT (~22 °C), **(iii)** heated (90 °C) and healed state,

and **(iv)** re-stretched state (~100% strain) after cooled back to RT. The scale bar is 0.5 mm; **b)** Snapshots of puncture closure and puncture rebonding when the sample was unloaded from the clamps of the LinkAm tensile stage and heated up to the temperatures revealed above (stereo micrographs scale bar is 0.5 mm).

**Figure 4-7.** Self-healing efficiency vs l-PCL wt. % content. The damage type is puncture.  $\eta_1$ :  $\circ$ ,  $\eta_2$ :  $\bullet$ .

**Figure 4-8.** Optical microscope images of **a)** a hot compacted 80:20 sample showing **(i)** the virgin state, **(ii)** scratch (on both sides) damaged and stretched (~40% strain) state at RT(~22 °C), **(iii)** heated (90 °C) and healed state, and **(iv)** re-stretched state (~100% strain) after being cooled back to RT; **b)** a hot compacted 80:20 sample showing **(i)** the virgin state, **(ii)** double-edge notched and stretched (~40% strain) state at RT(~22 °C), **(iii)** heated (90 °C) and healed state, and **(iv)** re-stretched state (~100% strain) after being cooled back to RT. The scale bar is 0.5 mm.

**Figure 4-9.** **a)** SEM imaging cross-sectional views of **a)** a puncture damaged 80:20 sample, **b)** a scratch damaged 80:20 sample, and **c)** a notch damaged 80:20 sample for **(i)** the damaged state, **(ii)** the damaged state upon 40% strain, **(iii)** the healed state, and **(iv)** the healed state upon 100% strain. The scale bar is 100  $\mu\text{m}$ . The red arrows indicate the damages accordingly.

**Figure 4-10.** Stress vs strain curves for the virgin state, damaged state, and healed state of a hot compacted 80:20 sample under application of different types of damages: puncture (bottom), scratch (middle), and notch (upper), respectively.

**Figure 4-11.** Optical microscope images of **a)** an isotropic 60:40, **b)** an oriented 60:40 whose stretching direction is perpendicular to original fiber orientation (90°), and **c)** an oriented 60:40 whose stretching direction is parallel with original fiber orientation (0°), respectively, showing **(i)** the virgin state, **(ii)** puncture damaged state, **(iii)** stretched (~40% strain) state at RT(~22 °C), **(iv)** heated (90 °C) and healed state, and **(v)** re-stretched state (~100% strain) after cooled back to RT. The scale bar is 0.5 mm. The loading direction and film long axis direction are both horizontal.

**Figure 4-12.** **a)** 2D WAXS patterns and **b)** SAXS patterns of **(i)** an oriented, electrospun 60:40, **(ii)** an oriented, hot compacted 60:40, **(iii)** an isotropic, electrospun 60:40, and **(iv)** an isotropic, hot compacted 60:40. The X-ray wavelength ( $\lambda$ ) is 1.5405 Å.

**Figure 4-13.** **a)** WAXS, **b)** SAXS, and **c)** azimuthal profiles (0 and 180° = meridional) of **(i)** an oriented, electrospun 60:40, **(ii)** an oriented, hot compacted 60:40, **(iii)** an isotropic, electrospun 60:40, and **(iv)** an isotropic, hot compacted 60:40. The X-ray wavelength ( $\lambda$ ) is 1.5405 Å.

**Figure 4-14.** Stress vs strain curves for **a)** oriented 60:40 and isotropic 60:40 in comparison for the virgin, puncture damaged and healed states and for **b)** the virgin, puncture damaged and healed states of the sample whose stretching direction is parallel with fiber orientation (0°) and the sample whose stretching direction is perpendicular to fiber orientation (90°).

**Figure 4-15.** Thermogravimetric analysis (TGA) graph of electrospun fiber mats: 100:0 (black), 90:10 (red), 80:20 (green), 70:30 (blue), 60:40 (pink), and 50:50(F) (cyan).

**Figure 4-16.** Tan  $\delta$  vs temperatures for **a)** electrospun fiber mats and **b)** hot compacted fiber mats, respectively: 100:0 (black), 90:10 (red), 80:20 (green), 70:30 (blue), 60:40 (pink), and 50:50 (cyan).

**Figure 4-17.** Young's Modulus (RT) vs l-PCL wt. % content. Damage type is puncture.

**Figure 5-1.** Scanning electron microscope (SEM) images of Bilayer01: Pellethane side **a)** before curing and **b)** after curing, x-PU side **c)** before curing and **d)** after curing, and **e)** cross-sectional view of cured sample; of Bilayer02: Pellethane side **g)** before curing and **h)** after curing, x-PU side **i)** before curing and **j)** after curing, and **f)** cross-sectional view of cured sample. Scale bar = 10  $\mu\text{m}$  in **a)**, **b)**, **c)**, **d)**, **g)**, **h)**, **i)** and **j)**; 50  $\mu\text{m}$  in **e)** and **f)**.

**Figure 5-2.** 2D WAXS patterns of bilayers before and after thermal curing: **a)** uncured Bilayer01, **b)** uncured Bilayer02, **c)** cured Bilayer01, and **d)** cured Bilayer02. The X-ray wavelength ( $\lambda$ ) is 1.5405 Å. Both the principle orientation of fiber axis and strip's long axis are horizontal.

**Figure 5-3.** Azimuthal scanning profiles for bilayers before and after thermal curing: (i) uncured Bilayer01, (ii) cured Bilayer01, (iii) uncured Bilayer02, and (iv) cured Bilayer02. The X-ray wavelength ( $\lambda$ ) is 1.5405 Å.

**Figure 5-4.** Thermogravimetric analysis (TGA) profiles of neat Pellethane (black), Bilayer01 (red), Bilayer02 (blue), and neat x-PU (pink). Heating rate of 10 °C/min.

**Figure 5-5.** Differential Scanning Calorimetry (DSC) analysis graph of cured bilayers and substituent polymers: (i) neat Pellethane, (ii) cured Bilayer01, (iii) cured Bilayer02, and (iv) cured x-PU. The second heating was recorded at a rate of 10 °C/min.

**Figure 5-6.** Differential Scanning Calorimetry (DSC) analysis graph of **a**) uncured electrospun bilayers: (i) first heating and (ii) second heating of Bilayer01, and, (iii) first heating and (iv) second heating of Bilayer02; and of **b**) cured bilayers and substituent polymers: (i) neat Pellethane, (ii) Bilayer01, (iii) Bilayer02, and (iv) neat x-PU. Heating rate is 10 °C/min.

**Figure 5-7.** Tensile storage modulus ( $E'$ ) vs temperatures for cured bilayers and substituent polymers: neat Pellethane (black), Bilayer01 (red), Bilayer02 (blue), and neat x-PU (pink).  $E'$  was recorded at a heating rate of 3 °C/min with frequency of 1 Hz.

**Figure 5-8.** Tensile two-way actuation under stress-free condition for **a**) Bilayer01 and **b**) Bilayer02, both cured thermally. The samples were heated to 80 °C without applying external stress except preloading force of 0.001 N, following which alternate cooling and heating process was adopted at a rate of 2 °C/min.

**Figure 5-9. a)** Tensile two-way actuation under stress-free condition for neat Pellethane. The samples were heated to 80 °C without applying external stress except preloading force of 0.001 N, following which alternate cooling and heating process was adopted at a rate of 2 °C/min; **b)** two-way shape memory cycles for crosslinked x-PU under 220 kPa. The sample was deformed under each constant stress at 80 °C, followed by cooling and heating steps (2 °C/min).

**Figure 5-10. a)** Snapshots of two-way actuation of bending actuator. The sample changed from a bent shape to a more bent/curled shape by heating in a  $\sim 58$  °C water bath. Then its shape recovered by cooling in a  $\sim 0$  °C water-ice bath. The reversible actuation can be repeated by alternate heating and cooling; **b)** Quantification of reversible two-way actuation of bending actuator. Curvature ( $\mathcal{K}$ ) was calculated from Radius which was directly measured using ImageJ.

**Figure 5-11. a)** Snapshots of two-way actuation of twisting actuator. The sample changed from a twisted shape to a more twisted shape by heating in a  $\sim 55$  °C water bath. Then its shape recovered by cooling in a  $\sim 0$  °C water-ice bath. The reversible actuation can be repeated by alternate heating and cooling; **b)** Quantification of reversible two-way actuation of twisting actuator. Spiral radius ( $\mathcal{R}$ ) and spiral pitch (center-to-center spacing,  $\mathcal{P}$ ) were estimated using ImageJ.

**Figure 5-12. a)** Snapshots of two-way actuation of flattening actuator. The sample changed from a curled shape to a flat shape by heating in a  $\sim 58$  °C water bath. Then its shape recovered by cooling in a  $\sim 0$  °C water-ice bath. The reversible actuation can be repeated by alternate heating and cooling; **b)** Quantification of reversible two-way actuation of flattening actuator. Curvature ( $\mathcal{K}$ ) was calculated from Radius which was directly measured using ImageJ.

**Figure 5-13. a)** Snapshots of two-way actuation of untwisting actuator. The sample changed from a twisted shape to a flat shape by heating in a  $\sim 55$  °C water bath. Then its shape recovered by cooling in a  $\sim 0$  °C water-ice bath. The reversible actuation can be repeated by alternate heating and cooling; **b)** Quantification of reversible two-way actuation of untwisting actuator. Spiral radius ( $\mathcal{R}$ ) and spiral pitch (center-to-center spacing,  $\mathcal{P}$ ) were estimated using ImageJ.

**Figure 5-14.**  $\tan \delta$  vs temperatures for cured bilayers and substituent polymers: neat Pellethane (black), Bilayer01 (red), Bilayer02 (blue), and neat x-PU (pink).

**Figure 5-15.** 2D WAXS profiles of bilayers before and after thermal curing: (i) uncured Bilayer01, (ii) uncured Bilayer02, (iii) cured Bilayer01, and (iv) cured Bilayer02. The X-ray wavelength ( $\lambda$ ) is 1.5405 Å.

**Figure 5-16.** 2D WAXS patterns of bilayers before and after thermal curing: **a)** neat Pellethane and **b)** neat x-PU. The X-ray wavelength ( $\lambda$ ) is 1.5405 Å.

**Figure 5-17.** 2D WAXS profiles of (i) neat Pellethane, (ii) cured Bilayer01, and (iii) cured x-PU. The X-ray wavelength ( $\lambda$ ) is 1.5405 Å.

**Figure 6-1.** Simplified presentation of a polymer jetting 3D printer with separate support and build material channels; where each layer is planarized and cured by UV exposure immediately after its deposition.

**Figure 6-2.** Schematic of off-centered co-electrospinning system.

**Figure 6-3.** Cartoon showing preparation of dual-cure network stress-free actuators.

## List of Videos

**Video 5-1.** Self-reversible two-way actuation of bending actuator. The sample was actuated at  $\sim 58\text{ }^{\circ}\text{C}$  above  $T_m$  of x-PU, turning to a more bent shape towards Pellethane side as Pellethane fibers were exerting compressive stress onto x-PU. Then the initial shape was recovered by cooling at  $\sim 0\text{ }^{\circ}\text{C}$ . Such free standing reversible actuation can be repeated by alternate heating and cooling.

**Video 5-2.** Self-reversible two-way actuation of twisting actuator. The sample was actuated at  $\sim 55\text{ }^{\circ}\text{C}$  above  $T_m$  of x-PU, turning to a more twisted, spiral shape with Pellethane side being inside as Pellethane fibers were exerting compressive stress onto x-PU. Then the initial shape was recovered by cooling at  $\sim 0\text{ }^{\circ}\text{C}$ . Such free standing reversible actuation can be repeated by alternate heating and cooling.

**Video 5-3.** Self-reversible two-way actuation of flattening actuator. The sample was actuated at  $\sim 58\text{ }^{\circ}\text{C}$  above  $T_m$  of x-PU, turning to a completely flat shape as oriented x-PU contracted extensively. Then the initial shape was recovered by cooling at  $\sim 0\text{ }^{\circ}\text{C}$ . Such free standing reversible actuation can be repeated by alternate heating and cooling.

**Video 5-4.** Self-reversible two-way actuation of untwisting actuator. The sample was actuated at  $\sim 55\text{ }^{\circ}\text{C}$  above  $T_m$  of x-PU, turning to a flat shape as oriented x-PU contracted extensively. Then the initial shape was recovered by cooling at  $\sim 0\text{ }^{\circ}\text{C}$ . Such free standing reversible actuation can be repeated by alternate heating and cooling.

# Chapter 1: Introduction

## 1.1 Background

### 1.1.1 Polymer Basics

A *polymer* is defined as a substance made up of long chain molecules which have long sequence of one or more species of small subunits (*monomers* (Scheme 1-1 (a))) covalently bonded together through a chemical reaction known as polymerization.<sup>1,2</sup> This particular long chain nature sets polymers apart from other substances or materials and gives rise to their characteristic properties.<sup>3,4</sup> The emphasis upon this nature presented up to this point implies the importance of molecular weight that for polymers, typically falls in the range from thousands to millions. Broadly speaking, 25,000 g/mol is the minimum molecular weight required for good physical and mechanical features in terms of many commercialized polymers.<sup>5</sup> Molecular weight takes different forms, given different sources, the most important two of which are *number average molecular weight* ( $M_n$ ) and *weight average molecular weight* ( $M_w$ ). Note that most synthetic polymers and natural polymers have a distribution in molecular weights, indicative of different chain lengths generated during one single synthesis batch of a polymer. The breadth of such distribution is described by *polydispersity index* (PDI) represented by the ratio of  $M_w$  to  $M_n$ . In general, condensation polymers reveal a PDI of around 2 and to date no successful polymer reaction has been reported to yield a PDI of 1 except the case of proteins,<sup>3</sup> though modern, controlled polymerizations can approach this ideally.

### 1.1.2 Polymer Classifications



Several fundamental terms and concepts relating to structure must be understood in order to get a more comprehensive insider's view of polymer's characteristics. There are four conventional types of polymer skeletal structures that account for most industrial polymers in use today: *linear* (Scheme 1-1 (b)), *cyclic*, *branched*, and *network*.<sup>2</sup> It is important to recognize that the variations in skeletal may result in major differences in such properties as transition temperature, solvent resistance, tensile strength, and etc. Notably, network polymers can be not only formed by polymerization, but also by crosslinking together pre-existing chains, either physically or chemically (covalently). Crosslink density plays a significant role in physical and mechanical properties of network polymers, for example of the vulcanization of natural rubber. Also, polymers can be classified, on a species-basis of their constituent monomers, into two categories: *homopolymers* that are derived from one species of monomer, and *copolymers* that are composed of more than one species of monomer. Specifically, copolymers can be further categorized into four structural types: *random copolymers* in which the distribution of repeat units is statistically random, *alternating copolymers* in which repeat units are arranged alternately along the polymer chain, *block copolymers* in which repeat units line up only in blocks of the same kind, and *graft copolymers* that are branched polymers where the branches have a different chemical structure to that of the backbone chain. Furthermore, there is another common way of classifying polymers in which way polymers are separated, essentially based upon the underlying molecular structure, into three groups: *thermoplastics*, *elastomers*, and *thermosets*<sup>2,4</sup> (Scheme 1-1 (c), (e), and (f)). Thermoplastics are oftentimes referred to as a class of linear or lightly branched polymers, which become liquid when heat is applied. They constitute the largest portion of the polymers in commercial production thus far as their great ability to be processed into virtually any configuration in aid of many traditional processing techniques like injection-molding and extrusion.

Unlike thermoplastics, elastomers are highly stretchable rubbery networks that recover their original shape immediately when the applied stress is removed. This feature is quite useful in many design of mechanical devices in both academic institution and industry. In contrast to elastomers, thermosets are network polymers with a high degree of crosslinking so as to be very rigid and mechanically stable. In this dissertation, we are particularly interested in thermoplastic polymers that can later be crosslinked to form networks that exhibit certain thermomechanical and shape memory properties.

### **1.1.3 Thermal Transitions**

Two primary types of polymer physical structures are in common use: *semicrystalline* and *amorphous*.<sup>3</sup> The term semicrystalline is adapted as these polymers contain a small portion of amorphous domains elsewhere crystalline structures are well formed, while, amorphous polymers are defined by having no long-range order of underlying molecular structure (Scheme 1-2). It is known that mechanical properties of semicrystalline polymers (e.g. Young's modulus) vary significantly as these polymers go through one of three major thermal transitions: glass transition, recrystallization (on cooling) transition, and melting (on heating) transition (Figure 1-1). Below the glass transition temperature ( $T_g$ ), the polymer chains are largely immobilized and only vibrational motions are possible so that the polymer appears to be glassy along with high Young's modulus. When the polymer is heated above  $T_g$ , the polymer becomes soft and rubbery associated with several orders of magnitude drop in modulus. The region between  $T_g$  and  $T_m$  is called the rubber plateau in which modulus doesn't change drastically as temperature increases. The melting transition temperature ( $T_m$ ) is the temperature at which long-range order of crystalline regions loses and the polymer transitions from solid to liquid. Note that covalently crosslinked polymers

(networks) doesn't become liquid but just softens. The recrystallization transition temperature ( $T_c$ ) is the temperature at which formation of polymer crystals occurs on cooling (or, in some cases due to thermal history, upon heating). These transitions are pivotal because that is where molecular rearrangements take place and it could be the origin of shape memory effects.

#### 1.1.4 Polymerization

As mentioned previously, polymers are synthesized through a chemical reaction known as polymerization which takes a number of different approaches based upon comparison of the molecular formula of the polymer with that of corresponding monomers from which it was formed.<sup>3</sup> One approach is through *condensation polymerizations* in which the elimination of small molecules is involved in order to form covalent bonds between monomers. *Addition polymerizations* usually yield a polymer containing the same repeat units, and without need of eliminating small molecules. However, this method of classification turned out imperfect due to some overlap between these two polymerization categories. As a better method that focuses on the underlying polymerization mechanisms, two general types have been created by the modern preference: *step polymerization* and *chain polymerization*.<sup>2,3,5,6</sup> The common chain polymerization mechanisms include *free radical polymerization* and *ring opening polymerization*, while, *condensation polymerization* belongs to step polymerization. More specifically, free radical polymerization can be divided into three distinct basic steps: *initiation*, *propagation*, and *termination* (Scheme 1-3). Note that a further process known as chain transfer can occur with initiator, monomer, solvent and transfer agent, to cause termination of an actively growing chain. Similarly, the reactions through ring opening polymerization also generate active radicals but only one with two active ends instead of two individual radicals in free radical polymerization mechanism. As for condensation polymerization mechanism, polyurethane condensation reactions

will be one of the primary method by which I synthesize the polymers I used for this dissertation. Put simply, these reactions occur in a form of reacting a di- or poly-isocyanate with a polyol.

### 1.1.5 Crosslinking

A crosslink is defined as a linkage that bonds two individual polymer chains together to form a network.<sup>7</sup> It can be a *physical* or a *chemical* (covalent) crosslink depending on its nature and mechanism of bonding. The crosslinked polymers, which we refer to as thermoset, have many advantageous properties some of which are as following: (1) outstanding ability to maintain original shape as well as to minimize dimensional creep, (2) improved solvent resistance, and (3) great resistance to heat distortion.

Physical crosslinks are usually reversible so that they can be reset or reformed by heat, light or other means. One example involving intermolecular interaction is that Si-O:B (B = boron) weak bonding has been used to form reversible physical crosslinks in order to develop an optional simple method to modulate the viscoelastic properties of polymer in practical applications.<sup>8</sup> Another way to form physical crosslinks involves use of a distinct architecture that places the higher thermal transition macromer groups on the backbone of the crystallizable polymer in the form of a graft copolymer. The backbone polymer may act as the switching phase (soft segment) with a lower transition temperature, while the graft polymer may serve as hard segment that has a noticeably higher transition temperature and thus physically crosslinks the material. Polyhedral oligomeric silsesquioxane (POSS), which consists of an inner  $(\text{SiO}_{1.5})_n$  core and an organic substituent cage-shaped shell in a diameter ranging from 1 to 3 nm, offers the ability serve as such hard segment due to its high tendency to aggregation of its own kind, as the kinetics favored the formation of small nano-phase-separated POSS regions.<sup>9-13</sup> In addition, it has been reported that physical

crosslinking can be achieved by the photoinduced anisotropy of a synthesized linear polymer within which the azobenzene groups responds to light triggering while alkyl chains aggregate together to generate physical crosslinks by tail-to-tail associations.<sup>14</sup> More interestingly, physical crosslinks can be formed via ionic bonding/crosslinking. For instance, ionic crosslinks can be created between the sulfonate groups attached to the polymer backbones of a polymer electrolyte membrane, to reduce the water sorption and to also improve dimensional stability.<sup>15</sup>

Ordinarily, chemical (covalent) crosslinks are more favored in many practical applications as they allow materials to accommodate greater strain or stress without losing the capacity to fully recover following mechanical deformation.<sup>16-18</sup> Several efficient methods of polymer covalent crosslinking are discussed in the following. To begin with, network polymers can be obtained by copolymerizing a mono-olefin with a branched *crosslinking monomer* that has multiple carbon-carbon double bonds (C=C).<sup>3</sup> During the last century, the reactions, which are capable of yielding a whole array of functional synthetic molecules and organic materials, have been termed click reactions out of which a famous one is called *thiol-ene click chemistry* (Scheme 1-4).<sup>19</sup> Such a chemistry takes two forms of particular note: thiol-ene free radical addition to electron-rich/electron-poor C=C and catalyzed thiol Michael addition to electron-poor C=C. However, the largest drawback of this strategy is the lack of processability as synthesis reaction and covalent crosslinking will be completed simultaneously.

As discussed earlier in this dissertation, sulfur vulcanization is widely used to crosslink most rubbers containing C=C in their polymer chains, while a few non-sulfur methods have been invented for covalent crosslinking of rubbers in spite of saturation. Speaking of non-sulfur crosslinking, initiators that produce active, free radicals upon activation, can be employed to affect such crosslinking. *Peroxides*, in particular, prevail over the other common initiators because of

their advantage of being able to crosslink both saturated and unsaturated polymers.<sup>20-22</sup> The initiators include, but are not limited to, thermal-, photo-, and ionic-initiators.<sup>23,24</sup> For unsaturated polymers, the alkoxy radicals derived from the peroxide assist in forming chemical bonds based upon double bonds in the polymer.<sup>25</sup> On the contrary, the likelihood of covalently crosslinking saturated polymers essentially relies on the nature of the hydrogen atom most probably pulled out and the polymer structure surrounding the radical.<sup>25</sup> Other methods of chemical crosslinking have been developed but these are beyond the scope of this dissertation.

## 1.2 Polymer Mechanical Properties

The mechanical properties of polymers could differ to a large extent due to their temperature-dependent viscoelastic behaviors. Specifically, glassy polymers often are hard and easy to crack and then break when only a few percent of dimensional extension is applied. Semicrystalline polymers tend to be more elastic and ductile as its crystalline and amorphous regions have very low  $T_g$ 's. Also, all linear polymers become fluid upon heating above their glass transition or melting transition temperature and thus are unable to withstand external force any longer in their molten state, while network polymers turn soft but still keep their initial shapes. A quantitative way of investigating the mechanical properties of various polymers is to monitor variation in stress as a function strain in the uniaxial tensile testing, and hypothetical profiles of *fibers*, *rigid plastic*, *flexible plastic*, and *elastomer* are provided in this chapter (Figure 1-2). The maximum strain for each type of material is defined as *yield point* or *strain-to-failure*, an extremely important figure pertaining to basic mechanical properties of polymers. Moreover, the linear portion of these profiles indicates the elastic region of polymer and the slopes are defined by *Young's Modulus*. The value of this modulus is oftentimes used to preliminarily determine the most suitable

application for the material. Elastomers with a  $T_g$  significantly below room temperature can be stretched to above a strain of 500% but usually with only modest tensile strength.<sup>26</sup> In general, the mechanical properties of polymers are strongly associated with the molecular weight, degree of crystallinity, crosslink density, degree of crosslinking, and ambient temperature relative to polymer transition temperatures,<sup>2,3,27-29</sup> all of which factors have been discussed previously.

The viscoelastic properties of a polymer is usually studied using *dynamic mechanical analysis* (DMA), a modern characterization technique in which an oscillating stress is applied at varying temperatures or frequencies while the displacement of the material is recorded and measured to assess the complex modulus.<sup>30</sup> In normal DMA testing, the *storage modulus* ( $E'$ ) represents the elasticity in the form of stored energy, while the *loss modulus* ( $E''$ ) accounts for the viscous portion in the form of dissipated energy. Therefore, DMA can be utilized to measure transition temperature of polymer based upon the change of modulus associated with the change of molecular energy.

## **1.3 Shape Memory Polymers**

### **1.3.1 Shape Memory Effects**

*Shape memory polymers* (SMPs) are a class of smart materials that have the ability to permanently memorize a macroscopic shape, be deformed and fixed to a temporary and dormant shape under specific conditions of stress and temperature, and then later relax to the original, stress-free condition under certain environmental command.<sup>31-35</sup> During the past few decades, they have attracted a lot of interest, both academically and industrially, based on the ability to set a temporary, non-equilibrium shape until they are triggered to revert to original shape by a specific external stimulus. Several environmental stimuli that can trigger shape changing of SMPs have been well studied thus far, such as heat,<sup>36,37</sup> light,<sup>38</sup> solvent,<sup>39,40</sup> electric field,<sup>41</sup> magnetic field,<sup>42</sup>

and variation of pH.<sup>43</sup> Out of all the external stimuli, heat is the most widely investigated and used, as a result of the ease in ability to tailor thermo-mechanical properties of thermally actuated SMPs. Shape memory behavior gives materials great potential for sensors, actuators, smart devices of great potential for automotive applications of interest to many worldwide companies. To exhibit shape memory behavior, there are two primary requisites in need: (1) physical or covalent crosslinks with retractable, reversible extension and (2) network chains with mobility switching relating to glass transition or melting transition. In fact, shape memory polymers have been grouped into four classes on account of their dynamic mechanical properties.<sup>18,35</sup> Such classes include (1) chemically crosslinked glassy thermosets, (2) chemically crosslinked semicrystalline rubbers, (3) physically crosslinked amorphous thermoplastics, and (4) physically crosslinked semicrystalline block copolymers. The temperature-dependent dynamic mechanical behavior regarding the SMPs listed above is posted accordingly being typical examples (Figure 1-3).

The shape memory (SM) effects in polymers can take two quite distinct forms: conventional *one-way shape memory* (1WSM) and reversible *two-way shape memory* (2WSM).<sup>44</sup> The conventional SM behavior is ordinarily illustrated in a 3D stress-temperature-strain plot on a three-cycle basis (Figure 1-4 (a)). In this case, the SMP is first heated above such a transition temperature as its glass transition temperature or melting temperature and held isothermal at the elevated temperature for the SMP to reach thermal equilibrium. Then a tensile stress is applied onto the SMP for a prescribed deformation while temperature is unaltered. This step of 1WSM cycle is referred to as *deformation*, which is followed by *cooling/fixing* as described below. With the load maintained, the SMP is cooled below the critical transition temperature to allow vitrification or recrystallization to occur so as to prevent elastic recovery. After the load is removed, the SMP relaxes in some degree depending on its molecular characteristics and finally maintains the



programmed, temporal shape (*unloading*). At the last step of 1WSM cycle, so called *recovery*, the temporarily fixed shape is reverted back to the original form of the SMP heating above the transition temperature. This recovery is a result of polymer chains relaxing to their maximum entropy state.

In contrast, 2WSM features reversible actuation that undergoes a reversible elongation and contract in strain through cooling and heating process at a single applied stress (Figure 1-4 (b)). Since that the applied stress is maintained constant throughout the entire course of testing, 2WSM data is usually presented in a 2D strain-temperature plot. Note that 2WSM behavior requires the SMP to be semicrystalline in most cases. More specifically, the SMP is heated to a high temperature above its  $T_m$  and stretched to a prescribed strain or by ramping force to a predetermined stress at that temperature, following which the stress associated with the strain is kept unchanged for the duration of three cycles. On cooling, a unique “soft elasticity” characteristic of the liquid crystalline phase (or simply stress-induced crystallization) of the SMP gives rise to a crystallization-induced elongation in strain, while on heating, the SMP contracts due to melting of polymer crystals in order to ultimately achieve the strain that matches tensile modulus under the isotropic condition of the SMP.<sup>45</sup> The 2WSM case is the one most easily exploited for actuation purpose of interest for the present dissertation, while 1WSM is required more for controlled, one-time deployment events,<sup>46-48</sup> such as expansion of slender medical device or unfolding of a complex structure.

### **1.3.2 Two-way Shape Memory Polymers**

Although greater than 95% of the literature on SMPs is dedicated to the 1WSM effect, 2WSM offers special potential to create practical materials or devices that essentially demands no external

manipulation. Back in 1959 it was first reported, but largely ignored, that crosslinked polyethylene fibers underwent reversible contraction on heating and elongation on cooling when tensioned.<sup>49</sup> In particular, the oriented polyethylene fibers were crosslinked through electron-radiation, yielding a molecularly aligned polyethylene network that features 25% reversible dimensional variation. This work technically launched a new era in 2WSM effect that presents in polymer network, but, unfortunately, further investigation into a number of factors affecting 2WSM behavior was not conducted. Subsequently, many researchers looked into a similar phenomenon in soft, liquid crystalline siloxanes.<sup>50</sup> As for reversible shape memory behavior, *liquid crystalline elastomers* (LCEs) have been shown to exhibit excellent performance, attributed to the coupling of the self-organization of liquid crystalline phase and the entropy elasticity of polymer networks.<sup>51,52</sup> Remarkably “monodomain” samples feature actuation along the orientation axis with no external stress bias.<sup>53</sup>

In our own lab, 2WSM effect has been studied deeply for a chemically crosslinked semicrystalline network of poly(cyclooctene) (PCO).<sup>45,54</sup> It is also reported that the crosslinked PCO in film exhibits reversible actuation near room temperature. Furthermore, the generality of this particular phenomenon is demonstrated in a totally different composition, an end-linked poly( $\epsilon$ -caprolactone) (PCL).<sup>55</sup> Additionally, the LCEs containing mesogen have been reported to be capable of changing shapes reversibly in response to variation in temperature.<sup>56,57</sup> Considering potential application for tissue engineering, regenerative medicine, and the study of cell mechanobiology, lots of efforts have been put on the fabrication of smart polymers with shape memory triggering at body temperature. Numerous thiol-ene crosslinked poly( $\epsilon$ -caprolactone)-*co*-poly(ethylene glycol) foams with varying PCL-to-PEG compositions were found to exhibit reversible actuation in compression, and also with  $T_m$ 's in the range around body temperature.<sup>58</sup>

More surprisingly, these new shape memory foams are characteristic of profound cooling-induced compression and heating-induced expansion, a completely opposite way as opposed to typical 2WSM. It was found that this special SM effect results from additional contraction, which is reversed upon heating through  $T_m$ , during crystallization of the foams under a compressive stress, other than from normal thermal expansion effects.

Besides our prior studies, Bai et al elaborated a new graft polymer in which PCL chains are grafted onto polydopamine (PDA) with phenolic hydroxyl groups as active points by ring-opening polymerization.<sup>59</sup> This polymer can then be crosslinked using diisocyanate to afford semicrystalline polymer networks in order to attain 2WSM. Pandini et al prepared an  $\alpha,\omega$ -triethoxysilane-terminated PCL with silica-based domains that were chemically crosslinked through hydrolysis using HCl as catalyst.<sup>60</sup> The mild sol-gel curing allows covalent crosslinking of this PCL polymer with Si-O-Si linkage to achieve promising 2WSM behavior. In addition, such compositions may have multiple SM effects by synthesizing a semicrystalline network with two well separated crystalline phases that can lead to two parallel crystallization-induced elongation upon cooling as well as two distinct melting-induced contraction upon heating. Consequently, poly(ethylene-vinyl acetate) (EVA), a low cost polymer in industrial production, was crosslinked with dicumyl peroxide, a commonly used thermal initiator, to undergo 2WSM behavior along with the  $T_m$  of EVA ranging from 75 °C to 95 °C.<sup>61</sup>

In many scenarios, a complex chemistry synthesis is required to crosslink polymers for 2WSM effect, which negatively influences the breadth of practical applications of these SMPs largely. Therefore, physical methods or designs have been greatly developed to bridge the gap. Chen et al described a laminated shape memory polymer composite exhibiting reversible blending/flattening behavior (Figure 1-6) by combining the pre-strained, PHA-based shape memory polyurethane

(SMPU) with the isotropic elastic polyurethane (EPU).<sup>62</sup> Continuing on this lamination approach, they further demonstrated a good electro-active 2WSM behavior using the carbon black/SMPU-EPU laminated composite due to excellent electricity conduction of carbon black.<sup>63</sup> Another way of controlling SM behavior was proven utilizing phase morphology of covalent networks based on crystallizable polymer blends.<sup>64</sup>

The need exists for rapid and reliable reversible actuation in SMPs in order to make artificial muscles or other actuators.<sup>65,66</sup> Behl et al developed a reversible shape memory copolymer network that consists of poly( $\omega$ -pentadecalactone) segment determining the shape-changing geometry and poly( $\epsilon$ -caprolactone) segment providing the thermally activated actuation.<sup>67</sup> Zhou et al synthesized an end-capped poly(octylene adipate) that showcased both one-way and two-way reversible shape memory after thio-crosslinked and acrylate crosslinked by exposing to 365 nm light.<sup>68</sup> Plus, a bimorph structure was designed (Scheme 1-5), using dicumyl peroxide crosslinked PCO acting as SMP and an acrylate-based polymer with a  $T_g$  below actuator thermal cycle temperature range acting as elastic matrix.<sup>69</sup> Such bimorph revealed the free-standing 2WSM behavior at temperatures ranging from 15 °C to 60 °C.

### **1.3.3 Shape Memory Assisted Self-healing**

Polymers and their composites have been extensively applied in a variety of such practical fields as transport vehicles, sporting goods, civil engineering, and electronics owing to their light weight, good processibility, resistance to corrosion, etc.<sup>70,71</sup> However, decomposition, damage, and failure could take place naturally to such materials in exposure to harsh environment wherein there exist mechanical, chemical, thermal, UV radiation, or a combination of these factors. Also, unfortunately, eventual failure still is a matter of time for most engineered materials regardless of

the improved robustness or the development of nondestructive inspection method.<sup>72</sup> The detection and repair to the failing material or device is often costly.<sup>73</sup> Inspired by biological systems that perfectly textbook regeneration, *self-healing* (SH), and reproduction, biomimetic SH materials offer an exceptional solution to extending their working life and condition because of the built-in capability to repair damage as well as to recover functionality autonomously or using the resources or signals available inherently.<sup>74,75</sup> Such resources can be mechanical,<sup>76</sup> thermal,<sup>77</sup> or electrical forms of energy.<sup>78</sup> A typical example of mechanically activated SH composites is the fabrication of core-shell nanofibers via coaxial electrospinning reported by Wu et al.<sup>79</sup> Speaking of this unique geometry, the dicyclopentadiene (DCPD) is encapsulated by a thin polyacrylonitrile shell containing Ruthenium-based Grubbs' catalyst that can initiate the ring-opening metathesis polymerization of DCPD. Once the fibers are ruptured, the DCPD flows towards the damage location and then reacts with the catalyst to polymerize so as to restore the bulk mechanical properties. However, the number of available SH agent is very limited and, further, the ruptured shells might act as mechanical defects that compromise mechanical properties.

Hence, a novel concept has risen up with introducing thermal-responsive shape memory polymers to facilitate the SH process, providing an effective mechanism to partially or completely close and rebond the crack or other types of damage. This concept has been termed *shape memory assisted self-healing* (SMASH) by our lab originally, generally being demonstrated in at least two approaches. In the first approach, locally prepositioned shape memory alloy (SMA) wires<sup>80,81</sup> or shape memory polymer (SMP) fibers<sup>82,83</sup> are used so that upon activation they impose a contractual force that pulls the crack surface closer. The second approach relies on bulk shape memory effect from the material to close the crack.<sup>84-86</sup> For example from our own lab, Rodriguez *et al* reported a PCL-based molecular composite system, a single-phase, two-component blend that consists of a

thiol-ene crosslinked PCL (n-PCL) network and a high molecular weight linear PCL (l-PCL) interpenetrating the network.<sup>87</sup> With “reversible plasticity”, the n-PCL network features a special form of SM where a stable temporary state can be achieved through both elastic and plastic deformation regions at a temperature (here RT) below its  $T_m$  and also is fully resettable upon heating above  $T_m$ . Due to their near-identical  $T_m$  values, the heating step is simultaneously used to trigger the SH mechanism in which the crack surfaces are rebonded by the l-PCL chains that diffuse to and ultimately across the surfaces of damage (Figure 1-7).

A new SMASH strategy has been introduced by Luo et al, opening the door to develop a phase-separate morphology in favor of allowing the healing of larger cracks and defects as opposed to the single-phase n-PCL/l-PCL blend.<sup>88</sup> The overall design was based on a two-step process including electrospinning and impregnation, to fabricate an fiber-matrix composite system wherein the randomly oriented, nonwoven PCL nano- and microfibers are uniformly spread out in a continuous, crosslinked epoxy matrix, which enables more significant flow of the liquefied PCL well as larger interfacial area and more sustained healing agent delivery because of the high aspect ratio fibers. Along this line, Nejad et al undertook the SMASH strategy as mentioned above, to develop thermally activated SH coatings.<sup>89</sup> In addition to that a second approach involving polymerization induced phase separation (PIPS) of PCL and epoxy was adopted for comparison purpose. Generally, the SMASH materials prepared by both approaches revealed excellent and similar structural and functional SH outcomes, and, furthermore, the PIPS technique has turned out to be more suitable for scale-up application given its processing simplicity.

#### **1.4 Biodegradable Polymers**

Biodegradable polymers have been widely and primarily utilized for tissue engineering, medical device, and drug delivery due to the ease in ability to break down into smaller constituents into body's environment.<sup>90,91</sup> Degradation could take place to polymers through one of two fundamental modes: *bulk* or *surface degradation*.<sup>92</sup> In bulk degradation, the whole material including both the surface and the interior will degrade equally, as often indicated by drop in molecular weight and also by the fading color or change of opacity. On the other hand, surface erosion occurs only at the exterior surface of the material that is in direct contact with the environment. In another words, the interior portions of the material will not be affected at all until its outer portion has been degraded and removed, which means that a time-dependent, dimensional decrease of the material is always expected but that the overall molecular weight does not vary. Note that, in fact, a great deal of materials undergo degradation by a combined mode of bulk and surface degradation.<sup>93</sup> Another method of classifying degradation behavior of polymers is by mechanism: *enzymatic* or *hydrolytic*. Enzymatic degradation literally suggests that polymers can be degraded by the enzymes secreted by microorganisms in the environment.<sup>94</sup> For instance, key enzymes which have been used for degradation of various polymers are listed, but are not limited to, in the following: (1) dehydrogenase for polyethylene glycol, polypropylene glycol, and polytetramethylene glycol; (2) Oxidase or dehydrogenase or hydrolase for polyvinyl alcohol; (3) lipase and cutinase for polycaprolactone; and (4) protease and lipase for polylactic acid. In hydrolytic degradation, polymers degrade with the presence of water, which breaks a covalent bond.<sup>95</sup> However, these two mechanisms are not mutually exclusive as some hydrolytically degrading polymers can also be degraded enzymatically.

Given the fact that PCL is a bioresorbable polymer FDA-approved devices such as long-term implants and controllable drug release, with a  $T_m$  near room temperature, PCL and its derivatives

receive attention in this dissertation. Kinetically, lipases could enhance the hydrolysis of the ester bonds in PCL. In 1997, Gan et al reported that PCL film could be degraded completely within 4 days in the phosphate buffer solution containing *pseudomonas lipases* (PS) but no such accelerated degradation behavior was found for *porcine pancreatic lipase* or *candida cylindracea lipase*.<sup>96</sup> Wu et al claimed an approximate 1000-fold increase in enzymatic degradation of PCL nanoparticles with the presence of the PS as compared with their pure hydrolyses.<sup>97</sup> Further, it is discovered that the degradation kinetics of several PCL-based multiblock polymers can be adjusted by varying PCL content or PCL molecular weight.<sup>98</sup> In addition to that, the enzymatic degradation rate of radiation crosslinked PCL samples could be reduced by increasing crosslink density due to the formation of network structure.<sup>99</sup> The recommended temperatures of enzymatic degradation in radiation crosslinked PCL paper are 50 °C for uncrosslinked and 55 °C for crosslinked one, respectively. Also, an appropriate enzyme concentration for degradation was found to be 1.67 mg/ml.<sup>100</sup> However, in this dissertation, the enzyme concentration of 0.4 mg/ml and degradation temperature of 37 °C have been implemented because of the following reasons: firstly, in the context of previous work from our own lab,<sup>101</sup> the degradation data of PCL-containing polymers obtained at 37 °C is quite useful for present or future application of tissue engineering; secondly, 0.4 mg/ml was determined to be the lower threshold of completely degrading polymers containing PCL subunits at 37 °C within ca. 10 days (Figure 1-8).<sup>102</sup>

## 1.5 Electrospinning

*Electrospinning* is a fabrication process of applying electric force to draw fiber with diameters in the range from nanometers to micrometers. Historically, the term “electrospinning” was first recognized and described technically in 1920 by J. F. Cooley, and since 1995 the driving mechanisms for electrospinning process have been further investigated extensively.<sup>103</sup> Today,



electrospinning has become a sophisticated, versatile technique that allows the formation of continuous, fine fibers from polymers (both synthetic and natural), and even metal alloys, ceramics.<sup>104</sup> A commonly used electrospinning setup (Scheme 1-6) is composed of a syringe with small diameter needle to carry the polymer solution, a syringe pump on which the syringe is mounted, a high voltage supply which provides the electrostatic repulsion needed by the charged polymer solution to counteract its surface tension, and a rotating, grounded mandrel which is used to collect the resulting fibers. The working mechanism<sup>105,106</sup> of such a setup is that only a cone of polymer solution is formed at the needle tip in the absence of electric field but a jet of charged polymer solution will be ejected from the cone once surface tension was overridden by electrostatic repulsion in the effect of electric driving force. The ejected jet will then travel towards the grounded collector, during which the electric force stretches the jet extensively along the traveling direction. Meanwhile, solvent evaporates quickly due to the large aspect ratio of the jet, further reducing jet diameter and increasing the surface charge density. When the surface charge density reaches at a critical point, the jet will split into a few smaller jets. This jet splitting, along with jet “whipping”, will be repeated a couple times while all solvent is removed from the jets prior to arriving at the mandrel, leaving multiple treads of tremendously stretched polymer fibers.<sup>107</sup> Generally speaking, electrospinning technique offers exceptional processability to produce highly porous, fibrous mats which are ideal not only for designing new devices and composites but also for applications including cell culture, wound dressing, and membrane filtration.<sup>108-110</sup> More importantly, lots of studies have highlighted the capacity of using a rotating mandrel in different rotation speeds to introduce fiber orientation along a common axis.<sup>111</sup> It is highly likely to encompass the mechanical properties of polymers like tensile strength and Young’s modulus, especially in the fiber direction, by manipulating molecular structure.

More recently, a new method, which is referred to as *dual-electrospinning* or *co-electrospinning*, has derived from the basic electrospinning for the purpose of achieving an interwoven polymeric composite of otherwise immiscible polymers.<sup>112,113</sup> Such method enables precise control over the relative composition for each component so as to tune the thermal, mechanical, and/or other related properties. A dual-electrospinning setup has been designed by Madhugiri et al to have the capability of ejecting two polymer solutions at the same time.<sup>114,115</sup> This setup is nearly identical to the one for the basic electrospinning but features different polymer solutions contained in two syringes located on the opposite sides of the collecting mandrel. Regarding practical applications, this technique has been employed to develop thermal-responsive SMASH materials as discussed previously.

## **1.6 Scope of Dissertation**

The objective of this dissertation is to design, fabricate, and characterize novel crosslinkable semicrystalline polymeric materials utilizing different techniques and mechanisms in order to explore their special thermomechanical features as well as the possibilities for potential industrial application based on shape memory (SM) effects. Also, this dissertation details our particular strategy of combining electrospinning process with thermally crosslinkable polymers with reversible SM properties.

### **1.6.1 2WSM Polymers**

**Chapter 2** concentrates on the fabrication and analysis of a semicrystalline polymer system via ROMP to achieve reversible actuation triggered at temperatures in the 20 – 40 °C range. Here, in light of prior work, poly(cyclooctene) (PCO) was used as the foundation of this work to design an array of crosslinkable, semicrystalline copolymers with varying chemical compositions.

Additionally, different second monomers featuring distinct steric structures were used to shift the  $T_m$ 's of corresponding resulting products, and these second monomers include 1,5-cyclooctadiene (COD), norbornene (NO), and cycloheptene (CH). The copolymers were covalently crosslinked using peroxide by compression molding. Molecular, thermal, dynamic mechanical, and shape memory properties of the synthesized copolymers were well studied. Results revealed effective control over reversible actuation behavior of the crosslinked copolymers based on the two variables: second monomer content and second monomer species.

**Chapter 3** presents the design, synthesis, and characterization of a novel, soft, biodegradable PCL-based thermoplastic polyurethane containing unsaturated allyl groups pendent to the backbone. Latent crosslinking to network form can be easily introduced by crosslinking the unsaturation covalently with a thermal initiator, enabling 1WSM and 2WSM behavior. Importantly, this material allows facile thermal and solvent processing prior to crosslinking, the latter allowing formation of fine, nano-scale fibers via ordinary electrospinning technique. Such processing enables the preparation of unique microstructures and associated of robust shape memory properties. Additionally, with presence of PCL segment, the latent-crosslinkable polyurethanes exhibited desirable biodegradability that depends on the micro- and crystalline structures. Thus, we investigated the effect of processing this material by different means (casting versus electrospinning) on properties before and after crosslinking, respectively. The molecular, thermomechanical and shape memory properties were studied, in particular. In-vitro enzymatic degradation behavior was examined, revealing a dependence on crosslinking state. We envision that this versatile polymeric material will have broad applications in the biomedical field, especially due to latent crosslinking that allows thermal or solvent processing followed by crosslinking.

### 1.6.2 SMASH Materials

The ability of shape memory polymeric materials to repair physical damage and to then restore original functionality possesses significance in the field of self-healing for a broad range of applications. In **Chapter 4**, we report on a novel, electrospun SMASH polymer blend that is built upon prior work involving a latent crosslinkable polyurethane (x-PU). This unique blend system is developed for the first time by employing a solution in which crosslinkable polyurethane and linear polyurethane (l-PU) are mixed homogeneously for electrospinning. After preparing a family of blends with varying compositions, comprehensive characterizations and various healing tests are done to reveal the effect of composition on healing performance of the materials. Moreover, damage type and molecular anisotropy were studied, respectively, in order to evaluate the dependence of healing efficiency on such factors.

### 1.6.3 Self-reversible Polymeric Actuators

In **Chapter 5**, we explore the designs and methods to attain 2WSM behavior under stress-free condition in mechanical and/or biomedical application such as self-reversible actuators. Based on the work accomplished in Chapter 3, we come up with a strategy of adjusting electrospinning parameters (i.e. ejecting flowrate and time) to yield geometrically biased bilayer without bonding issue as compared with conventional bilayers or laminated films. Besides the latent-crosslinkable polyurethane, a commercially available thermoplastic elastomer, namely Pellethane® 5863-80A, is used to provide constant stress field required for SMP to exhibit 2WSM. Increase mandrel uptake speeds during electrospinning process serves to create molecular orientation that is adopted to polarize stress difference between layers. Basic thermal, mechanical, and shape memory properties are analyzed in order to better understand the principle and to then optimize the designing. X-ray

scattering is studied to reveal the molecular orientation that exists in the composite. At the end, bench actuation testing is demonstrated by snapshots and videotaping. Further designing and optimization approaches are discussed in-depth.

## 1.7 References

1. Flory, P. J.: *Principles of Polymer Chemistry*; Cornell University Press, 1953.
2. Young, R. J.; Lovell, P. A.: *Introduction to Polymers*; 3rd; CRC Press: Boca, Florida, 2011.
3. Sperling, L. H.: *Introductions to Physical Polymer Science*; 4th; John Wiley & Sons: Hoboken, New Jersey, 2006.
4. Stevens, M. P.: *Polymer Chemistry*; Oxford University Press: New York, 1990.
5. Odian, G.: *Principles of Polymerization*; John Wiley & Sons: Hoboken, New Jersey, 2004.
6. Cowie, J. M. G.; Arrighi, V.: *Polymers: Chemistry and Physics of Modern Materials*; Taylor and Francis Group: Boca, Florida, 2008.
7. Brazel, C. S.; Rosen, S. L.: *Fundamental Principles of Polymeric Materials*; 3rd; John Wiley & Sons: Hoboken, New Jersey, 2012.
8. Li, X.; Zhang, D.; Xiang, K.; Huang, G.: Synthesis of Polyborosiloxane and its Reversible Physical Crosslinks. *RSC Adv.* **2014**, 4, 32894.
9. Zhao, J.; Fu, Y.; Liu, S.: Polyhedral Oligomeric Silsesquioxane (POSS)-modified Thermoplastic and Thermosetting Nanocomposites: A Review. *Polym. Polym. Compos.* **2008**, 16, 483 – 500.
10. McMullin, E.; Rebar, H. T.; Mather, P. T.: Biodegradable Thermoplastic Elastomer Incorporating POSS: Synthesis, Microstructure, and Mechanical Properties. *Macromolecules* **2016**, 49, 3769 – 3779.
11. Hebda, E.; Ozimek, J.; Raftopoulos, K. N.; Michałowski, S.; Pielichowski, J.; Jancia, M.; Pielichowski, K.: Synthesis and Morphology of Rigid Polyurethane Foams with POSS as Pendant Groups or Chemical Crosslinks. *Polym. Adv. Technol.* **2015**, 26, 932 – 940.

12. Matějka, L.; Murias, P.; Pleštil, J.: Effect of POSS on Thermomechanical Properties of Epoxy-POSS Nanocomposites. *European Polymer Journal* **2012**, 48, 260 – 274.
13. Lee, K. M.; Knight, P. T.; Chung, T.; Mather, P. T.: Polycaprolactone-POSS Chemical/Physical Double Networks. *Macromolecules* **2008**, 41, 4730 – 4738.
14. Victorel, M.; Sáiz, L. M.; Galante, M. J.; Oyanguren, P. A.: Effects of Physical Crosslinks on the Photoresponse of Epoxy-based Polymers. *European Polymer Journal* **2016**, 76, 256 – 265.
15. Gasa, J. V.; Weiss, R. A.; Shaw, M. T.: Ionic Crosslinking of Ionomer Polymer Electrolyte Membranes using Barium Cations. *J. Membr. Sci.* **2007**, 304, 173 – 180.
16. Qian, C.; Dong, Y.; Zhu, Y.; Fu, Y.: Two-way Shape Memory Behavior of Semicrystalline Elastomer under Stress-free Condition. *Smart Mater. Struct.* **2016**, 25, 085023.
17. Hou, H.; Di Vona, M. L.; Knauth, P.: Building Bridges: Crosslinking of Sulfonated Aromatic Polymers – A review. *J. Membr. Sci.* **2012**, 423 – 424, 113 – 127.
18. Rousseau, I. A.: Challenges of Shape Memory Polymers: A Review of the Progress Toward Overcoming SMP's Limitations. *Polym. Eng. Sci.* **2008**, 48, 2075 – 2089.
19. Hoyle, C. E.; Bowman, C. N.: Thiol-ene Click Chemistry. *Angew. Chem. Int. Ed.* **2010**, 49, 1540 – 1573.
20. Gagnon, K. D.; Lenz, R. W.; Farris, R. J.: Chemical Modification of Bacterial Elastomers: 1. Peroxide Crosslinking. *Polymer* **1994**, 35, 4358 – 4367.
21. Coran, A. Y.: *Science and Technology of Rubber*; Academic Press, New York, 1978.
22. Brydson, J. A.: *Rubbery Materials and Their Compounds*; Elsevier Applied Science, New York, 1988.

23. Imai, Y.; Kadoma, Y.; Kojima, K.: Importance of Polymerization Initiator Systems and Interfacial Initiation of Polymerization in Adhesive Bonding of Resin to Dentin. *J. Dent. Res.* **1991**, 70, 1088 – 1091.
24. Yu, Y. S.; Dubois, Ph.; Jérôme, R.; Teyssié, Ph.: Difunctional Initiators Based on 1,3-Diisopropenylbenzene. 3. Synthesis of a Pure Dilithium Adduct and Its Use as Difunctional Anionic Polymerization Initiator. *Macromolecules* **1996**, 29, 2738 – 2745.
25. Loan, L. D.: Peroxide Crosslinking Reactions of Polymers. *Pure Appl. Chem.* **1972**, 30, 173 – 180.
26. Bielinski, D. M.; Kozlowski, R.; Zaikov, G. E.: *High Performance Elastomer Materials: An Engineering Approach*; Apple Academic Press, 2014.
27. Tjong, S. C.: Structural and Mechanical Properties of Polymer Nanocomposites. *Mater. Sci. Eng. R* **2006**, 53, 73 – 197.
28. Bedi, R.; Chandra, R.; Singh, S. P.: Mechanical Properties of Polymer Concrete. *J. Compos.* **2013**, 2013, 948745.
29. Erenkov, O. Y.; Igumnov, P. V.; Nikishechkin, V. L.: Mechanical Properties of Polymer Composites. *Russ. Eng. Res.* **2010**, 30, 373 – 375.
30. Meyers, M. A.; Chawla, K. K.: *Mechanical Behavior of Materials*; 2rd; Cambridge University Press, New York, 2009.
31. Sun, L.; Huang, W. M.; Ding, Z.; Zhao, Y.; Wang, C. C.; Purnawali, H.; Tang, C.: Stimulus-responsive Shape Memory Materials: A Review. *Mater. Des.* **2012**, 33, 577 – 640.
32. Huang, W. M.; Ding, Z.; Wang, C. C.; Wei, J.; Zhao, Y.; Purnawali, H.: Shape Memory Materials. *Mater. Today* **2010**, 13, 54 – 61.



33. Lendlein, A.; Kelch, S.: Shape Memory Polymers. *Angew. Chem. Int. Ed.* **2002**, 41, 2034 – 2057.
34. Ratna, D.; Karger-Kocsis, J.: Recent Advances in Shape Memory Polymers and Composites: A Review. *J. Mater. Sci.* **2008**, 43, 254 – 269.
35. Liu, C.; Qin, H.; Mather, P. T.: Review of Progress in Shape Memory Polymers. *J. Mater. Chem.* **2007**, 17, 1543 – 1558.
36. Torbati, A. H.; Nejad, H. B.; Ponce, M.; Sutton, J. P.; Mather, P. T.: Properties of Triple Shape Memory Composites Prepared via Polymerization-induced Phase Separation. *Soft Matter* **2014**, 10, 3112 – 3121.
37. Santiago, D.; Ferrando, F.; De la Flor, S.: Influence of Holding Time on Shape Memory Recovery in a Polyurethane Shape Memory Polymer. *J. Mater. Eng. Perform.* **2014**, 23, 2567 – 2573.
38. Lendlein, A.; Jiang, H.; Junger, O.; Langer, R.: Light-induced Shape Memory Polymers. *Nature* **2005**, 434, 879 – 882.
39. Gu, X.; Mather, P. T.: Water-triggered Shape Memory of Multiblock Thermoplastic Polyurethanes (TPUs). *RSC Adv.* **2013**, 3, 15783 – 15791.
40. Lv, H.; Leng, J.; Liu, Y.; Du, S.: Shape Memory Polymer in Response to Solution. *Adv. Eng. Mater.* **2008**, 10, 592 – 595.
41. Luo, X.; Mather, P. T.: Conductive Shape Memory Nanocomposites for High Speed Electrical Actuation. *Soft Matter* **2010**, 6, 2146 – 2149.
42. Schmidt, A. M.: Electromagnetic Activation of Shape Memory Polymer Networks Containing Magnetic Nanoparticles. *Macromol. Rapid Commun.* **2006**, 27, 1168 – 1172.

43. Chen, H.; Li, Y.; Liu, Y.; Gong, T.; Wang, L.; Zhou, S.: Highly pH-sensitive Polyurethane Exhibiting Shape Memory and Drug Release. *Polym. Chem.* **2014**, 5, 5168 – 5174.
44. Mather, P. T.; Luo, X.; Rousseau, I. A.: Shape Memory Polymer Research. *Annu. Rev. Mater. Res.* **2009**, 39, 445 – 471.
45. Chung, T.; Romo-Uribe A.; Mather, P. T.: Two-way Reversible Shape Memory in a Semicrystalline Network. *Macromolecules* **2008**, 41, 184 – 192.
46. Kunzelman, J.; Chung, T.; Mather, P. T.; Weder, C.: Shape Memory Polymers with Built-in Threshold Temperature Sensors. *J. Mater. Chem.* **2008**, 10, 1082 – 1086.
47. Knight, P. T.; Lee, K. M.; Qin, H.; Mather, P. T.: Biodegradable Thermoplastic Polyurethanes Incorporating Polyhedral Oligosilsesquioxane. *Biomacromolecules* **2008**, 9, 2458 – 2467.
48. Lendlein, A.; Langer, R.: Biodegradable, Elastic Shape-memory Polymers for Potential Biomedical Applications. *Science* **2002**, 296, 1673 – 1676.
49. Mandelkern, L.; Robert, D. E.; Diorio, A. F.; Posner, A. S.: Dimensional Changes in Systems of Fibrous Macromolecules: Polyethylene. *J. Am. Chem. Soc.* **1959**, 81, 4148 – 4157.
50. Thomsen III, D. L.; Keller, P.; Naciri, J.; Pink, R.; Jeon, H.; Shenoy, D.; Ratna, B. R.: Liquid Crystal Elastomers with Mechanical Properties of a Muscle. *Macromolecules* **2001**, 34, 5868 – 5875.
51. Yu, Y.; Ikeda, T.: Soft Actuators Based on Liquid-crystalline Elastomers. *Angew. Chem. Int. Ed.* **2006**, 45, 5416 – 5418.
52. Ohm, C.; Brehmer, M.; Zentel, R.: Liquid Crystalline Elastomers as Actuators and Sensors. *Adv. Mater.* **2010**, 22, 3366 – 3387.

53. Krause, S.; Zander, F.; Bergmann, G.; Brandt, H.; Wertmer, H.; Finkelmann, H.: Nematic Main-chain Elastomers: Coupling and Orientational Behavior. *Comptes Rendus Chimie* **2009**, 12, 85 – 104.
54. Liu, C.; Chun, S. B.; Mather, P. T.: Chemically Cross-linked Polycyclooctene: Synthesis, Characterization, and Shape Memory Behavior. *Macromolecules* **2002**, 35, 9868 – 9874.
55. Chung, T.: *New Shape Memory Effects in Semicrystalline Polymeric Network*; Ph.D. Dissertation, Case Western Reserve University, 2009.
56. Burke, K. A.; Mather, P. T.: Soft Shape Memory in Main-chain Liquid Crystalline Elastomers. *J. Mater. Chem.* **2010**, 20, 3449 – 3457.
57. Qin, H.; Mather, P. T.: Combined One-way and Two-way Shape Memory in a Glass-forming Nematic Network. *Macromolecules* **2009**, 42, 273 – 280.
58. Baker, R. M.; Henderson, J. H.; Mather, P. T.: Shape Memory Poly( $\epsilon$ -caprolactone)-*co*-poly(ethylene glycol) Foams with Body Temperature Triggering and Two-way Actuation. *J. Mater. Chem. B* **2013**, 1, 4916 – 4920.
59. Bai, Y.; Zhang, X.; Wang, Q.; Wang, T.: A Tough Shape Memory Polymer with Triple-shape Memory and Two-way Shape Memory Properties. *J. Mater. Chem. A* **2014**, 2, 4771 – 4778.
60. Pandini, S.; Baldi, F.; Paderni, K.; Messori, M.; Toselli, M.; Pilati, F.; Gianoncelli, A.; Brisotto, M.; Bontempi, E.; Riccò, T.: One-way and Two-way Shape Memory Behavior of Semi-crystalline Networks Based on Sol-gel Cross-linked Poly( $\epsilon$ -caprolactone). *Polymer* **2013**, 54, 4253 – 4265.
61. Li, J.; Rodgers, W. R.; Xie, T.: Semi-crystalline Two-way Shape Memory Elastomer. *Polymer* **2011**, 52, 5320 – 5325.

62. Chen, S.; Hu, J.; Zhuo, H.: Properties and Mechanism of Two-way Shape Memory Polyurethane Composites. *Compos. Sci. Technol.* **2010**, 70, 1437 – 1443.
63. Chen, S.; Yang, S.; Li, Z.; Xu, S.; Yuan, H.; Chen, S.; Ge, Z.: Electroactive Two-way Shape Memory Polymer Laminates. *Polym. Compos.* **2015**, 36, 439 – 444.
64. Kolesov, I.; Dolynchuk, O.; Borrech, S.; Radush, H.: Morphology-controlled Multiple One- and Two-way Shape-memory Behavior of Cross-linked Polyethylene/poly( $\epsilon$ -caprolactone) blends. *Polym. Adv. Technol.* **2014**, 25, 1315 – 1322.
65. Shenoy, D. K.; Thomsen III, D. L.; Srinivasan, A.; Keller, P.; Ratna, B. R.: Carbon Coated Liquid Crystal Elastomer Film for Artificial Muscle Applications. *Sensors and Actuators A* **2002**, 96, 184 – 188.
66. Leng, J.; Lan, X.; Liu, Y.; Du, S.: Shape Memory Polymers and Their Composites: Stimulus Methods and Applications. *Prog. Mater. Sci.* **2011**, 56, 1077 – 1135.
67. Behl, M.; Kratz, K.; Zotzmann, J.; Nöchel, U.; Lendlein, A.: Reversible Bidirectional Shape-memory Polymers. *Adv. Mater.* **2013**, 25, 4466 – 4469.
68. Zhou, J.; Turner, A.; Brosnan, S.; Li, Q.; Carrillo, J. Y.; Nykypanchuk, D.; Gang, O.; Ashby, V. S.; Dobrynin, A. V.; Sheiko, S. S.: Shapeshifting: Reversible Shape Memory in Semicrystalline Elastomers. *Macromolecules*, **2014**, 47, 1768 – 1776.
69. Westbrook, K. K.; Mather, P. T.; Parakh, V.; Dunn, M. L.; Ge, Q.; Lee, B. M.; Qi, H. J.: Two-way Reversible Shape Memory Effects in a Free-standing Polymer Composite. *Smart Mater. Struct.* **2011**, 20, 065010.
70. Wool, R. P.: Self-healing Materials: A Review. *Soft Matter* **2008**, 4, 400 – 418.

71. Yuan, Y. C.; Yin, T.; Rong, M. Z.; Zhang, M. Q.: Self-healing in Polymers and Polymer Composites. Concepts, Realization and Outlook: A Review. *eXPRESS Polym. Lett.* **2008**, 2, 238 – 250.
72. Blaiszik, B. J.; Kramer, S. L. B.; Olugebefola, S. C.; Moore, J. S.; Sottos, N. R.; White, S. R.: Self-healing Polymers and Composites. *Annu. Rev. Mater. Res.* **2010**, 40, 179 – 211.
73. Wu, D. Y.; Meure, S.; Solomon, D.: Self-healing Polymeric Materials: A Review of Recent Developments. *Prog. Polym. Sci.* **2008**, 33, 479 – 522.
74. Yang, Y.; Urban, M. W.: Self-healing Polymeric Materials. *Chem. Soc. Rev.* **2013**, 42, 7446 – 7467.
75. Trask, R. S.; Williams, H. R.; Bond, I. P.; Self-healing Polymer Composites: Mimicking Nature to Enhance Performance. *Bioinspir. Biomim.* **2007**, 2, 1 – 9.
76. White, S. R.; Sottos, N. R.; Geubelle, P. H.; Moore, J. S.; Kessler, M. R.; Sriram, S. R.; Brown, E. N.; Viswanathan, S.: Automatic Healing of Polymer Composites. *Nature* **2001**, 409, 794 – 797.
77. Liu, Y.; Chuo, T.: Self-healing Polymers Based on Thermally Reversible Diels-Alder Chemistry. *Polym. Chem.* **2013**, 4, 2194 – 2205.
78. Yarlagadda, S.; Kim, H. J.; Gillespie, J. W.; Shevchenko, N. B.; Fink, B. K.: A Study on the Induction Heating of Conductive Fiber Reinforced Composites. *J. Compos. Mater.* **2002**, 36, 401 – 421.
79. Wu, X. F.; Rahman, A.; Zhou, Z.; Pelot, D. D.; Sinha-Ray, S.; Chen, B.; Payne, S.; Yarin, A. L.: Electrospinning Core-shell Nanofibers for Interfacial Toughening and Self-healing of Carbon-fiber/epoxy composites. *J. Appl. Polym. Sci.* **2013**, 129, 1383 – 1393.

80. Kirkby, E. L.; Rule, J. D.; Michaud, V. J.; Sottos, N. R.; White, S. R.; Manson, J. E.: Embedded Shape-memory Alloy Wires for Improved Performance of Self-healing Polymers. *Adv. Funct. Mater.* **2008**, 18, 2253 – 2260.
81. Neuser, S.; Michaud, V.; White, S. R.: Improving Solvent-based Self-healing Materials through Shape Memory Alloys. *Polymer* **2012**, 53, 370 – 378.
82. Li, G.; Meng, H.; Hu, J.: Healable Thermoset Polymer Composite Embedded with Stimuli-responsive Fibers. *J. R. Soc. Interface* **2012**, 9, 3279 – 3287.
83. Li, G.; Shojaei, A.: A Viscoplastic Theory of Shape Memory Polymer Fibers with Application to Self-healing Materials. *Proc. R. Soc. A* **2012**, 468, 2319 – 2346.
84. Lu, X.; Fei, G.; Xia, H.; Zhao, Y.: Ultrasound Healable Shape Memory Dynamic Polymers. *J. Mater, Chem. A* **2014**, 2, 16051 – 16060.
85. Rivero, G.; Nguyen, L. T.; Hillewaere, X. K. D.; Du Prez, F. E.: One-pot Thermoremendable Shape Memory Polyurethanes. *Macromolecules* **2014**, 47, 2010 – 2018.
86. Zhang, J.; Niu, Y.; Huang, C.; Xiao, L.; Chen, Z.; Yang, K.; Wang, Y.: Self-healable and Recyclable Triple-shape PPDO-PTMEG Co-network Constructed through Thermoreversible Diels-Alder Reaction. *Polym. Chem.* **2012**, 3, 1390 – 1393.
87. Rodriguez, E. D.; Luo, X.; Mather, P. T.: Linear/network Poly( $\epsilon$ -caprolactone) Blends Exhibiting Shape Memory Assisted Self-healing (SMASH). *ACS Appl. Mater. Interfaces* **2011**, 3, 152 – 161.
88. Luo, X.; Mather, P. T.: Shape Memory Assisted Self-healing Coating. *ACS Macro Lett.* **2013**, 2, 152 – 156.
89. Nejad, H. B.; Garrison, K. L.; Mather, P. T.: Comparative Analysis of Shape Memory-based Self-healing Coatings. *J. Polym. Sci., Part B: Polym. Phys.* **2016**, 54, 1415 – 1426.

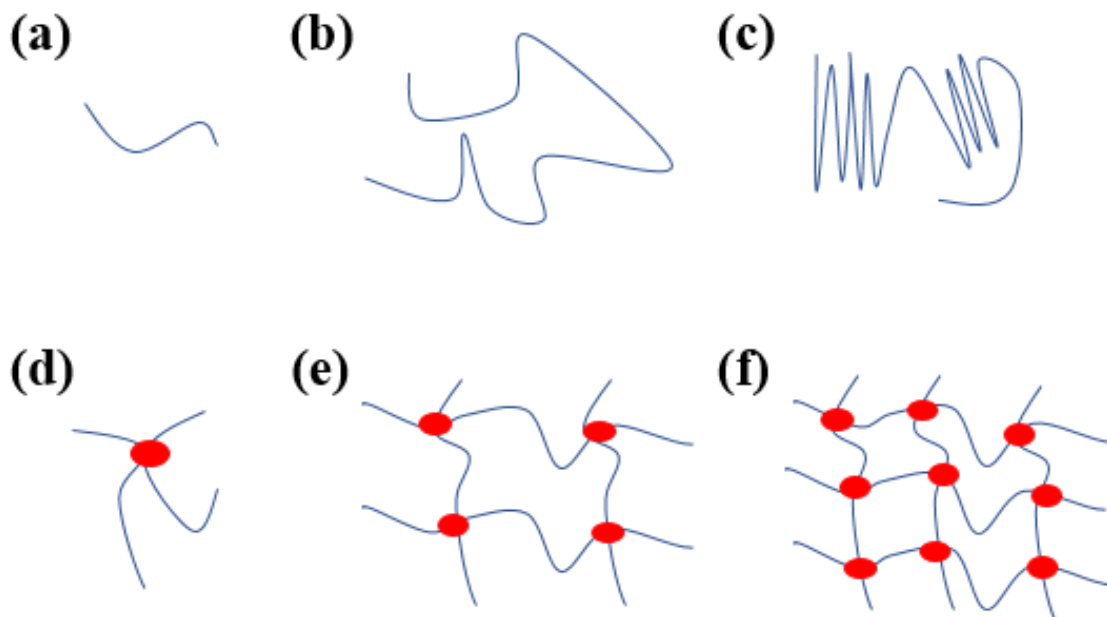
90. Freed, L. E.; Vunjal-Novakovic, G.; Biron, R. J.; Eagles, D. B.; Lesnoy, D. C.; Barlow, S. K.; Langer, R.: Biodegradable Polymer Scaffolds for Tissue Engineering. *Bio/Technology* **1994**, 12, 689 – 693.
91. Young, C. S.; Terada, S.; Vacanti, J. P.; Honda, M.; Bartlett, J. D.; Yelick, P. C.: Tissue Engineering of Complex Tooth Structures on Biodegradable Polymer Scaffolds. *J. Dent. Res.* **2002**, 81, 695 – 700.
92. Nair, L. S.; Laurencin, C. T.: Biodegradable Polymers as Biomaterials. *Prog. Polym. Sci.* **2007**, 32, 762 – 798.
93. Uhrich, K. E.; Cannizzaro, S. M.; Langer, R. S.; Shakesheff, K. M.: Polymeric Systems for Controlled Drug Release. *Chem. Rev.* **1999**, 99, 3181 – 3198.
94. Banerjee, A.; Chatterjee, K.; Madras, G.: Enzymatic Degradation of Polymers: A Brief Review. *Mater. Sci. Technol.* **2014**, 30, 567 – 573.
95. Hofmann, D.; Entrialgo-Castaño, M.; Kratz, K.; Lendlein, A.: Knowledge-based Approach Towards Hydrolytic Degradation of Polymer-based Biomaterials. *Adv. Mater.* **2009**, 21, 3237 – 3245.
96. Gan, Z.; Liang, Q.; Zhang, J.; Jing, X.: Enzymatic Degradation of Poly( $\epsilon$ -caprolactone) Film in Phosphate Buffer Solution Containing Lipases. *Polym. Degrad. Stab.* **1997**, 56, 209 – 213.
97. Wu, C.; Jim, T. F.; Gan, Z.; Wang, S.: A Heterogeneous Catalytic Kinetics for Enzymatic Biodegradation of Poly( $\epsilon$ -caprolactone) nano-particles in Aqueous Solution. *Polymer* **2000**, 41, 3593 – 3597.

98. Kulkarni, A.; Reiche, J.; Hartmann, J.; Kratz, K.; Lendlein, A.: Selective Enzymatic Degradation of Poly( $\epsilon$ -caprolactone) Containing Multiblock Copolymers. *Eur. J. Pharm. Biopharm.* **2008**, 68, 46 – 56.
99. Darwis, D.; Mitomo, H.; Enjoji, T.; Yoshi, F.; Makuuchi, K.: Enzymatic Degradation of Radiation Crosslinked Poly( $\epsilon$ -caprolactone). *Polym. Degrad. Stab.* **1998**, 62, 259 – 265.
100. Kaplan, D. L.; Mayer, J. M.; Greenberger, M.; Gross, R.; McCarthy, S.: Degradation Methods and Degradation Kinetics of Polymer Films. *Polym. Degrad. Stab.* **1994**, 45, 165 – 172.
101. Gu, X.; Wu, J.; Mather, P. T.: Polyhedral Oligomeric Silsesquioxane (POSS) Suppresses Enzymatic Degradation of PCL-based Polyurethanes. *Biomacromolecules* **2011**, 12, 3066 – 3077.
102. Rice, M. A.; Sanchez-Adams, J.; Anseth, K. S.: Exogenously Triggered, Enzymatic Degradation of Photopolymerized Hydrogels with Polycaprolactone Subunits: Experimental Observation and Modeling of Mass Loss Behavior. *Biomacromolecules* **2006**, 7, 1968 – 1975.
103. Stanger, J.; Tucker, N.; Staiger, M.: *Electrospinning*; Rapra Technology Ltd., 2008.
104. Greiner, A.; Wendroff, J. H.: Electrospinning: A Fascinating Method for the Preparation of Ultrathin Fibers. *Angew. Chem. Int. Ed.* **2007**, 46, 5670 – 5703.
105. Huang, Z.; Zhang, Y.; Kotaki, M.; Ramakrishana, S.: A Review on Polymer Nanofibers by Electrospinning and Their Applications in Nanocomposites. *Compos. Sci. Technol.* **2003**, 63, 2223 – 2253.
106. Doshi, J.; Reneker, D. H.: Electrospinning Process and Applications of Electrospun Fibers. *J. Electrostat.* **1995**, 35, 151 – 160.

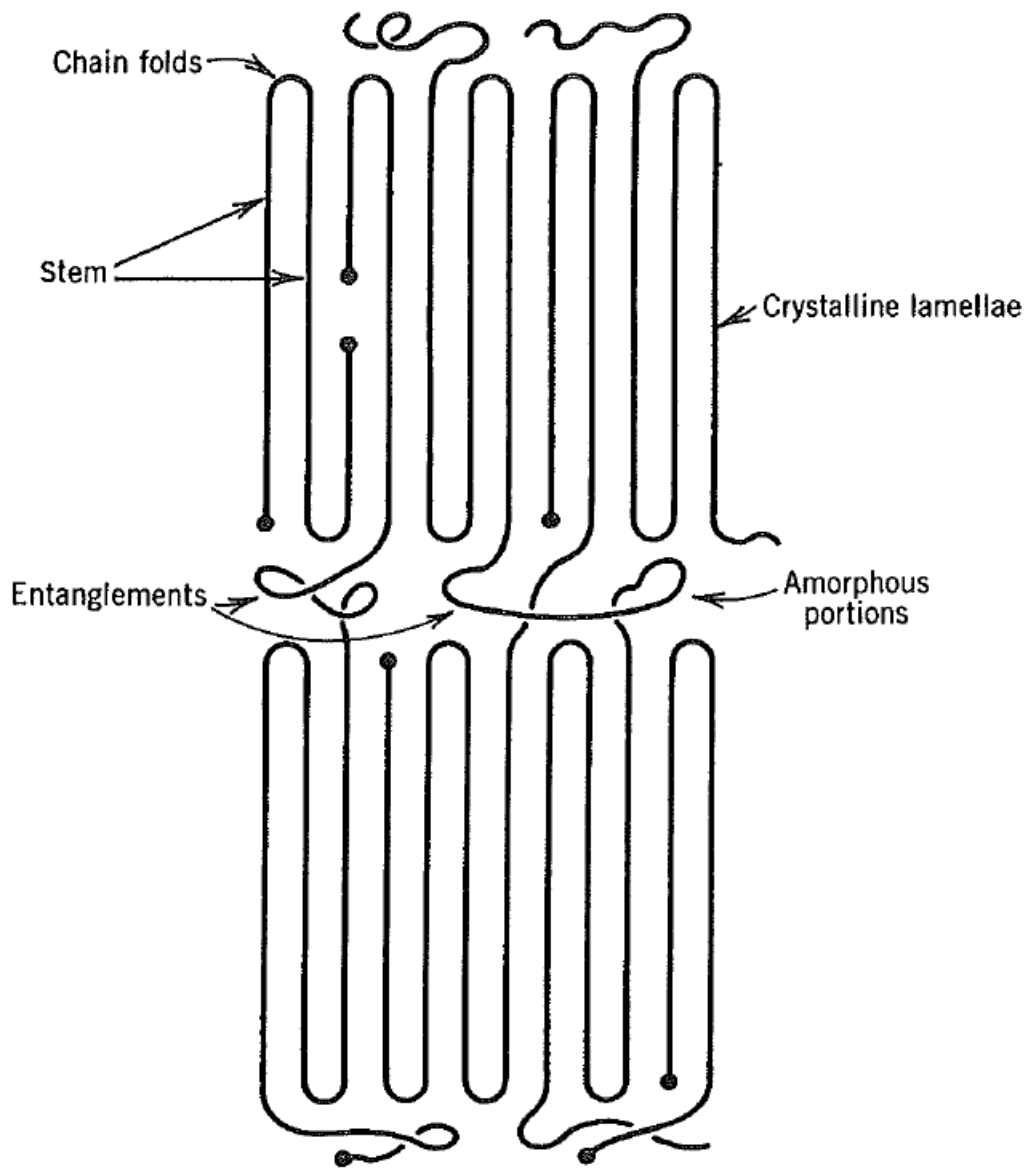


107. MacDiarmid, A. G.; Jones Jr., W. E.; Norris, I. D.; Gao, J.; Johnson Jr., A. T.; Pinto, N. J.; Hone, J.; Han, B.; Ko, F. K.; Okuzaki, H.; Llaguno, M.: Electrostatically-generated Nanofibers of Electronic Polymers. *Synth. Met.* **2001**, 119, 27 – 30.
108. Choi, D. J.; Choi, S. M.; Kang, H. Y.; Min, H.; Lee, R.; Ikram, M.; Subhan, F.; Jin, S. W.; Jeong, Y. H.; Kwak, J.; Yoon, S.: Bioactive Fish Collagen/polycaprolactone Composite Nanofibrous Scaffolds Fabricated by Electrospinning for 3D Cell Culture. *J. Biotechnol.* **2015**, 205, 47 – 58.
109. Hong, Y.; Li, Y.; Zhuang, X.; Chen, X.; Jing, X.: Electrospinning of Multicomponent Ultrathin Fibrous Nonwovens for Semi-occlusive Wound Dressings. *J. Biomed. Mater. Res. A* **2009**, 89, 345 – 354.
110. Cho, B. M.; Nam, Y. S.; Cheon, J. Y.; Park, W. H.: Residual Charge and Filtration Efficiency of Polycarbonate Fibers Membranes Prepared by Electrospinning. *J. Appl. Polym. Sci.* **2015**, 132, 41340.
111. Edwards, M. D.; Mitchell, G. R.; Mohan, S. D.; Olley, R. H.: Development of Orientation During Electrospinning of Fibers of Poly( $\epsilon$ -caprolactone). *Eur. Polym. J.* **2010**, 46, 1175 – 1183.
112. Robertson, J. M.; Nejad, H. B.; Mather, P. T.: Dual-spun Shape Memory Elastomeric Composites. *ACS Macro Lett.* **2015**, 4, 436 – 440.
113. Nejad, H. B.; Robertson, J. M.; Mather, P. T.: Interwoven Polymer Composites via Dual-electrospinning with Shape Memory and Self-healing Properties. *MRS Commun.* **2015**, 5, 211 – 221.

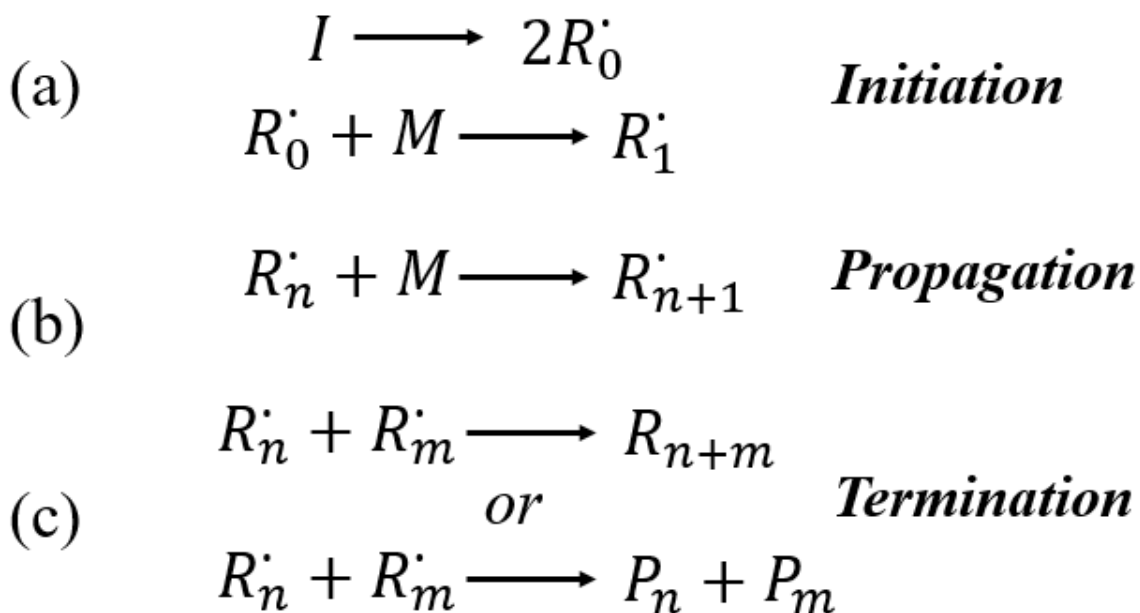
114. Madhugiri, S.; Dalton, A.; Gutierrez, J.; Ferraris, J. P.; Balkus, K. J.: Electrospun MEH-PPV/SBA-15 Composite Nanofibers Using A Dual Syringe Method. *J. Am. Chem. Soc.* **2003**, 125, 14531 – 14538.
115. Voorneveld, J.; Oosthuysen, A.; Franz, T.; Zilla, P.; Bezuidenhout, D.: Dual Electrospinning with Sacrificial Fibers for Engineered Porosity and Enhancement of Tissue Ingrowth. *J. Biomed. Mater. Res. B: Appl. Biomater.* **2016**. DOI: 10.1002/jbm.b.33695.



**Scheme 1-1.** Schematic Drawings of (a) monomer, (b) linear polymer, (c) thermoplastic, (d) crosslink, (e) elastomer, and (f) thermoset.

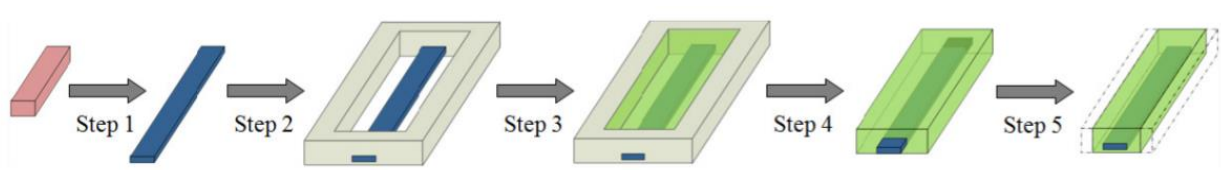


**Scheme 1-2.** Polymer molecular structure and morphology. (Adapted with permission from Sperling, L. H.: *Introductions to Physical Polymer Science*; 4th; John Wiley & Sons: Hoboken, New Jersey, 2006; p 5.).

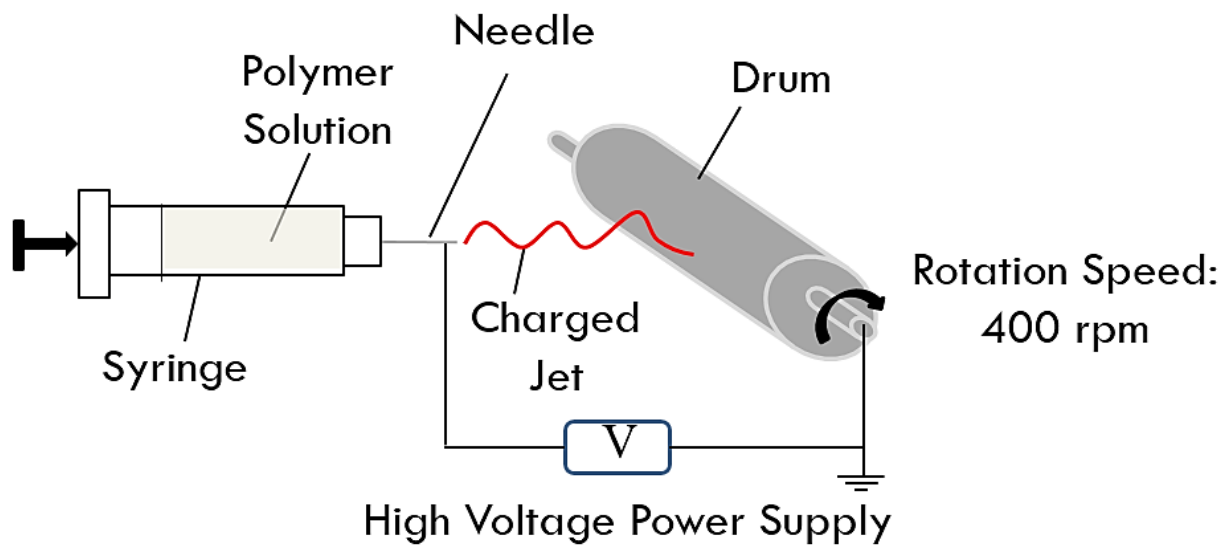


**Scheme 1-3.** Free radical polymerization divided into three distinct stages: (a) initiation, (b) propagation, and (c) termination. *I* represents the initiator,  $R_0^\cdot$  stands for active radical, *M* is the monomer,  $R_1^\cdot$  is the active polymer chain at early stage.  $R_n^\cdot$  is the extending chain with *n* number of monomers and  $R_{n+1}^\cdot$  is after the addition of one repeat unit.  $R_{n+m}$  is the resulting polymer terminated by recombination where  $P_n + P_m$  are by disproportionation.





**Scheme 1-5.** Schematic detailing the bimorph actuator fabrication process. Step 1: the DCP-crosslinked PCO strip is programmed above its  $T_m$  and its shape is fixed by cooling below its  $T_m$ ; Step 2: the programmed strip is mounted inside the custom-made aluminum mold; Step 3: the matrix material is injected inside the mold and photo-cured; Step 4: the mold is further thermally cured and the pre-sectioned actuator is removed; Step 5: the actuator is sectioned to the required geometry. (Adapted with permission from Westbrook, K. K.; Mather, P. T.; Parakh, V.; Dunn, M. L.; Ge, Q.; Lee, B. M.; Qi, H. J.: Two-way Reversible Shape Memory Effects in a Free-standing Polymer Composite. *Smart Mater. Struct.* **2011**, 20, 065010.).



**Scheme 1-6.** Schematic of electrospinning setup used for producing polymer fibers. Polymer fibers are formed during flight of polymer solution jet over electric field while solvent evaporates.



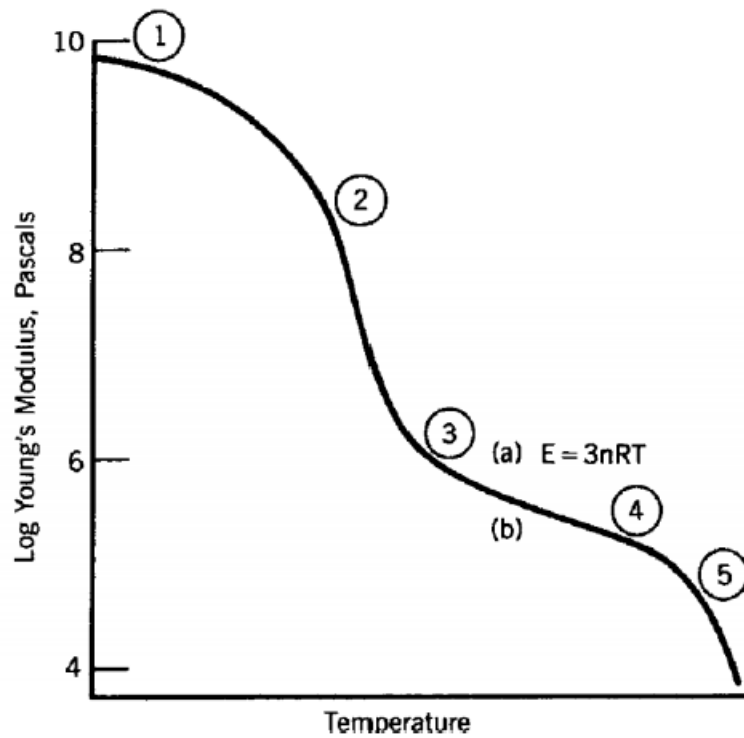


**Figure 1-1.** Idealized Young's Modulus profile of a polymer as a function of temperature: ① glassy region; ② glass transition; ③ rubbery plateau region; ④ rubbery flow region; ⑤ viscous flow region. (Adapted with permission from Sperling, L. H.: *Introductions to Physical Polymer Science*; 4th; John Wiley & Sons: Hoboken, New Jersey, 2006; p 8.).

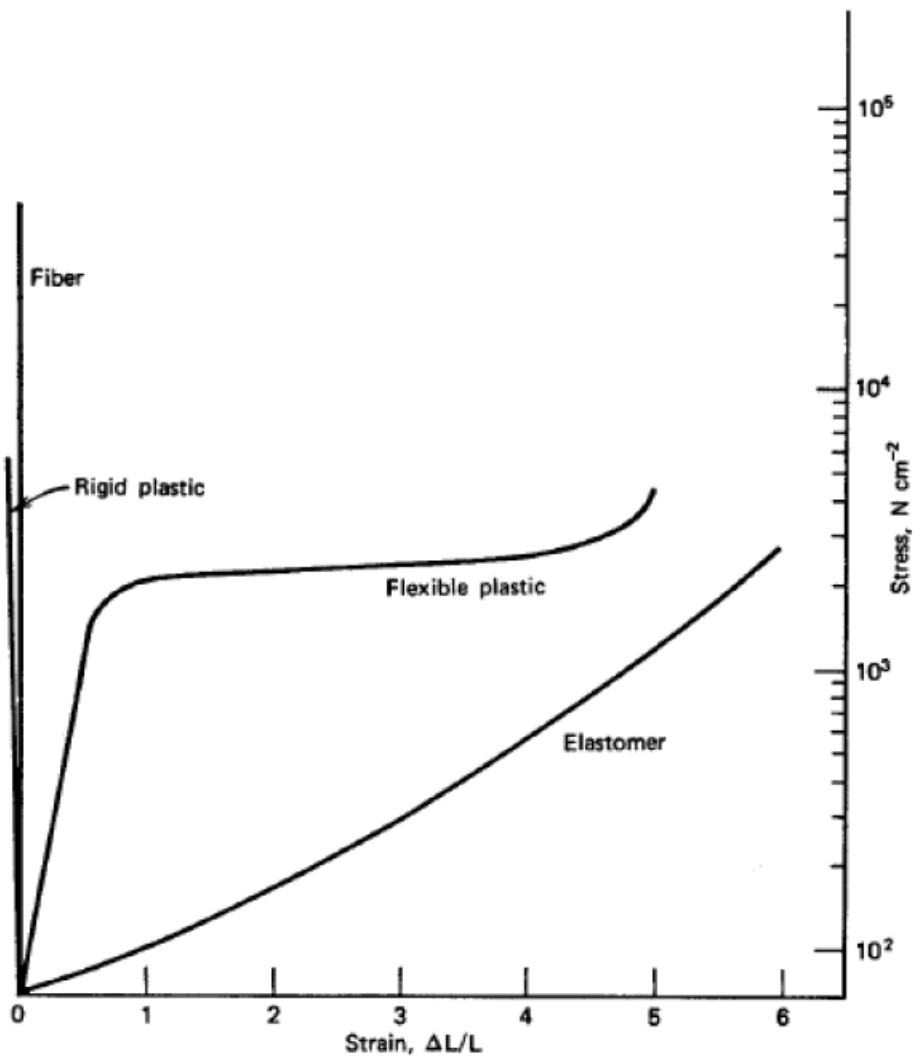


**Figure 1-2.** Stress-strain behaviors of common fiber, rigid plastic, flexible plastic, and elastomer. (Adapted with permission from Odian, G.: *Principles of Polymerization*; John Wiley & Sons: Hoboken, New Jersey, 2004; p 812.).

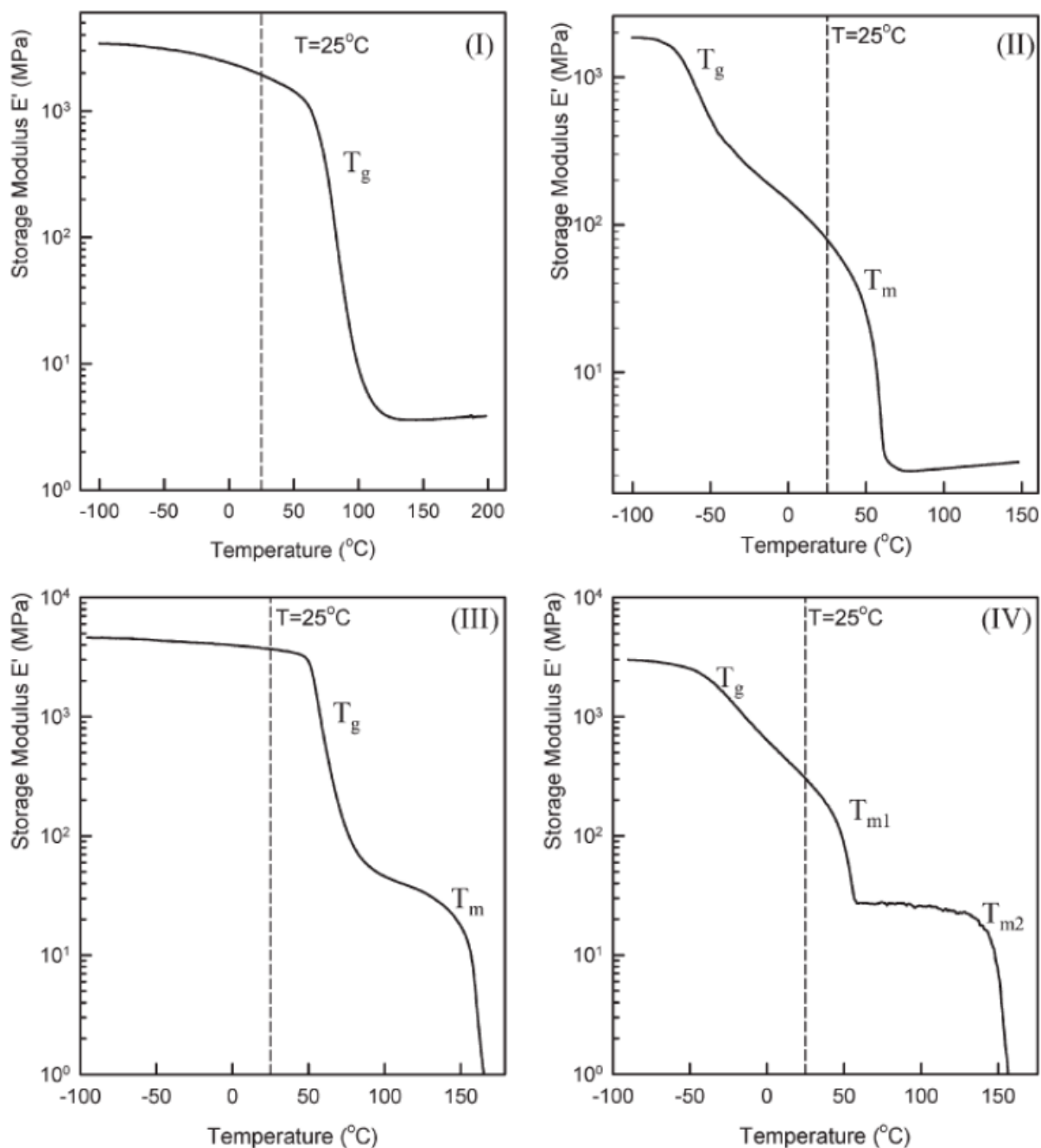


**Figure 1-3.** Demonstration of four classes of shape memory polymers in terms of their dynamic mechanical behavior: (I) chemically crosslinked glassy thermosets, (II) chemically crosslinked semicrystalline rubbers, (III) physically crosslinked thermoplastics, and (IV) physically crosslinked block copolymers. (Adapted with permission from Liu, C.; Qin, H.; Mather, P. T.: Review of Progress in Shape Memory Polymers. *J. Mater. Chem.* **2007**, 17, 1543 – 1558.).

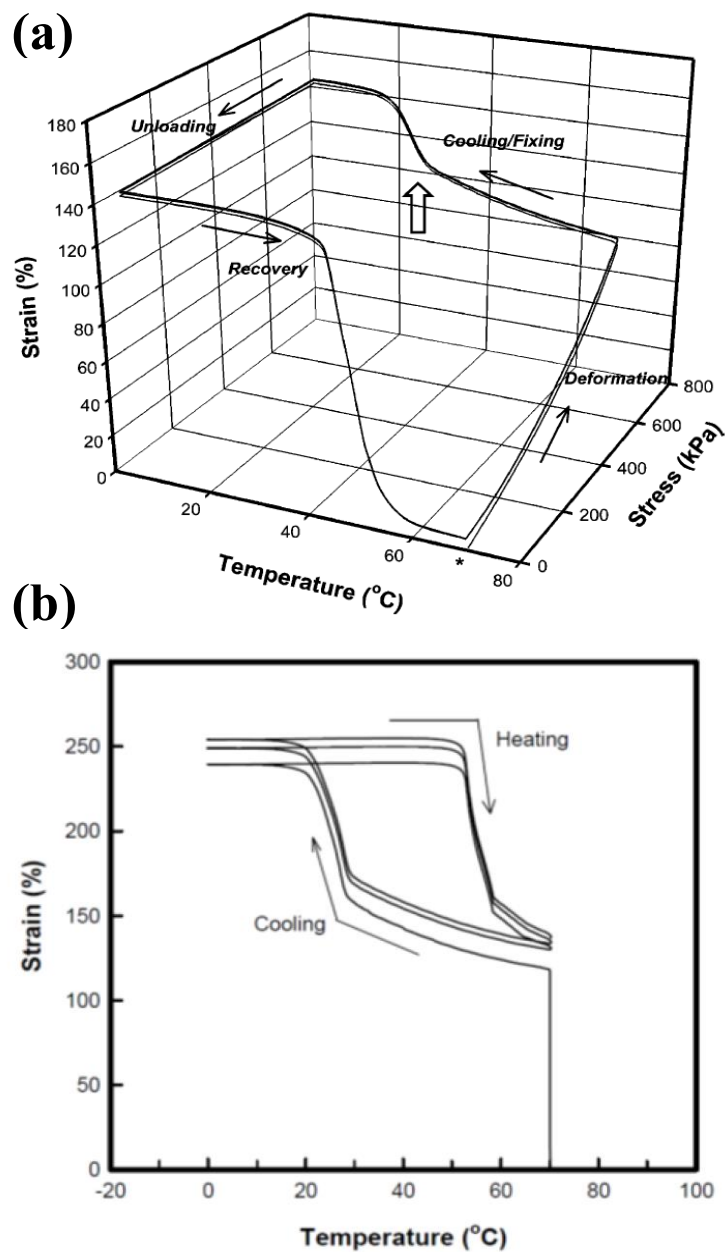


**Figure 1-4.** (a) One-way shape memory (1WSM) cycles/loops for an example of a crosslinked poly(cyclooctene). (b) Two-way shape memory (2WSM) cycles/loops for an example of an end-linked polycaprolactone. (Adapted with permission from Chung, T.; Romo-Uribe A.; Mather, P. T.: Two-way Reversible Shape Memory in a Semicrystalline Network. *Macromolecules* **2008**, 41, 184 – 192.).

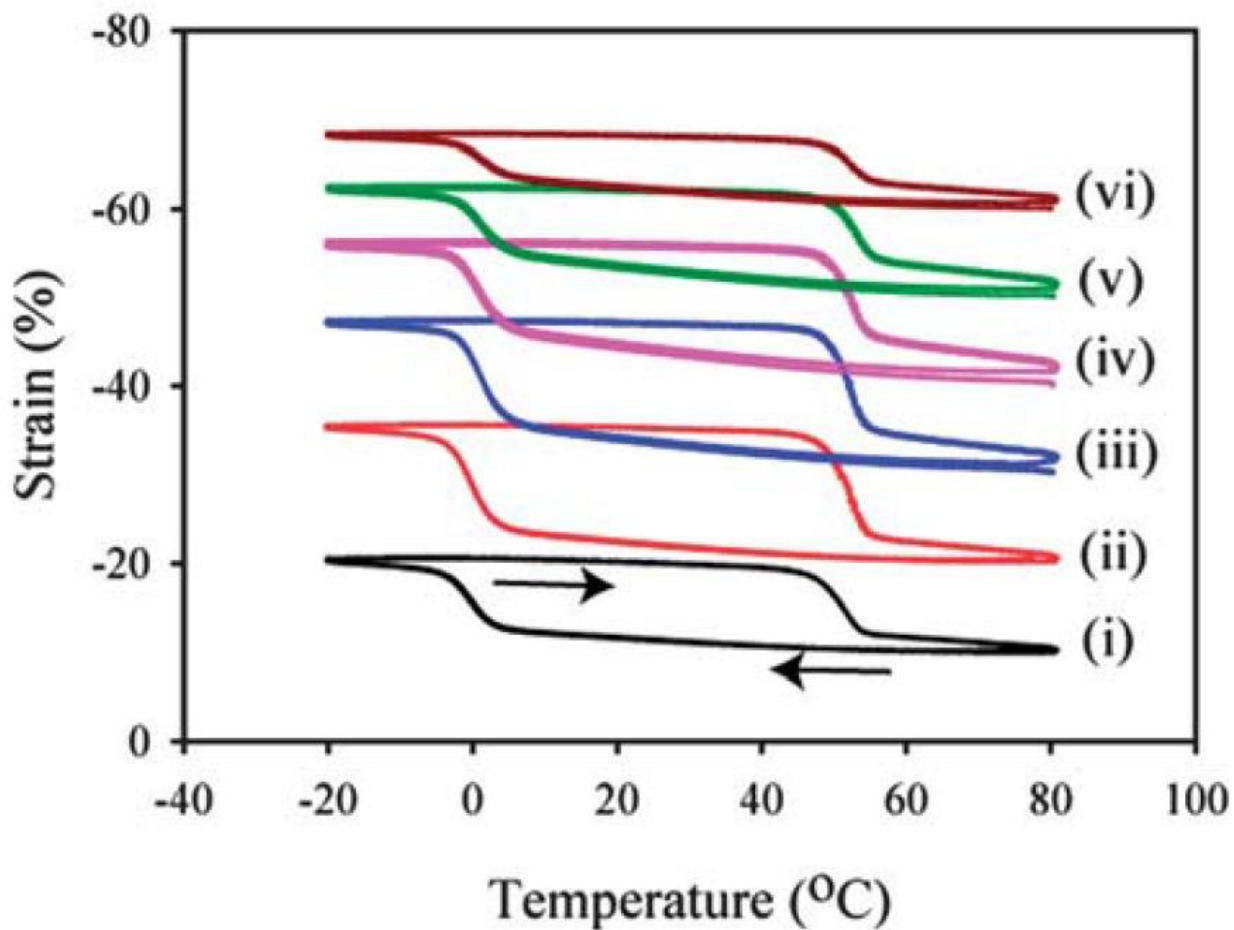


**Figure 1-5.** Two-way reversible actuation of an PCL-*co*-PEG SMP foam with (i) 10%, (ii) 20%, (iii) 30%, (iv) 40%, (v) 50%, and (vi) 60% initial applied strain. (Adapted with permission from Baker, R. M.; Henderson, J. H.; Mather, P. T.: Shape Memory Poly( $\epsilon$ -caprolactone)-*co*-poly(ethylene glycol) Foams with Body Temperature Triggering and Two-way Actuation. *J. Mater. Chem. B* **2013**, 1, 4916 – 4920.).

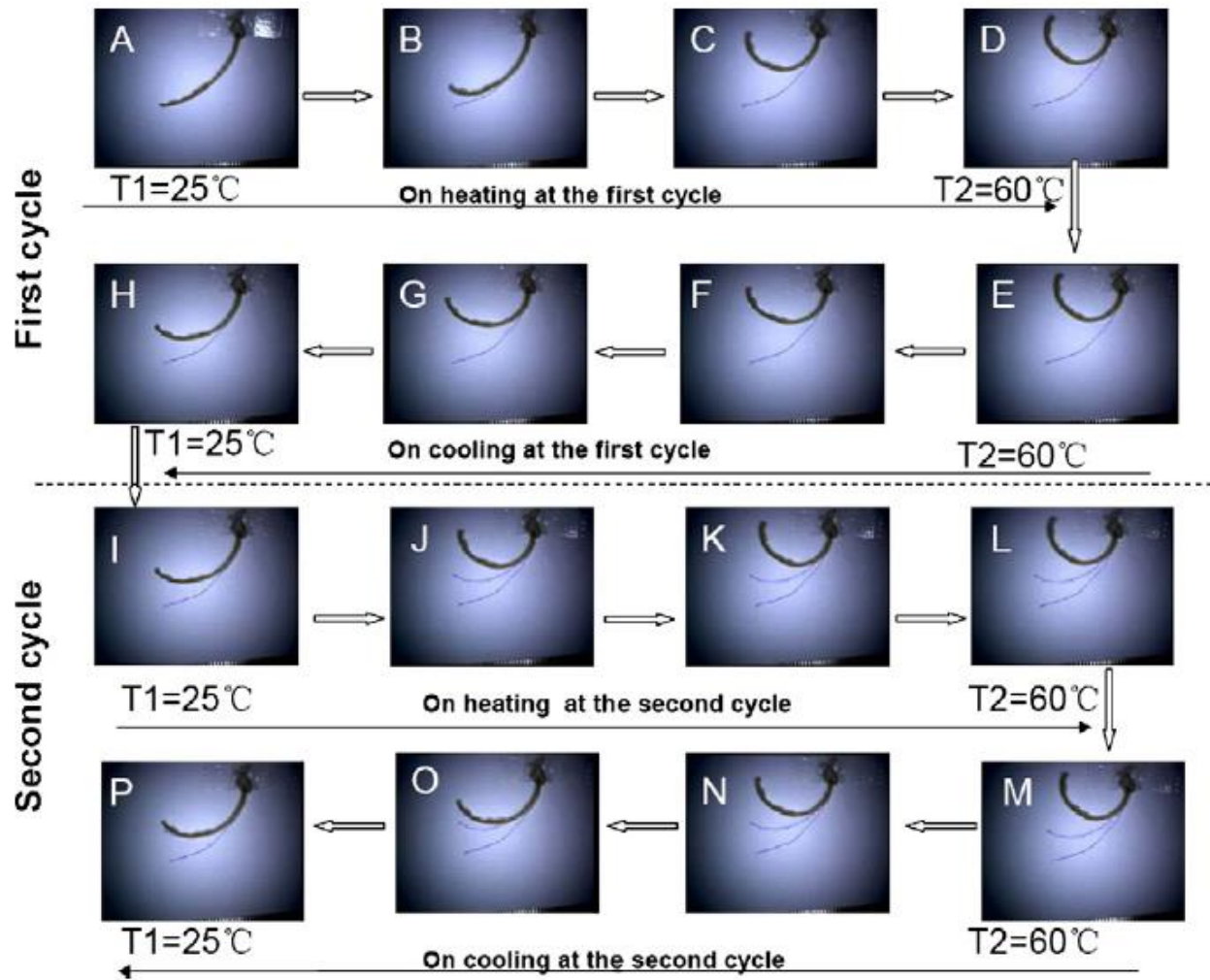


**Figure 1-6.** Two-way shape memory behavior of the SMPU-EPU laminated composite. (Adapted with permission from Chen, S.; Hu, J.; Zhuo, H.: Properties and Mechanism of Two-way Shape Memory Polyurethane Composites. *Compos. Sci. Technol.* **2010**, 70, 1437 – 1443.).

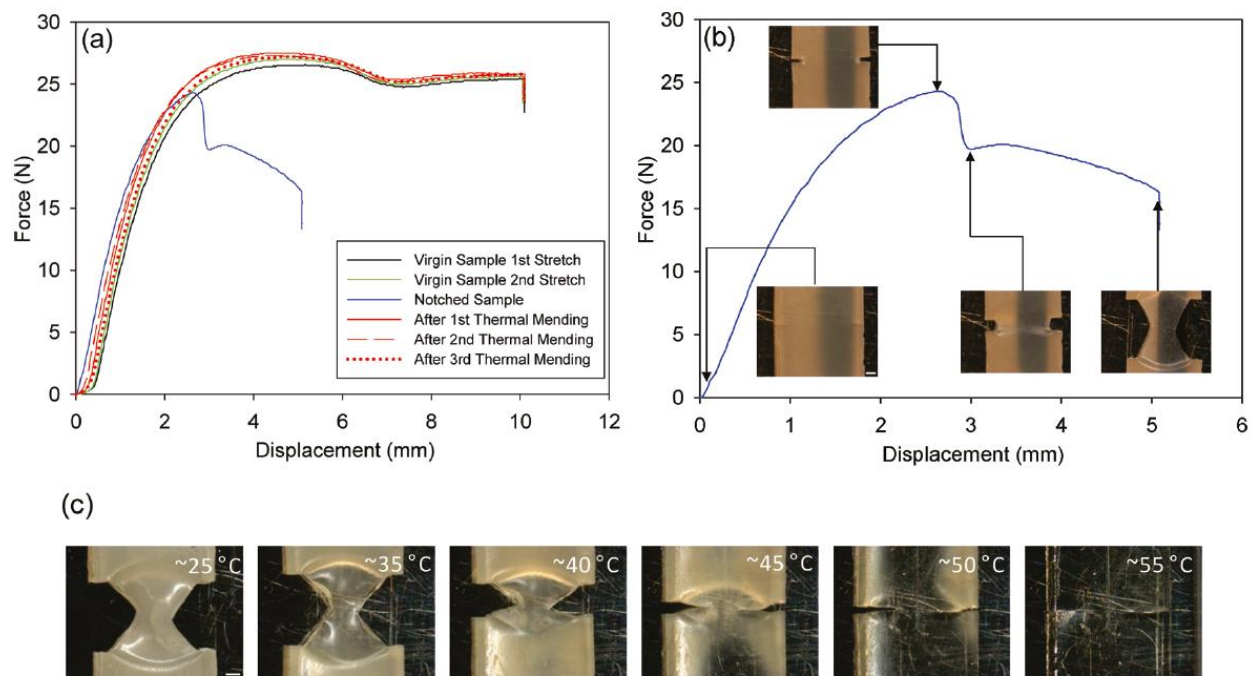


**Figure 1-7.** (a) Force-displacement profiles for the virgin, damaged, and healed state of a l-PCL:n-PCL blend. (b) Notched l-PCL:n-PCL blend showing stereo micrographs of deformation and crack growth clamped in the Linkam tensile stage (scale bar: 500  $\mu\text{m}$ ). (c) Snapshots of crack closure and crack rebonding when the sample was unclamped from the Linkam tensile stage and heated to the temperature indicated above (stereo micrographs scale bar: 500  $\mu\text{m}$ ). (Adapted with permission from Rodriguez, E. D.; Luo, X.; Mather, P. T.: Linear/network Poly( $\epsilon$ -caprolactone) Blends Exhibiting Shape Memory Assisted Self-healing (SMASH). *ACS Appl. Mater. Interfaces* **2011**, 3, 152 – 161.).

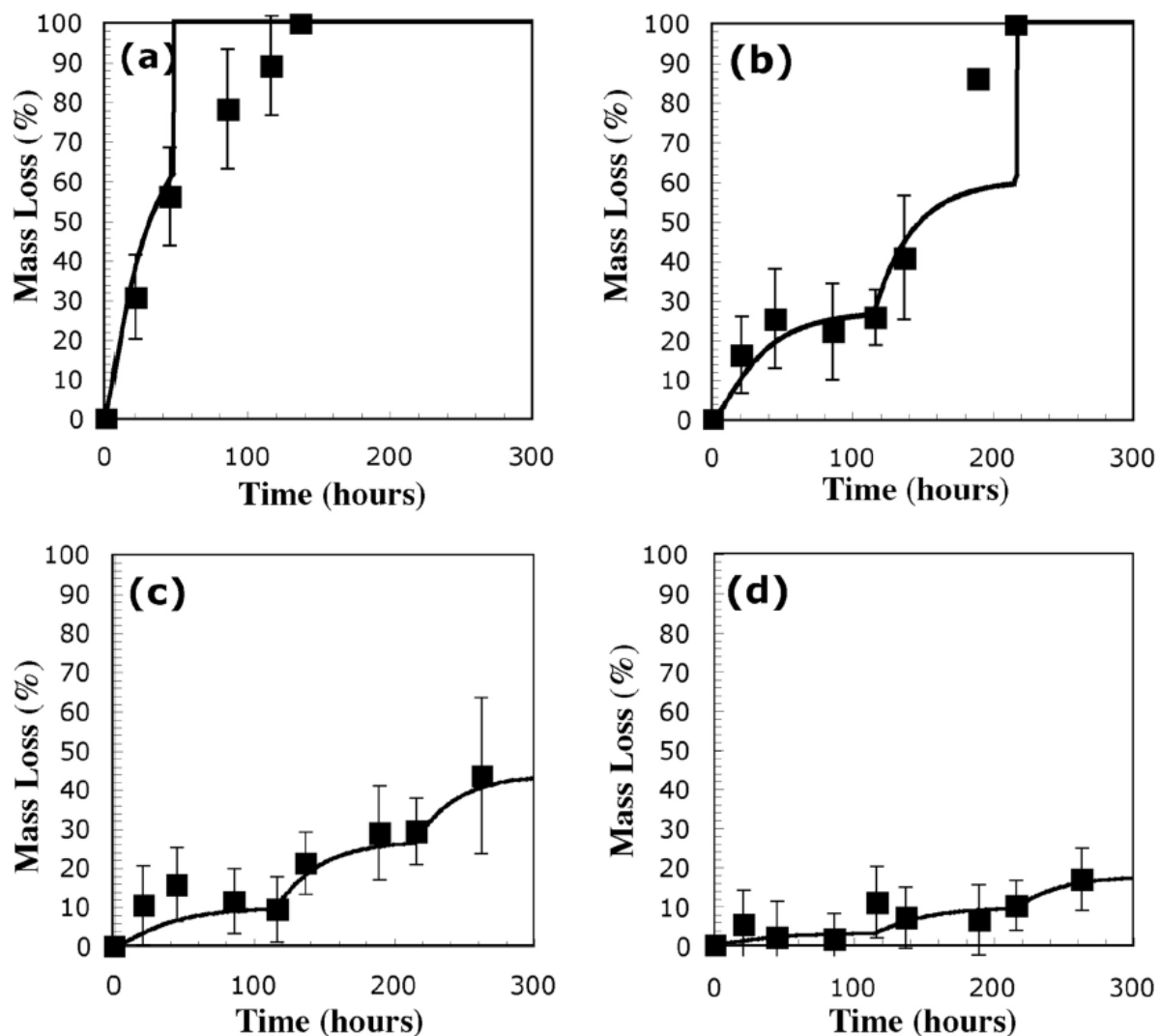


**Figure 1-8.** Experimental mass loss data for hydrogels synthesized from end-methacrylated PEG-PCL macromonomers and incubated in solutions with (a) 1.0 mg/ml, (b) 0.4 mg/ml, (c) 0.2 mg/ml, and (d) 0.1 mg/ml *pseudomonas lipase*. (Adapted with permission from Rice, M. A.; Sanchez-Adams, J.; Anseth, K. S.: Exogenously Triggered, Enzymatic Degradation of Photopolymerized Hydrogels with Polycaprolactone Subunits: Experimental Observation and Modeling of Mass Loss Behavior. *Biomacromolecules* **2006**, 7, 1968 – 1975.).



## Chapter 2: Tuning of Reversible Actuation via ROMP-based Copolymerization of Semicrystalline Polymers

### 2.1 Synopsis

There exists a need for reversible actuation involving two-way shape memory polymers that can respond to ambient temperatures in the 20 °C – 40 °C range, especially for soft actuators in specific applications. In this chapter, we report on the fabrication and analysis of a family of soft, semicrystalline copolymers based upon *cis*-cyclooctene via ring-opening metathesis polymerization (ROMP). Reversible actuation behavior of such copolymers was tuned by varying not only the species and the content of a second comonomer but also the concentration of an incorporated crosslinker. Results of thermal and shape memory characterization revealed that actuation was tuned to occur near to room temperature (25 °C) or body temperature (37 °C) when certain composition and crosslink densities were employed. Also, all crosslinked copolymers feature actuation magnitude greater than 50% and recovery magnitude greater than 94%, while thermal strain hysteresis was 17.5 °C on average.

### 2.2 Introduction

Shape memory polymers (SMPs) are a class of smart materials that have the ability to permanently memorize a macroscopic shape, be deformed and fixed to a temporary and dormant shape under specific conditions of stress and temperature, and then later relax to the original, stress-free condition under certain environmental command like heat.<sup>1-5</sup> This final step can execute useful mechanical work. During the past few decades, significant effort has gone into developing soft actuators that utilize SMPs to obtain attractive properties ideal for several applications such

as sensors, actuators, soft robots, and artificial muscles.<sup>6-9</sup> Such properties include, but are not limited to, unique functionality, mechanical flexibility, light weight, and low production cost. However, conventional SMPs have problems associated with their practical use in actuators, given the fact that their shape memory behavior often undergoes in a one-way manner only.<sup>10-12</sup> Although greater than 95% of the literature on SMPs is dedicated to the one-way shape memory (1WSM), two-way shape memory (2WSM) effect, which indicates reversible elongation on cooling and contraction on heating at a single applied stress, is largely favored for actuation purpose of interest. Back in 1959 it was first reported, but largely ignored, that crosslinked polyethylene fibers exhibited such reversible phenomenon when tensioned.<sup>13</sup> In particular, oriented polyethylene fibers were crosslinked through electron-radiation, yielding a molecularly aligned polyethylene network that features 25% reversible dimensional variation. This work technically launched a new era in 2WSM effect that presents in polymer network, but, unfortunately, further investigation into a number of factors affecting 2WSM behavior was not conducted. Baker *et al* developed an array of thiol-ene crosslinked poly( $\epsilon$ -caprolactone)-*co*-poly(ethylene glycol) foams with varying PCL-to-PEG compositions which exhibit reversible actuation in compression, and also with melting transitions ( $T_m$ ) in the range around body temperature.<sup>14</sup> Similarly, Bai et al elaborated a new graft polymer in which PCL chains are grafted onto polydopamine with phenolic hydroxyl groups as active points by ring-opening polymerization, allowing the formation of semicrystalline networks by diisocyanates for 2WSM behavior.<sup>15</sup> However, the aforementioned two methods do not achieve our goal of malleable post-synthesis processing required for large-scale industrial production of 2WSM articles.

Seeking a facile synthesis approach to 2WSM polymers without significant processing limitation, we selected the chain growth polymerization process known as ring-opening metathesis

polymerization (ROMP), recognizing that it has become a powerful and broadly applicable tool for a variety of complex macromolecular architectures.<sup>16</sup> The mechanism of such polymerization is based on olefin metathesis, a characteristic metal-mediated unsaturation (C=C) exchange process, during which any saturation associated with the original cyclic olefins is transferred to the corresponding polymer. This feature provides a benefit over other common approaches because the unsaturation maintained throughout polymerization can be used for chemical crosslinking following processing. Bielawski *et al* systematically described highly efficient ROMP using ruthenium catalysts for various low-strain cyclic olefins such as *cis*-cyclooctene (CO), 1,5-cyclooctadiene (COD), 2-methylcyclopentene, norbornene (NO), *N*-methyl-7-oxanorbornenedicarbimide norbornene, etc.<sup>17</sup> Further, Alonso-Villanueva *et al* studied the influence of temperature, addition of chain transfer agent, and solvent on ROMP of CO, utilizing second generation Grubbs' catalyst owing to its excellent stability, group tolerance and high metathesis activity.<sup>18</sup> However, none of the aforementioned ROMP work has ever attempted to covalently crosslink the polymers to yield shape memory properties in the resulting materials.

Along this line, in our own lab, Liu *et al* first synthesized poly(cyclooctene) (PCO) from *cis*-cyclooctene with the presence of first generation Grubbs' catalyst, and then demonstrated sound 1WSM of crosslinked PCO film by thermal initiator dicumyl peroxide (DCP).<sup>19</sup> The  $T_m$  and viscoelastic properties of crosslinked PCO showed a strong dependence on crosslink density that was resulted from the concentration of DCP added during thermal curing. In light of that achievement, Chung *et al* unveiled a surprising reversible behavior of covalently crosslinked PCO, which behavior tightly associates with crosslink density and the tensile stress applied during cooling and heating.<sup>20</sup> More specifically, the lowest  $T_m$ , at which temperature the SMP is actuated to change programmed shape, was achieved at ca. 42 °C by increasing DCP concentration to 2

wt%. Nonetheless, no 2WSM polymer has been reported to date that would allow environmental stimulus at temperatures in the 20 °C – 40 °C range; i.e. conveniently near body temperature. We note that extremely high crosslinker concentration could make the polymer too stiff/brittle to be useful due to over-crosslinking.<sup>21</sup> Of relevance, Lu et al reported on the copolymerization of L-lactide with varying level of  $\epsilon$ -caprolactone (CL) in the range of 0 to 30 mol%, revealing that  $T_m$  considerably decreased from 174 °C to 125 °C, which is attributed to the increase of chain flexibility and mobility resulted from incorporation of CL units.<sup>22</sup> As a similar approach to tune  $T_m$  of polymer, Tan et al prepared a couple poly(butylene succinate-*co*-hexamethylene succinate) copolyesters with  $T_m$  decreasing from ca. 114 °C to 68 °C as hexamethylene succinate content increased from 0 mol% to 40 mol%.<sup>23</sup> Therefore, copolymerization with a monomer whose derivative polymer has a relatively low crystallinity was proven capable of tuning  $T_m$  effectively.

In this work, we have carried out experimental investigations on the possibility to develop reversible actuation with tunable thermal and shape memory properties via ROMP copolymerization of CO with varying second monomers, respectively. Such second monomers used in copolymerization include COD, NO, and cycloheptene (CH). In particular, a COD content range from 0 mol% to 10 mol% was explored to understand its influence on  $T_m$  of the corresponding copolymers. Subsequently, all CO-based copolymers were covalently crosslinked with variation in crosslink density to form a series of semicrystalline thermoset SMPs. Herein, our first aim was to quantify the thermally 1WSM and 2WSM behavior individually for each crosslinked copolymer utilizing a dynamic mechanical analyzer (DMA) in custom modes of testing. Then, the second aim was to understand, by comparing the results harvested from shape memory testing, the role of molecular architecture and crosslink density in view of tailoring reversible actuation performance. Finally, wide-angle X-ray scattering (WAXS) was adopted to

gain understanding of the origin of the observed reversible actuation phenomena, within the context of knowledge gained from prior studies.

## 2.3 Experimental

### 2.3.1 Materials

The ruthenium catalyst (1,3-Bis(2,4,6-trimethylphenyl)-2-imidazolidinylidene) Dichloro (phenylmethylene) (tricyclohexylphosphine) ruthenium (Grubbs' 2<sup>nd</sup> Generation) was purchased from Sigma-Aldrich and stored in -4 °C freezer prior to use. *cis*-Cyclooctene (95%, Acros Organics; Fisher Scientific) was distilled over calcium hydride (95% Reagent grade; Sigma-Aldrich) at 180 °C for 2 h under reduced pressure before further use. 1,5-Cyclooctadiene (99%), norbornene (bicyclo[2.2.1]hept-2-ene 99%), and cycloheptene (97%) were all purchased from Sigma-Aldrich and dehydrated over 4Å molecular sieves in a 10 w/v basis for at least 4 d prior to use. Dichloromethane (99%; Fisher Scientific) was distilled at 80 °C following a 2-hour refluxing and further dehydrated with 4Å molecular sieves (Sigma-Aldrich) for 2 d before use. Dicumyl peroxide (98%), HPLC-grade tetrahydrofuran (THF), and deuterated chloroform (chloroform-d, 99.8% atom D) were purchased from Sigma-Aldrich and used as received. Other reagents and solvents were obtained from Fisher Scientific and used as received: ethyl vinyl ether (99%, Stabilized, Acros Organics), tris(hydroxymethyl)phosphine (95%, Acros Organics), methanol (Certified ACS), and 2-propanol (Certified ACS).

### 2.3.2 ROMP Copolymerization

A set of PCO-based copolymers with varying relative content and species of the second monomer were synthesized via ROMP polymerization or copolymerization under strictly air-free

environment, as shown in Scheme 2-1. The second monomers include COD, NO, and CH. As a representative example, we here specify the preparation of poly(cyclooctene-*co*-cyclooctadiene) (PCO-COD) with a feed CO:COD mol. ratio of 0.97:0.03 (subsequently referred to as 3COD) in the following. A Schlenk line (AF-0452, purchased from Chemglass) was utilized to enable an air- and water-free reaction environment during the course of polymerization. Moisture was intentionally removed by flushing the whole reaction system nitrogen for 20 min. A 250-mL, three-neck flask (Chemglass, CG-1524-36, round bottom) was evacuated and refilled with nitrogen at least three times before both 5.13 mg (6  $\mu$ mol) Grubbs' 2<sup>nd</sup> and a magnetic stir bar were put into the flask. In parallel, a 250-mL, one-mouth flask (Chemglass, CG-1506-92, round bottom) was purged by three evacuate-refill cycles to carry 100 mL distilled dichloromethane (DCM), 0.24 mL (1.8 mmol) COD, and 7.64 (58.2 mmol) CO. Note that the monomer:catalyst ratio was kept at a value of 10,000 regardless of composition. Solvent and monomers in this one-mouth flask was further deaerated using an ultrasonic cleaner (Branson M1800) under vacuum for 10 min before reaction.

To begin the copolymerization process, the solvent and reagents were transferred from the one-mouth flask to the three-neck one containing Grubbs' catalyst through a long, double-tipped needle (Sigma-Aldrich, Gauge 20). Reduced pressure was applied to the three-neck flask to drive the motion of the monomer solution so that no air and moisture in the atmosphere would enter the reaction system during the reagent transfer. The ROMP copolymerization underwent at room temperature ( $\sim 22$  °C) for 30 min during which vortex stirring was maintained. Following that, 2 mL ethyl vinyl ether (300 mL excess to the catalyst) was injected to terminate the reaction and another 30 min was allowed for complete termination. In order for removal of water-soluble, toxic ruthenium phosphine complexes generated from ROMP copolymerization,

tris(hydroxymethyl)phosphine (THMP) was used in our work as it has been reported to capable of effectively reducing those ruthenium byproducts.<sup>24-26</sup> Subsequently, 0.045 g (0.065 mmol) THMP was dissolved in 2 mL 2-propanol, yielding a 0.181 M solution. The removal of ruthenium catalyst was performed by adding 0.35 mL of such solution while stirring was kept for 24 h. Finally, the polymer solution was drop-wisely precipitated in 500 mL methanol and deionized water mixed by 9:1 v/v. The precipitates were collected by filtration and dried in the fume hood overnight prior to complete drying in vacuum oven at room temperature for 7 d before processing.

### 2.3.3 Molecular Characterization

The copolymers synthesized as described above were prepared using deuterated chloroform ( $\text{CDCl}_3$ ) at a concentration ranging from 20 to 30 mg/mL. The proton Nuclear Magnetic Resonance ( $^1\text{H}$  NMR) spectra were generated using a Bruker Avance III HD 400 MHz spectrometer, to quantitatively measure the molar concentration of primary and second monomers. The relaxation delay time is 1 s at a temperature of 25 °C. Gel Permeation Chromatography (GPC) was performed to determine weight-average molecular weight ( $M_w$ ) and polydispersity index (PDI,  $M_w/M_n$ ), using a Waters Isocratic HPLC system equipped with a temperature-controlled differential refractometer (Waters 2414). Multi-angle laser light scattering (Wyatt miniDAWN) was introduced at three characteristic angles (45 °, 90 °, and 135 °) for in-line absolute molecular weight determination. The flow rate of THF as mobile phase in this GPC system was set at 1 mL/h constantly. Polymer-THF solutions (2 – 5 mg/mL) were passed through a 0.2  $\mu\text{m}$  PTFE filter (Waters) prior to injection at 40 °C.

### 2.3.4 Peroxide Curing and Gel Fraction Measurement

The various copolymers were blended with a DCP concentration of 0.25 wt% and 0.50 wt%, respectively, using a Carver 3851-0 press with heating platens in the following custom method: (1) 1.5 g sample was first pressed into a film applying two polished stainless-steel sheets coated with mold release agent (Pol-Ease® 2300, Polytek); (2) prescribed amounts of DCP were sprinkled uniformly onto the surface of the film that was then folded multiple times; (3) the pressing-folding process was repeated three more times for the purpose of optimal mixing; (4) after that, a 0.5 mm thick stainless steel spacer was placed in between two metal sheets to control the thickness; (5) a sheet specimen was formed by compression and thermally cured at 140 °C under a pressure of 1000 psi for 2 h; (6) finally, the resulting film was allowed to cool to room temperature in the mold.

In order to assess the extent of covalent crosslinking, network gel fraction values of the crosslinked films for each composition were examined using solvent-extraction and gravimetry. Each sample was weighed for its initial dry mass ( $m_i$ ) before being soaked in 20 mL THF at 37 °C in an Excella shaker for 48 h, during which the THF was refreshed every 12 h. Then samples were washed with deionized water, blotted with common towel, and vacuum dried for 2 d at 40 °C to remove residual solvent. The final dry mass ( $m_f$ ) was recorded for calculation of gel fraction values ( $G$ ), using the equation below:

$$G(\%) = \frac{m_f}{m_i} \times 100 \quad (2 - 1)$$

### 2.3.5 Wide-angle X-ray Scattering

To elucidate the thermally shape memory behavior at the microstructural level, wide angle X-ray scattering (WAXS) analysis was performed using a Rigaku S-MAX3000 for a 3COD sample cured with 0.50 wt% DCP (subsequently referred to as 3COD0.50) under different loading



conditions (i.e. unstretched, 100, 200, and 300 kPa). In particular, the sample with an increase of loading was prepared according to the first two steps of 1WSM cycle (i.e. loading and shape fixing as detailed below) using DMA apparatus prior to WAXS experiments. A Rigaku MicroMax-002+ generator was operated under an accelerating voltage of 45 kV and a current of 0.88 mA to yield a collimated beam of Cu *Ka* X-rays with a wavelength of 1.5405 Å. Scattering patterns were collected on image plates (see below) for 30 min. The sample-detector distance was fixed at 120.7 mm, leading to scattering angles  $3^\circ < 2\theta < 40^\circ$ . WAXS images were obtained and analyzed using a FujiFilm FLA7000 reader (with Fujifilm image plates CR HR-V) and SAXSgui software v2.03.04.

### **2.3.6 Thermal and Dynamic Mechanical Analysis**

Differential Scanning Calorimetry (DSC) was employed to investigate thermal properties of all copolymers before and after peroxide curing, using the TA Instruments Q200 apparatus. Samples weighing approximately 5 mg underwent a thermal program of first heating to 100 °C at 10 °C/min, cooling to -60 °C at 10 °C/min, and then reheating at 10 °C/min to 100 °C while heat flow data was recorded. The melting transition temperature ( $T_m$ , the peak of the endotherm) and the enthalpy of melting ( $\Delta H$ , area beneath endothermic peak) were recorded, respectively, on the basis of second heating curve (to minimize the effects of thermal history). We note that pure PCO has a  $T_g$  around -70 °C; however, exploration of  $T_g$  of our synthesized copolymers was beyond the scope of the present work.

A TA Instruments Q800 Dynamic Mechanical Analyzer (DMA) was adopted to explore the thermomechanical properties and also to assess success of crosslinking all kinds of copolymers. In the multi-frequency controlled-strain mode, each sample was equilibrated at -40 °C, held

isothermal for 10 min, and heated continuously up to 100 °C at 3 °C/min. An oscillating amplitude of ca. 15 μm, oscillation frequency of 1 Hz, preload force of 0.001 N, and force track of 108% were utilized to measure the storage and loss tensile moduli. Rectangle shaped samples with an approximate length-to-width ratio of 4:1 were used for this testing.

### 2.3.7 Shape Memory Characterization

To probe and analyze 1WSM and 2WSM behavior, dog bone shaped samples (ASTM D63 Type IV, scaled down by a factor of 4) were tested for various crosslinked copolymers, using DMA in controlled force mode. For 1WSM tests, samples were first strained to 70% at 70 °C, cooled at 2 °C/min to -10 °C under constant tension, released of their tensile stress, and finally heated up to 70 °C at 2 °C/min. This program was repeated three times for each sample. To quantify such behavior, the calculation of the shape fixing ( $R_f$ ) and shape recovery ( $R_r$ ) ratios for each individual cycle were performed using the equations below:<sup>27</sup>

$$R_f(\%) = \frac{\varepsilon_f - \varepsilon_i}{\varepsilon_d - \varepsilon_i} \times 100 \quad (2 - 2)$$

$$R_r(\%) = \frac{\varepsilon_f - \varepsilon_r}{\varepsilon_f - \varepsilon_i} \times 100 \quad (2 - 3)$$

Here,  $\varepsilon_f$  stands for the fixed strain after release stress,  $\varepsilon_i$  for the initial strain at starting point of each cycle,  $\varepsilon_d$  for the deformed strain before unloading, and  $\varepsilon_r$  for the recovered strain after complete heating.

In contrast, 2WSM tests were performed in the following procedures: at first, each sample was deformed by ramping the applied tensile load at 0.05 N/min to 70% strain at 70 °C. The stress required to achieve this strain was then held fixed for all subsequent steps. Next, the samples were

cooled to -10 °C at 2 °C/min. Finally, and after being held isothermally for 10 min, each sample was reheated to the initial elevated temperature at 2 °C/min. The strains were recorded as a function of temperatures while these procedures were done three times in succession. The quality of 2WSM behavior was subsequently evaluated by calculating the actuation magnitude ( $R_{a,m}$ ) and the recovery magnitude ( $R_{r,m}$ ) using the equations as follows:

$$R_{a,m}(\%) = (\varepsilon_{low} - \varepsilon_{high}) \times 100 \quad (2 - 4)$$

$$R_{r,m}(\%) = \frac{\varepsilon_{low} - \varepsilon_{high}^{final}}{\varepsilon_{low} - \varepsilon_{high}^{initial}} \times 100 \quad (2 - 5)$$

where  $\varepsilon_{low}$  and  $\varepsilon_{high}$  are the strains respectively at low and high temperatures under loading,  $\varepsilon_{high}^{final}$  is the final strain at high temperature with stress applied after recovery, and  $\varepsilon_{high}^{initial}$  is the initial strain under stress at high temperature. In addition, the magnitude of hysteresis for each sample was determined as the temperature difference between the 50% actuation strain upon heating (higher temperature) and cooling (lower temperature). We realize that this value is heating/cooling rate dependent.<sup>28</sup> Henceforth, as a representative example, a 3COD0.50 sample underwent four complete 2WSM cycles as described above, but with a decrease of heating/cooling rate from 3 °C/min for first cycle to 0.5 °C/min for last one.

## 2.4 Results and Discussion

### 2.4.1 Sample Preparation

The synthesis results of all CO-based copolymers via ROMP copolymerization were summarized in details in Table 2-1. These copolymers are, specifically, PCO (polymerized from neat CO and used as a control), 1COD, 3COD, 5COD, 10COD, 3NO, and 3CH. On the basis of

<sup>1</sup>H NMR spectra, it is found that the actual CO mol. content is not significantly different from that in feed for each individual copolymer, as an indicative of good control over ROMP copolymerization. Also, GPC results suggest that all  $M_w$ 's are greater than 250,000 g/mol, which value is 10 times higher than the minimum molecular weight (i.e. 25,000 g/mol) required for good physical and mechanical features in terms of several commercialized polymers.<sup>29</sup> Thermogravimetric analysis (TGA) data agreed as no thermal decomposition occur below 300 °C (Figure 2-1). In addition to that, higher molecular weights often indicate longer polymer chains in which more crosslinking sites (unsaturation) are available per chain given the fixed length of repeating subunits. We speculate that this could contribute to quality crosslinking in order to achieve high degree of crosslinking which usually implies great potential for favorable shape memory behaviors as well as resistance to mechanical “creep”.<sup>30,31</sup>

#### 2.4.2 Thermal and Dynamic Mechanical Analysis

Importantly, incorporating COD into PCO resulted in a remarkable decrease in  $T_m$  from 49.2 °C to 18.3 °C with an increase of COD mol. content from 0 mol% to 10 mol%, correspondingly. This is shown in Figure 2-2 in the form of DSC traces of the copolymers. In a similar trend, the enthalpies associated with  $T_m$  declines somewhat as more COD was incorporated. We attribute this to the deterioration in crystallinity – anticipated to negatively impact actuation magnitude – to be higher chain flexibility and mobility of COD versus CO. The same reason applies to both NO- and CH-incorporated samples (Figure 2-3). Besides, to compare the copolymers containing different second monomers, the feed concentrations of COD, NO, and CH were the same at 3 mol%. It turned out that 3COD showed the lowest  $T_m$  at 31.3 °C as opposed to 3NO at 35.1 °C and 3CH at 47.9 °C, which is in good agreement with their corresponding enthalpies: 3COD < 3CNO < 3CH.

Being thermally cured with DCP by compression molding, the crosslinked copolymers all revealed a decreasing  $T_m$  to varying degree as compared to their virgin states due to further diminution of crystallinity induced by covalent crosslinking,<sup>32</sup> as shown in Figure 2-4. Moreover, a noticeable effect of degree of crosslinking was observed on  $T_m$  when different DCP concentrations were applied for the same composition. It is important to point out that the  $T_m$  of 1COD was lowered from 43.5 °C to 38.7 °C for 0.25 wt% DCP crosslinking while that of 3COD from 31.3 °C to 26.1 °C for 0.50 wt% DCP crosslinking. The two reduced  $T_m$ 's have become quite close to body temperature and room temperature, respectively, as much as they may get while not being actuated. Also, Table 2-2 states gel fraction value for each copolymer cured with varying DCP concentrations, which value in the range from 66% to 92% appears to be much higher than the minimum value (~10%)<sup>30</sup> required for typical shape memory effect. From a different perspective, these values suggest the possibility to further tune thermal properties by boosting degree of crosslinking up to the high end of 90% if needed.

Revealing the direct impact of peroxide curing on the thermomechanical behavior, Figure 2-5a and b show the storage modulus profiles as a function of temperature at a DCP concentration of 0.25 wt% and 0.50 wt%, respectively. All copolymers cured with varying amounts of DCP are characteristic of a modest storage modulus of approximately 100 MPa for temperatures below 0 °C. Moreover, this modulus value appears to depend only weakly on crosslink density. However, the onset temperature at which the storage modulus starts dropping sharply exhibited an unneglectable dependence on crosslink density exactly like what we found in DSC studies. Note that the  $T_m$  measured by DMA oftentimes comes up higher than that by DSC because of the stress-induced crystallization during DMA testing.<sup>33,34</sup> The storage modulus for 0.25 wt% DCP crosslinking decreased by three orders of magnitude, while that for 0.50 wt% DCP crosslinking declined by

approximately two orders of magnitude, both with increasing temperature from 0 °C through melting transition to 70 °C. Such transitions can also be found in the Tan  $\delta$ -temperature profiles as shown in Figure 2-6. This difference is attributed to a constraining influence of crosslink junctions on chain mobility, which made network polymers more resistant to deformation in the non-crystalline state.

From the standpoint of shape memory capacity, increasing such resistance to deformation may allow the polymers to better recover from a larger deformation without having significant irreversible deformation known as “creep”. After the sharp drop in storage modulus through melting transition, each sample reached an extended rubbery plateau of modulus whose value is in direct effect of crosslink density. Being a representative example, 3COD revealed a 917% increase in storage modulus from 0.197 MPa for 0.25 wt% DCP curing to 2.004 MPa for 0.50 wt% DCP curing. The other compositions were found to follow an identical trend. More importantly, the presence of a stable rubbery plateau above  $T_m$  would allow polymer to be deformed extensively without macroscopic flow, being a prerequisite for an attractive shape memory effect.

### **2.4.3 Shape Memory Analysis**

The shape memory effects in polymers can take two quite distinct forms: conventional one-way shape memory (1WSM) and reversible two-way shape memory (2WSM), the former being ordinarily illustrated in a 3D stress-temperature-strain plot on a three-cycle basis. As detailed in the experimental section, the copolymers crosslinked with 0.25 wt% and 0.50 wt% DCP were tested using a DMA, yielding their corresponding 1WSM cycles demonstrated in Figure 2-7 and in Figure 2-8, respectively. Each cycle consists of three steps: (1) deformation: a strain of 70% was achieved at an elevated high temperature (70 °C) above  $T_m$ ; (2) fixing: each sample was

cooled to a low temperature (-10 °C) at a constant cooling rate of 2 °C/min, following which a temporal shape was obtained by removing the stress associated with that prescribed strain; (3) recovery: the temporarily fixed shape was reverted back to the original form owing to elasticity upon heating to that elevated high temperature at a constant heating rate of 2 °C/min. Such shape memory cycle was repeated three times for each sample as specified above. Notably, a “training” cycle, which is typically the first cycle with fairly low recovery ratio as compared with its succeeding cycles that become highly reproducible, has been observed for chemically crosslinked SMPs, as the processing and storage history of the SMPs play an important role in such cycle.<sup>4,35,36</sup> Surprisingly, our crosslinked copolymers exhibited a negligible or very subtle training cycle relating to 1WSM effect. We speculate that incorporating the highly flexible and mobile second monomers might largely facilitate the reorganization of polymer chains on the molecular scale upon deformation and first heating. Further, the associated shape fixing ( $R_f$ ) and shape recovery ( $R_r$ ) ratios were calculated to quantitatively evaluate the 1WSM behavior of the crosslinked copolymers (Table 2-3). Broadly speaking, all crosslinked samples revealed a  $R_f$  greater than 95% with a  $R_r$  no less than 94%, both on average of total three cycles. Thus, it is evident that these crosslinked copolymers exhibited exceptional 1WSM behavior along with both robust fixing and recovery.

The two-way shape memory (2WSM) effect (reversible actuation) of each crosslinked copolymer, being the focus of the present work, is presented in a 2D strain-temperature plot since that the applied stress is maintained constant throughout the entire course of 2WSM testing (Figure 2-9 through 2-11). In contrast to 1WSM cycle, here, the sample was heated to a high temperature (70 °C) above its  $T_m$  by 2 °C/min before stretched to a prescribed strain (70%) at that temperature, following which the stress associated with the strain was kept unchanged for the duration of three

cycles. On cooling, the stress-induced crystallization gave rise to an elongation in strain, while on heating, the sample contracted due to melting of polymer crystals in order to ultimately achieve the strain that matches tensile modulus under the isotropic condition.<sup>20</sup> Figure 2-9 showed the 2WSM cycles of various PCO-COD copolymers cured with 0.25 wt% DCP, while the amount of DCP used for crosslinking was increased to 0.50 wt% in Figure 2-10. The actuation magnitude ( $R_{a,m}$ ) and the recovery magnitude ( $R_{r,m}$ ) were calculated to better understand and compare the 2WSM effect for each sample (Table 2-3). Quite interestingly, a more remarkable training cycle was observed in 2WSM behavior as compared with corresponding 1WSM cycles, especially for lower COD mol. contents as well as for lower DCP concentrations. This distinctive characteristic is probably due to the constantly applied stress, which might hinder complete shape recovery to some degree, during 2WSM testing. However, the training cycle effect was found to be diminished significantly by increasing DCP concentration, as crosslink density is directly dependent on DCP concentration.

Additionally, “creep” is commonly considered as one of major mechanical deficiencies of SMPs, and it is well known that creep takes place as a direct consequence of both molecular conformations and rearrangements due to insufficient constraining effect of polymer network.<sup>37,38</sup> In 2WSM testing, creep presents in a form of irrecoverable strain from one cycle to another, which is more likely to be observed, in our case, for the samples cured with smaller amount of DCP (e.g. Fig. 9(ii) and (iii)). When more DCP was employed for crosslinking, higher crosslink density was achieved to alleviate creep as shown correspondingly in Figure 2-10(ii) and (iii). More specifically, the  $R_{r,m}$ 's of 1COD and 3COD samples increased from 94.3% and 94.8% to 97.0% and 96.5%, respectively, as DCP concentration increased from 0.25 wt% to 0.50 wt%. However, such trend was not found for 5COD samples despite increasing DCP concentration ( $R_{r,m} = 97.6%$  for 0.25



wt% DCP and 97.1 for 0.50 wt% DCP), which we attribute to equally good establishment of a heavily crosslinked network under either curing condition ( $G = 89.6\%$  for 0.25 wt% DCP and  $92.1\%$  for 0.50 wt% DCP). We point out that the noticeable creep in PCO samples was caused by low gel fractions not significantly dependent of DCP concentration ( $G < 80\%$ ).

To investigate the influence of different second monomers on reversible actuation, 2WSM cycles for 3COD0.50, 3NO0.50 and 3CH0.50 were compiled in Figure 2-11. The reversible behavior for each sample was further quantified and compared in Figure 2-15. Out of three kinds of copolymers, 3COD0.50 displayed the most favorable reversible actuation due to its lowest actuation temperature ( $T_m$ ), highest actuation magnitude ( $R_{a,m} \sim 78\%$ ), and minimized creeping phenomenon ( $R_{r,m} \sim 96\%$ ). We reason that its highest  $R_{a,m}$  is due to the highest stress (0.83 MPa) required to achieve the same strain at 70% as compared with the other two copolymers (i.e. 0.46 MPa for 3NO0.50 and 0.59 MPa for 3CH0.50).

Furthermore, considering reversible actuation in practical use, the actuation magnitude is particularly important since that it dictates the extent of shape changing for our crosslinked copolymers during cooling and heating. For comparison and optimization purpose,  $R_{a,m}$  is plotted as a function of COD mol% in Figure 2-13(a). It is evident that all copolymers revealed a relatively higher  $R_{a,m}$  than neat PCO did because of the better flexibility and mobility of COD. Also,  $R_{a,m}$  reached peak values at COD content of, respectively, 3 mol% for 0.25 wt% DCP ( $\sim 70.7\%$ ) and 1 mol% for 0.50 wt% DCP ( $\sim 83.9\%$ ). That  $R_{a,m}$  decreased with the COD content further increasing is probably due to the relatively high crosslink density which could constrain the local chain movement in the neighborhood of a crosslink site (Figure 2-12). Figure 2-13(b) reveals that the recovery magnitude follows the same trend with COD content as was found for gel fraction.

Besides the important 2WSM characteristics of  $R_{a,m}$  and  $R_{r,m}$ , thermal strain hysteresis ( $\Delta T$ ), as another one of high importance, is defined by the temperature difference at the half of strain loop generated during cooling and heating. The effect of COD content on thermal strain hysteresis is shown in Figure 2-14. Ideally, smaller this hysteresis is, the better the reversible actuation is deemed, in terms of the breadth of operating temperature span required for complete two-way actuation. It is observed that all  $\Delta T$ 's as a function of COD and DCP content concentrated around 17.5 °C with a deviation of ca. 1.5 °C, and such median value is averagely lower than that reported for a commercially available PCO cured with 2.0 wt% DCP.<sup>20</sup>

The influence of heating/cooling rates on the thermal hysteresis of 2WSM cycle was also investigated here in light of previous work accomplished by Burke et al.<sup>28</sup> The experiments were carried out using 3COD0.50 sample that exhibited the most favorable 2WSM properties as discussed above. More specifically, the sample was deformed under a tensile stress of 300 kPa at 70 °C, following which the 2WSM cycle at various heating/cooling rates was recorded in Figure 2-13a, including 0.5 °C/min (pink), 1.0 °C/min (blue), 2.0 °C/min (red), and 3.0 °C/min, respectively. It is obvious that the  $\Delta T$  was reduced notably by ca. 57.7% with decreasing the heating/cooling rate from 3.0 to 0.5 °C/min but  $R_{a,m}$  modestly increased by ca. 14.3% in the meanwhile, as quantitatively shown in Figure 2-16(b). We postulate such variation in  $\Delta T$  or  $R_{a,m}$  was rooted in the changing microstructure (and its time-dependence via crystallization kinetics), during temperature ramping, under a tensile stress that facilitated the elongated crystalline phases to rotate to align along the stretching direction. Likewise, the two-way actuation of 3COD0.50 at different stresses show that the hysteresis between the cooling and heating loop became ca. 24.4% narrower as stress increased from 100 to 300 kPa (Figure 2-17). Therefore, given all the characterization and analysis stated above, it is clearly concluded that this ROMP

copolymerization approach allows controllable tuning of reversible actuation based on  $T_m$  in the 20 °C– 40 °C range.

#### 2.4.4 WAXS Analysis

In prior work pertaining to the crosslinking of pure PCO, it was asserted that microstructure changes and molecular orientation effects are closely related to the 2WSM behavior. So, in this investigation, 2D wide-angle X-ray scattering (WAXS) patterns were systematically recorded from a 3COD0.50 sample under varying loading conditions. Samples were thermally annealed at 100 °C to eliminate the effect of thermal history before applying a range of stresses during crystallization upon cooling. The WAXS patterns for such samples are shown in Figure 2-18. Previous work suggested two sharp Debye-Scherrer rings for the unstretched PCO sample, and its pattern becomes polarized (oriented) more and more with an increase of the applied stress upon cooling.<sup>20,39,40</sup> Coincidentally, as indicated in Figure 2-15(i) the unstretched 3COD0.50 revealed a highly symmetric pattern that consists of two crystalline rings at  $2\theta = 17.1^\circ$  (5.18 Å) and  $19.9^\circ$  (4.46 Å), each corresponding to the (010) (inner ring) and ( $\bar{1}10$ ) (outer ring) reflections (Figure 2-19). We hypothesize that COD packs and crystallizes in a manner as similar as CO does owing to their similarity in chemistry and molecular structure. Further, molecular orientation was illustrated by the anisotropic patterns as indicated in Figure 2-18(ii), (iii), and (iv) under imposed stresses of 100, 200, and 300 kPa, respectively. More specifically, when the largest deformation was introduced during cooling (Figure 2-18(iv)), the azimuthal spread of the (010) reflection divided into two bands which were close to the equatorial axis (horizontal), indicating a meridional (vertical) orientation of crystallites, whereas the ( $\bar{1}10$ ) reflection split into four isolated, off-equatorial bands representing stress-induced crystallite orientations in both equatorial and meridional directions.

Considering closely macromolecular orientation, the angular position and d-spacing did not change with increasing stress, as an indication of unaltered microstructure (packing) of the copolymer. Further, the stress-induced increase in degree of crystallinity was studied based on the intensity-azimuthal angle profiles as plotted in Figure 2-20. It is seen that the intensity peaks turned azimuthally sharper as stress increased from 100 to 300 kPa, suggesting that polymer molecules oriented to a larger extent. That both molecular orientation and crystallization were increasingly promoted along the stretching axis is in good agreement with our observation of improved reversible actuation under increasing stress level (Figure 2-17). In addition, this molecular orientation appeared to be bimodal because the single peak split into two narrow peaks when stress was induced. Such observation seems not to be in alignment with the findings related to the DCP-crosslinked PCO. Concerning this discrepancy, we reason that it might be due to the presence of second monomer which responded to stress rather differently from the neat PCO.

## 2.5 Conclusions

In this study, a family of semicrystalline copolymers with low  $T_m$  in the 20 – 40 °C span was successfully developed via ring-opening metathesis copolymerization of *cis*-cyclooctene (CO) with varying second monomers such as 1,5-cyclooctadiene (COD), norbornene (NO) and cycloheptene (CH). Covalent crosslinking the resulting copolymers into networks, with the presence of dicumyl peroxide (DCP) acting as a thermal initiator, enabled excellent two-way shape memory (2WSM) behavior. Tuning of such reversible actuation was further achieved by systematic variation in chemical composition and DCP concentration. The thermal, dynamic mechanical, and shape memory properties of these copolymer networks were comprehensively characterized using differential scanning calorimetry (DSC), dynamic mechanical analysis (DMA), and wide-angle X-ray scattering (WAXS). Results suggest that the melting transition temperatures

( $T_m$ ) of copolymer networks was reduced progressively with increasing COD content, DCP concentration, or a combination thereof. Importantly, poly(cyclooctene-co-cyclooctadiene) (PCO-COD) containing 3 mol% COD showed a  $T_m$  (26.1 °C) quite near to room temperature after cured with 0.50 wt% DCP, allowing specific applications which require two-way actuation in the vicinity of room temperature.

Reversible actuation (i.e. 2WSM) behavior was analyzed and compared, both qualitatively and quantitatively, for each individual copolymer network. We found that both crystalline structure and crosslink density played pivotal roles in achieving good control over the reversible actuation. Among three second co-monomers, COD was the best from the point of view of lowering  $T_m$  while preserving actuation magnitude. With further investigation, 3COD exhibited the best performance of reversible actuation, despite the crosslinker concentration, in terms of actuation magnitude, recovery magnitude and thermal hysteresis. Furthermore, the effects of different heating/cooling rates and different tensile stresses on the reversible actuation of a 3COD0.50 sample were investigated, respectively, revealing that actuation magnitude increased with thermal hysteresis decreased when either lower heating/cooling rate or higher stress was applied. WAXS analysis lent a significant support in interpreting the reversible behavior of copolymer networks at the molecular level. Therefore, in view of all observations discussed above, we envision that this work can serve as a perfect guidance on tuning the thermally reversible actuation of semicrystalline polymers.

## 2.6 References

1. Liu, C.; Qin, H.; Mather, P. T.: Review of Progress in Shape Memory Polymers. *J. Mater. Chem.* **2007**, 17, 1543 – 1558.
2. Sun, L.; Huang, W. M.; Ding, Z.; Zhao, Y.; Wang, C. C.; Purnawali, H.; Tang, C.: Stimulus-responsive Shape Memory Materials: A Review. *Mater. Des.* **2012**, 33, 577 – 640.
3. Huang, W. M.; Ding, Z.; Wang, C. C.; Wei, J.; Zhao, Y.; Purnawali, H.: Shape Memory Materials. *Mater. Today* **2010**, 13, 54 – 61.
4. Lendlein, A.; Kelch, S.: Shape Memory Polymers. *Angew. Chem. Int. Ed.* **2002**, 41, 2034 – 2057.
5. Ratna, D.; Karger-Kocsis, J.: Recent Advances in Shape Memory Polymers and Composites: A Review. *J. Mater. Sci.* **2008**, 43, 254 – 269.
6. Bay, L.; West, K.; Sommer-Larsen, P.; Skaarup, S.; Benslimane, M.: A Conducting Polymer Artificial Muscle with 12% Linear Strain. *Adv. Mater.* **2003**, 15, 310 – 313.
7. Shepherd, R. F.; Ilievski, F.; Choi, W.; Morin, S. A.; Stokes, A. A.; Mazzeo, A. D.; Chen, X.; Wang, M.; Whitesides, G. M.: Multigait Soft Robot. *Proc. Natl. Acad. Sci.* **2011**, 108, 20400 – 20403.
8. Ren, K.; Bortilin, R. S.; Zhang, Q. M.: An Investigation of A Thermally Steerable Electroactive Polymer/Shape Memory Polymer Hybrid Actuator. *Appl. Phys. Lett.* **2016**, 108, 062901.
9. Song, J. J.; Chang, H. H.; Naguib, H. E.: Biocompatible Shape Memory Polymer Actuators with High Force Capabilities. *Eur. Polym. J.* **2015**, 67, 186 – 198.

10. Imai, S.; Sakurai, K.: An Actuator of Two-way Behavior by Using Two Kinds of Shape Memory Polymers with Different  $T_g$ s. *Precis. Eng.* **2013**, 37, 572 – 579.
11. Ahmad, M.; Luo, J.; Miraftab, M.: Feasibility Study of Polyurethane Shape-memory Polymer Actuators for Pressure Bandage Application. *Sci. Technol. Adv. Mater.* **2012**, 13, 015006.
12. Behl, M.; Kratz, K.; Noechel, U.; Sauter, T.; Lendlein, A.: Temperature-memory Polymer Actuators. *Proc. Natl. Acad. Sci.* **2013**, 110, 12555 – 12559.
13. Mandelkern, L.; Robert, D. E.; Diorio, A. F.; Posner, A. S.: Dimensional Changes in Systems of Fibrous Macromolecules: Polyethylene. *J. Am. Chem. Soc.* **1959**, 81, 4148 – 4157.
14. Baker, R. M.; Henderson, J. H.; Mather, P. T.: Shape Memory Poly( $\epsilon$ -caprolactone)-*co*-poly(ethylene glycol) Foams with Body Temperature Triggering and Two-way Actuation. *J. Mater. Chem. B* **2013**, 1, 4916 – 4920.
15. Bai, Y.; Zhang, X.; Wang, Q.; Wang, T.: A Tough Shape Memory Polymer with Triple Shape Memory and Two-way Shape Memory Properties. *J. Mater. Chem. A* **2014**, 2, 4771 – 4778.
16. Bielawski, C. W.; Grubbs, R. H.: Living Ring-opening Metathesis Polymerization. *Prog. Polym. Sci.* **2007**, 32, 1 – 29.
17. Bielawski, C. W.; Grubbs, R. H.: Highly Efficient Ring-opening Metathesis Polymerization (ROMP) Using New Ruthenium Catalysts Containing *N*-heterocyclic Carbene Ligands. *Angew. Chem. Int. Ed.* **2000**, 39, 2903 – 2906.

18. Alonso-Villanueva, J.; Rodríguez, M.; Vilas, J. L.; Laza, J. M.; León, L. M.: Ring-opening Metathesis Polymerization Kinetics of Cyclooctene with Second Generation Grubbs' Catalyst. *J. Macromol. Sci., Pure Appl. Chem.* **2010**, 47, 1130 – 1134.
19. Liu, C.; Chun, S. B.; Mather, P. T.: Chemically Cross-linked Polycyclooctene: Synthesis, Characterization, and Shape Memory Behavior. *Macromolecules* **2002**, 35, 9868 – 9874.
20. Chung, T.; Romo-Uribe, A.; Mather, P. T.: Two-way Reversible Shape Memory in A Semicrystalline Network. *Macromolecules* **2008**, 41, 184 – 192.
21. Cromwell, O. R.; Chung, J.; Guan, Z.: Malleable and Self-healing Covalent Polymer Networks through Tunable Dynamic Boronic Ester Bonds. *J. Am. Chem. Soc.* **2015**, 137, 6492 – 6495.
22. Lu, X. L.; Cai, W.; Gao, Z.; Tang, W. J.: Shape Memory Effects of Poly(L-lactide) and Its Copolymer with Poly( $\epsilon$ -caprolactone). *Polym. Bull.* **2007**, 58, 381 – 391.
23. Tan, B.; Bi, S.; Emery, K.; Sobkowicz, M. J.: Bio-based Poly(butylene succinate-co-hexamethylene succinate) Copolyesters with Tunable Thermal and Mechanical Properties. *Eur. Polym. J.* **2017**, 86, 162 – 172.
24. Higham, L. J.; Whittlesey, M. K.; Wood, P. T.: Water-soluble Hydroxyalkylated Phosphines: Examples of Their Differing Behaviour towards Ruthenium and Rhodium. *Dalton Trans.* **2004**, 0, 4202 – 4208.
25. Cho, J. H.; Kim, B. M.: An Efficient Method for Removal of Ruthenium Byproducts from Olefin Metathesis Reactions. *Org. Lett.* **2003**, 5, 531 – 533.
26. Hong, S. H.; Grubbs, R. H.: Efficient Removal of Ruthenium Byproducts from Olefin Metathesis Products by Simple Aqueous Extraction. *Org. Lett.* **2007**, 9, 1955 – 1957.



27. Robertson, J. M.; Nejad, H. B.; Mather, P. T.: Dual-spun Shape Memory Elastomeric Composites. *ACS Macro Lett.* **2015**, 4, 436 – 440.
28. Burke, K. A.; Rousseau, I. A.; Mather, P. T.: Reversible Actuation in Main-chain Liquid Crystalline Elastomers with Varying Crosslink Densities. *Polymer* **2014**, 55, 5897 – 5907.
29. Sperling, L. H.: *Introductions to Physical Polymer Science*; 4th; John Wiley & Sons: Hoboken, New Jersey, 2006.
30. Zhu, G.; Liang, G.; Xu, Q.; Yu, Q.: Shape-memory Effects of Radiation Crosslinked Poly( $\epsilon$ -caprolactone). *J. Appl. Polym. Sci.* **2013**, 90, 1589 – 1595.
31. Merlettini, A.; Pandini, S.; Agnelli, S.; Gualandi, C.; Paderni, K.; Messori, M.; Toselli, M.; Focarete, M. L.: Facile Fabrication of Shape Memory Poly( $\epsilon$ -caprolactone) Non-woven Mat by Combining Electrospinning and Sol-gel Reaction. *RSC Adv.* **2016**, 6, 43964 – 43974.
32. Krumova, M.; López, D.; Benavente, R.; Mijangos, C.; Pereña, J. M.: Effect of Crosslinking on The Mechanical and Thermal Properties of Poly(vinyl alcohol). *Polymer* **2000**, 41, 9265 – 9292.
33. Stadler, R.; Gronski, W.: Stress Induced Crystallization in Thermoplastic Elastomers. *Colloid Polym. Sci.* **1986**, 264, 323 – 331.
34. Guo, J.; Narh, K. A.: Simplified Model of Stress-induced Crystallization Kinetics of Polymers. *Adv. Polym. Technol.* **2002**, 21, 214 – 222.
35. Defize, T.; Riva, R.; Raquez, J.; Dubois, P.; Jérôme, C.; Alexandre, M.: Thermoreversibly Crosslinked Poly( $\epsilon$ -caprolactone) as Recyclable Shape-memory Polymer Network. *Macromol. Rapid Commun.* **2011**, 32, 1264 – 1269.

36. Ohki, T.; Ni, Q.; Ohsako, N.; Iwamoto, M.: Mechanical and Shape Memory Behavior of Composites with Shape Memory Polymer. *Compos. Part A Appl. Sci. Manuf.* **2004**, 35, 1065 – 1073.
37. Rao, K. V.; Ananthapadmanabha, G. S.; Dayananda, G. N.: Effect of Crosslinking Density on Creep-recovery Behavior in Epoxy-based Shape Memory Polymers (SMEPs) for Structural Applications. *J. Mater. Eng. Perform.* **2016**, 25, 5314 – 5322.
38. Wu, X. L.; Huang, W. M.; Tan, H. X.: Characterization of Shape Recovery via Creeping and Shape Memory Effect in Ether-vinyl Acetate Copolymer (EVA). *J. Polym. Res.* **2013**, 20, 150 – 160.
39. Bassi, I. W.; Fagherazzi, G.: The Triclinic Structure of Trans-polyoctenamer. *Eur. Polym. J.* **1968**, 4, 123 – 132.
40. Natta, G.; Bassi, I. W.; Fagherazzi, G.: The Monoclinic Structure of Even Trans-polyalkenamers. *Eur. Polym. J.* **1967**, 3, 339 – 352.

**Table 2-1.** Synthesis Summary of CO-based copolymers

Sample	Actual CO composition (mol. %) <sup>b</sup>	Yield (Mass %)	Molecular weight ( $M_w$ , kDa)	PDI	$T_m$ (°C) <sup>c</sup>	$\Delta H_m$ (J/g)
PCO	-	80.3	267.3	1.33	49.2	41.74
1COD <sup>a</sup>	98.1	80.0	574.3	2.93	43.5	41.16
3COD	96.7	81.2	415.4	1.38	31.3	26.56
5COD	95.4	91.8	401.2	1.36	22.7	18.05
10COD	90.5	70.1	616.9	1.38	18.3	26.54
3NO	98.5	70.0	384.5	1.44	35.1	29.22
3CH	96.0	73.4	327.7	1.51	47.9	36.91

<sup>a</sup> Nomenclature: **1** stands for 1 mol. % COD added in feed, **COD** for 1,5-cyclooctadiene.

<sup>b</sup> Determined by NMR spectra.

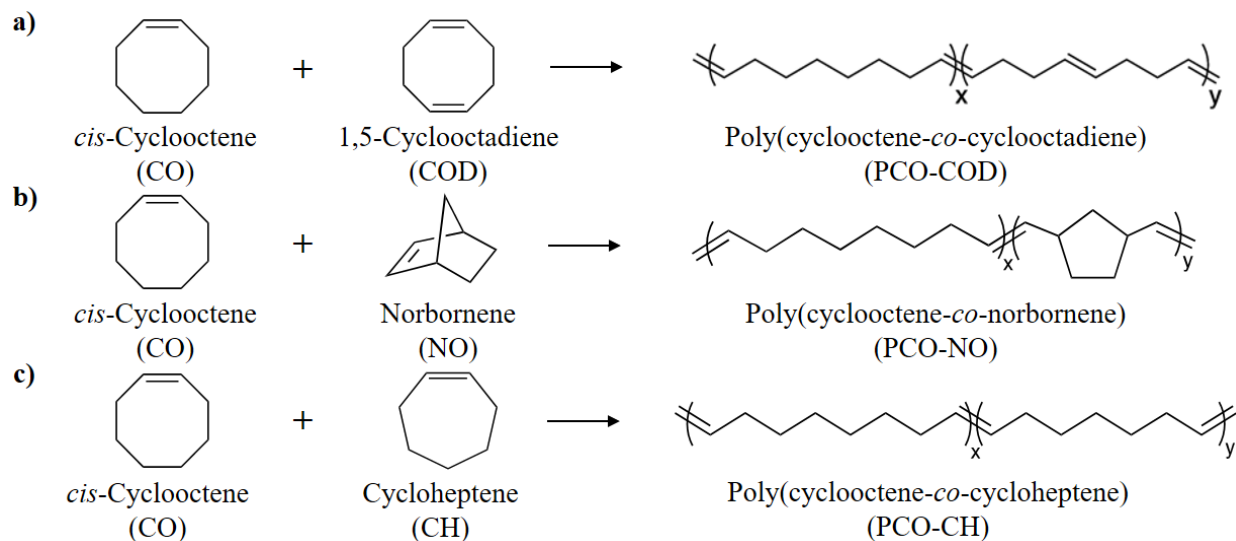
<sup>c</sup> Peak values of second heating in DSC curves.

**Table 2-2.** Thermal and Microstructural Characteristics as A Function of DCP wt.%

Sample	$T_m^{Pristine}$ (°C)	$T_m^{0.25DCP}$ (°C)	$G^{0.25DCP}$ (%)	$T_m^{0.50DCP}$ (°C)	$G^{0.50DCP}$ (%)
PCO	49.2	47.5	77.4	45.9	79.5
1COD	43.5	38.7	85.6	32.4	87.6
3COD	31.3	27.8	83.0	26.1	88.2
5COD	22.7	20.5	89.6	16.3	92.1
3NO	35.1	-	-	34.8	70.4
3CH	47.9	-	-	44.9	81.2

**Table 2-3.** 1WSM and 2WSM characteristics as A Function of composition and DCP wt.%

Sample	$R_f$ (%)	$R_r$ (%)	$R_{a,m}$ (%)	$R_{r,m}$ (%)	$\Delta T$ (°C)
PCO0.25	97.5±0.1	99.0±0.2	33.8±1.5	86.8±4.6	15.9±0.5
1COD0.25	96.2±0.5	97.5±0.7	55.4±0.5	94.3±3.2	16.0±0.4
3COD0.25	97.8±4.6	96.2±0.8	70.7±1.5	94.8±2.1	18.9±0.2
5COD0.25	94.8±1.9	95.2±0.5	62.4±0.6	97.6±1.5	17.2±0.1
PCO0.50	97.7±0.2	96.3±0.3	45.6±0.4	90.4±3.7	18.4±0.2
1COD0.50	96.6±0.2	95.7±0.6	83.9±0.3	97.0±1.1	18.8±0.1
3COD0.50	98.1±3.4	95.9±0.2	78.0±1.1	96.5±1.3	17.6±0.1
5COD0.50	95.0±2.8	97.3±0.7	57.5±0.5	97.1±0.7	19.9±0.3
3NO0.50	97.6±1.2	98.2±0.4	45.2±0.4	90.7±4.2	14.8±0.2
3CH0.50	97.9±0.3	94.6±1.0	61.3±0.6	95.4±2.3	17.3±0.5



**Scheme 2-1.** Copolymerization of *cis*-cyclooctene (CO) with various second monomers: **a)** poly(cyclooctene-*co*-cyclooctadiene) (PCO-COD), **b)** poly(cyclooctene-*co*-norbornene) (PCO-NO), and **c)** poly(cyclooctene-*co*-cycloheptene) (PCO-CH) via ring opening polymerization in the presence of Grubbs catalyst 2<sup>nd</sup> generation. The reaction is held at room temperature (~22 °C) for 30 min under nitrogen environment before terminated by ethyl vinyl ether, followed by addition of tris(hydroxymethyl)phosphine in 2-propanol to cleanse residual catalyst.

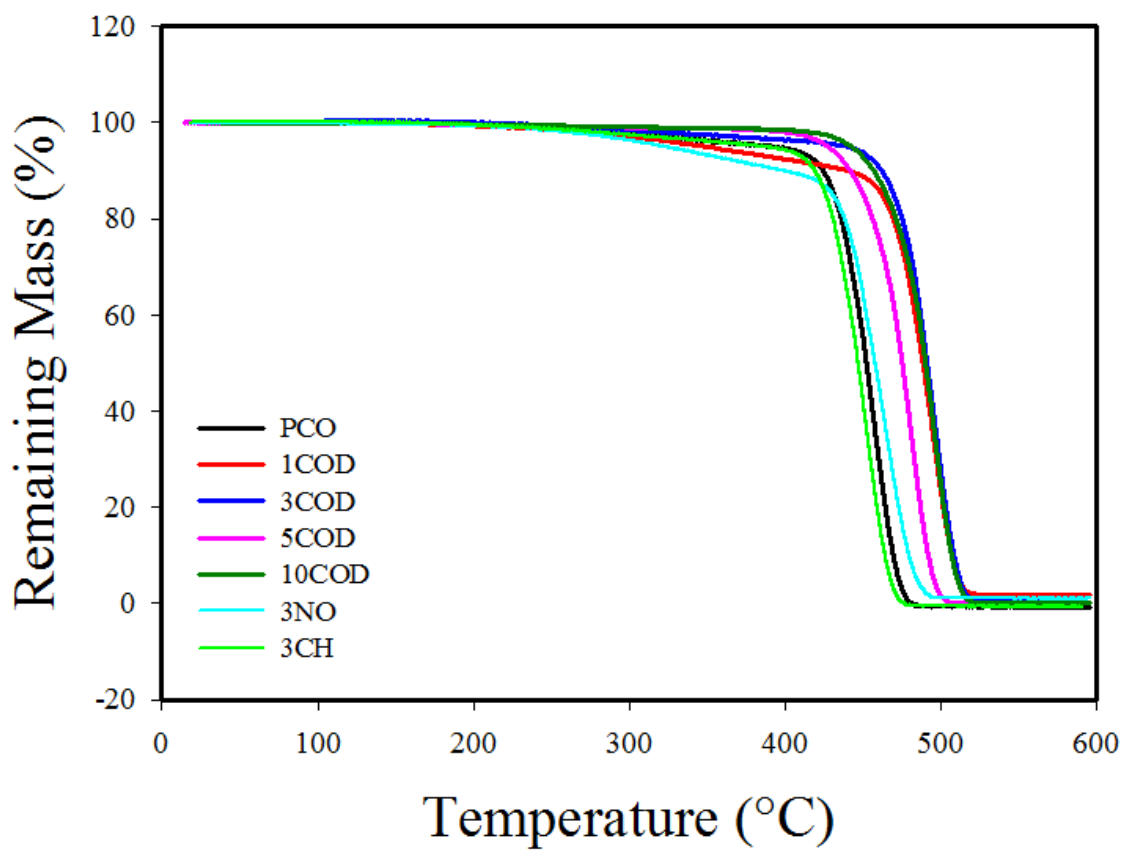


**Figure 2-1.** Thermogravimetric analysis (TGA) graph of all synthesized polymers: PCO (black), 1COD (red), 3COD (blue), 5COD (pink), 10COD (dark green), 3NO (cyan), and 3CH (green).

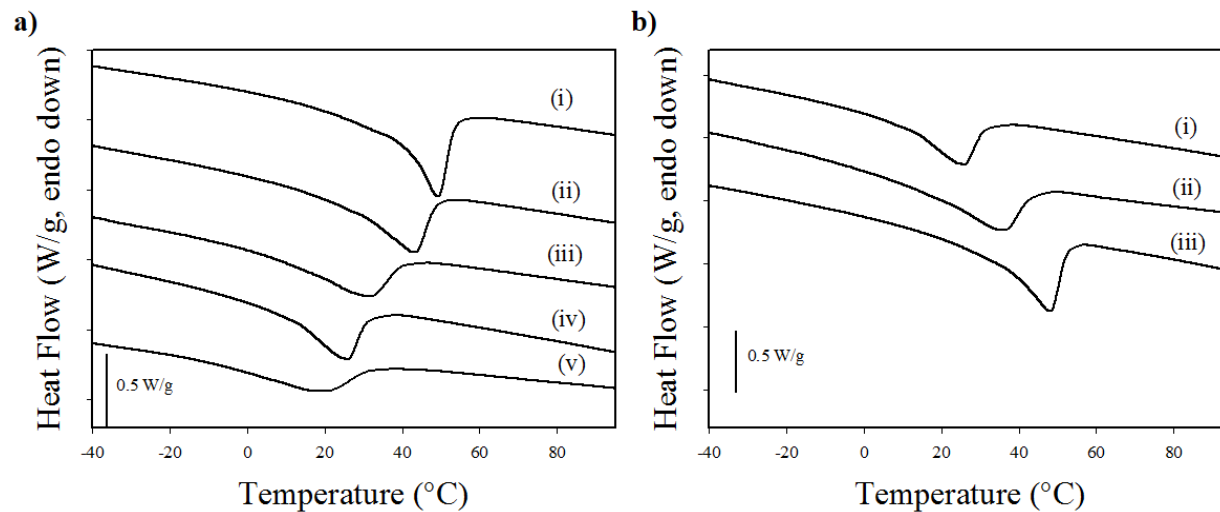


**Figure 2-2.** Differential Scanning Calorimetry (DSC) analysis graph of **a)** pristine PCO-COD polymers with varying COD mol. % contents: (i) PCO, (ii) 1COD, (iii) 3COD, (iv) 5COD, and (v) 10COD; and of **b)** pristine PCO-based copolymers with different second monomers: (i) 3COD, (ii) 3NO, and (iii) 3CH. Heating rate is 10 °C/min.



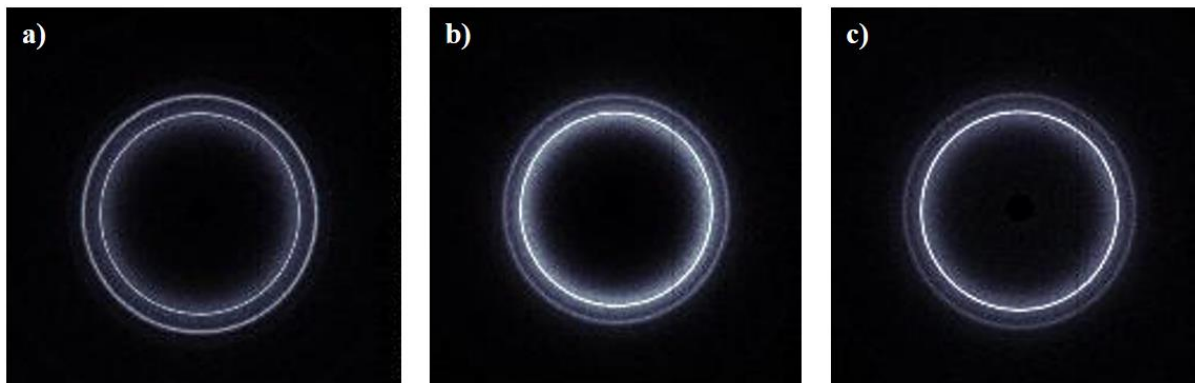


**Figure 2-3.** 2D WAXS pattern **a)** of the PCO0.50 sample, **b)** of the 3NO0.50 sample and **c)** of the 3CH0.50 sample. The X-ray wavelength ( $\lambda$ ) is 1.5405 Å.

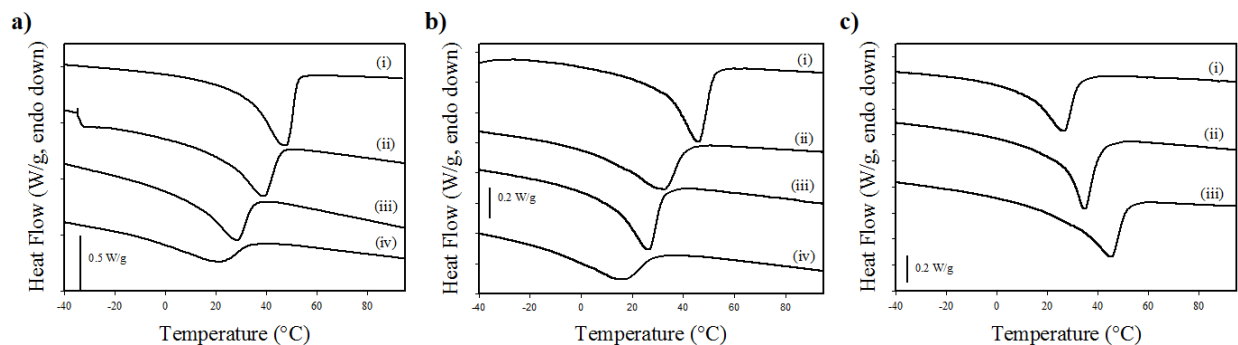


**Figure 2-4.** Differential Scanning Calorimetry (DSC) analysis graph of **a)** crosslinked PCO-COD polymers with DCP concentration of 0.25 wt. %: (i) PCO0.25, (ii) 1COD0.25, (iii) 3COD0.25, and (iv) 5COD0.25; and of **b)** crosslinked PCO-COD copolymers with DCP concentration of 0.50 wt. %: (i) PCO0.50, (ii) 1COD0.50, (iii) 3COD0.50, and (iv) 5COD0.50; and of **c)** crosslinked PCO-based copolymers with varying second monomers at a DCP concentration of 0.50 wt. %: (i) 3COD0.50, (ii) 3NO0.50, and (iii) 3CH0.50. Heating rate is 10 °C/min.

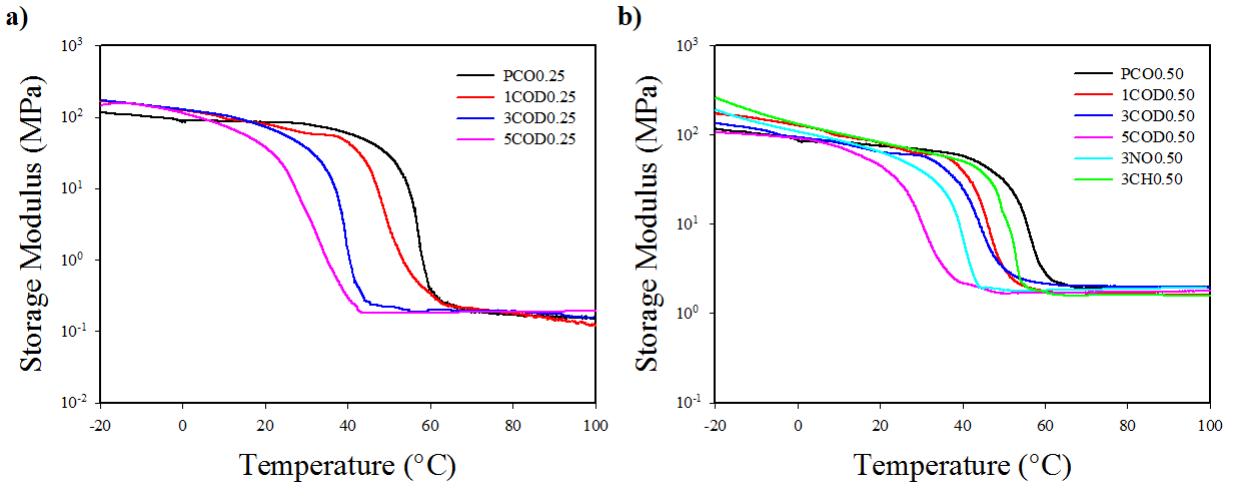


**Figure 2-5.** Storage modulus ( $E'$ ) vs temperatures for crosslinked copolymers with DCP concentration of **a)** 0.25 wt. % and **b)** 0.50 wt. %, respectively: PCO (black), 1COD (red), 3COD (blue), 5COD (pink), 3NO (cyan), and 3CH (green).  $E'$  was recorded at a heating rate of 3 °C/min with frequency of 1 Hz.

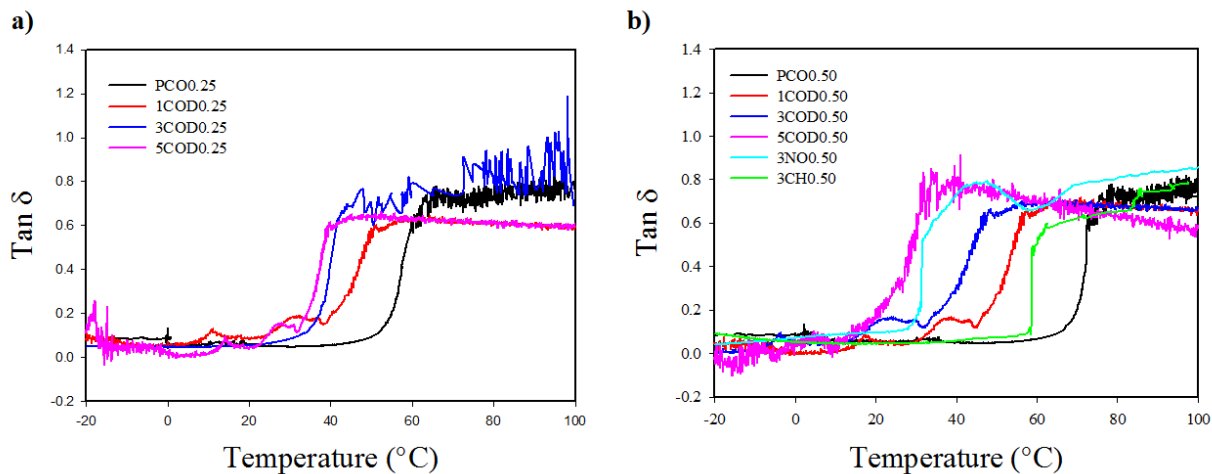


**Figure 2-6.**  $\tan \delta$  vs temperatures for crosslinked copolymers with DCP concentration of **a)** 0.25 wt. % and **b)** 0.50 wt. %, respectively: PCO (black), 1COD (red), 3COD (blue), 5COD (pink), 3NO (cyan), and 3CH (green).

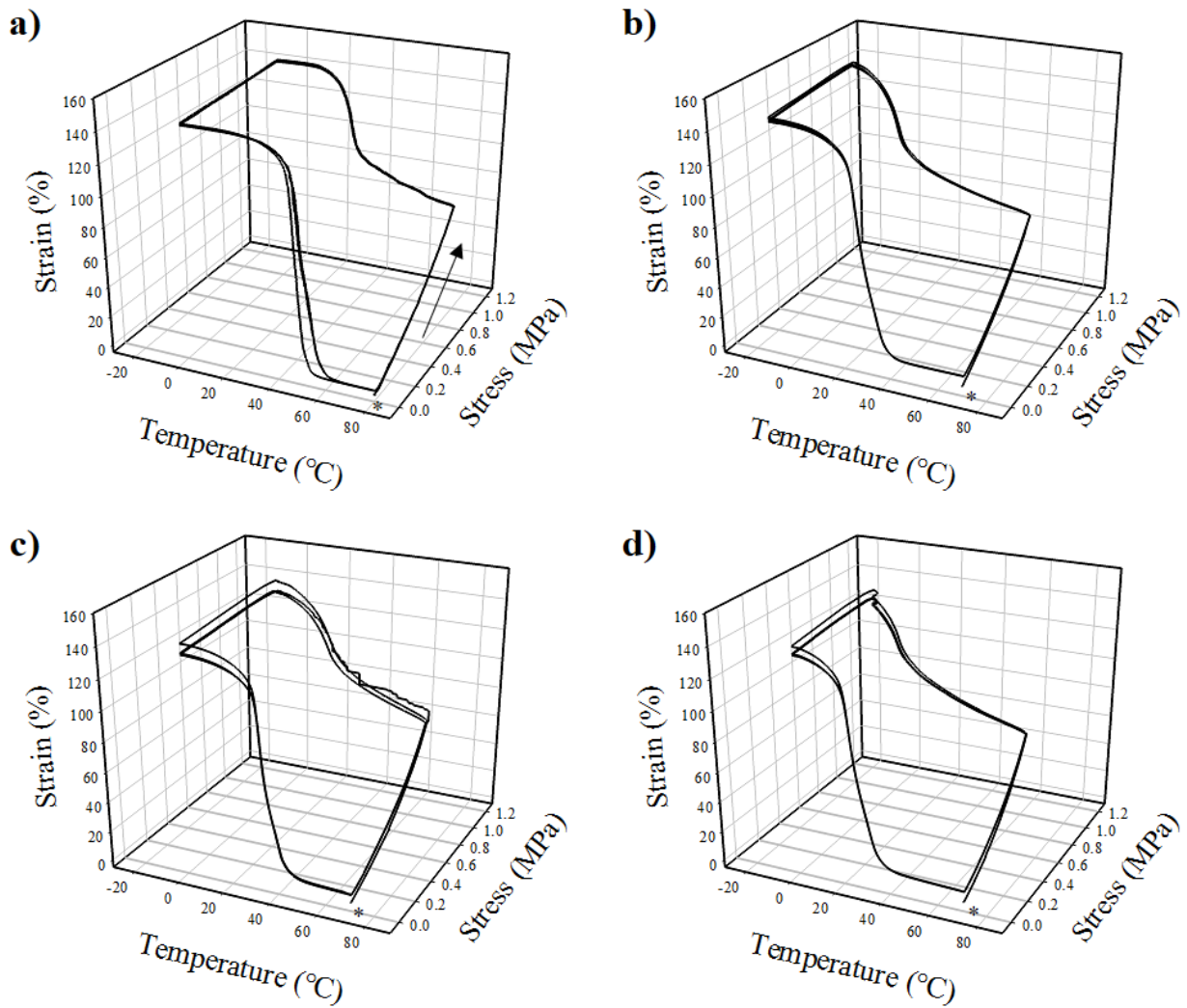


**Figure 2-7.** One-way shape memory cycles for a) PCO0.25, b) 1COD0.25, c) 3COD0.25, and d) 5COD0.25, respectively. The sample is deformed by increasing stress at 70 °C. A temporary shape was fixed by cooling at a rate of 2 °C/min and unloading, and then the original shape was recovered by heating at 2 °C/min. “\*” indicates starting point.

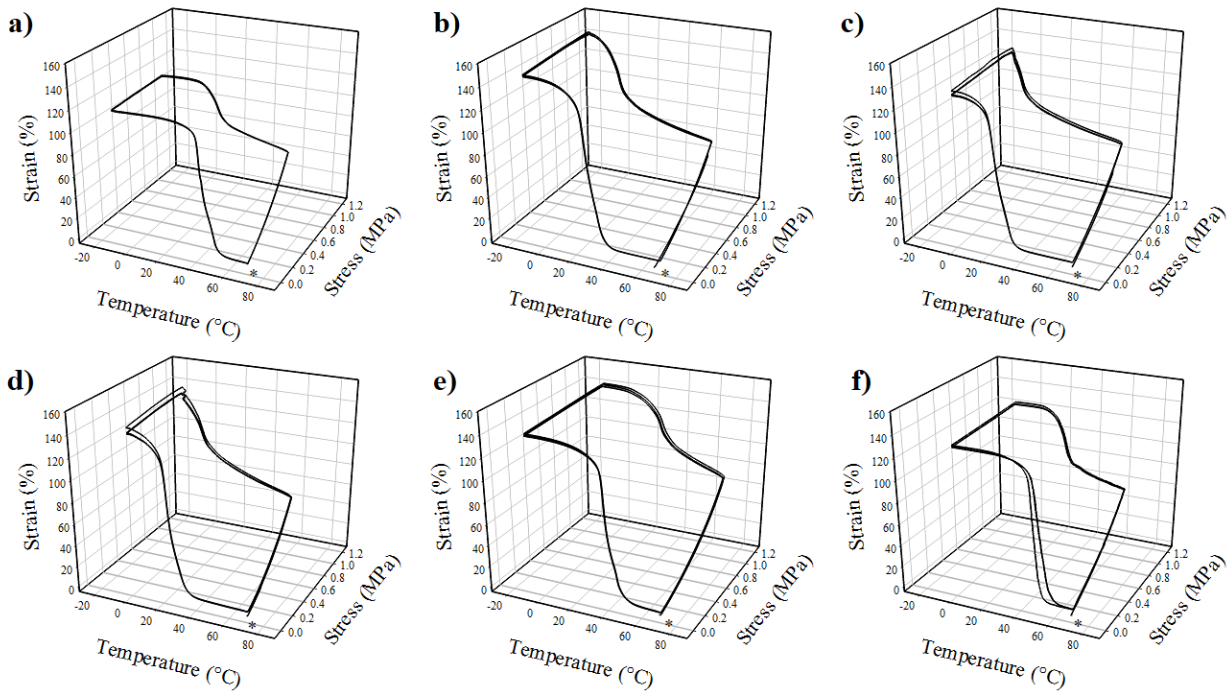


**Figure 2-8.** One-way shape memory cycles for a) PCO0.50, b) 1COD0.50, c) 3COD0.50, d) 5COD0.50, e) 3NO0.50, and f) 3CH0.50, respectively. The sample is deformed by increasing stress at 70 °C. A temporary shape was fixed by cooling at a rate of 2 °C/min and unloading, and then the original shape was recovered by heating at 2 °C/min. “\*” indicates starting point.

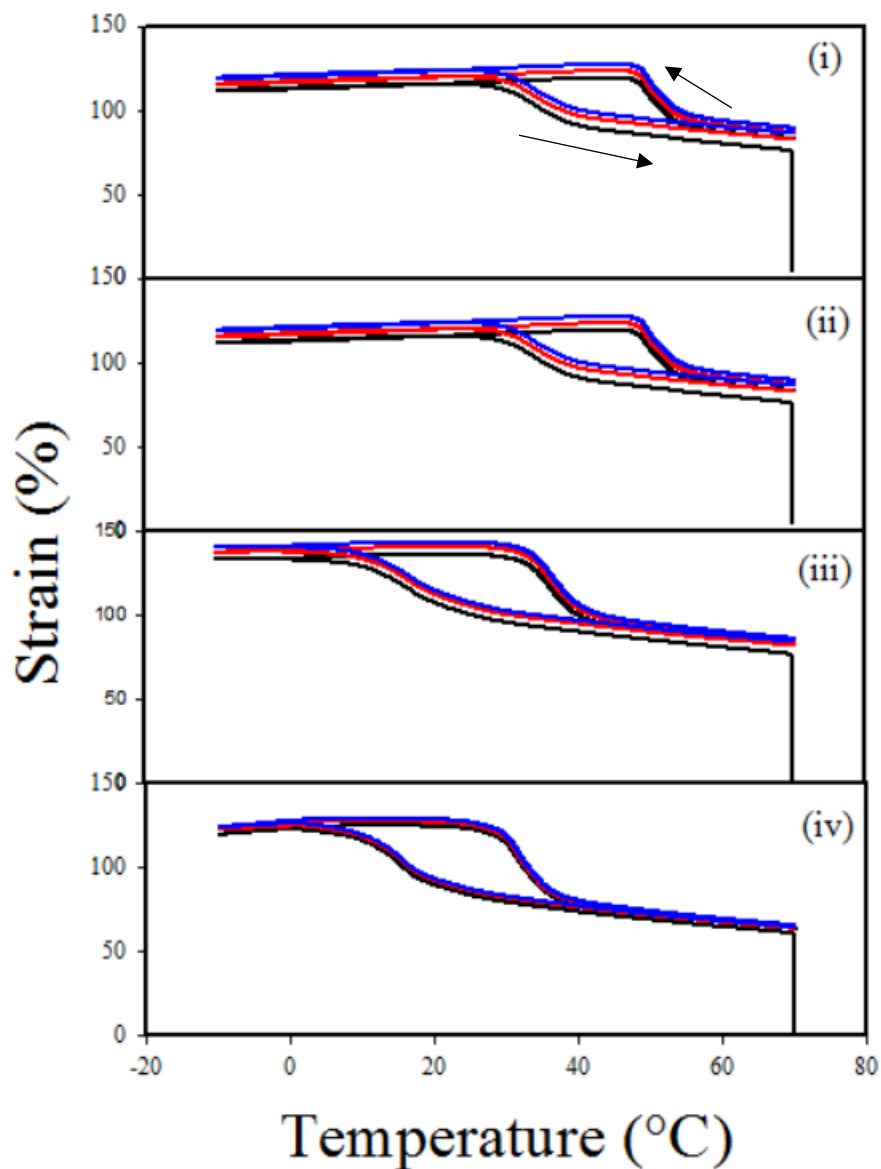


**Figure 2-9.** Two-way shape memory behavior of PCO-COD copolymers containing different COD contents cured with 0.25 wt. % DLP: (i) PCO0.25, (ii) 1COD0.25, (iii) 3COD0.25, and (iv) 5COD0.25. The samples were stretched under high temperature (70 °C) at a constant strain of 70%. The deformation step is followed by a cooling process at a rate of 2 °C/min, inducing an increase in strain. Then, the increased strain decreases by a heating process at a rate of 2 °C/min to 70 °C. Cycle: first (black), second (red), third (blue).

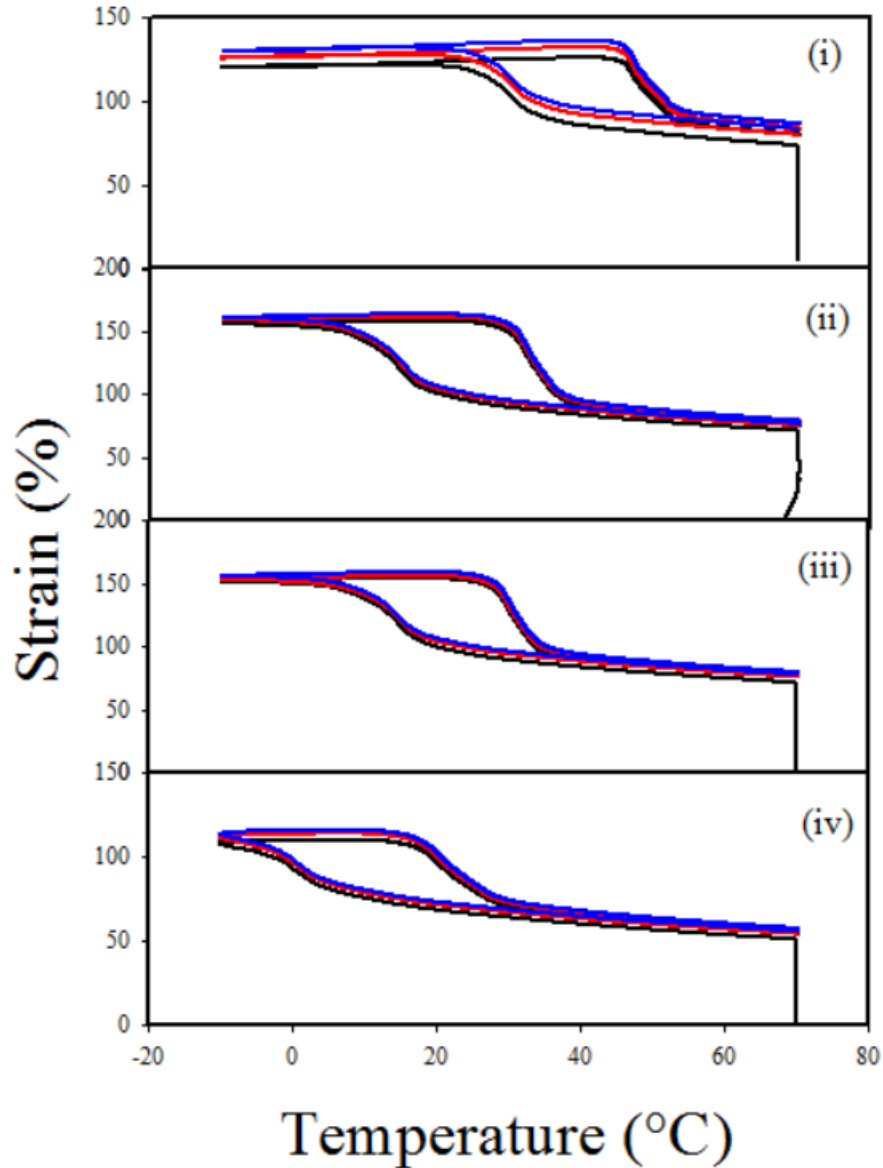


**Figure 2-10.** Two-way shape memory behavior of PCO-COD copolymers containing different COD contents cured with 0.50 wt. % DLP: (i) PCO0.50, (ii) 1COD0.50, (iii) 3COD0.50, and (iv) 5COD0.50. The samples were stretched under high temperature (70 °C) at a constant strain of 70%. The deformation step is followed by a cooling process at a rate of 2 °C/min, inducing an increase in strain. Then, the increased strain decreases by a heating process at a rate of 2 °C/min to 70 °C. Cycle: first (black), second (red), third (blue).



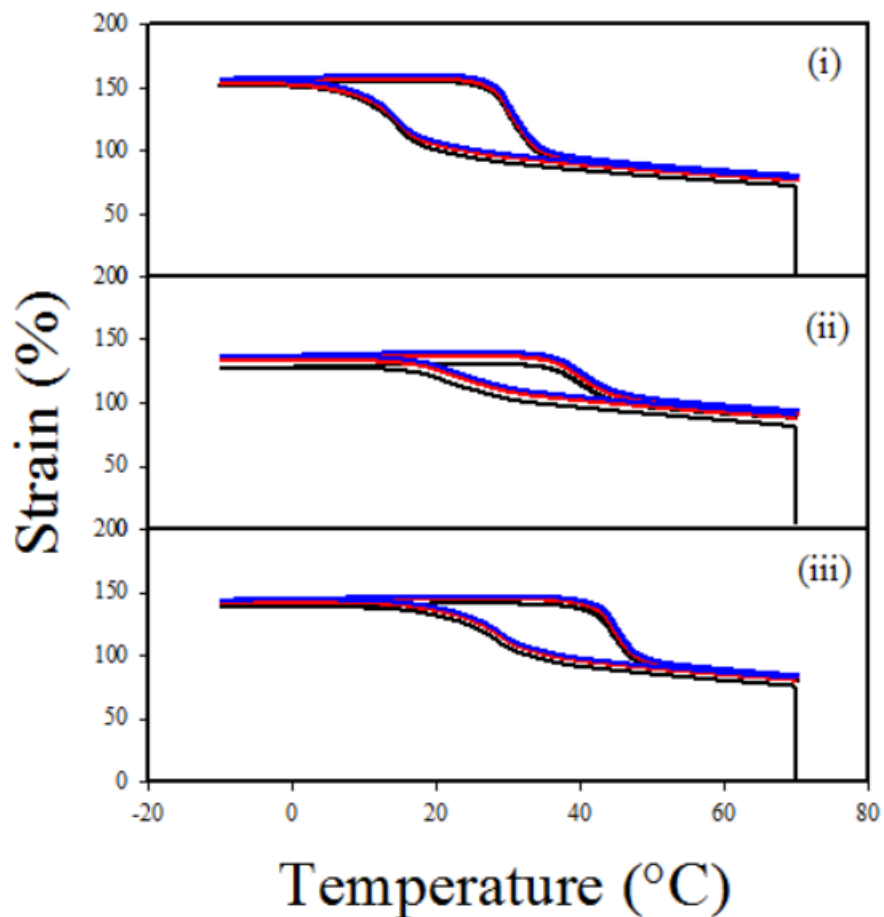


**Figure 2-11.** Two-way shape memory behavior of copolymers containing various second monomer cured with 0.50 wt. % DLP: (i) 3COD0.50, (ii) 3NO0.50, and (iii) 3CH0.50. The samples were stretched under high temperature (70 °C) at a constant strain of 70%. The deformation step is followed by a cooling process at a rate of 2 °C/min, inducing an increase in strain. Then, the increased strain decreases by a heating process at a rate of 2 °C/min to 70 °C. Cycle: first (black), second (red), third (blue).

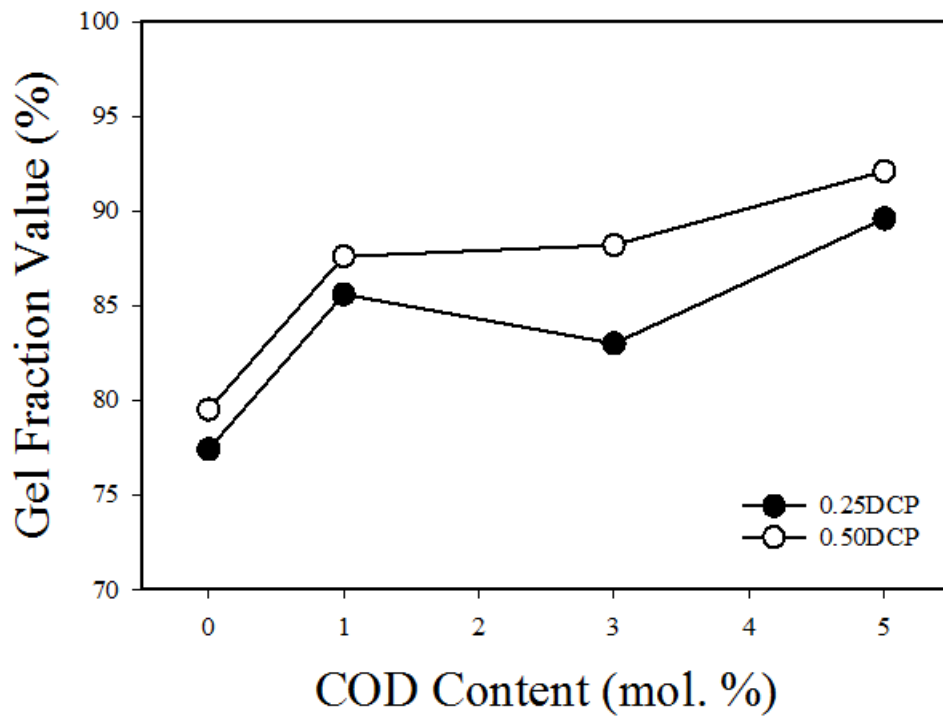


**Figure 2-12.** Gel fraction value ( $G$ ) as a function of COD content cured with different DCP concentrations. ( $\circ$ ) indicates 0.25 wt. % DLP and ( $\bullet$ ) 0.50 wt. % DLP.

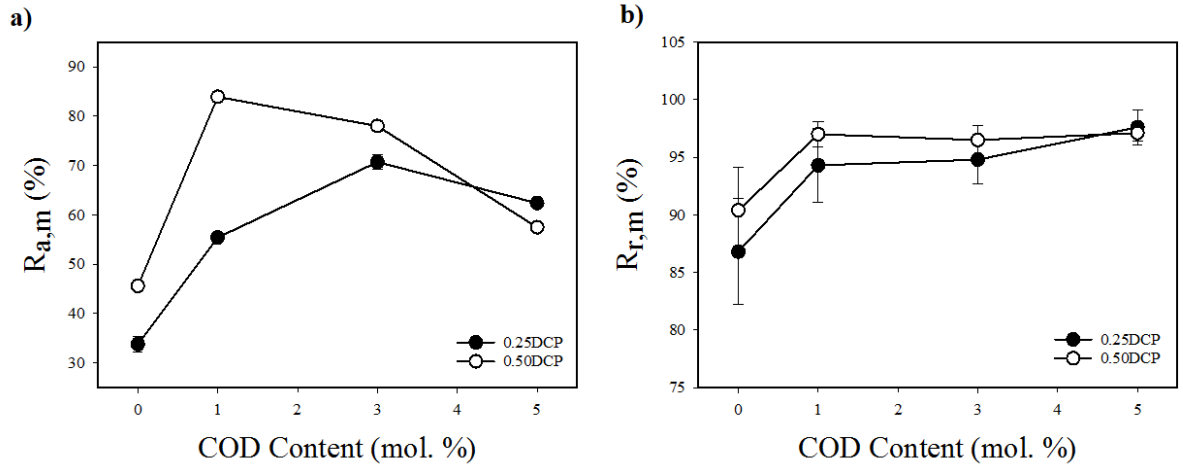


**Figure 2-13.** a) Actuation magnitude ( $R_{a,m}$ ) and b) recovery magnitude ( $R_{r,m}$ ) as a function COD content at different DCP concentrations for PCO, 1COD, 3COD, and 5COD. ( $\circ$ ) indicates 0.25 wt. % DCP and ( $\bullet$ ) 0.50 wt. % DCP.

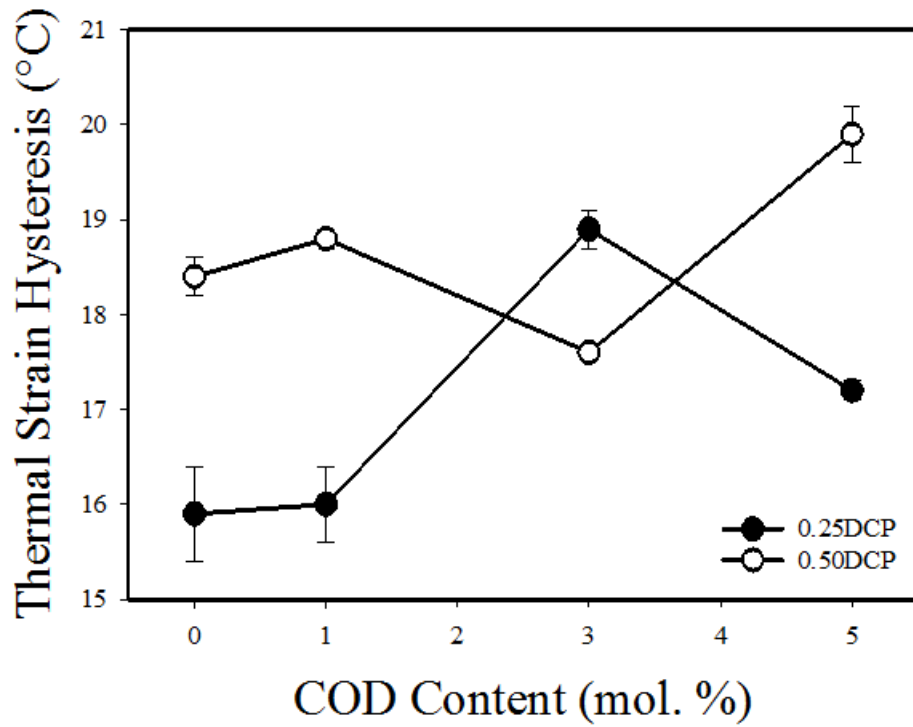


**Figure 2-14.** Thermal strain hysteresis ( $\Delta T$ ) as a function of COD content cured with different DCP concentrations. Thermal strain hysteresis was calculated from the temperature difference at the half of strain loop generating during cooling and heating. (○) indicates 0.25 wt. % DCP and (●) 0.50 wt. % DCP.

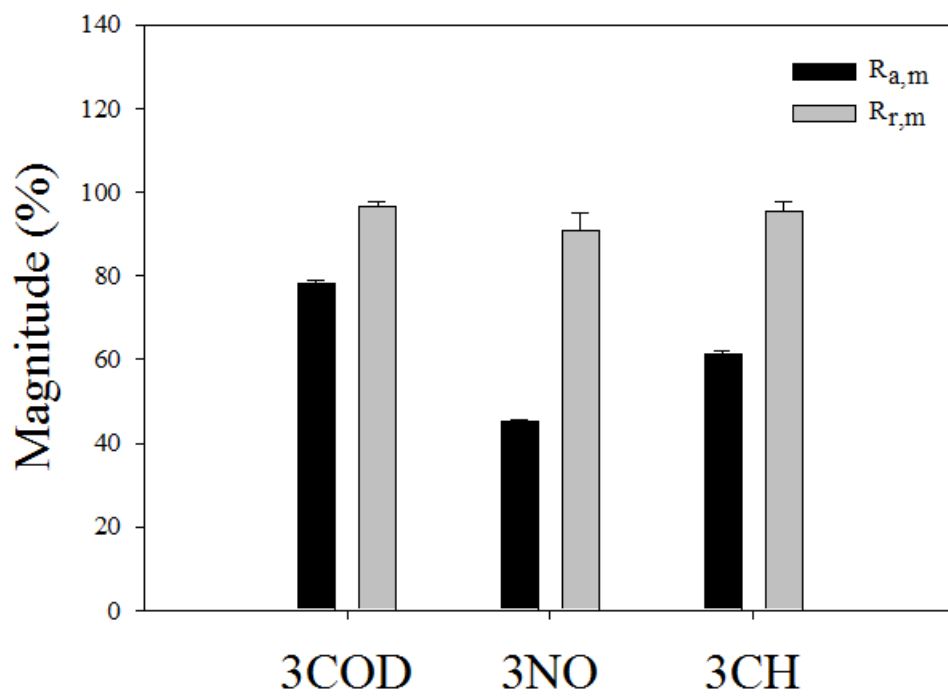


**Figure 2-15.** 2WSM characteristics of copolymers with varying second monomers in comparison in terms of actuation magnitude and recovery magnitude.

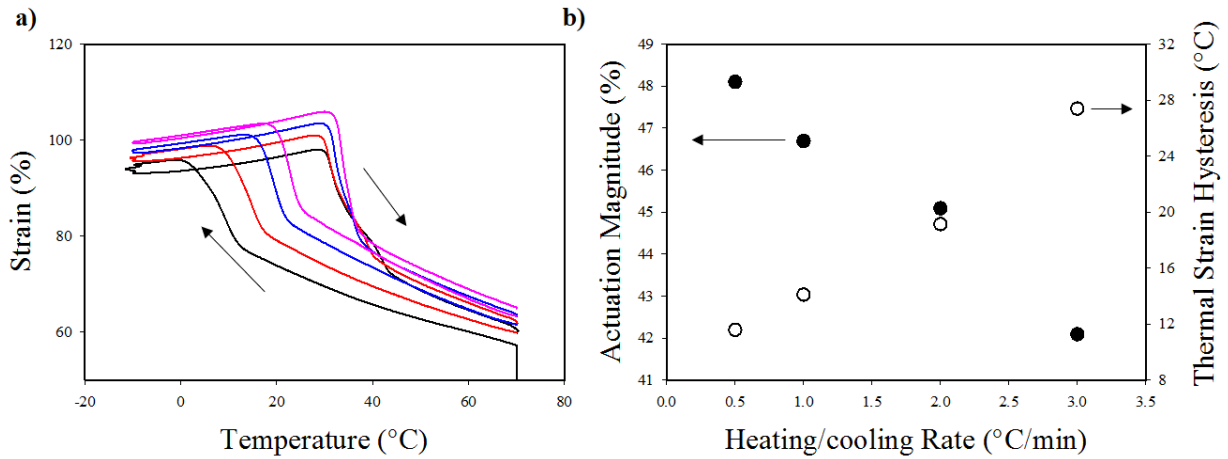


**Figure 2-16. a)** Two-way shape memory behavior for 3COD0.50 at different heating/cooling rates, 0.5 °C/min (pink), 1.0 °C/min (blue), 2.0 °C/min (red), and 3.0 °C/min (black). The sample was deformed under a tensile stress of 300 kPa at 70 °C; **b)** Actuation magnitude ( $R_{a,m}$ ) and strain hysteresis ( $\Delta T$ ) versus heating/cooling rate based on the two-way shape memory behavior of the 3COD0.50 sample, respectively. Maximum  $R_{a,m}$  (●) and  $\Delta T$  (○). The strain hysteresis was calculated from the temperature difference ( $\Delta T$ ) at the half of strain loop in two-way shape memory cycles.

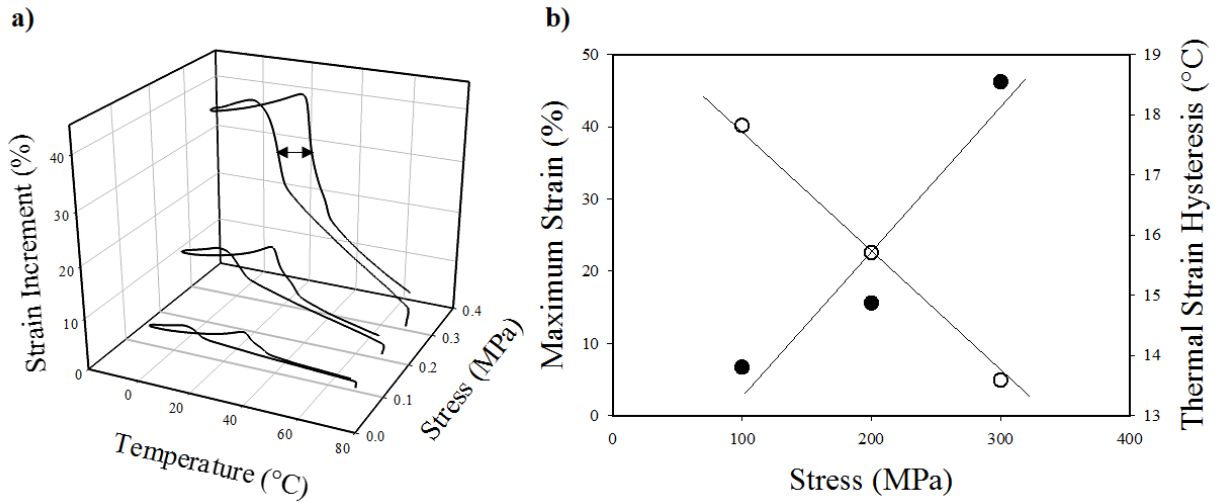


**Figure 2-17. a)** 3D two-way shape memory behavior for 3COD0.50 at different stresses, (i) 100 kPa, (ii) 200 kPa, and (iii) 300 kPa. The sample was deformed under each constant stress at 70 °C, followed by cooling and heating steps (2 °C/min), respectively; **b)** Maximum strain and strain hysteresis versus stress based on the two-way shape memory behavior of the 3COD0.50 sample, respectively. Maximum strain (●) and strain hysteresis (○). The strain hysteresis was calculated from the temperature difference ( $\Delta T$ ) at the half of strain loop in two-way shape memory cycles.

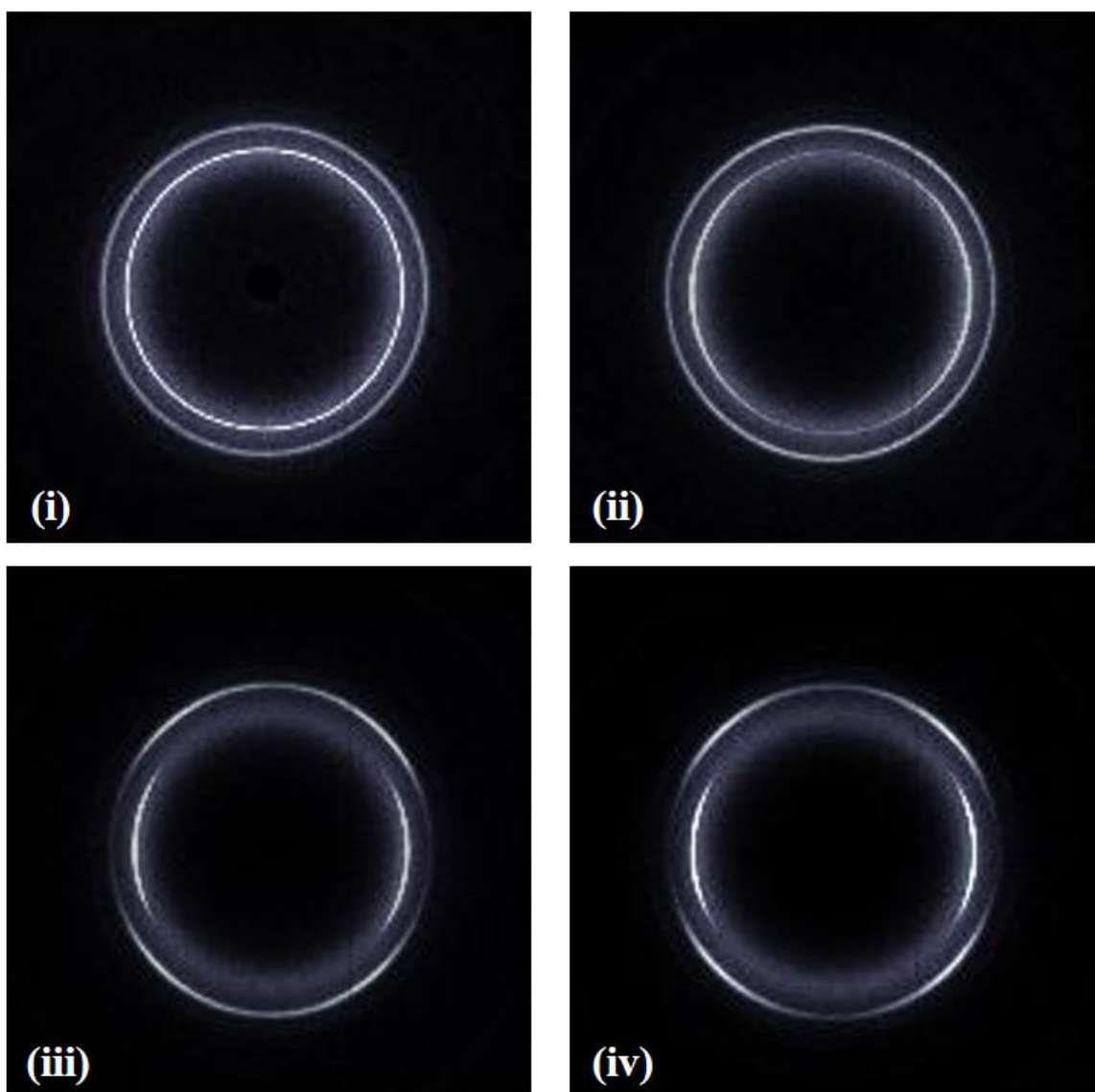


**Figure 2-18.** 2D WAXS patterns of the 3COD0.50 sample with an increase of loading after cooling: (i) unstretched, (ii) 100 kPa, (iii) 200 kPa, and (iv) 300 kPa. Stretching direction is vertical. The X-ray wavelength ( $\lambda$ ) is 1.5405 Å.



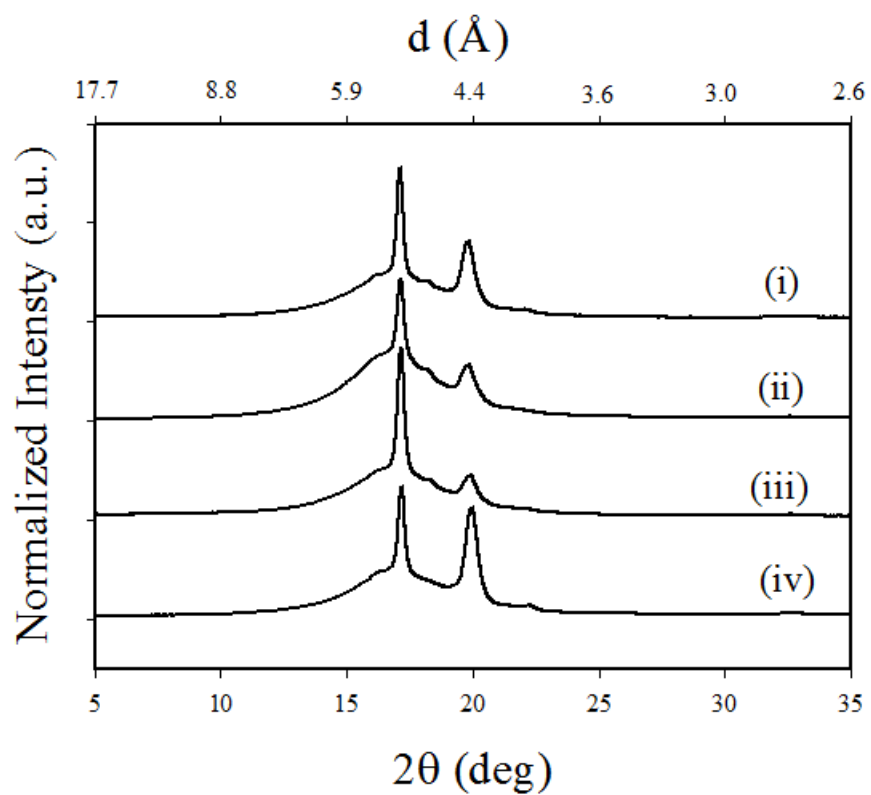


**Figure 2-19.** WAXS plots of (i) 3COD0.50, (ii) 3NO0.50, (iii) 3CH0.50, and (iv) PCO0.50. The X-ray wavelength ( $\lambda$ ) is 1.5405  $\text{\AA}$ .

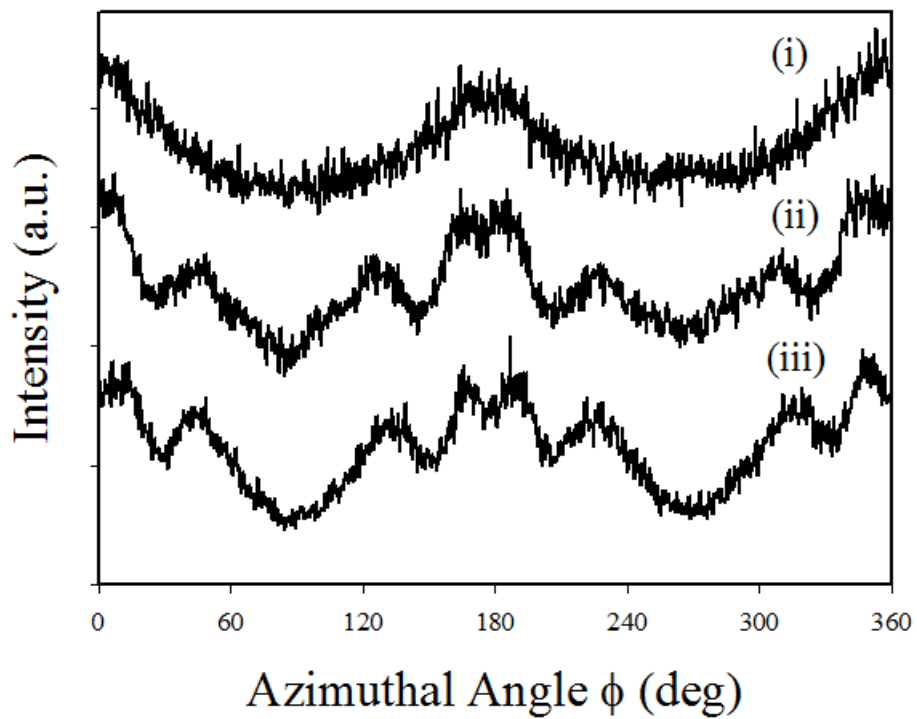


**Figure 2-20.** Azimuthal scanning profiles for the 3COD0.50 sample as a function of the applied stress: (i) 100 kPa, (ii) 200 kPa, and (iii) 300 kPa. The X-ray wavelength ( $\lambda$ ) is 1.5405 Å.

## **Chapter 3: A Latent-crosslinkable Poly( $\epsilon$ -caprolactone) (PCL)-based Thermoplastic Polyurethane: Synthesis, Shape Memory, and Degradation**

### **3.1 Synopsis**

In this chapter, seeking a latent-crosslinkable, mechanically flexible, fully thermoplastic shape memory polymer, we have developed a simple but effective macromolecular design that includes pendant crosslinking sites via the chain extender of a polyurethane architecture bearing semi-crystalline poly( $\epsilon$ -caprolactone) (PCL) soft segments. This new composition was used to prepare fibrous mats by electrospinning and films by solvent casting, each containing thermal initiators for chemical crosslinking. The one-step synthesis strategy proved successful, and the crosslinking sites within PCL segments resulted in two-way (reversible) shape memory: repeatable elongation (cooling) and contraction (heating) under constant tensile stress. Being fully characterized, the crosslinked fiber mats revealed promising one-way and two-way (reversible) shape memory phenomena, with lower storage moduli though, compared to uncrosslinked films. We observed for both fibrous mats and films that increasing the applied tensile stress led to greater crystallization-induced elongation upon cooling as well as smaller strain hysteresis, particularly for covalently crosslinked sample. Relevant to medical applications, the materials were observed to feature unique, two-stage enzymatic degradation that was sensitive to differences in crystallinity and microstructure among samples.

### **3.2 Introduction**

Shape memory polymers (SMPs) have attracted a lot of interest, both academically and industrially, based on the ability to set a temporary, non-equilibrium shape until they are triggered

to revert to original shape by a specific external stimulus <sup>1-3</sup>. Several environmental stimuli that can trigger shape changing of SMPs have been well studied thus far, such as heat, light, humidity, electric field, magnetic field, and variation of pH. Out of all the external stimuli, heat is the most widely investigated and used, as a result of the ease in ability to tailor thermo-mechanical properties of thermally actuated SMPs <sup>3</sup>. Consequently, thermally activated SMPs offer complexity of material response, including multistage shape change behavior <sup>4-6</sup> and reversible (two-way shape memory) actuation <sup>7,8</sup>. Such response complexity can then be manipulated and tuned through variations in material composition, fabrication method, and post-synthesis processes.

A need exists for rapid and reliable reversible actuation in SMPs in order to make artificial muscles or other actuators <sup>6,9,10</sup>. Addressing this need, liquid crystalline elastomers (LCEs) <sup>11,12</sup> have been shown to exhibit excellent performance, attributed to the coupling of the self-organization of liquid crystalline phase and the entropy elasticity of polymer networks. In general, when an external stress is applied, LCEs elongate during cooling from isotropic (amorphous) state to liquid crystalline phase, and contract during heating by achieving the strain associated with tensile modulus at isotropic state. Remarkably, “monodomain” samples feature actuation along the orientation axis with no external stress bias <sup>13</sup>. Toward attaining this reversible actuation behavior in a simple synthetic way, researchers have unveiled multiple macromolecular designs beyond LCEs that can also give rise to actuation. In our own lab, Chung et al <sup>14</sup> reported on tunable two-way shape memory behavior of crosslinked poly(cyclooctene) by variation of peroxide concentrations. In another approach, Baker et al <sup>15</sup> fabricated porous foams with body temperature triggering shape memory by crosslinking functionalized PCL and poly(ethylene glycol) (PEG) via thiol-ene chemistry, and, interestingly, the foams revealed reversible actuation behavior in compression other than in tension as commonly investigated. Besides the work accomplished by

our own lab, Behl et al <sup>16</sup> developed a reversible shape memory copolymer network that consists of poly( $\omega$ -pentadecalactone) segment determining the shape-changing geometry and poly( $\epsilon$ -caprolactone) segment providing the thermally activated actuation. Zhou et al <sup>17</sup> synthesized an end-capped poly(octylene adipate) that showcased both one-way and two-way reversible shape memory after thio crosslinked and acrylate crosslinked by exposing to 365 nm light.

With growing need in biomaterials and environmentally friendly materials, biodegradable PUs have been studied extensively as one of the specialized SMPs in the field of shape memory research. Teramoto et al <sup>18</sup> elaborated a novel approach that employed a multi-step copolymerization of L-lactide,  $\epsilon$ -caprolactone and ethylene glycol oligomer to yield a biodegradable, semicrystalline copolymer containing backbone C=C double bond. This copolymer could subsequently be crosslinked chemically, enabling the two-way shape memory behavior. Additionally, the compositional selection of diisocyanates and the molecular weight of soft segments have been found to play leading roles in tailoring select thermal, mechanical, and shape memory properties of PUs <sup>19,20</sup>. Beyond composition, material form and microstructural characteristics of SMPs may impose an equal influence on these properties. Electrospinning, as a highly versatile and widely used technique that allows fabrication of continuous, fine fibers, has been primarily applied on polymers (both synthetic and natural), and even metal alloys, ceramics <sup>21,22</sup>. Demir et al <sup>23</sup> obtained a electrospun PU based on poly(tetramethylene oxide), and also studied the effect of electric field, surrounding temperature, conductivity and viscosity of the polymer solution on structural properties of resulting fibers. However, to our best knowledge, no one has yet to combine electrospinning with thermal curing, especially for biodegradable PUs with a relatively low melting temperature.

For the present study, we sought to prepare fine fibers via electrospinning and to then post-cure the fibrous web to achieve two-way shape memory behavior. In this work, the approach we have implemented involves the use of 3, 4-dihydroxy-1-butene (DHB), functioning as a chain extender in polyurethane chemistry with a pendant allyl group that, simultaneously, serves to enable crosslinking while controlling the melting transition and crystallinity<sup>24-26</sup>. As variation in  $T_m$  near room temperature impacts crystallinity, and therefore shape memory behavior, manipulating thereof offers an effective approach to tune thermomechanical and potentially biological functions as a biomaterial. Our specific goal with current work was to develop crosslinkable, electrospinnable, biodegradable thermoplastic polyurethanes that feature two-way reversible shape memory behavior while maintaining comparable thermal and mechanical properties after processing and curing. Our approach was first to synthesize linear PCL-based thermoplastic polyurethanes<sup>27</sup> (subsequently referred to as PCL-TPUs) from polycaprolactone-diol, as a short, biodegradable soft segment and DHB, as a crosslinkable unit with a diisocyanate as segment linker. We next processed the synthesized PUs into both fiber mats (by electrospinning) and films (by compression molding), each containing initiators for thermal curing, respectively. Thermal, mechanical, and shape memory properties of the crosslinked materials were characterized, to further investigate the effect of processing and curing on these properties. Moreover, based on the knowledge gained from previous work<sup>28-30</sup>, enzymatic degradation study was conducted to study the degradation behavior and reveal possible mechanisms.

### **3.3 Experimental**

#### **3.3.1 Materials**

Poly(caprolactone)-diols (PCL<sub>2k</sub>, average M<sub>n</sub> ~ 2,000 g/mol, purchased from Sigma-Aldrich; PCL<sub>3k</sub>, average M<sub>n</sub> ~ 3,000 g/mol, purchased from Scientific Polymer Products, Inc.) were vacuum dried for 2 d prior to use. 3, 4-Dihydroxy-1-butene (DHB, ≥99%), dilauroyl peroxide (DLP, Luperox® LP, 97%), phosphate buffered saline (PBS, dry powder, pH 7.4 containing TWEEN® 20), and sodium azide (ReagentPlus®, ≥99.5%) were purchased from Sigma-Aldrich and used as received. Hexamethylene diisocyanate (HDI, purum, ≥98%) was purchased from Sigma-Aldrich and stored over 3 Å molecular sieves (Sigma-Aldrich) for 3 d before further use. Tin-POMS catalyst was purchased from Hybrid Plastics and vacuum dried extensively for a week prior to use. Lipase from *Pseudomonas cepacia* (powder, light beige, ≥30 U/mg) was purchased from Sigma-Aldrich and stored at -20 °C freezer before use. Toluene, chloroform, and n-hexanes were all purchased from Fisher Scientific. Toluene was dehydrated by refluxing over calcium hydride (Sigma-Aldrich) multiple times until collection and stored over 3 Å molecular sieves for 3 d before use. *N, N*-Dimethylformamide (DMF, anhydrous, 99.8%), HPLC-grade tetrahydrofuran (THF), and deuterated chloroform (Chloroform-d, 99.8% atom D) were purchased from Sigma-Aldrich and used as received.

### 3.3.2 Polyurethane Synthesis

A one-port synthesis method was adopted to synthesize the PCL-TPUs from PCL-diol, HDI, and DHB, as shown in Scheme 3-1. A Schlenk line (AF-0452, purchased from Chemglass Life Sciences) was utilized to create air-free reaction environment during the course of polymerization. Moisture was intentionally removed from the whole reaction system by evacuating and refilling clean nitrogen at least three times. A 500-mL Schlenk flask (AF-0528, single neck, round bottom) was oven dried at 80 °C and flame dried right before use. As a representative example, we specify the preparation of PCL<sub>3k</sub>-TPU as below. A mass of 9.0 g (3.0 mmol) PCL<sub>3k</sub> was dissolved in 100

mL distilled toluene within a 500-mL flask that was subsequently heated to and kept at 100 °C for about 30 min, while 100 mg (1 wt. %) Tin-POMS catalyst was dissolved into 5 mL distilled toluene for further use. Once the polymer solution became transparent, indicating that polymer was fully dissolved, 0.18 mL (2.1 mmol) DHB, 0.96 mL (6.0 mmol) HDI, and 5 mL toluene containing Tin-POMS were added into the flask via a syringe under an inert atmosphere of nitrogen. Incubation as such was maintained at 100 °C for 24 h to accomplish polymerization while stirring was kept to assure good mixing. A noticeable increase in viscosity during polymerization was witnessed. Following polymerization as described, the resulting polymer solution was precipitated by dropwisely addition into an 8-fold excess of n-hexane, followed by washing with deionized water. The precipitates were collected and dried in the fume hood overnight prior to complete drying in vacuum oven at room temperature for another 3 d.

### **3.3.3 Molecular Characterization**

The PCL<sub>2k</sub>-TPU and PCL<sub>3k</sub>-TPU harvested by method mentioned above were prepared using deuterated chloroform (CDCl<sub>3</sub>) at a concentration ranging from 20 to 30 mg/mL. The proton Nuclear Magnetic Resonance (<sup>1</sup>H NMR) spectra were generated using a Bruker Avance III HD 400 MHz spectrometer, to qualitatively verify chemical structure of synthesis products as well as to quantitatively analyze PCL-to-DHB mol. ratio per chain. The relaxation delay time is 1 s at a temperature of 25 °C. Gel Permeation Chromatography (GPC) was performed to determine number-average molecular weight ( $M_n$ ) and polydispersity index (PDI,  $M_w/M_n$ ), using a Waters Isocratic HPLC system equipped with a temperature-controlled differential refractometer (Waters 2414). Multi-angle laser light scattering (Wyatt miniDAWN) was introduced at three characteristic angles (45 °, 90 °, and 135 °) for in-line absolute molecular weight determination. The flow rate



of THF as mobile phase in this GPC system was set at 1 mL/h constantly. Polymer-THF solutions (2 – 5 mg/mL) were passed through a 0.2  $\mu\text{m}$  PTFE filter (Waters) prior to injection at 40 °C.

### 3.3.4 Sample Preparation

Seeking to understand the effect of PCL<sub>3k</sub>-TPU before and after processing and curing on thermal, mechanical and shape memory properties, polymers as synthesized were processed into films, by solvent casting, and, fiber mats, by electrospinning, respectively. To make films, 2 g PCL<sub>3k</sub>-TPU and 40 mg (2 wt. %) DLP were dissolved together into 20 mL chloroform, and the solutions then incubated in an Excella shaker (Excella E24, New Brunswick Scientific) at 37 °C until becoming completely transparent and homogeneous. The uniform solutions were then cast into a 5-inch Teflon dish above a large balanced platen afterwards, and allowed 48 h to dry completely. Cast films were further dried in vacuum oven at room temperature. To prepare electrospun fiber mats, a 17% (w/v) PCL<sub>3k</sub>-TPU solution was prepared by adding 2 g PCL<sub>3k</sub>-TPU and 40 mg DLP into a mixture of 8 mL chloroform and 4 mL DMF. The resulting solution was then heated to and kept at 37 °C with constant stirring. After dissolution completion, each polymer solution was processed into a nonwoven fibrous web (thickness ~ 0.15 mm) using a custom electrospinning set-up that has been previously reported by our group.<sup>31</sup> The ejecting needle was held at a potential of 16 kV, the tip-to-collector distance was 10 cm, the rotation rate of a 57.1 mm collecting mandrel was maintained at 400 rpm while the drum was held at a potential of negative 0.5 kV and a flow rate of polymer solution supplying the 22 gauge needle was 1.5 mL/h, all employed over the 8-hour electrospinning process. Complete drying of spun fiber mats was subsequently achieved in vacuum oven at room temperature before further use.

Eventually, the dried films and fiber webs were cured thermally by the following method. Samples (~ 2 g) were sandwiched between two polished stainless steel sheets coated with mold release agent (Pol-Ease® 2300, Polytek), and a 0.15 mm thick stainless steel spacer was placed in between to control the thickness of the final film. A 0.25 MPa compressive stress and a customized ramping heating method (temperature was set at 60 °C initially, ramping up to 90 °C by 20 °C/h, and finally kept at 90 °C for 30 min) were implemented throughout entire 2 h of curing, using a Carver 3851-0 press with heating platens. Afterwards, the platens were cooled down to room temperature, following which the compressive pressure was released.

### 3.3.5 Gel Fraction Measurement

In order to assess the extent of covalent crosslinking, network gel fraction values of the crosslinked films and crosslinked fiber mats were examined using solvent-extraction and gravimetry. Each sample was weighed for its dry mass before being soaked in 20 mL THF at 37 °C in an Excella shaker for 48 h, during which the THF was refreshed every 12 h. Then samples were washed with deionized water, blotted with common towel, and vacuum dried for a week at room temperature to remove residual solvent or water. The final dry mass was recorded for calculation of gel fraction. Calculation of gel fraction values involves the initial dry mass,  $m_i$ , and the final dry mass,  $m_f$ , using the equation below

$$G(\%) = \frac{m_f}{m_i} \times 100 \quad (3 - 1)$$

Depending on favorability of polymers interacting with THF, this  $G$  value typically falls into a range from 0% for a totally soluble polymer up to 100% for a perfectly crosslinked network where no free linear polymer chains exist.

### 3.3.6 Microstructural Characterization

To visualize surface morphology and structural geometry of cast films and electrospun fiber mats of PCL<sub>3k</sub>-TPU, Scanning Electron Microscopy (SEM) was conducted using a JEOL JSM-5600 microscope under an accelerating voltage of 5 kV. Both samples were gold-sputtered for 60 s prior to imaging by a Fujifilm FLA7000 reader. Also, to ascertain the molecular ordering and crystalline microstructure, wide angle X-ray scattering (WAXS) analysis was performed using a Rigaku S-MAX3000 for virgin cast films, crosslinked cast films, virgin electrospun fiber mats, and crosslinked electrospun fiber mats of PCL<sub>3k</sub>-TPUs. A Rigaku MicroMax-002+ generator was operated under an accelerating voltage of 45 kV and a current of 0.88 mA to yield a collimated beam of Cu *Ka* X-rays with a wavelength of 1.5405 Å. Scattering patterns were collected (see below) for 30 min except virgin fiber mat for 15 min due to high transmittance to X-rays. The sample-detector distance was fixed at 120.7 mm, leading to scattering angles  $3^\circ < 2\theta < 40^\circ$ . WAXS images were obtained and analyzed using a FujiFilm FLA7000 reader (with Fujifilm image plates CR HR-V) and SAXSgui software v2.03.04.

### 3.3.7 Thermal and Dynamic Mechanical Analysis

Differential Scanning Calorimetry (DSC) was employed to investigate thermal properties of all samples using the TA Instruments Q200 apparatus. Samples weighing approximately 5 mg underwent a thermal program of first heating to 140 °C at 10 °C/min, cooling to -60 °C at 10 °C/min, and then reheating at 10 °C/min to 140 °C while heat flow data was recorded. The melting transition temperature ( $T_m$ , the peak of the endotherm), crystallization transition temperature ( $T_c$ , the peak of the exotherm), and the enthalpy of melting ( $\Delta H$ , area beneath endothermic peak) were recorded, respectively, on the basis of second heating curve (to minimize the effects of thermal

history). Crystallinity of PCL<sub>3k</sub>-TPU was determined using the latent heat of melting relative to an accepted value for fully crystallized PCL<sub>3k</sub>, using the equation

$$X_c(\%) = \frac{\Delta H_{PCL_{3k}}}{\Delta H_{o,PCL_{3k}}} \times 100 \quad (3 - 2)$$

where  $\Delta H_{o,PCL_{3k}}$  is 64.92 J/g. We recognize that this is a rough estimation, due to the variation in synthesis from batch to batch.

A TA Instruments Q800 Dynamic Mechanical Analyzer (DMA) was adopted to explore the thermomechanical properties and also to assess success of crosslinking PCL<sub>3k</sub>-TPUs (i.e. crosslinked cast film and crosslinked spun fiber mat). In the multi-frequency controlled-strain mode each sample was equilibrated at -60 °C, held isothermal for 10 min, and heated continuously up to 100 °C at 3 °C/min. An oscillating frequency of 1 Hz, amplitude of 15 μm (ca. 0.2%), a preload force of 0.001 N, and a force track of 108% were utilized. Rectangle shaped samples with an approximate length-to-width ratio of 4:1 were used for testing.

### 3.3.8 Shape Memory Characterization

To probe and analyze one-way and two-way (reversible) shape memory behavior, dog bone shaped samples (ASTM D63 Type IV, scaled down by a factor of 4) were tested for crosslinked PCL<sub>3k</sub>-TPUs only, using DMA in controlled force mode. For one-way shape memory tests, samples were first strained to 40% at 90 °C, cooled at 2 °C/min to -30 °C under constant tension, released of their tensile stress, and finally heated up to 90 °C at 2 °C/min. This program was repeated three times for each sample. To quantify the one-way shape memory behavior, the calculation of the shape fixing ( $R_f$ ) and shape recovery ( $R_r$ ) ratios<sup>32</sup> for each individual cycle were performed using the equations below:

$$R_f(\%) = \frac{\varepsilon_f - \varepsilon_i}{\varepsilon_d - \varepsilon_i} \times 100 \quad (3 - 3)$$

$$R_r(\%) = \frac{\varepsilon_f - \varepsilon_r}{\varepsilon_f - \varepsilon_i} \times 100 \quad (3 - 4)$$

Here,  $\varepsilon_f$  stands for the fixed strain after release stress,  $\varepsilon_i$  for the initial strain at starting point of each cycle,  $\varepsilon_d$  for the deformed strain before unloading, and  $\varepsilon_r$  for the recovered strain after complete heating.

In contrast, two-way shape memory tests were performed in the following procedures: at first, each sample was deformed by ramping the applied tensile load at 0.01 N/min to 40% strain at a prescribed elevated temperature. The stress required to achieve this strain was then held fixed for all subsequent steps. Next, the samples were cooled to a prescribed low temperature at 2 °C/min. Finally, and after being held isothermally for 10 min, each sample was reheated to the initial elevated temperature at 2 °C/min. The strains were recorded as a function of temperatures while these procedures were done three times in succession. The quality of two-way shape memory behavior was subsequently evaluated by calculating the actuation magnitude ( $R_{a,m}$ ) and the recovery magnitude ( $R_{r,m}$ )<sup>14</sup>, using the equations as follows:

$$R_{a,m}(\%) = (\varepsilon_{low} - \varepsilon_{high}) \times 100 \quad (3 - 5)$$

$$R_{r,m}(\%) = \frac{\varepsilon_{low} - \varepsilon_{high}^{final}}{\varepsilon_{low} - \varepsilon_{high}^{initial}} \times 100 \quad (3 - 6)$$

where  $\varepsilon_{low}$  and  $\varepsilon_{high}$  are the strains respectively at low and high temperatures under loading,  $\varepsilon_{high}^{final}$  is the final strain at high temperature with stress applied after recovery, and  $\varepsilon_{high}^{initial}$  is the initial strain under stress at high temperature. In addition, the magnitude of hysteresis for each sample was determined as the temperature difference between the 50% actuation strain upon

heating (higher temperature) and cooling (lower temperature). We note that this value is heating/cooling rate dependent<sup>33</sup>; however, exploration of this dependence was beyond the scope of the present work.

### 3.3.9 Enzymatic Degradation Study

In vitro enzymatic degradation experiments were conducted at 37 °C in a PBS aqueous solution that contains 0.4 mg/mL<sup>34</sup> lipase from *Pseudomonas cepacia*. Sodium azide was added to the PBS buffer at a concentration of 1 mg/mL, to suppress microorganism growth. Virgin cast film, crosslinked cast film, virgin spun fiber mat and crosslinked spun fiber mat were cut into 10 mm squares with average thicknesses of 0.14, 0.12, 0.06 and 0.03 mm, respectively. Each sample was individually put into 20 mL vials with 5 mL PBS buffer prepared as above. The buffer was replaced with a fresh one every 4 d so as to sustain enzyme activity. At predetermined degradation time points, three samples from each composition were taken out of PBS buffer, rinsed with deionized water, blotted dry, further dried under vacuum for 4 d at room temperature, and finally weighed. The calculation of total percentage of mass loss involves in use of the following equation

$$\text{Mass Remaining (\%)} = \left( \frac{M_f}{M_i} \right) \times 100 \quad (3 - 7)$$

wherein  $M_f$  is the final dry weight and  $M_i$  is the initial dry weight of samples. The average value of three samples at the same time point was separately reported for different compositions and forms, error bars indicating one standard deviation. In addition, crystallinity changes during degradation were monitored using calorimetry (Eqn. (3-2)), to ascertain the degradability of a representative example of the new materials. To further study degradation mechanism, GPC ( $M_n$

measurements) experiments were applied to uncrosslinked PCL<sub>3k</sub>-TPU samples while gel fraction measurements (Eqn. (3-1)) were employed during degradation to crosslinked PCL<sub>3k</sub>-TPU samples.

### 3.4 Results and Discussion

#### 3.4.1 Molecular Characterization

Polyurethanes with varying soft segments were synthesized by condensation polymerization for both PCL<sub>2k</sub>-diol and PCL<sub>3k</sub>-diol with DHB and HDI in the presence of Tin-POMS catalyst (Scheme 3-1). The feed mol. ratio of three ingredients was determined, through trial-and-error method, to be 3:2.1:6 in order to maximize yield and molecular weight of resulting products. The reason why this ratio was not stoichiometric (2:1:3) is possibly that purity and reaction activities of three ingredients are not precisely equivalent. The results of the polyurethane syntheses are summarized in Table 3-1. <sup>1</sup>H NMR spectra confirmed success of incorporating unsaturation in both PCL<sub>2k</sub>-TPU and PCL<sub>3k</sub>-TPU in accordance with characteristic peaks at specific chemical shifts, and also showcased that actual DHB compositions are about 6 and 9.4 mol % for each case. Moreover, the incorporation of pendant allyl groups resulted in an average 19 °C or 10 °C drop of melting temperature for PCL<sub>2k</sub>-TPUs (~ 31 °C) or PCL<sub>3k</sub>-TPUs (~ 45 °C) compared to the melting temperature of their corresponding precursor, either PCL<sub>2k</sub>-diol (50 °C) or PCL<sub>3k</sub>-diol (55 °C), as shown in Figure 3-1. Increasing molecular weight of soft segment correspondingly increased enthalpy of melting, as a direct indication of crystallinity degree. Although high crystallinity might adversely influence shape memory effect of polyurethanes<sup>35,36</sup>, relatively low melting temperature that sits around room temperature would possibly cause poor shape fixing so that no good shape memory behavior would be expected if in practical use. As a result, we chose to use PCL<sub>3k</sub>-TPUs for following experiments and further study.

### 3.4.2 Microstructural Characterization

SEM images of all PCL<sub>3k</sub>-TPU samples described in sample preparation section are compiled in Figure 3-2, to study surface morphology and cross-sectional structure. Figure 3-2(a) and (e) show that a homogeneously distributed film with smooth surfaces were made by our customized compression molding method. As-spun fiber mat was imaged at different magnifications in Figure 3-2(b) and (f), indicating the outstanding capacity of this polymer to be easily processed into fibrous structure at a scale of a few hundreds of nanometers. More interestingly, following thermal curing process only caused partial melting of the spun fibers, resulting in a structural combination of fiber and matrix composed by the very same polymer (Figure 3-2(c) and (g)). Furthermore, a crosslinked spun fiber mat was hardened in liquid nitrogen for about 10 min, and then cut all the way through the thickness to unveil the cross-section. Cross-sectional views at different magnifications positively supported the previous conclusion in regard to that fiber-matrix composite structure, as we observed some continuous phase connecting to or wrapping around fibrous structure clearly in Figure 3-2(d) and (h). Evidently, part of PCL<sub>3k</sub>-TPU spun fibers preserved their original fibrous configuration, and kept their permanent shapes in that way other than being fully melted to form a uniform film during our customized thermal curing process. The coexistence of fiber and matrix, both made from the same polymer, also fits in the concept of Single Polymer Composite (SPC)<sup>37,38</sup>. This unique, porous structure could lead to some attractive mechanical and biological properties for broader range of applications.

To further characterize the microstructure of PCL<sub>3k</sub>-TPU, WAXS experiments were conducted on all four samples, revealing the independence of crystalline structure on processing or curing. All four samples showcased identical WAXS pattern (Figure 3-3(a), (b), (c), and (d)) and thus similar trend in the plot of intensity-versus-2 $\theta$  (Figure 3-3(e)). Out of all the WAXS patterns and



the peak intensities observed for virgin (uncrosslinked) spun fiber mat were relatively higher than the other three samples, attributed to high X-ray transmittance due to high porosity. In particular, the soft segment, PCL<sub>3k</sub>, exhibited two characteristic peaks (in Figure 3-3(e)) at  $2\theta = 21.42^\circ$  and  $23.66^\circ$ , respectively, within a broad range spanning  $2\theta = 18.80^\circ$  to  $26.60^\circ$ . These two peaks relate to  $d$ -spacings of 4.12 Å and 3.77 Å. Based on literature reports, the sharp peak at  $2\theta = 21.42^\circ$  (4.12 Å) corresponds specifically to the (110)<sup>39</sup> of PCL crystalline structure.

### 3.4.3 Thermal and Dynamic Mechanical Analysis

Thermal analyses were carried out for virgin cast film, crosslinked cast film, virgin spun fiber mat and crosslinked spun fiber mat using DSC, with analysis quantities summarized for comparison in Table 3-2. First cooling and second heating curves are shown in Figure 3-4 for these samples. In general, samples in different forms have been found to have identical  $T_m$ 's at around 46 °C, indicating no noticeable impact of crosslinking and form on melting transition. In contrast,  $T_c$ 's of spun fiber mats slightly shifted to lower temperatures, probably because the fibrous microstructure had a significant influence on thermal conductivity. A similar trend was found for enthalpies of melting, additionally revealing that crosslinked fiber mat featured the lowest value. The enthalpy of melting for each sample tested corresponds to crystallinity directly, as we use enthalpy to estimate crystallinity. Thus, we postulate that fibrous microstructure decreased crystallinity of the soft segments to some extent, which higher crosslinking degree decreased crystallinity even further<sup>40</sup>. The later postulation is well supported by gel fraction results. The gel fraction value for crosslinked film was 80% while that for crosslinked fiber mat was 90%. Given that the same curing condition was applied for both samples, the relatively high gel fraction value for crosslinked fiber mat imply that electrospinning process resulted in better mixing between the polymer and the crosslinker than solvent casting did.

The results of dynamic mechanical analysis (DMA) are compiled in Figure 3-5(a), for films and in Figure 3-6(a), for fiber mats, respectively. The storage modulus was monitored to investigate and compare their thermomechanical properties over temperature range spanning -60 °C to 100 °C. The storage modulus for each sample similarly dropped an order of magnitude, with increasing temperature from -60 °C to 20 °C prior to melting transition. Either films or fiber mats softened starting at around 37 °C, as the storage modulus began falling down quickly. Both virgin samples mat became too fluid to bear any stress just above 50 °C and finally yielded, as a result of complete melting of crystalline domain. On the contrary, both crosslinked samples were able to maintain stable rubbery states above their  $T_m$ 's. Beyond melting, the storage modulus for the crosslinked film leveled out at 1.49 MPa, which was about 3 times higher than crosslinked fiber mat (~0.50 MPa). We attribute this significant difference to the large fraction of void space existing in crosslinked spun fiber mat, with the support of prior SEM imaging data.

#### **3.4.4 Shape Memory Characterization**

In light of previous work<sup>13,41</sup> from our group, the presence of a stable rubbery plateau above  $T_m$  should allow such a polymeric sample to be deformed extensively without macroscopic flow, a prerequisite for decent shape memory effect. Hence, we should expect shape memory behavior for crosslinked samples only, because of the results discussed in previous section. The one-way shape memory cycles were plotted in a three-dimensional stress-temperature-strain graph (Figure 3-5(b) for crosslinked film and Figure 3-6(b) for crosslinked fiber mat), showing the response of the samples to shape fixing and recovery. Quantification of one-way shape memory behavior typically involves in the calculation of fixing and recovery ratios using eqn. (3-3) and (3-4), as summarized in Table 3-3. We observed that both types of crosslinked samples exhibited excellent fixing and recovery ratios, all above 99%, indicating the exceptional capacity of this material to sustain

programmed deformation upon loading as well as to recover precisely back to original shape. Furthermore, due to the remarkable increase in strain that occurred during crystallization of PCL<sub>3k</sub>-bearing TPUs upon cooling (See Figure 3-5(b) and 3-6(b)), it was expected that the crosslinked PCL<sub>3k</sub>-TPUs would be good candidates for two-way reversible shape memory phenomenon.

Two-way shape memory behavior features reversible elongation and contraction, under constant loading, upon cooling and heating through the melting transition, respectively. Two-way shape memory cycles for the new materials are shown in Figure 3-5(c), for crosslinked film and in Figure 3-6(c), for crosslinked fiber mat, revealing great potential to change in shape reversibly without noticeable creeps. More interestingly, in both cases, the strain barely changes or slightly increases with decreasing temperature, except during the crystallization where the strain spikes up drastically with an  $R_{a,m}$  of  $\sim 15\%$ , for crosslinked film and of  $\sim 24\%$ , for crosslinked fiber mat, respectively. The crosslinked fiber mat exhibited a higher actuation magnitude possibly because of its lower storage moduli above  $T_m$ . On the other hand, it was observed that the recovery magnitude of crosslinked film is approximately 10% higher than that of crosslinked fiber mat. We speculate that there are primarily two factors playing significant roles in affecting recovery magnitude, one being the highly porous structure, and the other being the relaxation of residual stresses imparted during the electrospinning and compression molding process. The latter speculation is favorably supported by two-way shape memory cycles of crosslinked fiber mat (Figure 3-6(c)), as we found a low recovery magnitude particularly for the first cycle ( $\sim 77\%$ ).

The estimation of a critical stress <sup>2,13</sup>,  $\sigma_c$ , beyond which stress-induced crystallization occurs is of great importance for consideration as actuators. It is also known that increasing of tensile stress applied would have a strong influence on actuation performance.<sup>13</sup> Therefore, two-way shape memory cycles at different stress levels were performed on the crosslinked film (Figure 3-5(d))

and crosslinked fiber mat (Figure 3-6(d)). From such testing, the maximum strain increment and strain hysteresis were collected and plotted as a function of the stress applied. We observed that the strain increment of crosslinked film was elevated from 27.3% up to 42.7% (a 56.4% increase) by increasing the tensile stress from 0.30 MPa to 0.70 MPa (a 133% increase) correspondingly. In comparison, crosslinked fiber mat revealed a 411% increase of the strain increment from 12.3% to 62.9%, as the stress increased from 0.15 MPa to 0.45 MPa (a 200% increase). Figure 3-7a and Figure 3-7b were then used, respectively, to calculate critical stress by extrapolating the maximum strain linearly to the stress axis, revealing a  $\sigma_c = -0.28$  MPa, for crosslinked film and a  $\sigma_c = 0.08$  MPa, for crosslinked fiber mat, respectively. Given the fact that crystallization-induced elongation is always inactivated below critical stress, these low critical stress value implied that, theoretically, the external stress would be minimal for this elongation to occur.

### 3.4.5 Enzymatic Degradation Study

For tissue engineering, medical device and drug delivery applications, controlled biodegradation properties are highly preferred for polymeric biomaterials. Enzymatic degradation studies, a common method by which the biodegradation rate could be measured rapidly in a short amount of time, have played an important role in characterizing the polymeric materials. In this work, we found a two-step, bulk degradation for the new PCL<sub>3k</sub>-TPUs, dependent on their crystalline structure and their crosslinking state. Figure 6a shows the results of enzymatic degradation profiles of all four types of PCL<sub>3k</sub>-TPU samples, including virgin cast film, crosslinked cast film, virgin spun fiber mat, and crosslinked spun fiber mat. In general, we found that all samples have experienced a two-stage degradation (Figure 3-8(a)): at the first stage, a much faster degradation phenomenon was found roughly over first two weeks, and at the second stage the degradation slowed down to the same rate for all samples through the rest of our experimental time range. To

further interpret this special degradation behavior, thermal analysis was done for all samples at different time points using DSC. The change in crystallinity for each sample was monitored individually over time during the entire degradation study, as shown in Figure 3-8(b). As for virgin fiber mat, no data was recorded after day 22 due to insufficient residual mass, which is beyond capability of our DSC. Then, except for this case, it was clearly observed that the crystallinities of virgin film, crosslinked film and crosslinked fiber mat increased to varying degrees with degradation time. Interestingly, crystallinity was observed to increase during early stage of degradation, follow by a leveling off that coincided with the observed degradation profiles. This observation can be understood by considering the fact that the enzymes would preferentially attack the amorphous phase since that amorphous phase is in much lower order than crystalline region.<sup>34</sup> Thus, in fact, the amorphous region was broken down at a higher rate, initially, resulting in a relatively fast degradation as well as a quick increase of crystallinity on a percentage basis. Consequently, at this point, the crystallinity at surface was assumed to be generically lower than the interior of the sample. However, as degradation proceeded, more crystalline domains were exposed to the buffer solution containing the lipases, which in return constrained the degradation progress to varying extents that depend on the microstructural properties of specific sample. Considering molecular weight evolution during enzymatic degradation, GPC tests (Figure 3-8(c)) suggested that bulk degradation<sup>42</sup> was occurring over the duration of the study for both virgin film and virgin fiber mat, consistent to the results from previous work.<sup>30</sup> Moreover, we found no obvious shrinkage for both samples by examining the sizes visually (Figure 3-9). On the other hand, the decreasing gel fraction during degradation (Figure 3-6(d)) suggests bulk degradation for crosslinked cast films and fiber mats.

Although sharing similar tendency of the enzymatic degradation, all four types of samples behaved differently from each other upon closer inspection. Among the four types of samples, the crosslinked film underwent degradation at the lowest rate, which we attribute to its highest crystallinity. Beyond our expectation, the crosslinked spun fiber mat showcased a slower degradation rate than the crosslinked cast film, despite its processing by the same compression molding process that usually eliminates structural discrepancy. We speculate that this could be primarily due to the difference on microstructure between two samples. In particular, as we showed previously in SEM images, the crosslinked fiber mat possessed a more porous structure, potentially allowing more enzymes to attach to and attack the polymers. Additionally, confirming this speculation further, we figured out that the density of the crosslinked film ( $\sim 1.19 \text{ g/cm}^3$ ) was approximately 45% higher than that of the crosslinked fiber mat ( $\sim 0.82 \text{ g/cm}^3$ ) as stated in Table 3-4. Out of these four types of samples, only virgin fiber mat achieved complete degradation within our experimental time span. We attribute this mainly to the larger surface-to-volume ratio due to the highly porous structure, resulting in a larger contact area for lipases with polymers.

The effect of the enzymatic degradation on surface morphology was studied for four different types of PCL<sub>3k</sub>-TPU samples, respectively, using SEM (Figure 3-10). For each type, the degraded samples at different select time points were compared to the control sample that was not treated with any PBS buffer. We observed that all samples, except virgin fiber mat, revealed uniform rough surface after exposed to enzymes, implying a lipase-specific erosion that is mainly dominated by a surface-limited mechanism<sup>43</sup>. As with gradual increase of surface roughness associated with erosion degree, more and larger spherical pores could be found on the surface, especially in the later period of the study. These porous structures showed up starting at day 2 for virgin film, but not until day 18 for crosslinked film, in coincidence with the conclusions drawn

from degradation profiles. For crosslinked fiber mat, the original surface morphology disappeared almost completely within 2 d in the course of degradation, leaving an extremely rough surface. This phenomenon could be attributed to the unique, non-uniform internal structure (Figure 3-1(d) and (h)). Specifically, we speculate that the porosity was relatively higher on the surface versus at the center, and thereof, the sample began degrading in a similar way like the films did, once the surface layer has been chipped away quickly. Different from the other three, the virgin fiber mat exhibited a characteristic “melted” structure where the fine, smooth fibers became relatively fluffy and swelled due to some bulk degradation. Moreover, the macroscopic transparency and appearance of the enzymatically eroded samples could be found in Figure 3-9.

### **3.5 Conclusions**

Novel, versatile thermoplastic polyurethanes containing unsaturation were prepared from a biodegradable soft segment, polycaprolactone-diol (PCL-diol), and a small functional diol with pendant allyl group, 3,4-dihydroxy-1-butene (DHB), and a diisocyanate using a one-pot synthesis technique. The molecular and thermal properties of these materials were investigated by GPC, DSC and  $^1\text{H}$  NMR initially, and PCL<sub>3k</sub>-TPU was picked out for further study due to a suitable melting temperature that would allow favorable shape fixing. In this work, PCL<sub>3k</sub>-TPU was successfully processed into films, by solvent casting and fiber mats, by electrospinning, respectively. Dilauroyl peroxide (DLP) was used as a thermal initiator to crosslink film and spun mat samples covalently via compression molding process. SEM images indicate successful formation of fiber at a scale of nanometers, and a unique structure containing partially melted fibers and homogeneously distributed phase. Analysis with a DMA illustrated that crosslinked PCL<sub>3k</sub>-TPUs, either in a form of film or spun mat, exhibited outstanding one-way and two-way shape memory behavior, both with good shape fixing and recovery. Furthermore, the critical

stresses were estimated, indicating that crosslinked PCL<sub>3k</sub>-TPUs needed no or very little stress for crystallization-induced elongation to be initiated, though increasing stress yielded proportionally increasing shape actuation.

An enzymatic degradation study revealed that the processing of samples resulted in quite different microstructures, playing a significant role in degradation behavior. We observed that the new PCL<sub>3k</sub>-TPUs underwent bulk degradation in a two-step way that the degradation progressed faster in the first a few days than after. Considering the easy processability, exceptional reversible actuation, and predictable biodegradability, we envision that this family of latent-crosslinkable, biodegradable polyurethanes can be utilized in mechanical and medical applications including reversible actuators, sensors, and stents.



### 3.6 References

1. Lendlein, A.; Kelch, S.: Shape Memory Polymers. *Angew. Chem. Int. Ed.* **2002**, 41, 2034 – 2057.
2. Ratna, D.; Karger-Kocsis, J.: Recent Advances in Shape Memory Polymers and Composites: A Review. *J. Mater. Sci.* **2008**, 43, 254 – 269.
3. Liu, C.; Qin, H.; Mather, P. T.: Review of Progress in Shape Memory Polymers. *J. Mater. Chem.* **2007**, 17, 1543 – 1558.
4. Xie, T.: Tunable Polymer Multi-shape Memory Effect. *Nature* **2010**, 464, 267 – 270.
5. Yu, K.; Xie, T.; Leng, J.; Ding, Y.; Qi, H. J.: Mechanisms of Multi-shape Memory Effects and Associated Energy Release in Shape Memory Polymers. *Soft Matter* **2012**, 8, 5687 – 5695.
6. Mather, P. T.; Luo, X.; Rousseau, I. A.: Shape Memory Polymer Research. *Annu. Rev. Mater. Res.* **2009**, 39, 445 – 471.
7. Li, J.; Rodgers, W. R.; Xie, T.: Semi-crystalline Two-way Shape Memory Elastomer. *Polymer* **2011**, 52, 5320 – 5325.
8. Westbrook, K. K.; Mather, P. T.; Parakh, V.; Dunn, M. L.; Qi, Q.; Lee, B. M.; Qi, H. J.: Two-way Reversible Shape Memory Effects in A Free-standing Polymer Composite. *Smart Mater. Struct.* **2011**, 20, 065010.

9. Shenoy, D. K.; Thomsen III, D. L.; Srinivasan, A.; Keller, P.; Ratna, B. R.: Carbon Coated Liquid Crystal Elastomer Film for Artificial Muscle Applications. *Sensors and Actuators A* **2002**, 96, 184 – 188.
10. Leng, J.; Lan, X.; Liu, Y.; Du, S.: Shape Memory Polymers and Their Composites: Stimulus Methods and Applications. *Prog. Mater. Sci.* **2011**, 56, 1077 – 1135.
11. Yu, Y.; Ikeda, T.: Soft Actuators Based on Liquid-crystalline Elastomers. *Angew. Chem. Int. Ed.* **2006**, 45, 5416 – 5418.
12. Ohm, C.; Brehmer, M.; Zentel, R.: Liquid Crystalline Elastomers as Actuators and Sensors. *Adv. Mater.* **2010**, 22, 3366 – 3387.
13. Krause, S.; Zander, F.; Bergmann, G.; Brandt, H.; Wertmer, H.; Finkelmann, H.: Nematic Main-chain Elastomers: Coupling and Orientational Behavior. *Comptes Rendus Chimie* **2009**, 12, 85 – 104.
14. Chung, T.; Romo-Uribe, A.; Mather, P. T.: Two-way Reversible Shape Memory in A Semicrystalline Network. *Macromolecules* **2008**, 41, 184 – 192.
15. Baker, R. M.; Henderson, J. H.; Mather, P. T.: Shape Memory Poly( $\epsilon$ -caprolactone)-copoly(ethylene glycol) Foams with Body Temperature Triggering and Two-way Actuation. *J. Mater. Chem. B* **2013**, 1, 4916 – 4920.
16. Behl, M.; Kratz, K.; Zotzmann, J.; Nöchel, U.; Lendlein, A.: Reversible Bidirectional Shape Memory Polymers. *Adv. Mater.* **2013**, 25, 4466 – 4469.

17. Zhou, J.; Turner, S. A.; Brosnan, S. M.; Li, Q.; Carrilo, J. Y.; Nykypanchuk, D.; Gang, O.; Ashby, V. S.; Dobrynin, A. V.; Sheiko, S. S.: Shape-shifting: Reversible Shape Memory in Semicrystalline Elastomers. *Macromolecules* **2014**, 47, 1768 – 1776.
18. Teramoto, N.; Kogure, H.; Kimura, Y.; Shibata, M.: Thermal Properties and Biodegradability of The Copolymers of L-Lactide,  $\epsilon$ -Caprolactone, and Ethylene Glycol Oligomer with Maleate Units and Their Crosslinked Products. *Polymer* **2004**, 45, 7927 – 7933.
19. Ping, P.; Wang, W.; Chen, X.; Jing, X.: The Influence of Hard-segments on Two-phase Structure and Shape Memory Properties of PCL-based Segmented Polyurethanes. *J. Polym. Sci. Pol. Phys.* **2007**, 45, 557 – 570.
20. Kim, B. K.; Lee, S. Y.: Polyurethanes Having Shape Memory Effects. *Polymer* **1996**, 37, 5781 – 5793.
21. Senador Jr., A. E.; Shaw, M. T.; Mather, P. T.: Electrospinning of Polymeric Nanofibers: Analysis of Jet Formation. *Mat. Res. Soc. Symp. Proc.* **2001**, 661, 5.9.1 – 6.
22. Greiner, A.; Wendorff, J. H.: Electrospinning: A Fascinating Method for The Preparation of Ultrathin Fibers. *Angew. Chem. Int. Ed.* **2007**, 46, 5670 – 5703.
23. Demir, M. M.; Yilgor, I.; Yilgor, E.; Erman, B.: Electrospinning of Polyurethane Fibers. *Polymer* **2002**, 43, 3303 – 3309.
24. Odian, G.: *Principles of Polymerization*; 4th; John Wiley & Sons, New Jersey, 2004.
25. Güven, O.: *Crosslinking and Scission in Polymers*; Springer, Netherlands, 1990.

26. Boire, P. C.; Gupta, M. K.; Zachman, A. IL.; Lee, S. H.; Balikov, D. A.; Kim K.; Bellan, L. M.; Sung, H.: Pendant Allyl Crosslinking as A Tunable Shape Memory Actuator for Vascular Applications. *Acta Biomater.* **2015**, 24, 53 – 63.
27. Lawton, M. I.; Tillman, K. R.; Mohammed, H. S.; Kuang, W.; Shipp, D. A.; Mather, P. T.: Anhydride-based Reconfigurable Shape Memory Elastomers. *ACS Macro. Lett.* **2016**, 5, 203 – 207.
28. Gan, Z.; Liang, Q.; Zhang, J.; Jing, X.: Enzymatic Degradation of Poly( $\epsilon$ -caprolactone) Film in Phosphate Buffer Solution Containing Lipases. *Polym. Degrad. Stabil.* **1997**, 56, 209 – 213.
29. Zeng, J.; Chen, X.; Liang, Q.; Xu, X.; Jing, X.: Enzymatic Degradation of Poly(L L-lactide) and Poly( $\epsilon$ -caprolactone) Electrospun Fibers. *Macromol. Biosci.* **2004**, 4, 1118 – 1125.
30. Gu, X.; Wu, J.; Mather, P. T.: Polyhedral Oligomeric Silsesquioxane (POSS) Suppresses Enzymatic Degradation of PCL-based Polyurethanes. *Biomacromolecules* **2011**, 12, 3066 – 3077.
31. Luo, X.; Mather, P. T.: Preparation and Characterization of Shape Memory Elastomeric Composites. *Macromolecules* **2009**, 42, 7251 – 7253.
32. Robertson, J. M.; Nejad, H. B.; Mather, P. T.: Dual-spun Shape Memory Elastomeric Composites. *ACS Macro Lett.* **2015**, 4, 436 – 440.
33. Burke, K. A.; Rousseau, I. A.; Mather, P. T.: Reversible Actuation in Main-chain Liquid Crystalline Elastomers with Varying Crosslink Densities. *Polymer* **2014**, 55, 5897 – 5907.
34. Rice, M. A.; Sanchez-Adams, J.; Anseth, K. S.: Exogenously Triggered, Enzymatic Degradation of Photopolymerized Hydrogels with Polycaprolactone Subunits:

- Experimental Observation and Modeling of Mass Loss Behavior. *Biomacromolecules* **2006**, 7, 1968 – 1975.
35. Lee, B. S.; Chun, B. C.; Chung, Y. C.; Sul, K. I.; Cho, J. W.: Structure and Thermomechanical Properties of Polyurethane Block Copolymers with Shape Memory Effect. *Macromolecules* **2001**, 34, 6431 – 6437.
36. Ahmad, M.; Xu, B.; Purnawali, H.; Fu, Y.; Huang, W.; Mirafteb, M.; Luo, J.: High Performance Shape Memory Polyurethane Synthesized with High Molecular Weight Polyol as The Soft Segment. *Appl. Sci.* **2012**, 2, 535 – 548.
37. Barkoula, N.; Peijs, T.; Schimanski, T.; Loos, J.: Processing of Single Polymer Composites Using the Concept of Constrained Fibers. *Polym. Composite.* **2005**, 26, 114 – 120.
38. Kim, N. K.; Fakirov, S.; Bhattacharyya, D.: Polymer-polymer and Single Polymer Composites Involving Nanofibrillar Poly(vinylidene fluoride): Manufacturing and Mechanical Properties. *J. Macromol. Sci. Phys.* **2014**, 53, 1168 – 1181.
39. Jiang, S.; He, C.; Men, Y.; Chen, X.; An, L.; Funari, S. S.; Chan, C.: Study of Temperature Dependence of Crystallization Transitions of A Symmetric PEO-PCL Diblock Copolymer Using Simultaneous SAXS and WAXS Measurements with Synchrotron Radiation. *Eur. Phys. J. E* **2008**, 27, 357 – 364.
40. Krumova, M.; López, D.; Benavente, R.; Mijangos, C.; Pereña, J. M.: Effect of Crosslinking on the Mechanical and Thermal Properties of Poly(vinyl alcohol). *Polymer* **2000**, 41, 9265 – 9272.
41. Liu, C.; Chun, S. B.; Mather, P. T.: Chemically Cross-linked Polycyclooctene: Synthesis, Characterization, and Shape Memory Behavior. *Macromolecules* **2002**, 35, 9868 – 9874.

42. Nair, L. S.; Laurencin, C. T.: Biodegradable Polymers as Biomaterials. *Prog. Polym. Sci.* **2007**, 32, 762 – 798.
43. Christenson, E. M.; Patel, S.; Anderson, J. M.; Hiltner, A.: Enzymatic Degradation of Poly(ether urethane) and Poly(carbonate urethane) by Cholesterol Esterase. *Biomaterials* **2006**, 27, 3920 – 3926.

**Table 3-1.** Synthesis Summary of CO-based copolymers

Samples <sup>a</sup> (n≥5)	Feed molar ratio <sup>b</sup> (PCL <sub>xk</sub> :DHB:H DI)	Actual molar PCL <sub>3k</sub> : DHB <sup>c</sup>	Yield (Mass %)	Molecular weight (M <sub>w</sub> , kDa)	PDI	T <sub>m</sub> (°C) <sup>d</sup>	ΔH <sub>m</sub> (J/g)
PCL <sub>2k</sub> -TPU	3:2.1:6	15.58:1	89.3±8.1	288±43.7	2.00±0.28	30.8±1.6	30.4±3.5
PCL <sub>3k</sub> -TPU	3:2.1:6	9.61:1	90.9±9.3	150.5±38.6	1.79±0.14	45.2±2.6	42.1±1.9

<sup>a</sup> Nomenclature: **PCL<sub>xk</sub>** stands for polycaprolactone-diol with Mn=x kDa, **DHB** for 3,4-dihydroxy-1-butene, **HDI** for hexamethylene diisocyanate.

<sup>b</sup> Tuned ratio by trial-and-error method.

<sup>c</sup> Determined by NMR spectra.

<sup>d</sup> Peak values of second heating in DSC curve.

**Table 3-2.** Thermal and Structural properties of PCL<sub>3k</sub>-based Thermoplastic Polyurethanes

Sample (n≥3)	DLP (wt. %)	$T_m$ (°C)	$T_c$ (°C)	$\Delta H_m$ (J/g)	$\chi C$ (%) <sup>a</sup>	G (%)
Virgin Cast Film	0.0%	45.44±0.19	10.38±0.49	42.36±0.85	66.79±0.01	0.0±0.0
Crosslinked Cast Film	2.0%	46.61±0.35	10.77±1.11	43.26±1.07	66.64±0.02	80.2±4.0
Virgin Spun fiber Mat	0.0%	46.09±0.13	9.08±0.04	41.11±0.43	63.32±0.07	0.0±0.0
Crosslinked Spun fiber Mat	2.0%	45.67±0.21	8.23±0.78	39.05±3.15	60.15±0.05	90.5±2.2

<sup>a</sup> Crystallinities were determined from  $\Delta H_{\text{crystal}} = 64.92$  J/g (Neat PCL<sub>3k</sub>).



**Table 3-3.** 1WSM and 2WSM characteristics for Crosslinked PCL<sub>3k</sub>-TPUs in Different Forms

---

Sample	Fixing ratio (%)	Recovery ratio (%)	Actuation Magnitude (%)	Recovery Magnitude (%)
Crosslinked Cast Film	99.34±0.01	99.04±0.42	14.88±0.33	96.90±1.64
Crosslinked Spun Fiber Mat	99.66±0.02	99.48±0.37	23.55±0.64	87.93±8.13

---

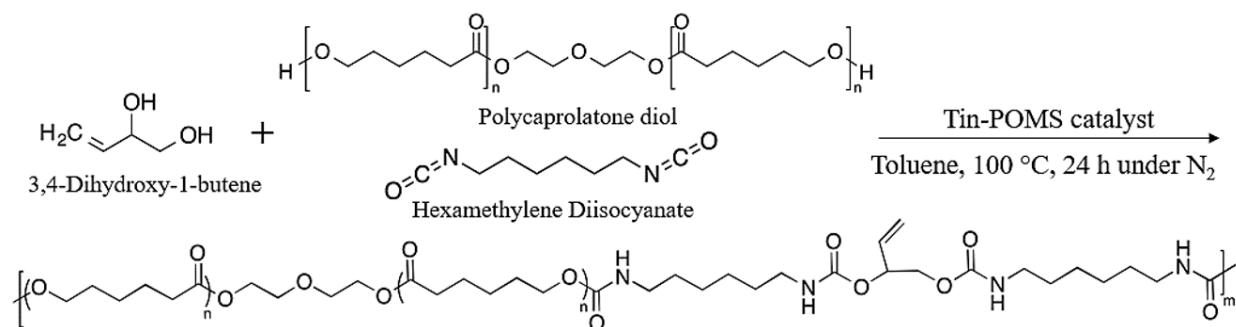
**Table 3-4.** Densities of PCL<sub>3k</sub>-TPU crosslinked cast film and crosslinked spun fiber mat

Sample (n≥3)	Length (mm) <sup>a</sup>	Width (mm) <sup>a</sup>	Thickness (mm) <sup>b</sup>	Volume (mm <sup>3</sup> )	Mass Weight (mg) <sup>c</sup>	Density (g/cm <sup>3</sup> )
Crosslinked Cast Film	9.353±0.051	8.235±0.065	0.115±0.038	8.858±0.107	10.56±0.872	1.192±0.098
Crosslinked Spun fiber Mat	10.331±0.077	9.247±0.040	0.033±0.009	3.153±0.065	2.58±0.107	0.818±0.034

<sup>a</sup> Measured by pixels in SEM images.

<sup>b</sup> Measured by ARG-2 Rheometer.

<sup>c</sup> Measured by advanced digital scale.



**Scheme 3-1.** Preparation of PCL-based thermoplastic polyurethanes (PCL-TPU) by reacting Polycaprolactone-diol (PCL-diol) and 3,4-Dihydroxy-1-butene (DHB) with Hexamethylene diisocyanate (HDI).

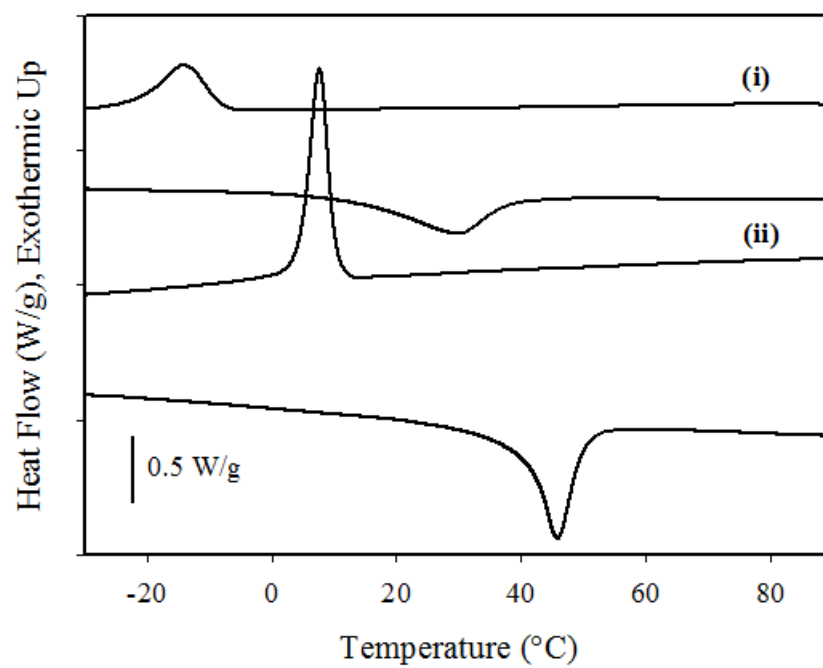


**Figure 3-1.** Differential Scanning Calorimetry (DSC) analysis graph of (i) PCL<sub>2k</sub>-TPU and (ii) PCL<sub>3k</sub>-TPU. Heating and cooling rates of 10 °C/min.

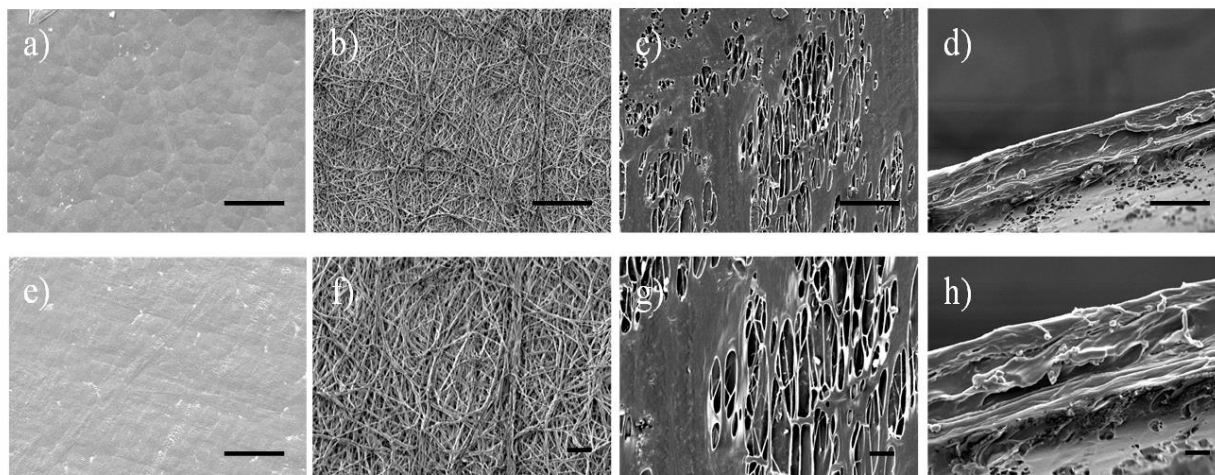


**Figure 3-2.** Scanning electron microscope (SEM) images of PCL<sub>3k</sub>-TPU: **a)** virgin cast film surface; **e)** crosslinked cast film surface; **b)** and **f)** virgin spun fiber mat surface (770 nm average diameter) at different magnifications; **c)** and **g)** crosslinked spun fiber mat at different magnifications; **d)** and **h)** cryofracture (cross-section) views of crosslinked spun fiber mat at different magnifications. Scale bar = 50 μm in **a)**, **b)**, **c)**, **d)**, and **e)**; 10 μm in **f)**, **g)**, and **h)**.

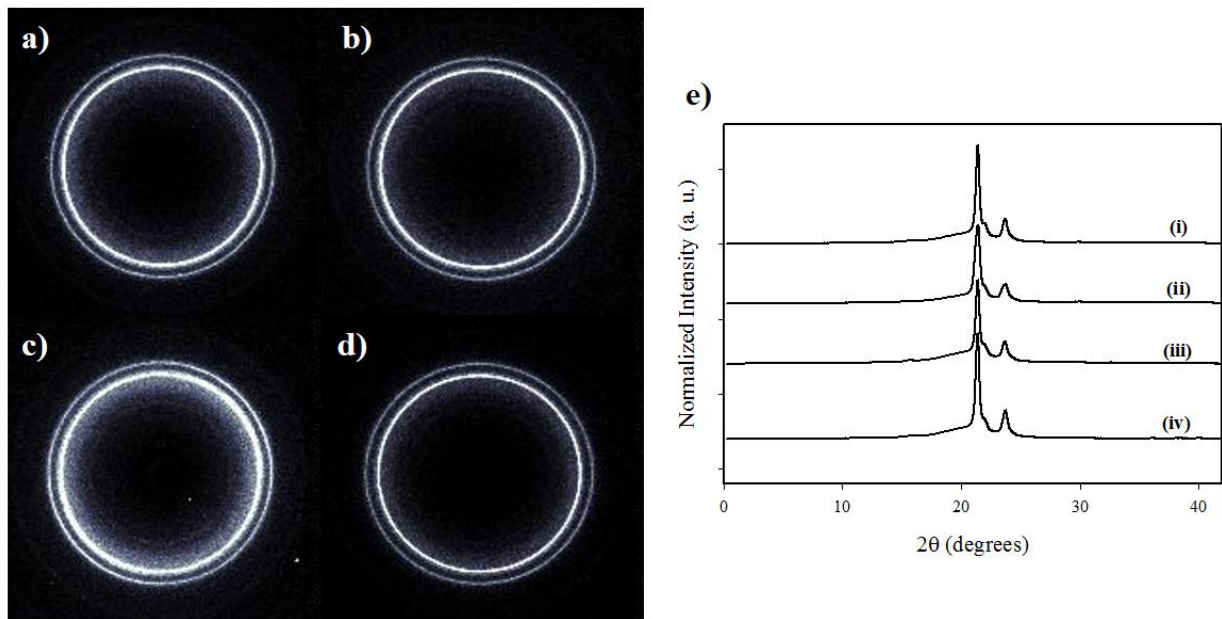


**Figure 3-3.** 2D Wide-angle X-ray Scattering (WAXS) patterns of **a)** virgin cast film, **b)** crosslinked cast film, **c)** virgin spun fiber mat, and **d)** crosslinked spun fiber mat of PCL<sub>3k</sub>-TPU; **e)** WAXS profiles of (i) virgin cast film, (ii) crosslinked cast film, (iii) virgin spun fiber mat, and (iv) crosslinked spun fiber mat. The X-ray wavelength ( $\lambda$ ) is 1.5405 Å.

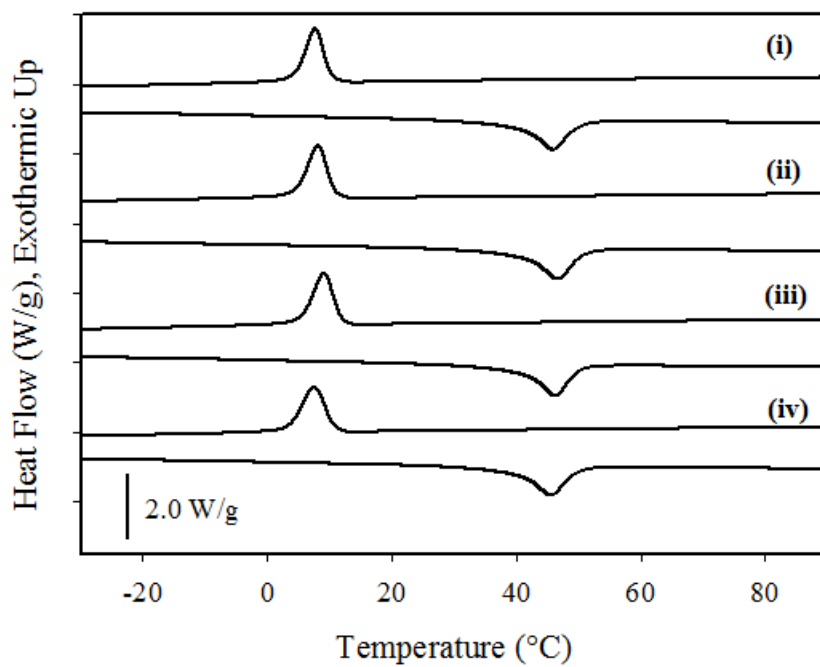


**Figure 3-4.** Differential Scanning Calorimetry (DSC) analysis graph of virgin cast film (i), crosslinked cast film (ii), virgin spun fiber mat (iii), and crosslinked spun fiber mat (iv) of PCL<sub>3k</sub>-TPU. Heating and cooling rates of 10 °C/min.

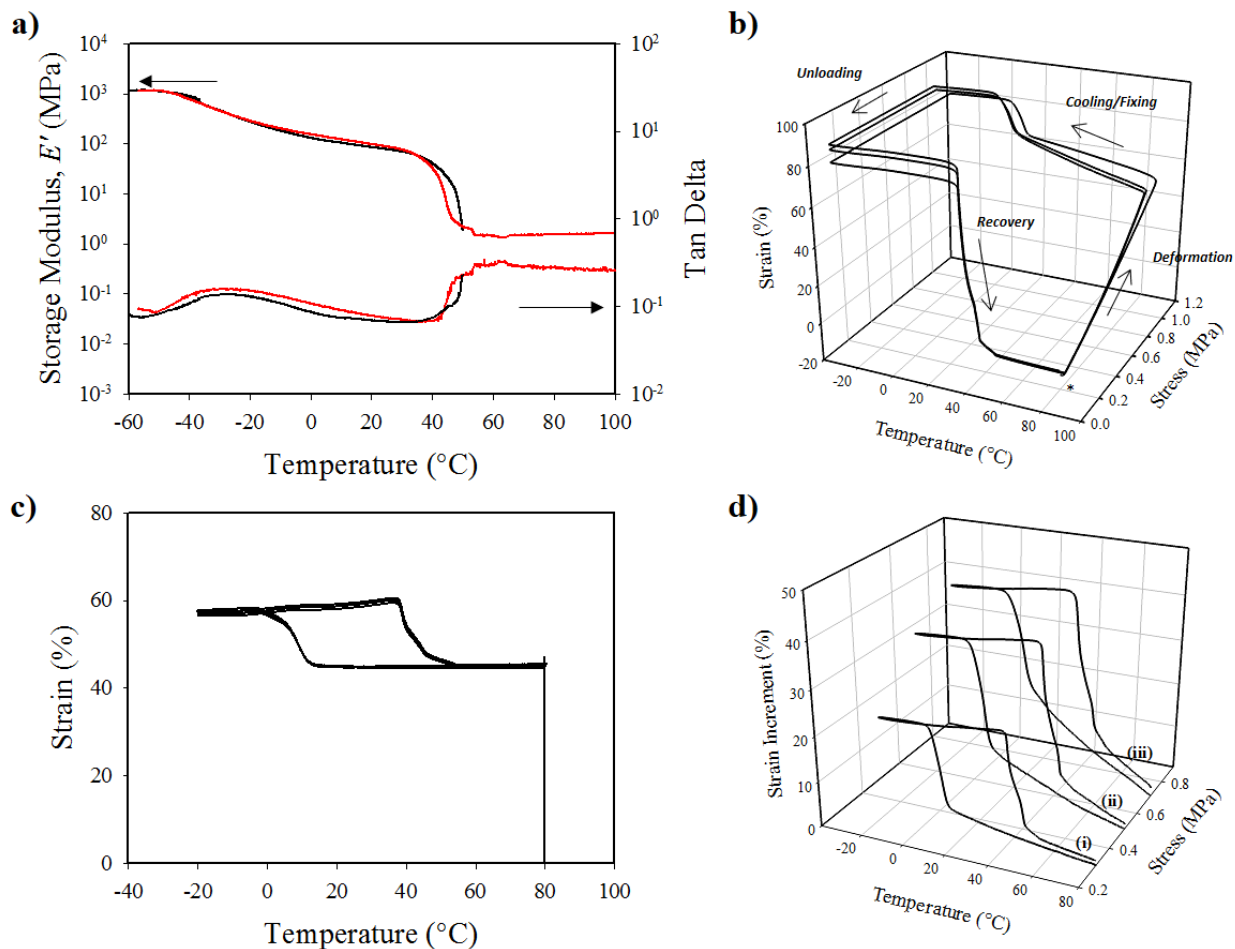


**Figure 3-5.** **a)** Storage modulus ( $E'$ ) vs temperatures for virgin cast film (black) and crosslinked cast film (red) of PCL<sub>3k</sub>-TPU.  $E'$  was recorded at a heating rate of 3 °C/min with frequency of 1 Hz; **b)** one-way and **c)** two-way shape memory cycles for crosslinked cast film of PCL<sub>3k</sub>-TPU. “\*” indicates starting point; **d)** two-way shape memory behavior for crosslinked cast film of PCL<sub>3k</sub>-TPU at different stresses, (i) 0.30 MPa, (ii) 0.50 Mpa, and (iii) 0.70 Mpa. The samples were deformed under each constant stress at 80 °C, followed by cooling and heating steps (2 °C/min), respectively.



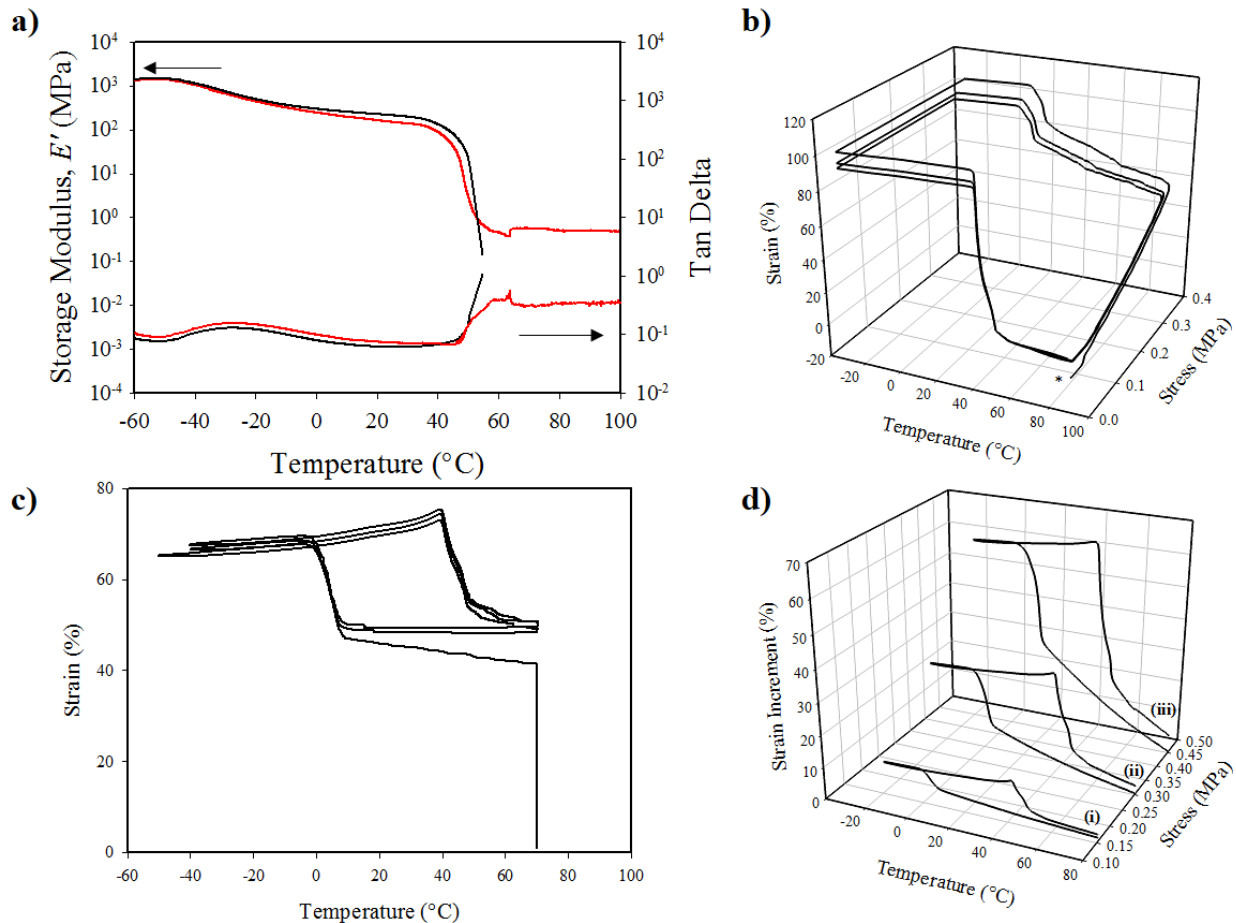


**Figure 3-6.** **a)** Storage modulus ( $E'$ ) vs temperatures for virgin spun fiber mat (black) and crosslinked spun fiber mat (red) of PCL<sub>3k</sub>-TPU.  $E'$  was recorded at a heating rate of 3 °C/min with frequency of 1 Hz; **b)** one-way and **c)** two-way shape memory cycles for crosslinked spun fiber mat of PCL<sub>3k</sub>-TPU. “\*” indicates starting point; **d)** two-way shape memory behavior for crosslinked spun fiber mat of PCL<sub>3k</sub>-TPU at different stresses, (i) 0.15 MPa, (ii) 0.30 Mpa, and (iii) 0.45 Mpa. The samples were deformed under each constant stress at 80 °C, followed by cooling and heating steps (2 °C/min), respectively.

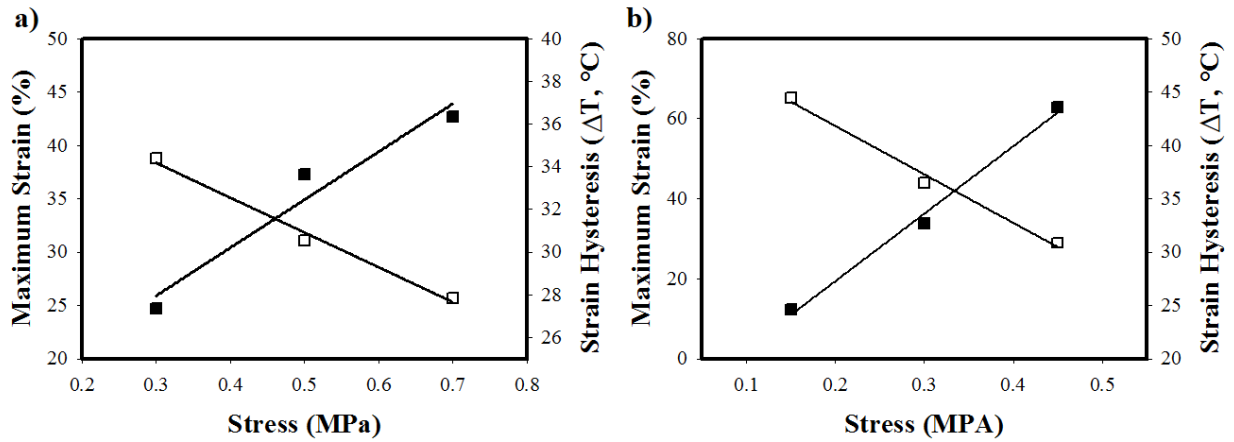


**Figure 3-7.** Maximum strain and strain hysteresis versus stress based on the two-way shape memory behavior of **a)** crosslinked cast film and **b)** crosslinked spun fiber mat, respectively. Maximum strain (■) and strain hysteresis (□). The strain hysteresis was calculated from the temperature difference ( $\Delta T$ ) at the half of strain loop in two-way shape memory cycles.

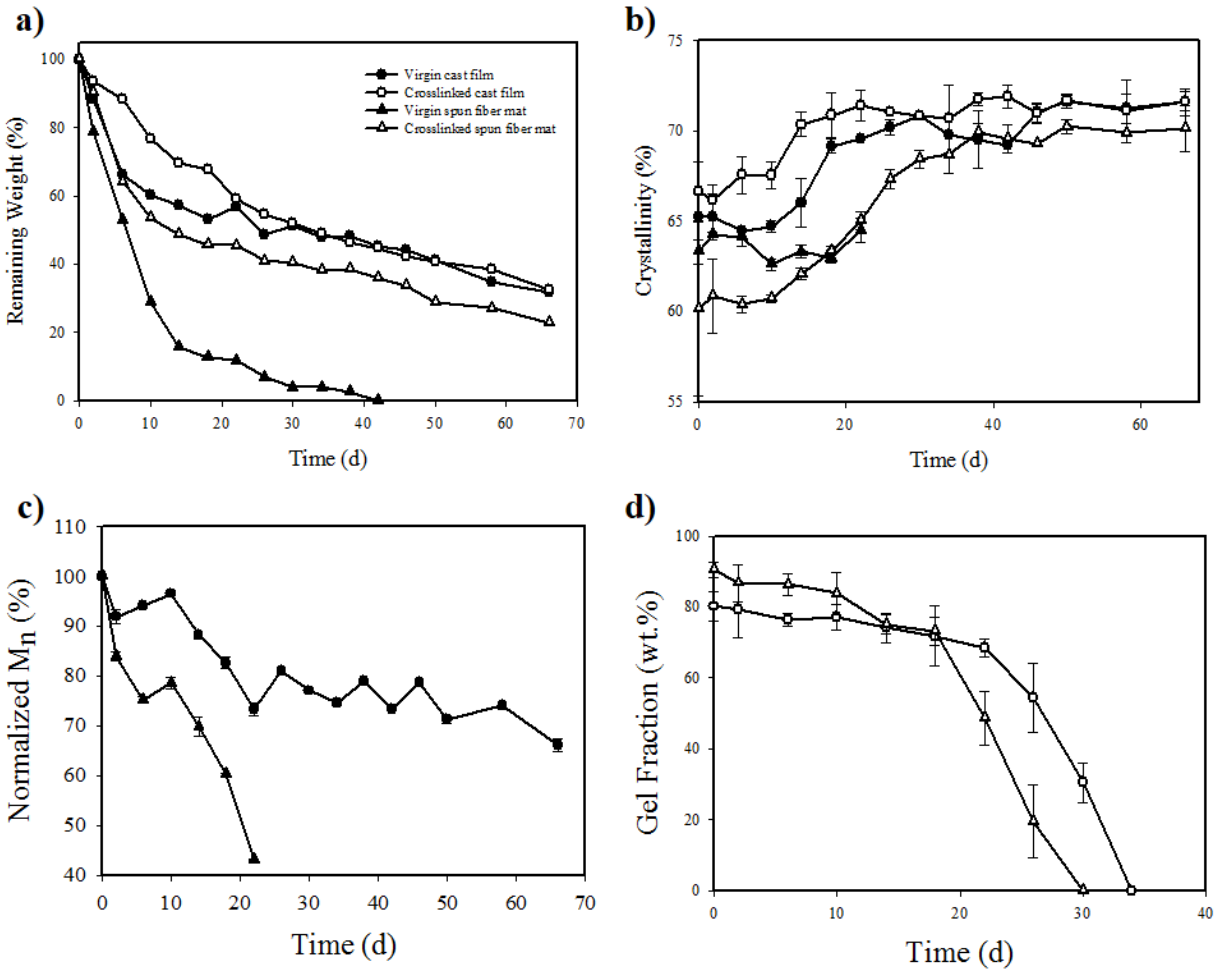


**Figure 3-8.** Enzymatic degradation study of PCL<sub>3k</sub>-TPU: **a)** Mass remaining profiles, **b)** crystallinities profiles, **c)** normalized number-average molecular weight ( $M_n$ ) remaining profiles for virgin samples only, and **d)** evolution profiles of gel fraction value for crosslinked samples only during degradation by Lipase PS (0.4 mg/mL) in a pH 7.4 PBS solution at 37 °C. Virgin cast film (●), crosslinked cast film (○), virgin spun fiber mat (▲), and crosslinked spun fiber mat (△).

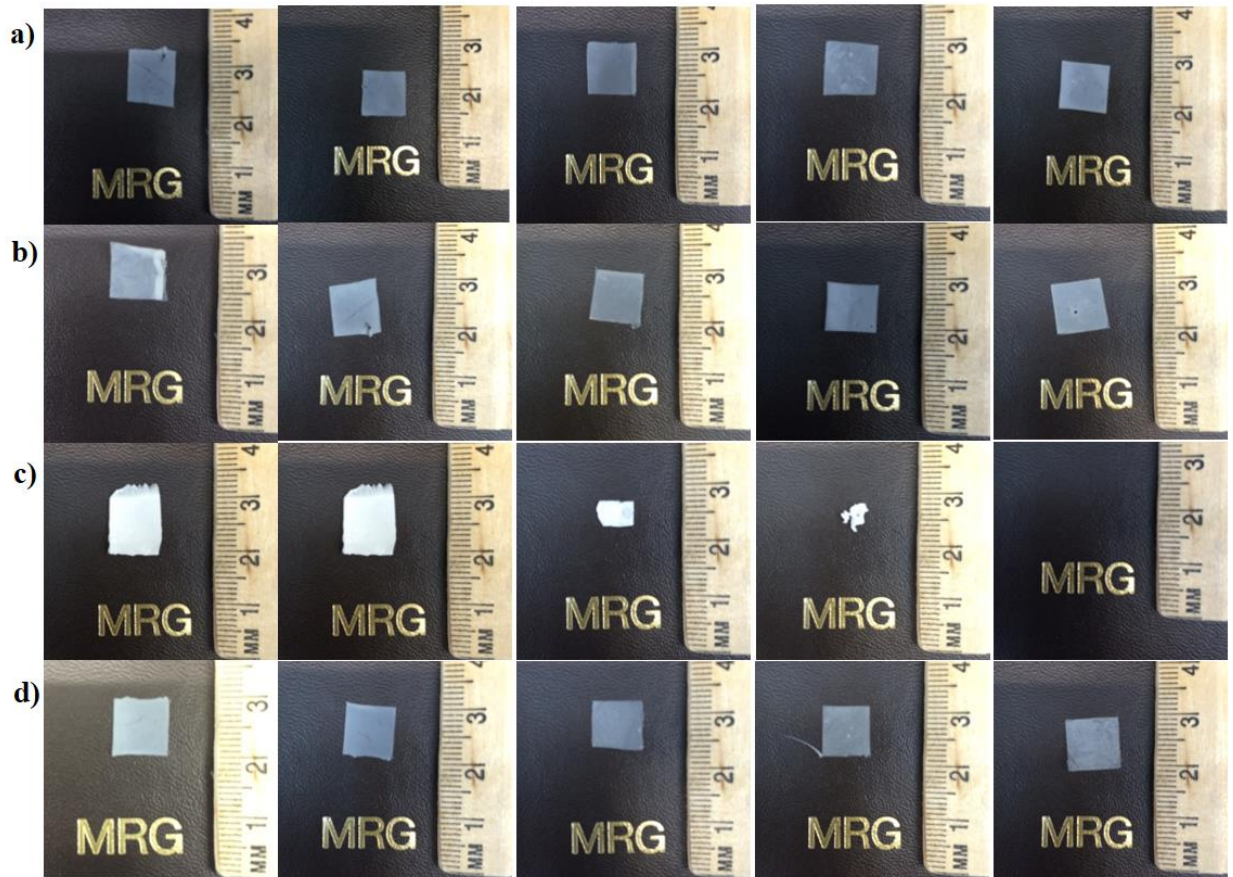


**Figure 3-9.** Photographs of PCL<sub>3k</sub>-TPU samples during enzymatic degradation: **a)** virgin cast film; **b)** crosslinked cast film; **c)** virgin spun fiber mat; **d)** crosslinked spun fiber mat. Columns from left to right refer to control, day 2, day 18, day 34, and day 66, respectively.

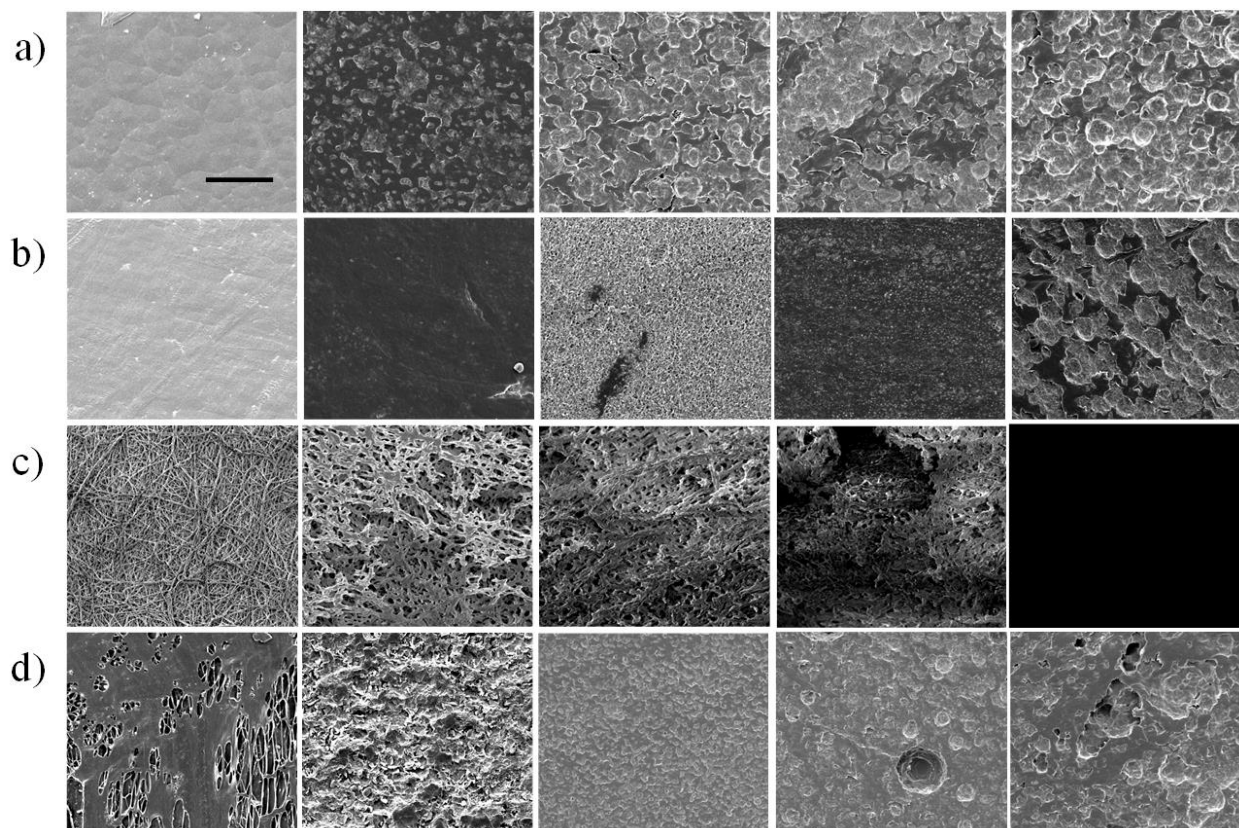


**Figure 3-10.** SEM images of PCL<sub>3k</sub>-TPU samples during enzymatic degradation: **a)** virgin cast film; **b)** crosslinked cast film; **c)** virgin spun fiber mat; **d)** crosslinked spun fiber mat. Columns from left to right refer to control, day 2, day 18, day 34, and day 66, respectively. Scale bar = 50  $\mu\text{m}$ .

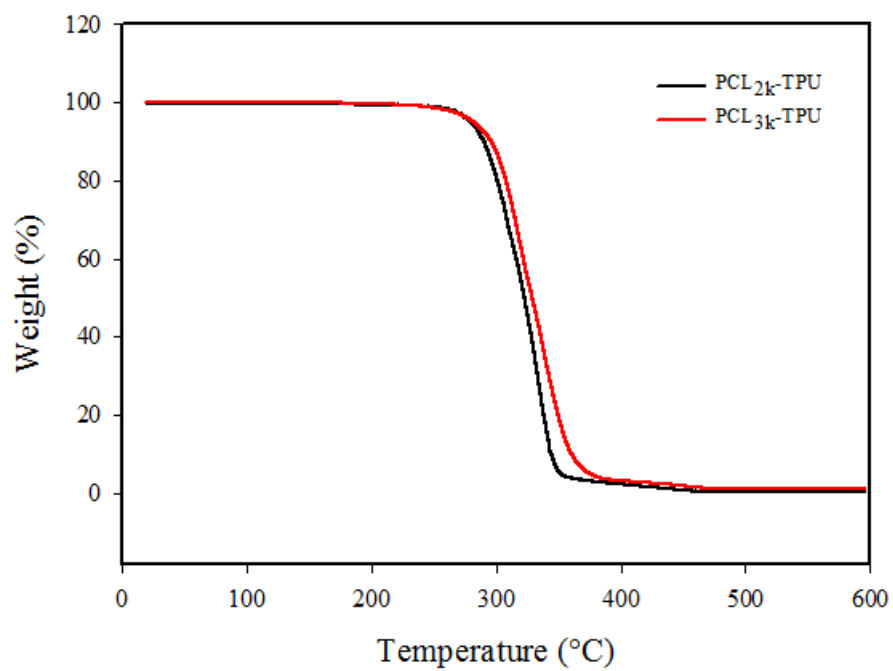


**Figure 3-11.** Thermogravimetric analysis (TGA) graph of PCL<sub>2k</sub>-TPU and PCL<sub>3k</sub>-TPU. Heating rate of 10 °C/min.

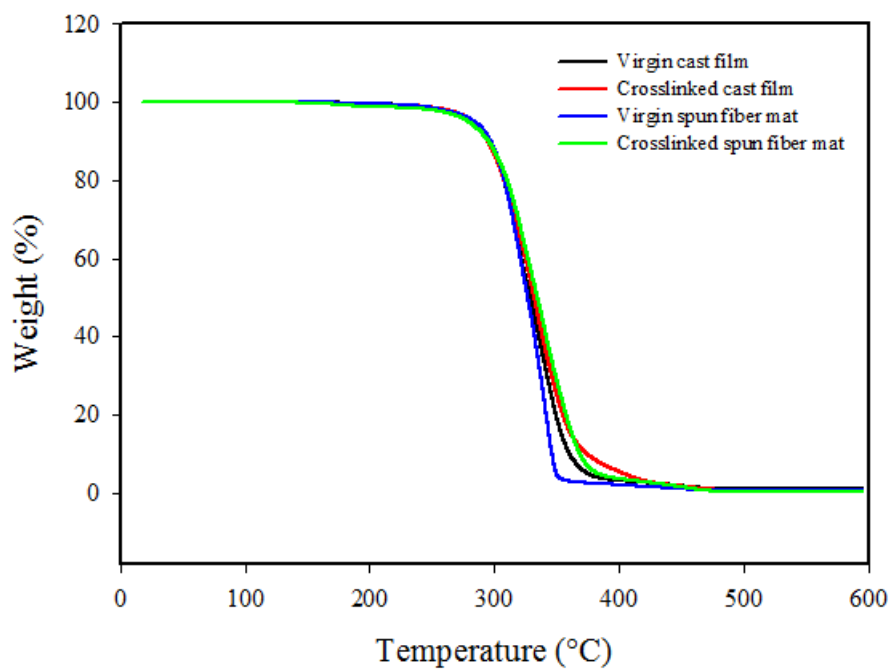


**Figure 3-12.** Thermogravimetric analysis (TGA) graph of virgin cast film (i), crosslinked cast film (ii), virgin spun fiber mat (iii), and crosslinked spun fiber mat (iv) of PCL<sub>3k</sub>-TPU. Heating rate of 10 °C/min.

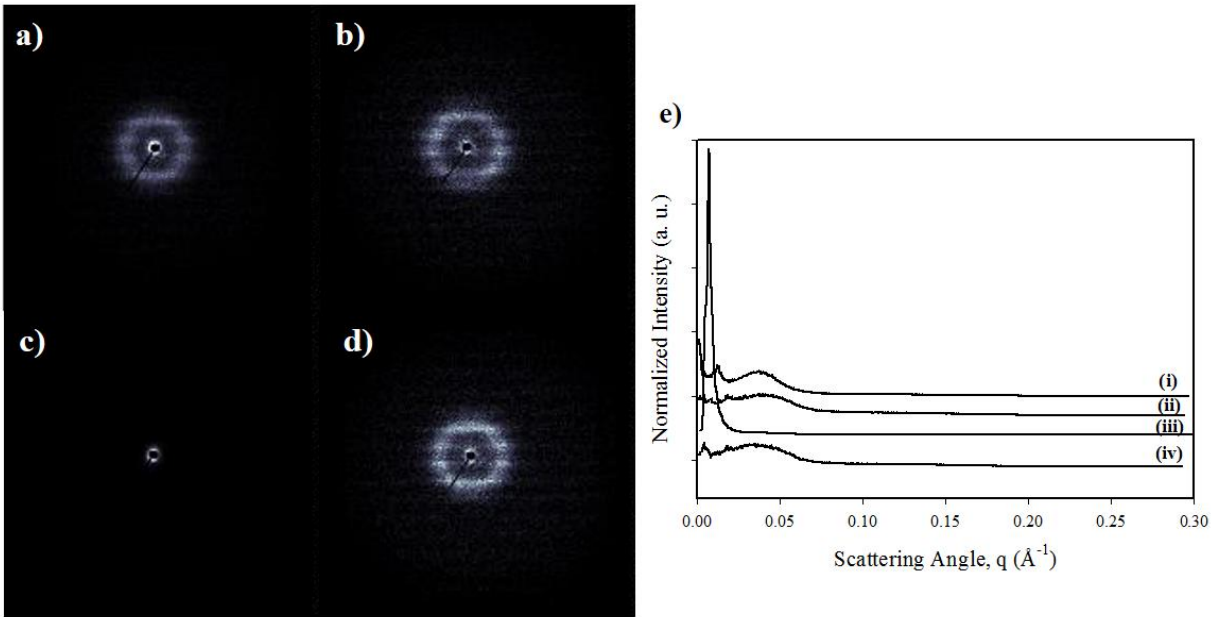


**Figure 3-13.** 2D Small-angle X-ray Scattering (SAXS) patterns of **a)** virgin cast film, **b)** crosslinked cast film, **c)** virgin spun fiber mat, and **d)** crosslinked spun fiber mat of PCL<sub>3k</sub>-TPU; **e)** SAXS profiles of (i) virgin cast film, (ii) crosslinked cast film, (iii) virgin spun fiber mat, and (iv) crosslinked spun fiber mat. The X-ray wavelength ( $\lambda$ ) is 1.5405  $\text{\AA}$ .



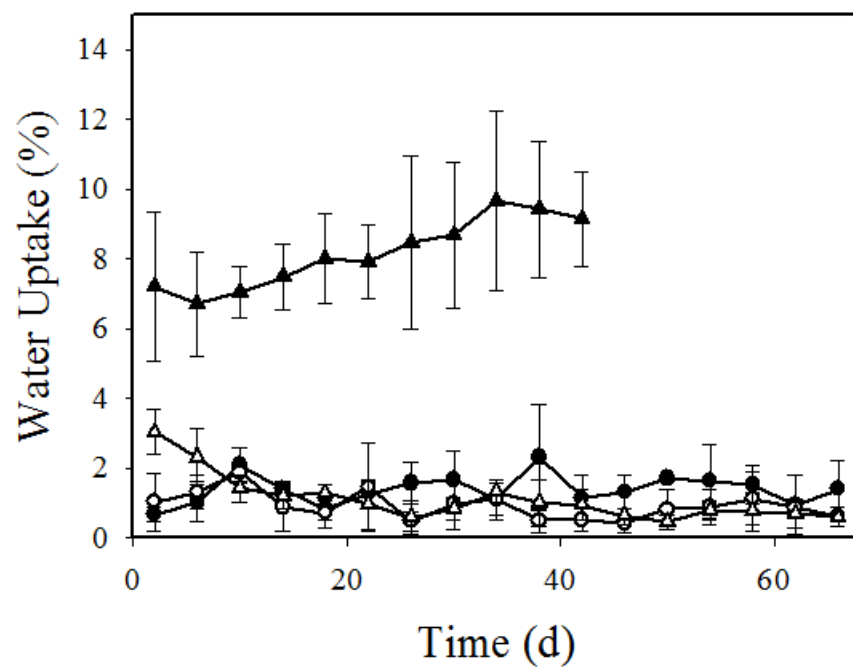


**Figure 3-14.** Water uptake profiles during degradation by Lipase PS (0.4 mg/mL) in a pH 7.4 PBS solution at 37 °C. Virgin cast film (●), crosslinked cast film (○), virgin spun fiber mat (▲), and crosslinked spun fiber mat (Δ).

# Chapter 4: Electrospun Polyurethane Blends Exhibiting Shape Memory and Self-healing Properties

## 4.1 Synopsis

The ability of shape memory polymeric materials to repair physical damage and to then restore original functionality possesses significance in the field of self-healing for a broad range of applications. In this chapter, we report on the design, fabrication and characterization of a new approach: electrospun shape memory assisted self-healing (SMASH) polymer blends that are built upon prior work involving a latent crosslinkable polyurethane (x-PU). This unique blend system is prepared by employing a solution in which both a crosslinkable polyurethane and a linear polyurethane (l-PU) are mixed homogeneously for electrospinning. After preparing a family of blends with varying compositions, comprehensive characterizations and various healing tests were done, revealing that 80:20 (w/w x-PU:l-PU) blend presents better healing performance than the other compositions. Further, it is found that the 80:20 blend features 98.7% of healing efficiency ( $\eta$ ) for vertical puncture damage. Introducing anisotropy in the materials resulted in a 40.7% increase in  $\eta$  for the 60:40 blend.

## 4.2 Introduction

Polymers and their composites have been extensively applied in a variety of such practical fields as transport vehicles, sporting goods, civil engineering, and electronics owing to their light weight, good processibility, resistance to corrosion, etc.<sup>1,2</sup> However, decomposition, damage, and failure could take place naturally for such materials upon exposure to harsh environments wherein there exists mechanical, chemical, thermal, UV radiation, or a combination of these factors. Also,

unfortunately, eventual failure still is a matter of time for most engineered materials regardless of the improved robustness or the development of nondestructive inspection method.<sup>3</sup> Inspired by biological systems that naturally exhibit regeneration, self-healing (SH), and reproductive, biomimetic SH materials offer an exceptional solution to extending their working life and condition because of the built-in capability to repair damage as well as to recover functionality autonomously or using the resources available inherently.<sup>4-6</sup> Such resources can be mechanical,<sup>7</sup> thermal,<sup>8</sup> or electrical energy,<sup>9</sup> among which thermal energy for healing is the focus of this work.

The shape memory effect in polymer materials entails an ability to store a temporary shape upon deformation (so-called “mechanical programming”) until later being stimulated to return to an equilibrium state by external heating or other means.<sup>10-13</sup> Hence, a novel concept has risen up with introducing thermal-responsive shape memory polymers to facilitate the SH process, providing an effective mechanism to partially or completely close and rebond associated cracks or other types of damage. This concept has been termed shape memory assisted self-healing (SMASH) by our lab originally, generally being demonstrated in at least two approaches. In the first approach, locally prepositioned shape memory alloy (SMA) wires<sup>14-16</sup> or shape memory polymer (SMP) fibers<sup>17,18</sup> are used, upon activation, to impose a contractile force that pulls the crack surfaces closer together. The second approach relies on bulk shape memory effect from the material to close the crack.<sup>19-22</sup> For example from our own lab, Rodriguez et al reported a poly( $\epsilon$ -caprolactone) (PCL) based molecular composite system, a single-phase, two-component blend that consists of a thiol-ene crosslinked PCL (n-PCL) network and a high molecular weight ( $M_w$ ) linear PCL (l-PCL) interpenetrating the network.<sup>23</sup> With “reversible plasticity”, the n-PCL network features a special form of shape memory (SM) where a stable temporary state could be achieved through both elastic and plastic deformation regions at a temperature (here RT) below its melting transition temperature

( $T_m$ ). This temporary shape could be fully reset to the equilibrium, undeformed shape upon heating above  $T_m$ . Due to their near-identical  $T_m$  values, the heating step is simultaneously used to trigger the SH mechanism in which the crack surfaces are rebonded by the l-PCL chains that diffuse to and ultimately bridge the surfaces of damage to allow rebonding a restoration of mechanical properties.

A new SMASH strategy has been introduced by Luo et al, opening the door to develop a phase-separated morphology in favor of allowing the healing of larger cracks and defects as opposed to the single-phase n-PCL/l-PCL blend.<sup>24</sup> The overall design was based on a two-step process including electrospinning and impregnation, to fabricate an fiber-matrix composite system wherein randomly oriented, nonwoven PCL nano- and microfibers are uniformly spread out in a continuous, crosslinked epoxy matrix, which enables more significant flow of the liquefied PCL well as larger interfacial area and more sustained healing agent delivery because of the high aspect ratio fibers. Along this line, Nejad et al undertook such a SMASH strategy, to develop thermally activated SH coatings.<sup>25</sup> In addition, a second approach involving polymerization induced phase separation (PIPS)<sup>26-29</sup> of PCL and epoxy was adopted for comparison purposes. Generally, the SMASH materials prepared by both approaches revealed excellent and similar structural and functional SH outcomes, and, furthermore, the PIPS technique has turned out to be more suitable for scale-up application given its processing simplicity.

In this present work, we report on a novel, simple but effective strategy to prepare a new SMASH blend with tailored thermal, mechanical, SM, and SH properties. This blend involves the use of a latent crosslinkable PCL-based polyurethane (x-PU) that has been developed and fully characterized in our previous work.<sup>30,31</sup> In the meantime, a linear PCL-based thermoplastic polyurethane (l-PU) was synthesized by reacting poly(caprolactone)-diol (PCL-diol) with

hexamethylene diisocyanate (HDI) as illustrated in Scheme 4-1. We next prepared a homogeneous, electro-spinnable organic solution consisting of the two polymers with varying x-PU-to-l-PU compositions and certain amount of select initiator for thermal curing, and then processed these miscible solutions into fibrous webs by electrospinning, respectively. The essential idea was to fabricate a single-phase, electrospun blend system that incorporates a covalently crosslinked network by crosslinking the x-PU upon hot compaction for SM properties and the l-PU as healing agent to provide SH properties. Unlike single-phase n-PCL/l-PCL system or PCL/epoxy blend with a phase-separated morphology, the potential advantages of creating such a SMASH material include convenient manufacturing, outstanding processibility, minimal heterogeneity that could cause local differences on healing performance, triggering temperature close to body temperature for biomedical application, the capability to introduce fiber alignment to improve SH properties, among others. Molecular, thermal, mechanical, SM, and SH properties were characterized, to further investigate and compare the effect of blend composition<sup>23,32,33</sup> on these properties. Additionally, the SH efficiency of our blend system was evaluated when three different types of damage were performed, including a pin-based puncture, surface scratch, and double-edge notches, respectively. Last but not least, recognizing that the molecular orientation introduced through electrospinning process could exert the recovery force of SMPs to an enhanced extent in the direction of the fiber axis,<sup>34-38</sup> we hypothesize that improvements in shape recovery would have a positive influence on SH outcome because of better damage closure. Consequently, isotropic and anisotropic x-PU:l-PU blends were compared, both qualitatively and quantitatively.

## **4.3 Experimental**

### **4.3.1 Materials**

Poly(caprolactone)-diol (PCL-diol, average  $M_n \sim 3,000 \text{ g mol}^{-1}$ , purchased from Scientific Polymer Products, Inc.) was vacuum dried for 2 d prior to use. Hexamethylene diisocyanate (HDI, purum,  $\geq 98\%$ ) was purchased from Sigma-Aldrich and stored over 3 Å molecular sieves (Sigma-Aldrich) for 3 d before further use. Tin-POMS catalyst was purchased from Hybrid Plastics and vacuum dried extensively for a week prior to use. Toluene, chloroform, and n-hexanes were all purchased from Fisher Scientific. Toluene was dehydrated by refluxing over calcium hydride (Sigma-Aldrich) multiple times until collection and stored over 3 Å molecular sieves for 3 d before use. 3, 4-Dihydroxy-1-butene (DHB,  $\geq 99\%$ ) and dilauroyl peroxide (DLP, Luperox® LP, 97%), *N,N*-Dimethylformamide (DMF, anhydrous, 99.8%), HPLC-grade tetrahydrofuran (THF), and deuterated chloroform (Chloroform-d, 99.8% atom D) were purchased from Sigma-Aldrich and used as received.

#### 4.3.2 Synthesis of Polyurethanes

The latent crosslinkable PCL-based polyurethane (x-PU) was synthesized using a one-step method as exactly stated in our previous work.<sup>31</sup> On the other hand, we prepared the linear PCL-based polyurethane (l-PU) in a similar fashion as shown in Scheme 4-1 (b). A Schlenk line (AF-0452, purchased from Chemglass Life Sciences) was utilized to create an air-free reaction environment during the course of polymerization. Moisture was intentionally removed from the whole reaction system by evacuating and refilling clean nitrogen at least three times. A 500-mL Schlenk flask (AF-0528, single neck, round bottom) was oven dried at 80 °C and flame dried right before use. 9 g (3.0 mmol) PCL-diol was dissolved in 100 mL distilled toluene within the 500-mL flask that was subsequently heated to and kept at 100 °C for about 30 min, while 100 mg (approximately 1 wt. %) Tin-POMS catalyst was dissolved into 5 mL distilled toluene for further use. Once the polymer solution became transparent, indicating that polymer was fully dissolved,

0.48 mL (3.0 mmol) HDI and 5 mL toluene containing Tin-POMS were added into the flask via a syringe under an inert atmosphere of nitrogen. Incubation was maintained at 100 °C for 24 h to accomplish polymerization while stirring was kept to assure good mixing. Henceforth, the resulting polymer solution was precipitated in a dropwise fashion into an 8-fold excess of n-hexane, and then washed with deionized water. The precipitates were collected and dried in the fume hood overnight prior to complete drying in vacuum oven at room temperature for another 3 d.

### 4.3.3 Molecular Characterization

The x-PU polymer products thus synthesized were dissolved in deuterated chloroform ( $\text{CDCl}_3$ ) at a concentration ranging from 20 to 30  $\text{mg mL}^{-1}$ . Proton Nuclear Magnetic Resonance ( $^1\text{H NMR}$ ) spectra were generated using a Bruker Avance III HD 400 MHz spectrometer, to qualitatively verify chemical structure of synthesis products as well as to quantitatively analyze PCL-to-DHB molar ratio per chain. The relaxation delay time utilized was 1 s at a temperature of 25 °C. Gel Permeation Chromatography (GPC) was performed to determine number-average molecular weight ( $M_n$ ) and polydispersity index (PDI,  $M_w/M_n$ ), using a Waters Isocratic HPLC system equipped with a temperature-controlled differential refractometer (Waters 2414). Multi-angle laser light scattering (Wyatt miniDAWN) was introduced at three characteristic angles (45°, 90°, and 135°) for in-line absolute molecular weight determination. The flow rate of THF as mobile phase in this GPC system was set at 1  $\text{mL h}^{-1}$  constantly. Polymer-THF solutions (2 – 5  $\text{mg mL}^{-1}$ ) were passed through a 0.2  $\mu\text{m}$  PTFE filter (Waters) prior to injection at 40 °C.

### 4.3.4 Fabrication of x-PU:l-PU Blends

A two-step process was implemented to make a series of electrospun x-PU:l-PU blends with x-PU wt. % increasing from 50 wt. % to 100 wt. % at an increment of 10 wt. % on the basis of the

total mass of 2 g. The first step utilized the electrospinning of two-component solution at each composition into fibrous web that, as the second step, was hot compacted to crosslink x-PU thereafter. Details of both steps are explained below.

#### **4.3.4.1 Electrospinning**

Seeking to understand the effect of blend composition on various properties, especially the SH properties, we aimed to create an x-PU composition gradient ranging from 50 wt. % to 100 wt. %. In particular, 6 x-PU-to-1-PU w/w compositions were prepared by solvent blending, including 50:50, 60:40, 70:30, 80:20, 90:10, and 100:0. Here, 80:20 is taken as a representative example to demonstrate the electrospinning process. In the first place, a 17% (w/v) two-component solution was prepared by adding 1.6 g x-PU and 0.4 g 1-PU along with 40.8 mg (2 wt. %) DLP into a mixture of 8 mL chloroform and 4 mL DMF. The resulting solution was then heated to and kept at 37 °C with constant stirring. After dissolution completion, the two-component solution was processed into a nonwoven fibrous web using a custom electrospinning set-up that has been previously reported by our group.<sup>39</sup> The ejecting needle was held at a potential of 16 kV, the tip-to-collector distance was 10 cm, the rotation rate of a 57.1 mm collecting mandrel was maintained at 400 rpm for isotropy, and at 1,500 rpm for anisotropy (fiber orientation), respectively, while the drum was held at a potential of 0.5 kV and a flow rate of polymer solution supplying the 22 Gauge needle was 1.5 mL h<sup>-1</sup>, all employed over the 8-hour electrospinning process, which led to a mat thickness of approximately 0.50 mm. Complete drying of spun fiber mats was subsequently achieved in vacuum oven at room temperature before further use.

#### **4.3.4.2 Hot Compaction**



The dried fibrous webs were treated thermally for crosslinking (or “cured”) by the following method. Each individual fibrous web (~ 1.8 g) was first cut into 4 equivalent rectangular pieces and they then were stacked to control the resulting thickness, a common structural variable of SH.<sup>24</sup> For anisotropic samples exclusively, all 4 pieces was aligned and piled up along the same orientation before being sandwiched between two polished stainless steel sheets coated with mold release agent (Pol-Ease® 2300, Polytek). Also, a 0.40 mm thick stainless steel spacer was placed in between to control the thickness of the final film. A 6.89 MPa compressive stress and a curing temperature of 90 °C were applied throughout entire 2 h of hot compaction, using a Carver 3851-0 press with heating platens. Afterwards, the platens were cooled down to room temperature, following which the compressive pressure was released.

In order to assess the extent of covalent crosslinking, network gel fraction values of the hot compacted blends were examined using solvent-extraction and gravimetry. Each sample was weighed for its dry mass before being soaked in 20 mL THF at 37 °C in an Excella shaker for 48 h, during which the THF was refreshed every 12 h. Then samples were washed with deionized water, blotted, and vacuum dried for a week at room temperature to remove residual solvent or water. The final dry mass was recorded for calculation of gel fraction. Calculation of gel fraction values involves the initial dry mass,  $m_i$ , and the final dry mass,  $m_f$ , using the equation below:

$$G(\%) = \frac{m_f}{m_i} \times 100 \quad (4 - 1)$$

#### **4.3.5 Microstructural Characterization**

To visualize surface morphology and structural geometry of as-electrospun and hot compacted blends, Scanning Electron Microscopy (SEM) was conducted using a JEOL JSM-5600 microscope

under an accelerating voltage of 10 kV. Both samples were gold-sputtered for 60 s prior to imaging. Also, to ascertain the molecular and nano-scale ordering and orientation of isotropic and anisotropic samples, wide angle (WAXS) and small angle (SAXS) X-ray scattering analyses were performed using a Rigaku S-MAX3000 pinhole camera system. A Rigaku MicroMax-002+ generator was operated under an accelerating voltage of 45 kV and a current of 0.88 mA to yield a collimated beam of Cu K $\alpha$  X-rays with a wavelength of 1.5405 Å. WAXS patterns were collected and analyzed using a Fujifilm image plates (CR HR-V) with a Fujifilm FLA7000 reader at a scan resolution of 100  $\mu$ m. The sample-detector distance was fixed at 120.7 mm, leading to scattering angles  $3^\circ < 2\theta < 40^\circ$ . Comparatively, SAXS patterns were obtained at a sample-detector distance of 1525 mm on a 2D Multiwire Area Detector. Exposure time was 30 min for both patterns. WAXS and SAXS images were further processed and analyzed utilizing SAXSgui software v2.03.04.

#### **4.3.6 Thermal and Dynamic Mechanical Analysis**

Differential Scanning Calorimetry (DSC) was adopted to investigate thermal properties of all samples using the TA Instruments Q200 apparatus. Samples weighing approximately 5 mg underwent a thermal program of first heating to 140 °C at 10 °C min<sup>-1</sup>, cooling to -40 °C at 10 °C min<sup>-1</sup>, and then reheating at 10 °C min<sup>-1</sup> to 140 °C while heat flow data was recorded. The melting transition temperature ( $T_m$ , the peak of the endotherm), crystallization transition temperature ( $T_c$ , the peak of the exotherm), the enthalpy of melting ( $\Delta H_m$ , area beneath endothermic peak), and the enthalpy of crystallization ( $\Delta H_c$ , area beneath exothermic peak) were recorded before and after thermal curing, respectively, on the basis of second heating curve (to minimize the effects of thermal history) and first cooling curve.

A TA Instruments Q800 Dynamic Mechanical Analyzer (DMA) was employed to explore the thermomechanical properties and also to assess indirectly the level of crosslinking x-PU for hot compacted samples. In the multi-frequency controlled-strain mode each sample was equilibrated at -60 °C, held isothermal for 10 min, and heated continuously up to 100 °C at 3 °C min<sup>-1</sup>. An oscillating frequency of 1 Hz, amplitude of ca. 20 μm, a preload force of 0.001 N, and a force track of 125% were utilized. Rectangle shaped samples with an approximate length-to-width ratio of 4:1 were used for such testing.

#### 4.3.7 Reversible Plasticity Shape Memory

A special form of SM, reversible plasticity shape memory (RPSM), was examined for all compositions using DMA in a controlled force mode. Dog bone shaped samples (ASTM D63 Type IV, scaled down by a factor of 4) were punched with an average thickness of 0.37±0.05 mm and then tested following a custom thermomechanical cycling method developed in light of prior work.<sup>23,40</sup> Prior to DMA testing, each sample was first preheated in an isothermal oven (Fisher Scientific Isotemp 825F) at 80 °C for 15 min and sat at room temperature (RT) for another 15 min to riden thermal history. The sample was next stretched at 25 °C (i.e. RT) from a preloading strain ( $\epsilon_i$ ) to a strain of 140% at a rate of 5% min<sup>-1</sup> and held at 140% strain for 20 min to allow stress relaxation, yielding the deformed strain ( $\epsilon_d$ ). The stress associated with  $\epsilon_d$  was ramped, at a rate of 5% min<sup>-1</sup>, down to the preloading force of 0.001 N, during which the plastic deformation sustained was referred to as the fixed strain ( $\epsilon_f$ ). The fixed shape was fully recovered by heating to 80 °C at 3 °C min<sup>-1</sup> and holding isothermal for 5 min, following which the recovered strain ( $\epsilon_r$ ) under preloading force was recorded for each sample tested. In the end of the SM cycle, a cooling step was programmed to reset temperature back to 25 °C at 3 °C min<sup>-1</sup>. To quantify the RPSM

behavior, the calculation of the shape fixing ( $R_f$ ) and shape recovery ( $R_r$ ) ratios were conducted using the eqn. (2) and (3) correspondingly:

$$R_f(\%) = \frac{\varepsilon_f - \varepsilon_i}{\varepsilon_d - \varepsilon_i} \times 100 \quad (4 - 2)$$

$$R_r(\%) = \frac{\varepsilon_f - \varepsilon_r}{\varepsilon_f - \varepsilon_i} \times 100 \quad (4 - 3)$$

#### 4.3.8 Self-healing Experimentation

To understand the effect of composition on SH performance, SH experiments were carried out, for all cured x-PU:l-PU compositions, using our newly developed tensile geometry of a centered, needle puncture, given the high practicability pertaining to repair of puncture damage but rarely investigated. To begin with, all hot compacted blend samples were punched into a dogbone geometry (ASTM D638-03 Type IV, scaled down by a factor of 4), with an average thickness of  $0.37 \pm 0.05$  mm, a width of 1.52 mm, and a gauge length of 6.25 mm, under application of a custom-made dogbone cutting tool (TestResources, Inc., Shakopee, MN). The specimens were thermally mended, to erase thermal history, in the way described in shape memory characterization section. A custom-made puncture (punch) device (Scheme 4-2) was used to create a single centered, vertical puncture with a gauge diameter of 1.6 mm. The puncture damaged sample was stretched to a displacement of 2.5 mm (corresponding to a strain of 40%) at  $0.1 \text{ mm s}^{-1}$  ( $1.6\% \text{ s}^{-1}$ ), in a Linkam TST350 apparatus (Linkam Scientific Instruments, Ltd.) with a 200 N load cell, to propagate the hole macroscopically and extensively. Next, shape recovery and SH process were triggered in an isothermal oven at  $90 \text{ }^\circ\text{C}$ , and the whole process took about 1 min only, which was monitored by real time imaging using a Zeiss Discovery V8 stereo microscope equipped with a Q-Imaging CCD camera. In the end, the healed sample was re-stretched to a displacement of 6.25

mm (corresponding to a strain of 100%) at 0.1 mm s<sup>-1</sup> (1.6% s<sup>-1</sup>) by the Linkam apparatus, to determine whether the damage has been healed properly.

In general, a TestResources Model 100P Universal Testing Machine (referred as to tensile stretcher) was utilized to record the stress vs strain curves of the sample's virgin, puncture damaged, and healed state, respectively. Each sample was loaded in the Testing Machine with a force transducer of 25 N and uniaxially stretched at a rate of 1.50 mm min<sup>-1</sup> at RT until the strain-to-failure was reached. Two versions of SH efficiency, i.e. ratio of peak stress  $\eta_1$  and ratio of strain-to-failure  $\eta_2$ , were calculated according to:

$$\eta_1(\%) = \frac{\sigma_{healed}^{max}}{\sigma_{virgin}^{max}} \times 100 \quad (4 - 4)$$

$$\eta_2(\%) = \frac{\varepsilon_{healed}^{max}}{\varepsilon_{virgin}^{max}} \times 100 \quad (4 - 5)$$

Here, the virgin ( $\sigma_{healed}^{max}/\varepsilon_{healed}^{max}$ ) and healed ( $\sigma_{virgin}^{max}/\varepsilon_{virgin}^{max}$ ) peak loading stress/strain-to-failure were harvested from the stress vs strain curves of the sample's virgin and healed state, respectively. Note that, in the following discussion, SH efficiency refers to the ratio of peak stress unless specified otherwise. We realize that all the values of stress in tensile testing were calculated by the instrument based on the cross-sectional area of undamaged sample and the damaged samples had smaller actual cross-sectional areas than those used in calculation. However, we assume that the damage size was negligible compared to the size of the whole sample.

In consideration of the composition variation study above, the best performing composition was further tested with two other tensile geometries, including double-edge notches and surface scratches, for the purpose of comparing SH capability of such blend under different damage types.

Regarding the former tensile geometry, a punch device modified from a custom-made double-edge notch punch<sup>23</sup> was used to create two collinear, double-edge cracks that were 0.2 mm long on each side of the dogbone neck, each oriented along the sample width. The second (latter) tensile geometry involved in the use of a custom-made scratch machine with a 100 g weight in the mass holder, also designed by our group.<sup>25</sup> For this case, the both faces were scratched in the width direction and at positions centered along the length of the dogbone films. Following such damage, samples underwent exactly the same process employed on the puncture damaged samples: damage propagation, shape recovery and SH, and then post-healing stretching. At each step of this sequence, SEM imaging was used to explore the SH process at micro-scale level. Meanwhile, the stress vs strain curves obtained and plotted for undamaged (“virgin”), notched, scratched or punctured samples, and thermally healed states. The healing efficiencies,  $\eta$ , for various damage types were determined using Eqn. (4) and then compared to unveil the effect of damage type on SH properties.

In an effort to examine the ability of structural anisotropy to enhance SM properties and therefore SH performance, we prepared a particular set of samples wherein we introduced alignment onto the electrospun fibers of the 60:40 blend. The blend selected for the study was the one exhibiting the worst performance from among all samples in the composition study. To achieve the high orientation, a rotation rate of collecting mandrel, 1500 rpm, was employed during electrospinning. This is high in comparison to the lower value of 400 rpm used to prepared randomly oriented fibers of the same composition in the prior study. For oriented fibrous webs, we sought to prevent heating induced contraction and associated fiber disorientation. For that purpose, samples were clamped among all edges during the entire course of hot compaction in the hot press. Following hot compaction, both oriented and isotropic samples were cooled down to room temperature naturally

to allow crystallization prior to releasing from clamping. We first cut the anisotropic, cured web into two dogbone shaped samples, one being oriented along the length ( $0^\circ$ ) and the other in the width direction ( $90^\circ$ ). These two samples were then tested for puncture-healing performance and compared to samples of the same composition but random fiber orientation. To quantitatively evaluate the results of the SH testing, all three samples were mounted onto the tensile stretcher and stretched to break at a rate of  $1.50 \text{ mm min}^{-1}$  at RT, yielding the stress vs strain curves of each sample's virgin, punctured, and healed state, respectively. Finally, healing efficiencies,  $\eta$ , were calculated and used to measure the dependence of SH capability on the structural anisotropy.

## **4.4 Results and Discussion**

### **4.4.1 Blends Preparation**

The results of polyurethane syntheses were summarized accordingly in Table 4-1. Because the x-PU was characterized and discussed in details in our previous work,<sup>31</sup> we will, here, focus more on the l-PU. Specifically, the l-PU has an average  $M_n$  of 33.1 kDa (standard deviation = 5.3 kDa) with an average polydispersity index (PDI) of 1.62 (standard deviation = 0.20), calculated from five synthesis batches. It is hypothesized that the low molecular weight of l-PU might lead to the high ability to flow in the molten state, implying that the healing agent (i.e. l-PU) should reach to and across the damage surfaces more easily. The absence of DHB in the synthesis of l-PU resulted in a higher  $T_m$  compared to that of x-PU, mainly because the pendant allyl groups can serve to lower crystallinity and  $T_m$  by introducing architectural “defects” in the backbone.<sup>42</sup>

Six compositions with varying x-PU and l-PU wt. % content were prepared by solvent blending (Table 4-4) followed by an eight-hour electrospinning process and a two-hour hot compaction procedure, as described above. The results of electrospinning and following hot compaction were

demonstrated in SEM images, accordingly, revealing surface morphology and cross-section structure. Figure 4-2(a), (c), (e), (i), and (l) suggested the great capacity of the blends to be easily processed into uniform fibrous structure with an average fiber diameter of  $2.80 \mu\text{m} \pm 1.16$  for 90:10 (x-PU:l-PU),  $2.24 \mu\text{m} \pm 0.76$  for 80:20,  $2.22 \mu\text{m} \pm 0.59$  for 70:30,  $2.02 \mu\text{m} \pm 0.70$  for 60:40, and  $2.45 \mu\text{m} \pm 0.59$  for 50:50 (measured by image analysis using ImageJ software, and with a sampling size of 100). The appearance of the given blends after hot compaction were visualized in Figure 4-2b, d, f, j, and m, correspondingly, indicating evenly distributed, interspersed blend film with a smooth surface that has some light traces of fibrous structure. Based on these observations, we reason that a portion of the x-PU concentrated fibers have crosslinked before being fully melted, yielding preservation of the original fibrous geometry. This interpretation is supported further by the cross-sectional SEM views (Figure 4-2g and h, representatively). Additionally, it is important to note that those traces of fibrous structure were observed not only at the surfaces but also across the entire thickness and that this even distribution could allow the blends to provide no-bias SM and SH properties, both geometrically and functionally.

#### **4.4.2 Thermal and Dynamic Mechanical Analysis**

The thermal properties of six electrospun blends were characterized using DSC, with analysis quantities summarized for comparison in Table 4-5. Interestingly each curve revealed single endothermic (heating as shown) or exothermic (cooling, not shown) peaks (Figure 4-1(a)) as an indirect indication of homogeneity. It was found that increasing l-PU wt. % content shifted  $T_m$  of the blend progressively from  $44.9 \text{ }^\circ\text{C}$  for 100:0 to  $47.9 \text{ }^\circ\text{C}$  for 50:50 that is quite close to  $T_m$  of neat l-PU at  $48.9 \text{ }^\circ\text{C}$ . The similar trend applies to  $T_c$ . However, we observed no such a trend on enthalpy of melting and enthalpy of crystallization possibly because they are highly dependent of extreme weighing accuracy that might be beyond capability of our weighing scale. Following



thermal cure (Table 4-6), the six samples with varying composition showed no significant change in  $T_m$  and associated trace (Figure 4-1b), suggesting potential low content of networked polymer, as the crosslinks oftentimes can disturb crystalline phase and thus lower  $T_m$ .<sup>43-45</sup> However, the 60:40 composition appears to have a slightly higher  $T_m$  than 50:50, which we attributed to probable low degree of crosslinking. Both speculations are in agreement with the results of gel fraction experiments conducted to determine the network content of the linear/network blends. The gel fraction values obtained shows a decrease from 85.7% for 100:0 to 44.3% for 70:30 monotonically, reaching a minimum at 32.8% for 60:40, and finally returning to 35.4% for 50:50. We interpret this unexpected, non-monotonic trend to batch-to-batch variation that, in this case, is associated with the fabrication process and/or thermal curing step.

Thermomechanical testing was conducted, on both as-spun and hot compacted fibrous webs with varying compositions, to understand the dependence of the linear viscoelastic properties on temperature as well as to determine whether cured samples had the potential of anticipated SM properties. This set of experiments is crucial to give context for further characterization of RPSM cycle. The storage modulus ( $E'$ ) as a function temperature was determined for all compositions before (Figure 4-3(a)) and after (4-3(b)) thermal curing (Tan  $\delta$  vs temperature curves are available in Figure 4-13). Furthermore, the tensile  $E'$  decreased from 100 MPa or greater below  $T_m$  sharply to ca. 1 MPa or lower beyond  $T_m$  for all cured blends. The steep drop in  $E'$  throughout melting transition was followed by a stable rubber elastic state, a  $E'$  plateau, proportional to the crosslink density. Note that this rubber elastic state is a necessary (but insufficient) characteristics of self-healing materials that controls the quality of damage closure triggered by SM.

#### **4.4.3 RPSM Analysis**

Reversible plasticity shape memory (RPSM) that we sought to exploit here is a form of SM cycle wherein the SMP can be fixed into a deformed shape below its  $T_m$  and both plastic and elastic strain will not recover until heating above  $T_m$ . RPSM cycles for each composition are shown and compared in Figure 4-4, in contrast to conventional SM cycle where only the elastic deformation is recovered from a desired temporal strain fixed above its critical transition temperature.<sup>46</sup> Generally, RPSM allows promoted contact between the damage surfaces so as to effectively facilitate the SH event.

As a representative composition, a 100:0 sample (Figure 4-4(a)) was stretched to and then kept at a strain of 140% at RT. We interpret this behavior to be accompanied by alignment of the PCL crystalline lamellae and constituent polyurethane chains, which experienced cold draw beyond the yield point, along the stretching direction. This is demonstrated well by the red curve representing a projection of the whole cycle on the stress-strain plane. We, next, allowed the sample to relax the stress at this strain that was, later, released for the initial elastic shape recovery. Finally, the sample was heated to 80 °C to recover completely, followed by cooling to RT for completion of the cycle. The remaining compositions were characterized in such a manner, unveiling a behavior similar but with a progressively evolving trend in which more of the strain was gained through plastic deformation region than through elastic deformation region (maximum strain before yield point), as l-PU wt. % content in the blend increased. This is due to the fact that the Young's modulus of the blend decreased markedly from 92.4 MPa to 8.0 MPa (ca. 91.3% drop) when there become more linear l-PU chains (Figure 4-14).

Table 4-2 summarizes our findings on the shape fixing ( $R_f$ ) and shape recovery ( $R_r$ ) ratios of high merits from the RPSM cycles for all compositions. The reader is reminded that all  $\epsilon_d$  values

were obtained after 20 min stress relaxation. Consequently, the targeted 140% strain led to achieved values at small variance with this value. Upon unloading, all compositions achieved a fixed temporary shape with a  $\varepsilon_f$  ranging from 95.1% to 122.7%, while, after shape recovery, the  $\varepsilon_r$ 's were all found to achieve values within a strain span of 10%, which we considered rather small given the fairly large temporal deformation prior to shape recovery. Furthermore,  $R_f$  increased from 69.4% to 86.5% as l-PU wt. % content increased, but  $R_r$  (all greater than 90%) remained almost unaltered. This is important, in the context of improving SH performance, because good shape recovery will contribute more profoundly to closing damage surfaces.

#### **4.4.4 Self-healing Study**

##### **4.4.4.1 Effect of Composition**

The self-healing (SH) capability as a function of l-PU wt. % content for the prepared x-PU:l-PU blends with varying compositions was first investigated, on a puncture-damaged basis, using the tensile stretcher (described in details in the Experimental Section). Each composition in its virgin, puncture damaged, and healed states was strained to failure at RT beyond its yield point, as demonstrated correspondingly by each individual stress-strain curve in Figure 4-5. Broadly speaking, it was observed that all compositions healed to near completion upon single heating with no sight of puncture reopening, which typically indicates good structural restoration. Qualitatively, the SH performance can be roughly estimated by comparing the curve at virgin state to that at healed state. In particular, the closer the two curves are to overlapping, the better SH was. Therefore, 80:20 was considered to show superior SH than the remaining compositions in that sense, as its healed sample was capable of experiencing nearly as much ultimate strength and strain-to-failure, without failing, as before the puncture damage was applied. It is noted that the

yield stress of this and other healed sample was lower than the virgin sample; however, that value depends strongly on crystallinity degree, which was not carefully controlled and evolves to greater values as the sample is stored at room temperature following the heat-treatment of healing. The SH process of an 80:20 sample upon puncture damage was followed in some detail by real time imaging using an optical microscope and a Linkam apparatus (Figure 4-6). The virgin sample (Figure 4-6a(i)) was pierced at the center and then stretched to ca. 40% strain to propagate the damage (ii), after which the hole completely disappeared upon heating at 90 °C for 1 min (iii) and, most importantly, didn't recur by re-stretching to ca. 100% strain (iv). In addition, snapshots were taken to show the progress of puncture closure and rebonding while the sample was heated from RT to 90 °C and cooled back to RT under load-free condition. It is evident that sample's response to temperature elevation has begun at 35 °C owing to obvious change in shape as well as in transparency that reflects the status of crystalline/amorphous structure. The most dramatic change happened between 50 °C and 55 °C where the melting transition maximized to allow faster polymer chain movement and the puncture became visible no longer.

To quantify SH performance, the SH efficiency ( $\eta$ ), for each composition, was calculated from the peak loading stresses/strain-to-failures achieved for the duration of tensile testing of the virgin and healed states of puncture damaged samples. According to the results reported in Table 4-3, all blends except 100:0 (neat x-PU;  $\eta_1=55.8\%$ ) revealed a  $\eta_1$  of 70% or higher, out of which 80:20 was found to show an approximate maximum  $\eta$  at 98.7%. This maximum at an intermediate level of l-PU suggests to us that there exists a functional balance between network and linear polymer where the amounts of both phases are perfectly optimal to provide sufficient SM well as SH properties. Also, the peak loading stresses corresponding to the virgin and healed states of this composition were 39.9 and 39.4 MPa, respectively. Note that the peak loading stresses associated

with the damaged state were consistently and noticeably lower than those of undamaged samples. However, the brief heating treatment gave rise to adequate SH, which resulted in comparable mechanical properties to the undamaged state. Then these  $\eta$  values were compiled into a plot of  $\eta$  vs 1-PU wt. % to better reveal the  $\eta$  trend (Figure 4-7). We realize that replications were not completed for statistics, but needed for quantitative conclusions. We speculate, though, that the trends observed could be expected to be reliable.

#### **4.4.4.2 Effect of Damage Type**

In realistic environments, there might be different types of damage happening to our SMASH material. Figure 4-8 showed the SH behavior for 80:20 composition under surface scratches (series (a)) and edge notches (series (b)). In particular, 80:20 dogbone shaped samples were damaged by either surface scratches or double-edge notches (image (i) in each series). Straining to ca. 40% caused damage/crack propagation (ii), followed by a 1-min heating step at 90 °C to trigger shape recovery and healing phenomenon (iii). Visually, we observed that, in either situations, the cracks closed up completely except some very light traces on the original damage sites. The samples were finally re-stretched to ca. 100% strain at RT with no evidence observed of crack reopening (iv), suggesting complete SH. In addition to that we imaged the cross-sectional view in damage evolution during the entire SH event at a micro-scale using SEM (Figure 4-9). In general, we found notable structural disruption for healing of all damage types and such disruption can't be healed without assistance of SM. Surprisingly, not even a single mark was spotted at the damage location after heating for either punctured or scratched sample, while, minor morphological discontinuity for the notched sample was observed in the form of misalignment when the crack surfaces were approaching each other under SM effect. We speculate that, for notched samples, this misalignment might cause imperfect SH and therefore poorer repair in mechanical features

compared to the other two damage types. Thicker films with smaller torsional compliance during deformation should mitigate the observed misalignment. More interestingly, fibrous or fiber-like structure was observed lining up along the stretching direction only when sample was in tensile tension (Figure 4-9(ii) and (iv) in each series). We attribute this observation to our unique electrospun x-PU that partially retains fibrous structure upon curing<sup>31</sup> as well as stress-induced orientation that is quite useful in yielding SM properties.

To quantitatively compare SH performance under different damage types, stress vs strain curves were recorded, using the tensile stretcher, for 80:20 at the virgin, damaged, and healed state upon puncture (a), scratch (b), and notch (c), respectively (Figure 4-10). It is evident that the healed sample restored mechanical properties to a quite large extent, by comparing the blue curve (healed) to the black curve (virgin), regardless of the damage type. The yield stress following healing was lower than that of virgin states, attributed to lower degree of crystallinity. However, out of three damage types, the double-edge notches caused the sample to fail at relatively low tensile strains. The reason behind that is that the notches represent the most severe damage type. In terms of evaluating mechanical properties before and after SH,  $\eta$  for each damage type was recorded from corresponding stress-strain plots and summarized in Table 4-7. The data revealed a modest difference between puncture damage ( $\eta=98.7\%$ ) and the other two types ( $\eta=85.5\%$  for scratched;  $\eta=83.0\%$  for notched). As discussed previously, the notched sample demonstrates the worst SH outcome because of the most severe degree in structural impairment, along with some healing imperfections due to surface misalignment, consistent to the observation by SEM imaging. Nonetheless, considering the fact that all healed samples showed a strain-to-failure of approximately 2000% or greater, we concluded that our 80:20 x-PU:l-PU blend is fully capable of

recovering, both structurally and functionally, from different damage types, including puncture, surface scratches, and double-edge notches, relying on the thermal-responsive SM characteristic.

#### **4.4.4.3 Effect of Anisotropy**

Recently, spatial and molecular orientation has been sought for use with uniaxial device fabrication in electrospinning process where fibers are collected onto a rotating mandrel collection apparatus.<sup>47,48</sup> Also, the reinforced mechanical and SM properties of oriented micro- and nanofibers are expected to differ drastically from their non-directional, nonwoven counterparts. To investigate and measure how orientation influences on SH performance of our blend systems, the 60:40 composition has been intentionally selected for such purpose since it showed the worst SH outcome in previous composition study and had the biggest potential for improvement. Further, the puncture form of damage was selected, due to ease of testing and demonstrated representative nature of damage for comparison purposes. In Figure 4-11, the SH processes were photo recorded and compared side by side for isotropic sample (a), oriented sample in 90 degrees off fiber direction (referred as to off-oriented sample subsequently; b), and oriented sample exactly in fiber direction (c), respectively. The puncture damage was studied exclusively in this case. Each sample went through four steps: (i) the initial state after thermally treated to erase thermal history, (ii) applying centered, thorough puncture damage, (iii) stretching to ca. 40% strain at RT, (iv) heating at 90 °C for 1 min, and (v) re-stretching to ca. 100% strain after being cooled back to RT.

Broadly speaking, we observed that all samples recovered from tensile deformation upon heating and closed the puncture hole completely. However, upon re-straining to a large extent, only the sample with its molecular orientation in fiber direction did not reveal any sign of the puncture reopening, which precisely met our preliminary anticipation. In contrast, perpendicularly oriented

samples hardly showed any significant healing as the hole seemed to reopen as wide as it was before heating. As the fiber direction is perpendicular to the film long axis direction, the enhanced SM properties could not assist in closing of puncture hole as much as when both directions were aligned. To complement the SH observations just discussed, the nature and level of molecular orientation was explored using X-ray scattering analysis. We sought, in particular, to quantify the level (or not) of molecular orientation for anisotropic and isotropic samples, respectively. Thus, WAXS was used to investigate the molecular structure of both anisotropic and isotropic samples before and after thermal curing. Figure 4-12(a)(i) suggested clearly that predominant molecular orientation has been introduced when high spinning speed was used during electrospinning since it showed an extremely oriented WAXS pattern in which two bright bands concentrate as equatorial reflections for the  $2\theta=18.4^\circ$  and  $20.8^\circ$  peaks of the orthorhombic unit cell of PCL. Although the compaction/crosslinking process diminished this orientation significantly (Figure 4-12(a)(ii)), the predominant orientation was not completely lost, with some concentration of the same reflections on the equator (top and bottom in this configuration) being evident. Similarly, SAXS patterns conveyed the same conclusion that molecular orientation remained post-curing, there with orientation of crystalline lamellae (perpendicular to the molecular chains) being evident. On the contrary, the isotropic sample disclosed no evidence of any molecular orientation in spite of thermal curing. Moreover, WAXS and SAXS plots are available in Figure 4-13(a) and (b). The azimuthal profiles, which are based on corresponding SAXS patterns, implied the strongest orientation of crystalline lamellae for the as-processed fibrous web, with full width at half-maximum of the meridional peak at a value of  $35.8^\circ$ . The cured and compacted sample had a diminished level of orientation and the isotropic sample was completely unoriented, as expected.



The stress-strain curves of the isotropic sample and the sample oriented in fiber orientation were compiled into Figure 4-14(a) for comparison purpose. The oriented samples showed superior ability to self-heal and restore mechanical properties from puncture damage, as evidenced by the curve of its healed state (blue) and that of its virgin state (black) being almost overlapped entirely. Moreover, the overall stress of oriented sample was found approximately 10 MPa greater than the stress level (yield stress and ultimate strength) of the isotropic sample in order to achieve the same strain, which means that the molecular orientation largely reinforced the mechanical strength in the direction of fiber alignment. Additionally, the oriented sample revealed much better SH capability and some mechanical characteristics compared to its counterpart, the off-oriented sample, as shown in Figure 4-14(b). We further quantified the SH behavior for all samples mentioned above in this section (Table 4-8). The  $\eta$  increased from 70.7% dramatically to 99.5% when molecular orientation was imposed and sustained in electrospinning. Besides, much worse  $\eta$  was obtained at a value of 66.7% when the stretching direction happened to be perpendicular to fiber alignment, which agrees with results described earlier.

#### **4.5 Conclusions**

A novel electrospun blend featuring shape memory assisted self-healing (SMASH) properties was developed by combining a network of the crosslinkable PCL-based polyurethane (x-PU) with linear PCL-based polyurethane (l-PU) using a simple but effective two-step method involving electrospinning and hot compaction (thermal curing). By varying the blend composition, the ability of each composition to exhibit self-healing (SH) of physical damage thereby restoring functionality was studied in-depth, revealing a dependence on l-PU wt. % content. We conclude that the 80:20 blend showcased exhibited the best SH capability among all compositions due to outstanding reversible plasticity shape memory at room temperature. This same composition

revealed excellent structural and functional SH with respect to different types of damage, including puncture, surface scratches, and double-edge notches. Given the fact that molecular anisotropy can aid in shape memory (SM) properties, a further investigation, which was performed on 60:40 blend, which had shown the worst SH performance in the composition study, led to a conclusion that fiber orientation improved shape recovery upon temperature triggering so that the closure and rebonding of damage were subsequently improved. The associated SH characteristics were improved with orientation significantly.

## 4.6 References

1. Wool, R. P.: Self-healing Materials: A Review. *Soft Matter* **2008**, 4, 400 – 418.
2. Yuan, Y. C.; Yin, T.; Rong, M. Z.; Zhang, M. Q.: Self Healing in Polymers and Polymer Composite. Concepts, Realization and Outlook: A Review. *eXPRESS Polym. Lett.* **2008**, 2, 238 – 250.
3. Blaiszik, B. J.; Kramer, S. L. B.; Olugebefola, S. C.; Moore, J. S.; Sottos, N. R.; White, S. R.: Self-healing Polymers and Composites. *Annu. Rev. Mater. Res.* **2010**, 40, 179 – 211.
4. Yang, Y.; Urban, M. W.: Self-healing Polymeric Materials. *Chem. Soc. Rev.* **2013**, 42, 7446 – 7467.
5. Wu, D. Y.; Meure, S.; Solomon, D.: Self-healing Polymeric: A Review of Recent Developments. *Prog. Polym. Sci.* **2008**, 33, 479 – 522.
6. Trask, R. S.; Williams, H. R.; Bond, I. P.: Self-healing Polymer Composites: Mimicking Nature to Enhance Performance. *Bioinsp. Biomim.* **2007**, 2, 1 – 9.
7. White, S. R.; Sottos, N.; Geubelle, P.; Moore, J.; Kessler, M. R.; Sriram, S.; Brown, E.; Viswanathan, S.: Autonomic Healing of Polymer Composites. *Nature* **2001**, 409, 794 – 797.
8. Liu, Y. L.; Chuo, T. W.: Self-healing Polymers Based on Thermally Reversible Diels-Alder Chemistry. *Polym. Chem.* **2013**, 4, 2194 - 2205.
9. Yarlagadda, S.; Kim, H. J.; Gillespie, J. W.; Shevchenko, N. B.; Fink, B. K.: A Study on the Introduction Heating of Conductive Fiber Reinforced Composites. *J. Compos. Mater.* **2002**, 36, 401 – 421.
10. Mather, P. T.; Luo, X. F.; Rousseau, I. A.: Shape Memory Polymer Research. *Annu. Rev. Mater. Res.* **2009**, 39, 445 – 471.

11. Lendlein, A.; Kelch, S.: Shape-memory Polymers. *Angew. Chem. Int. Ed.* **2002**, 41, 2034 – 2057.
12. Liu, C.; Qin, H.; Mather, P. T.: Review of Progress in Shape-memory Polymers. *J. Mater. Chem.* **2007**, 17, 1543 – 1558.
13. Rousseau, I. A.: Challenges of Shape Memory Polymers: A Review of the Progress towards Overcoming SMP's Limitations. *Polym. Eng. Sci.* **2008**, 48, 2075 – 2089.
14. Kirkby, E. L.; Rule, J. D.; Michaud, V. J.; Sottos, N. R.; White, S.R.; Månson, J. A. E.: Embedded Shape-memory Alloy Wires for Improved Performance of Self-healing Polymers. *Adv. Funct. Mater.* **2008**, 18, 2253 – 2260.
15. Kirby, E. L.; Michaud, V. J.; Månson, J. A. E.; Sottos, N. R.; White, S. R.: Performance of Self-healing Epoxy with Microencapsulated Healing Agent and Shape Memory Alloy Wires. *Polymer* **2009**, 50, 5533 – 5538.
16. Neuser, S.; Michaud, V.; White, S. R.: Improving Solvent-based Self-healing Materials through Shape Memory Alloys. *Polymer* **2012**, 53, 370 – 378.
17. Li, G.; Meng, H.; Hu, J.: Healable Thermoset Polymer Composite Embedded with Stimuli-responsive Fibers. *J. R. Soc. Interface* **2012**, 9, 3279 – 3287.
18. Li, G.; Shojaei, A.: A Viscoplastic Theory of Shape Memory Polymer Fibers with Application to Self-healing Materials. *Proc. R. Soc. A* **2012**, 468, 2319 – 2346.
19. Nji, J.; Li, G.: Damage Healing Ability of A Shape-memory-polymer-based Particulate Composite with Small Thermoplastic Contents. *Smart Mater. Struct.* **2012**, 21, 025011.
20. Lu, X.; Fei, G.; Xia, H.; Zhao, Y.: Ultrasound Healable Shape Memory Dynamic Polymers. *J. Mater. Chem. A* **2014**, 2, 16051 – 16060.

21. Rivero, G.; Nguyen, L. T. T.; Jillewaere, X. K.; Du Prez, F. E.: One-pot Thermo-remendable Shape Memory Polyurethanes. *Macromolecules* **2014**, 47, 2010 – 2018.
22. Zhang, J.; Niu, Y.; Huang, C.; Xiao, L.; Chen, Z.; Yang, K.; Wang, Y.: Self-healable and Recyclable Triple-shape PPDO-PTMEG Co-network Constructed Through Thermoreversible Diels-Alder Reaction. *Polym. Chem.* **2012**, 3, 1390 – 1393.
23. Rodriguez, E. D.; Luo, X.; Mather, P. T.: Linear/Network Poly( $\epsilon$ -caprolactone) Blends Exhibiting Shape Memory Assisted Self-healing (SMASH). *ACS Appl. Mater. Interfaces* **2011**, 3, 152 – 161.
24. Luo, X.; Mather, P. T.: Shape Memory Assisted Self-healing Coating. *ACS Macro Lett.* **2013**, 2, 152 – 156.
25. Nejad, H. B.; Garrison, K. L.; Mather, P. T.: Comparative Analysis of Shape Memory-based Self-healing Coatings. *J. Polym. Sci., Part B: Polym. Phys.* **2016**, 54, 1415 – 1426.
26. Luo, X.; Mather, P. T.: Triple-shape Polymeric Composites (TSPCs). *Adv. Funct. Mater.* **2010**, 20, 2649 – 2656.
27. Luo, X.; Lauber, K. E.; Mather, P. T.: A Thermally Responsive, Rigid, and Reversible Adhesive. *Polymer* **2010**, 51, 1169 – 1175.
28. Nejad, H. B.; Baker, R. M.; Mather, P. T.: Preparation and Characterization of Triple Shape Memory Composite Foams. *Soft Matter* **2014**, 10, 8066 – 8074.
29. Torbati, A. H.; Nejad, H. B.; Ponce, M.; Sutton, J. P.; Mather, P. T.: Properties of Triple Shape Memory Composites Prepared via Polymerization-induced Phase Separation. *Soft Matter* **2014**, 10, 3112 – 3121.

30. Lawton, M. I.; Tillman, K. R.; Mohammed, H. S.; Kuang, W.; Shipp, D. A.; Mather, P. T.: Anhydride-based Reconfigurable Shape Memory Elastomers. *ACS Macro Lett.* **2016**, *5*, 203 – 207.
31. Kuang, W.; Mather, P. T.: A Latent Crosslinkable PCL-based Polyurethane: Synthesis, Shape Memory, and Degradation. *J. Mater. Res.* **2017**, *xx*, xxx – xxx.
32. Canadell, J.; Goossens, H.; Klumperman, B.: Self-healing Materials Based on Disulfide Links. *Macromolecules* **2011**, *44*, 2536 – 2541.
33. Rhaman, M. A.; Renco, M.; Spagnoli, G.; Grande, A. M.; Landro, L. D.: Self-healing Behavior of Blends Based on Ionomers with Ethylene/Vinyl Alcohol Copolymer or Epoxidized Natural Rubber. *Macromol. Mater. Eng.* **2011**, *296*, 1119 – 1127.
34. Ji, F.; Zhu, Y.; Hu, J.; Liu, Y.; Yeung, L.; Ye, G.: Smart Polymer Fibers with Shape Memory Effect. *Smart Mater. Struct.* **2006**, *15*, 1547 – 1554.
35. Tseng, L.; Mather, P. T.; Henderson, J. H.: Shape-memory-actuated Change in Scaffold Fiber Alignment Directs Stem Cell Morphology. *Acta Biomater.* **2013**, *9*, 8790 – 8801.
36. Meng, Q.; Hu, J.: A Review of Shape Memory Polymer Composites and Blends. *Compos. Part A* **2009**, *40*, 1661 – 1672.
37. Murugan, R.; Ramakrishna, S.: Design Strategies of Tissue Engineering Scaffolds with Controlled Fiber Orientation. *Tissue Eng.* **2007**, *13*, 1845 – 1866.
38. Fennessey, S. F.; Farris, R. J.: Fabrication of Aligned and Molecularly Oriented Electrospun Polyacrylonitrile Nanofibers and the Mechanical Behavior of their Twisted Yarns. *Polymer* **2004**, *45*, 4217 – 4225.
39. Luo, X.; Mather, P. T.: Preparation and Characterization of Shape Memory Elastomeric Composites. *Macromolecules* **2009**, *42*, 7251 – 7253.

40. Koerner, H.; Price, G.; Pearce, N. A.; Alexander, M.; Vaia, R. A.: Remotely Actuated Polymer Nanocomposites–Stress-recovery of Carbon Nanotube-filled Thermoplastic Elastomers. *Nat. Mater.* **2004**, 3, 115 – 120.
41. Chung, T.: *New Shape Memory Effects in Semicrystalline Polymeric Networks*. Ph.D. Thesis, Case Western Reserve University, Cleveland, OH, 2009.
42. Boire, P. C.; Gupta, M. K.; Zachman, A. L.; Lee, S. H.; Balikov, D. A.; Kim, K.; Bellan, L. M.; Sung, H.: Pendant Allyl Crosslinking as A Tunable Shape Memory Actuator for Vascular Applications. *Acta Biomater.* **2015**, 24, 53 – 63.
43. Liu, C.; Chun, S. B.; Mather, P. T.: Chemically Cross-linked Polycyclooctene: Synthesis, Characterization, and Shape Memory Behavior. *Macromolecules* **2002**, 35, 9868 – 9874.
44. Chung, T.; Romo-Uribe, A.; Mather, P. T.: Two-way Reversible Shape Memory in A Semicrystalline Network. *Macromolecules* **2008**, 41, 184 – 192.
45. Robertson, J. M.; Rodriguez, R. X.; Holmes Jr., L. R.; Mather, P. T.; Wetzel, E. D.: Thermally Driven Microfluidic Pumping via Reversible Shape Memory Polymers. *Smart Mater. Struct.* **2016**, 25, 085043.
46. Lee, K. M.; Knight, P. T.; Chung, T.; Mather, P. T.: Polycaprolactone-POSS Chemical/Physical Double Networks. *Macromolecules* **2008**, 41, 4730 – 4738.
47. Lee, S.; Yoon, J.; Suh, M. H.: Continuous Nanofibers Manufactured by Electrospinning Technique. *Macromol. Res.* **2002**, 10, 282 – 285.
48. Pedicini, A.; Farris, R. J.: Mechanical Behavior of Electrospun Polyurethane. *Polymer* **2003**, 22, 6857 – 6862.

**Table 4-1.** Synthesis Summary of Polyurethanes

Samples (n≥5)	Feed molar ratio	Actual molar	Yield	Molecular	PDI	$T_m$ (°C)	$\Delta H_m$
	<sup>a, b</sup> (PCL <sub>3k</sub> :DHB:H DI)	PCL <sub>3k</sub> :DHB <sup>c</sup>	(Mass %)	weight ( $M_n$ , kDa)		<sup>d</sup>	(J/g)
x-PU	3:2.1:6	9.61:1	90.9±9.3	84.1±27.1	1.79±0.14	45.2±2.6	42.1±1.9
1-PU	1:0:1	-	84.0±6.0	33.1±5.3	1.62±0.20	48.9±0.1	50.5±0.3

<sup>a</sup> Nomenclature: **PCL** stands for polycaprolactone-diol with  $M_n=3$  kDa, **DHB** for 3,4-dihydroxy-1-butene, **HDI** for hexamethylene diisocyanate.

<sup>b</sup> Tuned ratio by trial-and-error method.

<sup>c</sup> Determined by NMR spectra.

<sup>d</sup> Peak values of second heating in DSC curve.



**Table 4-2.** RPSM Characteristics as A Function of l-PU wt.%

---

Sample	$\epsilon_d$ (%)	$\epsilon_f$ (%)	$\epsilon_r$ (%)	$R_f$ (%)	$R_r$ (%)
100:0	141.9	104.2	3.8	73.4	96.4
90:10	137.1	95.1	1.2	69.4	98.7
80:20	142.0	104.7	0.8	73.7	99.2
70:30	137.3	108.1	9.1	78.7	91.6
60:40	144.9	119.8	2.4	82.7	98.0
50:50	141.9	122.7	2.5	86.5	98.0

---

**Table 4-3.** Self-healing Efficiency as A Function of I-PU wt.%

Sample	$\varepsilon_{u,v}$ (%)	$\sigma_{u,v}$ (MPa)	$\varepsilon_{u,h}$ (%)	$\sigma_{u,h}$ (MPa)	$\eta_1$ (%)	$\eta_1$ (%)
100:0	2050.8	36.4	1752.1	20.3	55.8	85.4
90:10	2901.2	44.1	2698.2	41.4	93.9	93.0
80:20	2355.6	39.9	2253.8	39.4	98.7	95.7
70:30	2145.9	41.3	1726.5	35.2	85.2	80.5
60:40	2355.6	38.9	1593.6	27.5	70.7	67.7
50:50	1663.1	20.5	1586.9	15.8	77.1	95.4

**Table 4-4.** Preparation of Electrospinning Solutions for Various Compositions

Sample (x-PU:l-PU w/w)	x-PU (g)	l-PU (g)	Chloroform (mL)	<i>N,N</i> -Dimethylformamide (mL)	DLP (wt. %)
100:0	2.0	-	8.0	4.0	2.0
90:10	1.8	0.2	8.0	4.0	2.0
80:20	1.6	0.4	8.0	4.0	2.0
70:30	1.4	0.6	8.0	4.0	2.0
60:40	1.2	0.8	8.0	4.0	2.0
50:50	1.0	1.0	8.0	4.0	2.0

**Table 4-5.** Thermal and Structural properties of Electrospun Fiber Mats and Linear Polymer

Sample (x-PU:l-PU w/w)	$T_m$ (°C)	$\Delta H_m$ (J/g)	$T_c$ (°C)	$\Delta H_c$ (J/g)
100:0	44.9	38.8	7.9	41.8
90:10	45.8	37.6	10.5	39.9
80:20	46.8	45.6	12.4	41.6
70:30	47.3	35.2	15.8	38.7
60:40	47.6	49.5	17.3	41.8
50:50	47.9	43.3	16.6	46.7
0:100 <sup>a</sup>	48.9	52.4	19.7	53.8

<sup>a</sup> Precipitate from synthesis was analyzed directly after being fully vacuum dried.

**Table 4-6.** Thermal and Structural properties of Hot Compacted Fiber Mats

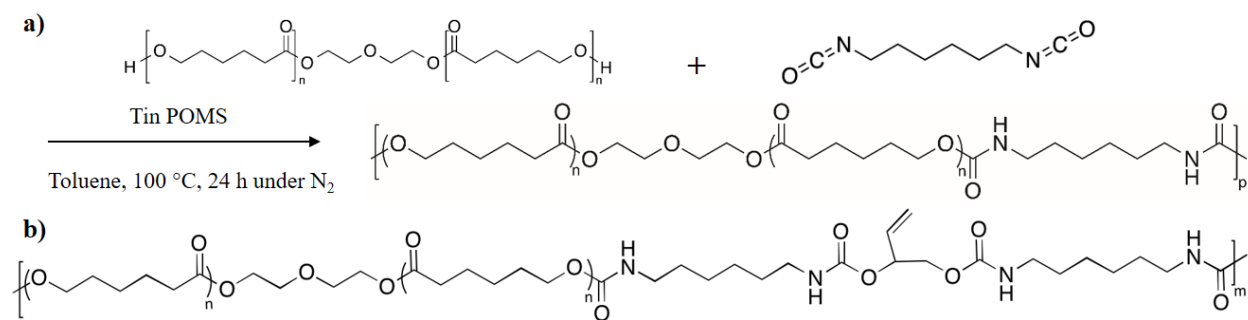
Sample (x-PU:l-PU w/w)	$T_m$ (°C)	$\Delta H_m$ (J/g)	$T_c$ (°C)	$\Delta H_c$ (J/g)	G (%)
100:0	44.3	40.8	8.35	39.5	85.7
90:10	46.7	39.0	14.2	40.6	68.9
80:20	46.9	39.2	14.6	41.7	61.3
70:30	47.3	45.6	15.1	39.7	44.3
60:40	47.1	41.0	15.9	47.0	32.8
50:50	48.3	45.6	18.8	47.3	35.4

**Table 4-7.** Self-healing Efficiency for Different Types of Damages

Type of Damage	$\varepsilon_{u,v}$ (%)	$\sigma_{u,v}$ (MPa)	$\varepsilon_{u,h}$ (%)	$\sigma_{u,h}$ (MPa)	$\eta$ (%)
Puncture	2355.6	39.9	2253.8	39.4	98.7
Scratch	2355.6	39.9	2209.3	34.1	85.5
Notch	2355.6	39.9	2038.0	33.1	83.0

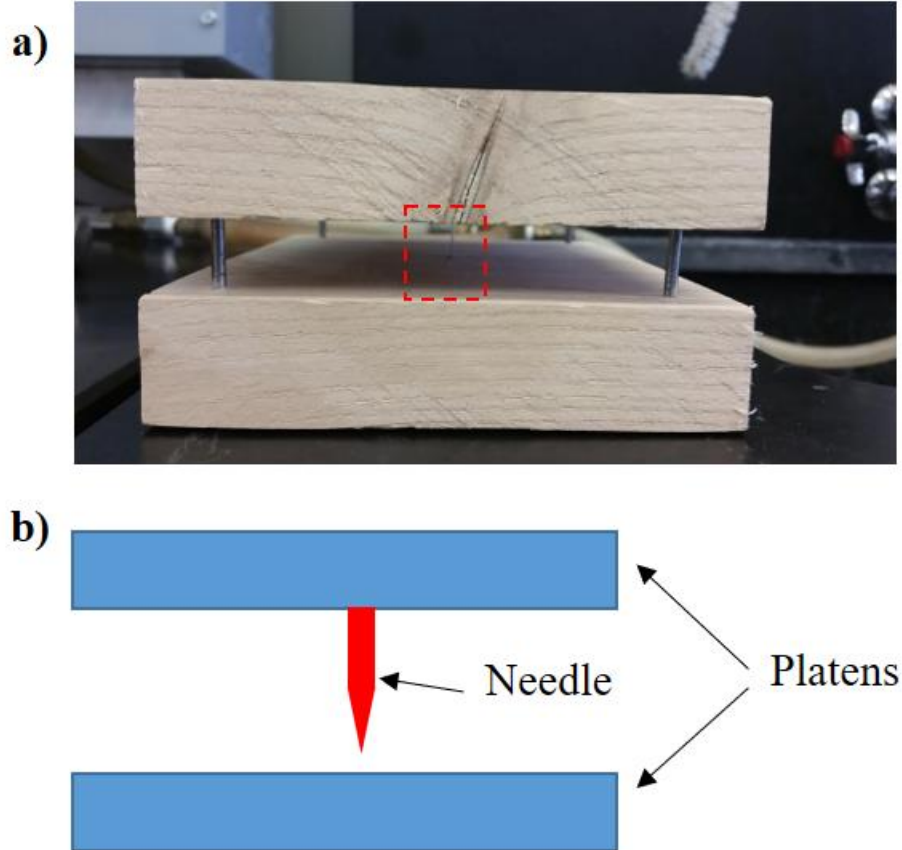
**Table 4-8.** Self-healing Efficiency as A Function of Anisotropy

Sample	$\varepsilon_{u,v}$ (%)	$\sigma_{u,v}$ (MPa)	$\varepsilon_{u,h}$ (%)	$\sigma_{u,h}$ (MPa)	$\eta$ (%)
60:40	2355.6	38.9	1593.6	27.5	70.7
60:40 (90°)	829.5	24.6	753.1	16.4	66.7
60:40 (0°)	1790.3	40.6	1773.6	40.4	99.5



**Scheme 4-1.** **a)** Synthesis of linear PCL-based thermoplastic polyurethane (l-PU) using polycaprolactone-diol with number-average molecular weight of 3,000 Da (PCL) and hexamethylene diisocyanate (HDI); **b)** Latent crosslinkable PCL-based thermoplastic polyurethane (x-PU) synthesized by the previously developed approach.





**Scheme 4-2.** a) The schematic of the custom-made device used to create consistent puncture (“wound”). A size 17 pin highlighted in dashed rectangular is installed perpendicularly in the center between two wooden platens with smooth surfaces; b) side (cross-sectional) view of the custom-made device.

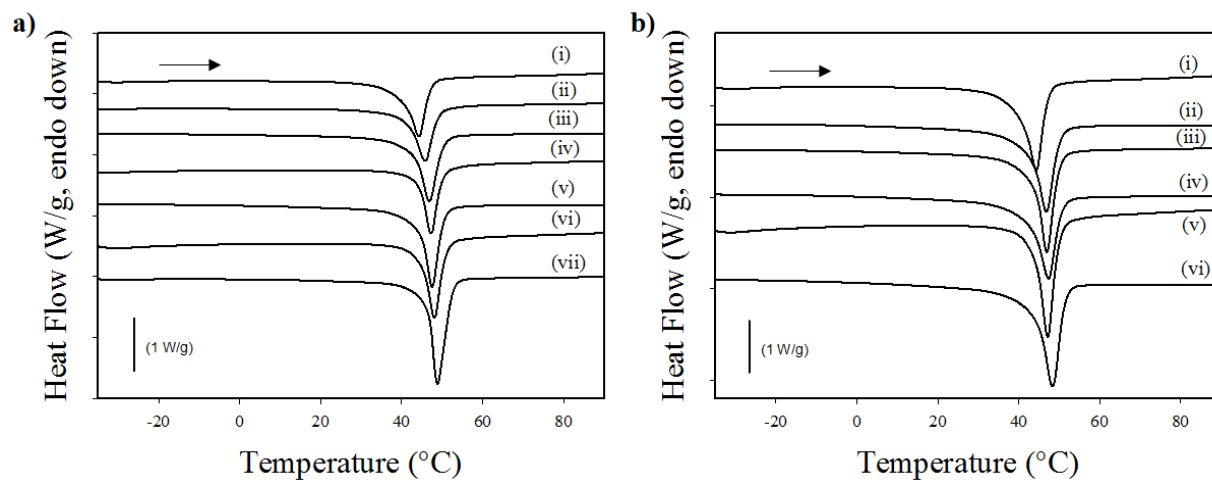


**Figure 4-1.** Differential Scanning Calorimetry (DSC) analysis graph of **a)** electrospun fiber mats and linear polymer: **(i)** 100:0, **(ii)** 90:10, **(iii)** 80:20, **(iv)** 70:30, **(v)** 60:40, **(vi)** 50:50, and **(vii)** 0:100; and of **b)** hot compacted fiber mats: **(i)** 100:0, **(ii)** 90:10, **(iii)** 80:20, **(iv)** 70:30, **(v)** 60:40, and **(vi)** 50:50.

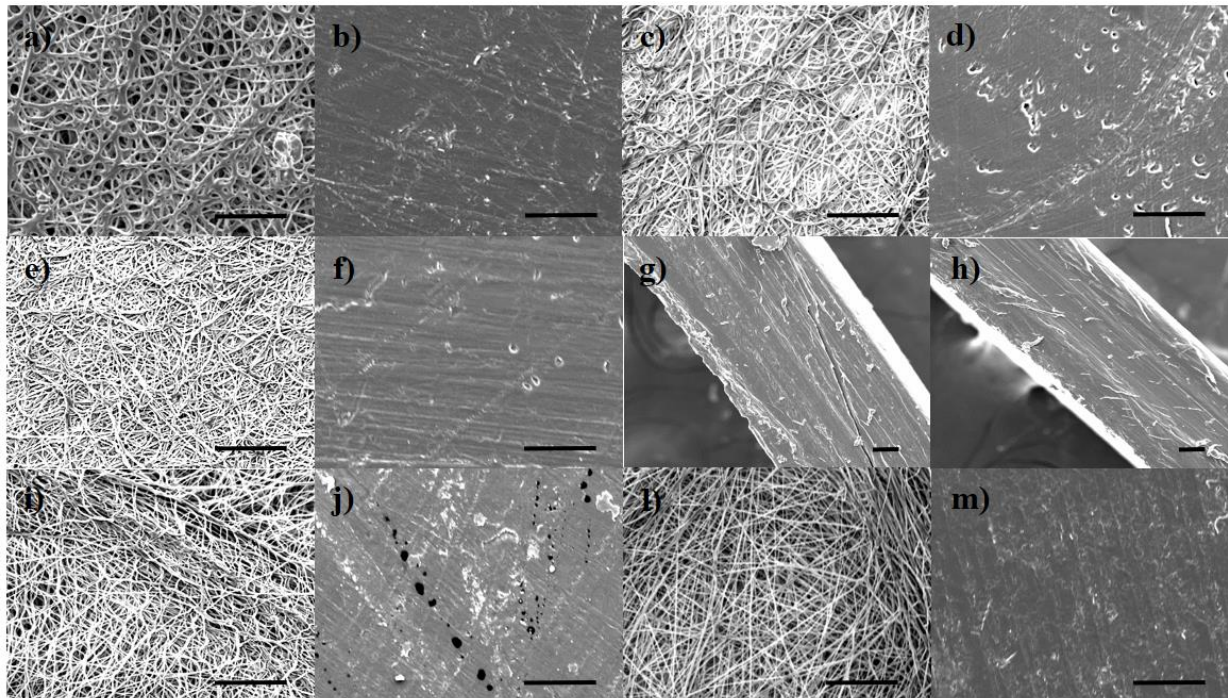


**Figure 4-2.** Scanning electron microscope (SEM) images of electrospun fiber mats: **a)** 90:10, **c)** 80:20, **e)** 70:30, **i)** 60:40, and **l)** 50:50; SEM images of hot compacted fiber mats: **b)** 90:10, **d)** 80:20, **f)** 70:30, **j)** 60:40, and **m)** 50:50. Cryofracture (cross-section) views of hot compacted **g)** 80:20 and **h)** 60:40 samples at high magnifications. The scale bar is 50  $\mu\text{m}$ .

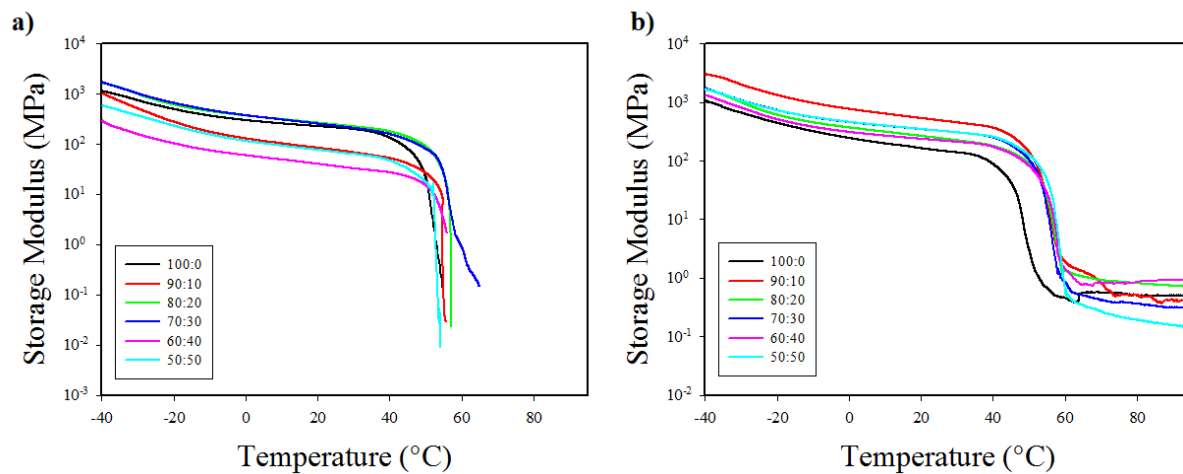
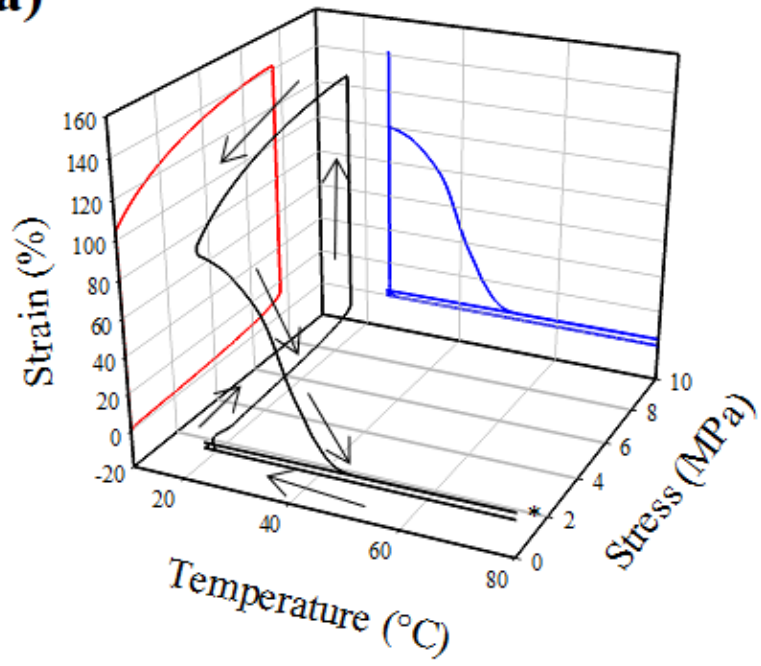
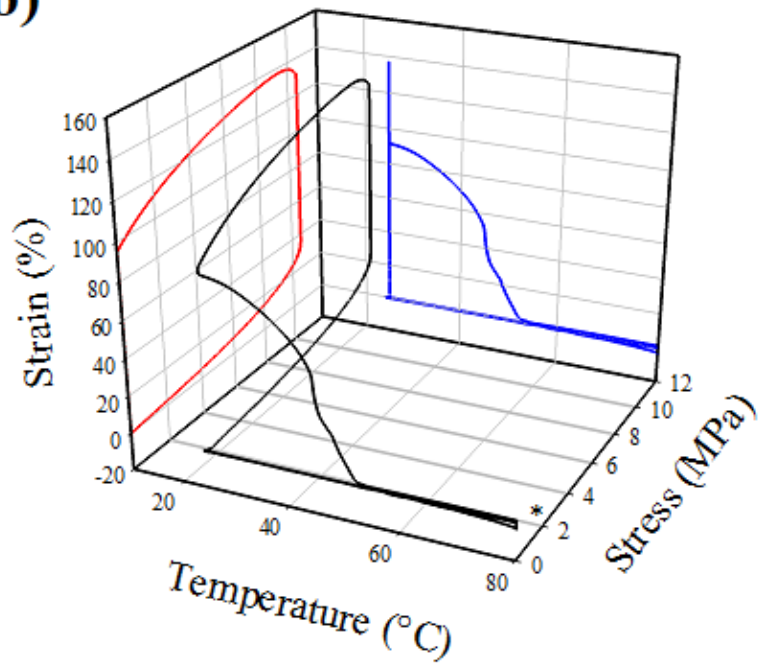


**Figure 4-3.** Storage modulus ( $E'$ ) vs temperatures for **a)** electrospun fiber mats and **b)** hot compacted fiber mats, respectively: 100:0 (black), 90:10 (red), 80:20 (green), 70:30 (blue), 60:40 (pink), and 50:50 (cyan).  $E'$  was recorded at a heating rate of 3 °C/min with frequency of 1 Hz.

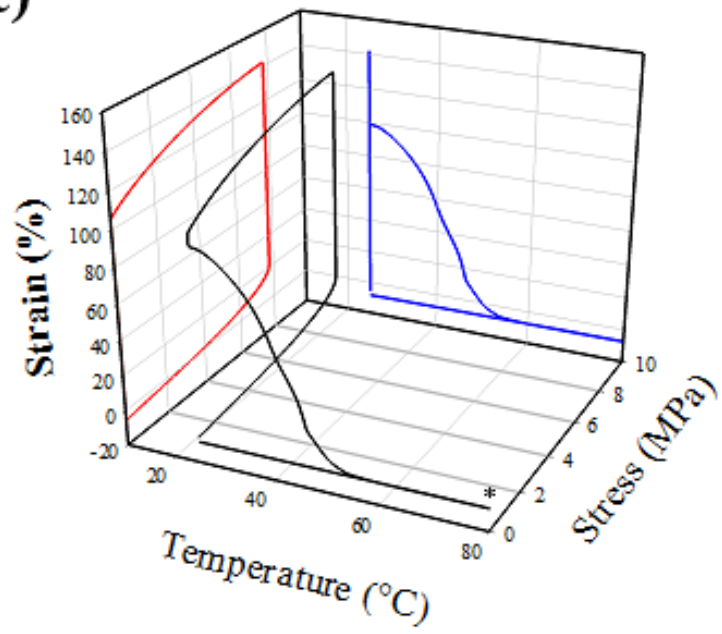
**a)**



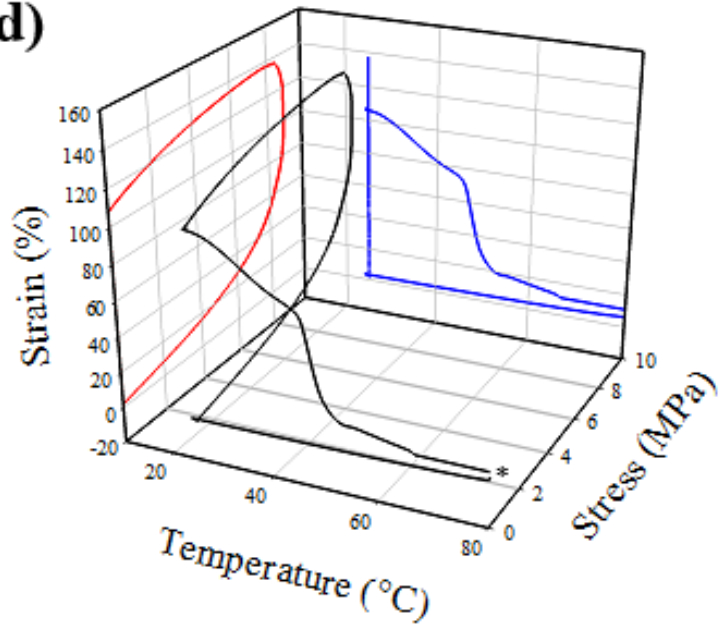
**b)**



c)



d)



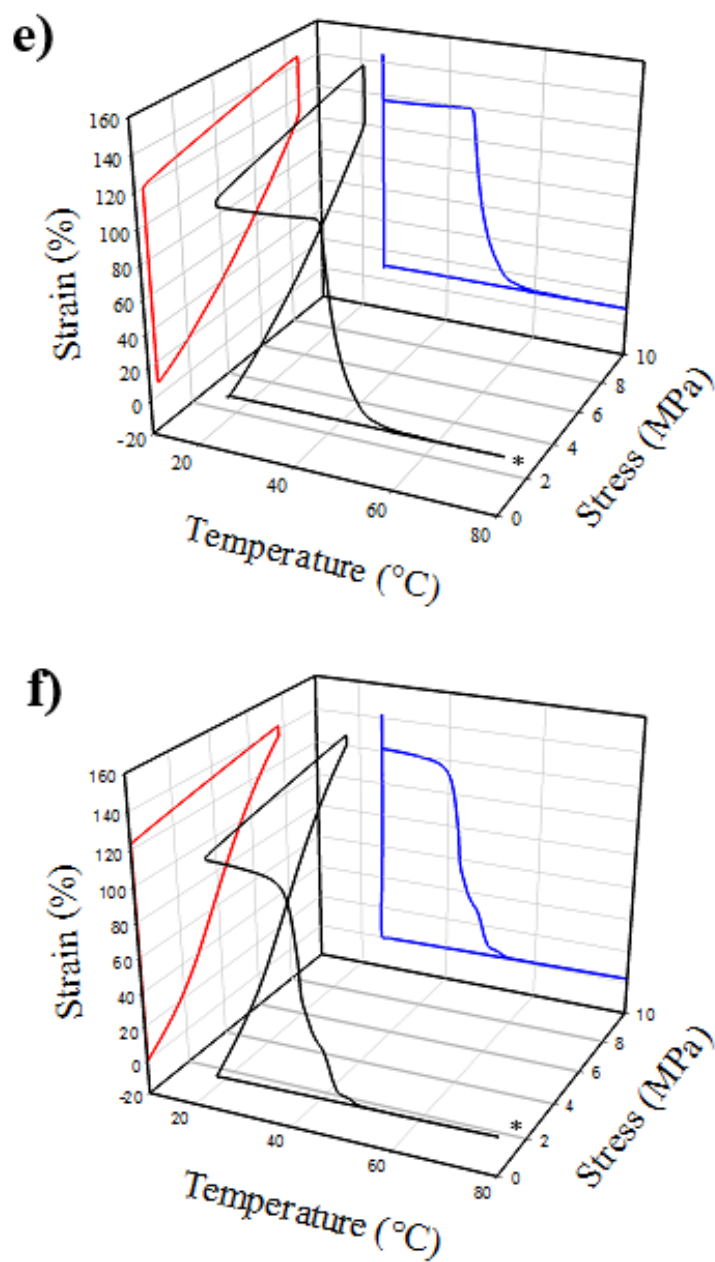
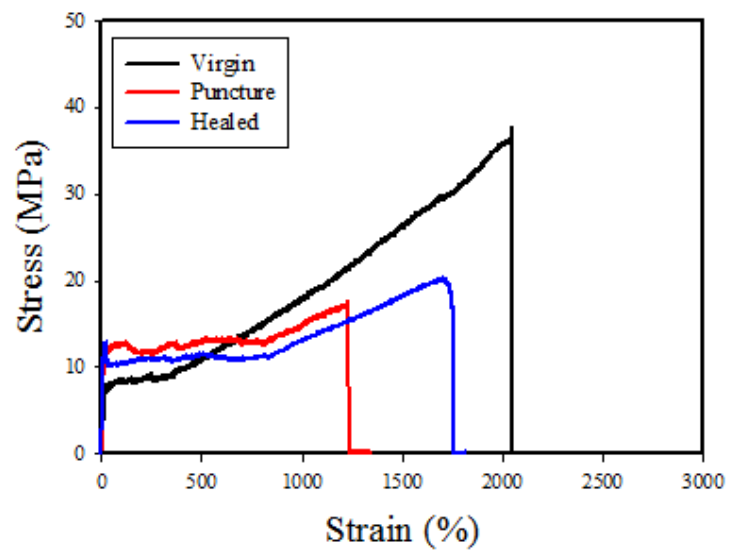
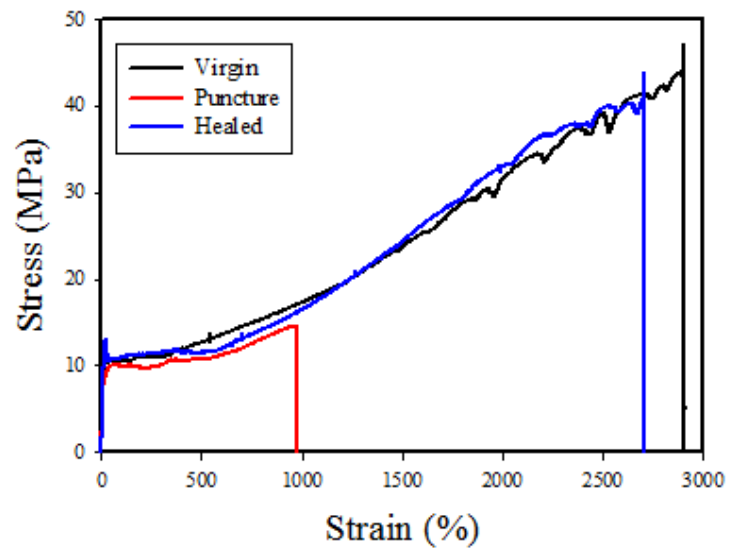


**Figure 4-4.** Reversible plasticity shape memory (RPSM) cycle of **a)** 100:0, **b)** 90:10, **c)** 80:20, **d)** 70:30, **e)** 60:40, and **f)** 50:50, respectively, where each sample was deformed to 140% strain at room temperature and recovered at 80 °C. Strain vs temperature curve (blue) and stress vs strain curve (red) are plotted for each composition. “\*” indicates starting point.

**a)**

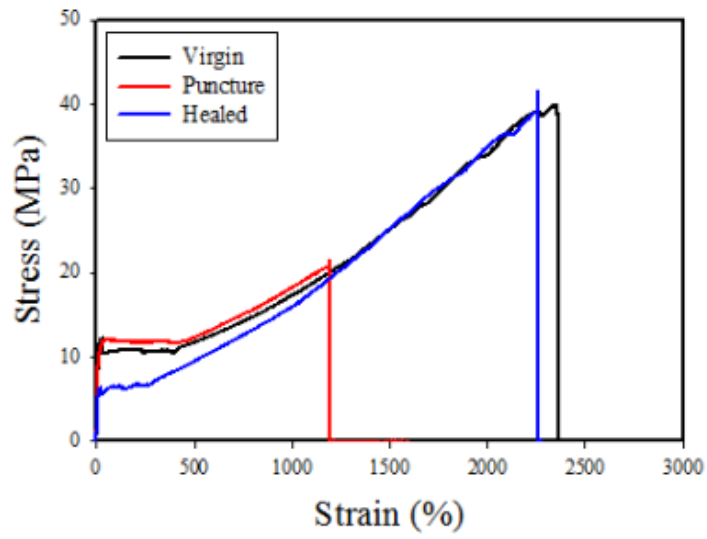


**b)**

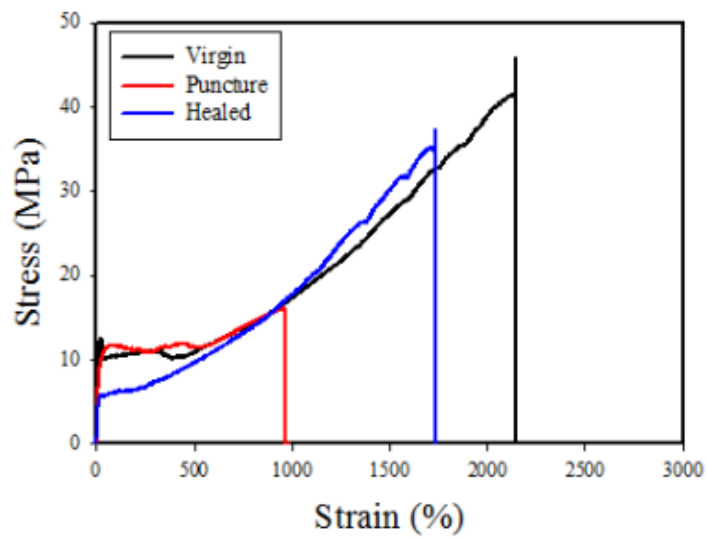




**c)**



**d)**



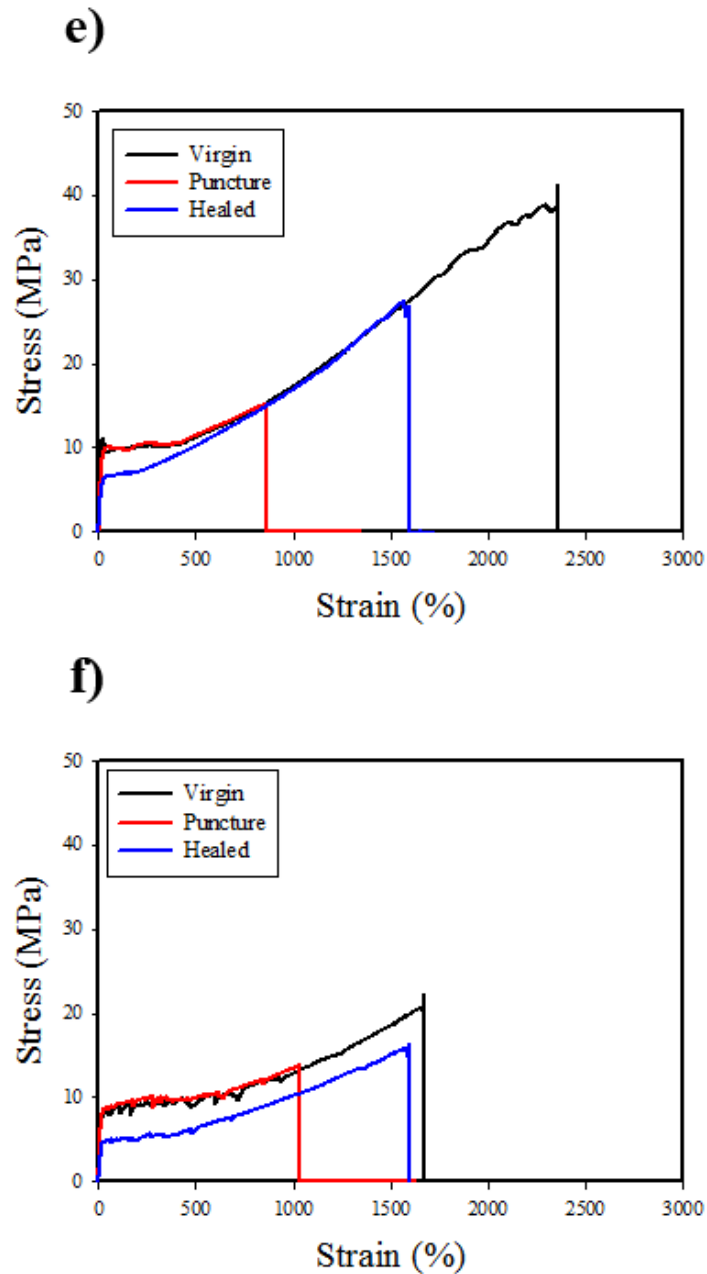


**Figure 4-5.** Stress vs strain curves for the virgin, puncture damaged and healed states of **a)** 100:0, **b)** 90:10, **c)** 80:20, **d)** 70:30, **e)** 60:40, and **f)** 50:50, respectively. In particular, the healed 80:20 sample shows a profile highly identical to the virgin state, indicating complete restoration of mechanical properties.

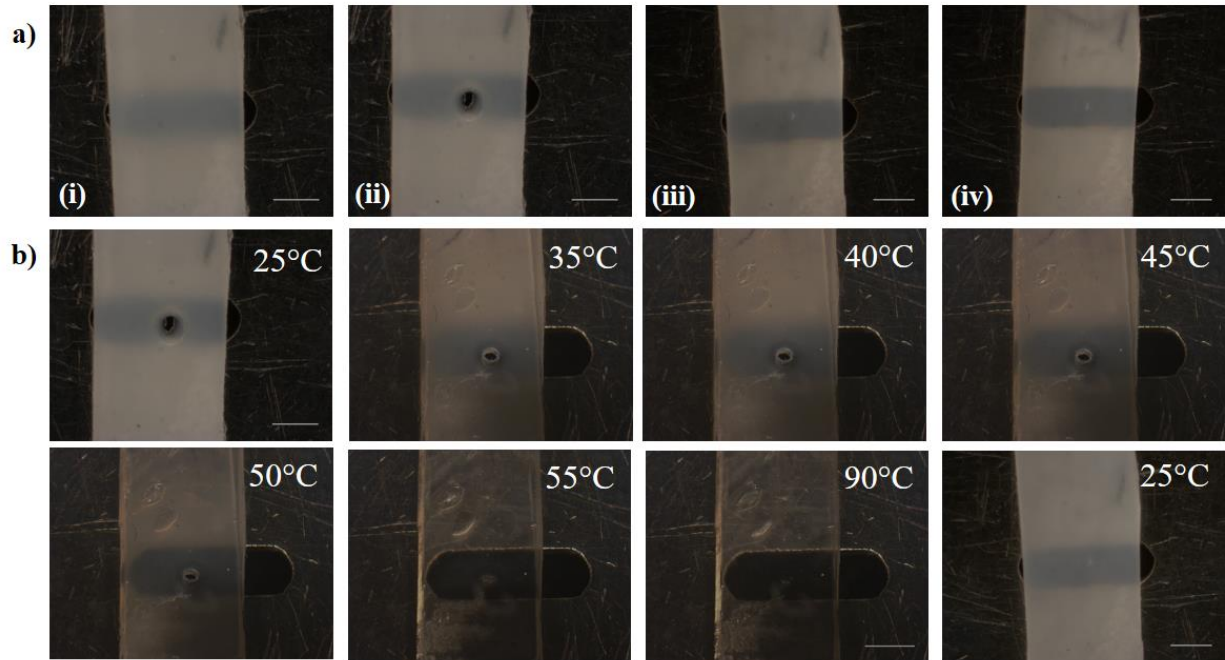


**Figure 4-6. a)** Optical microscope images of a hot compacted 80:20 sample showing **(i)** the virgin state, **(ii)** puncture damaged and stretched (~40% strain) state at RT (~22 °C), **(iii)** heated (90 °C) and healed state, and **(iv)** re-stretched state (~100% strain) after cooled back to RT. The scale bar is 0.5 mm; **b)** Snapshots of puncture closure and puncture rebonding when the sample was unloaded from the clamps of the LinkAm tensile stage and heated up to the temperatures revealed above (stereo micrographs scale bar is 0.5 mm).

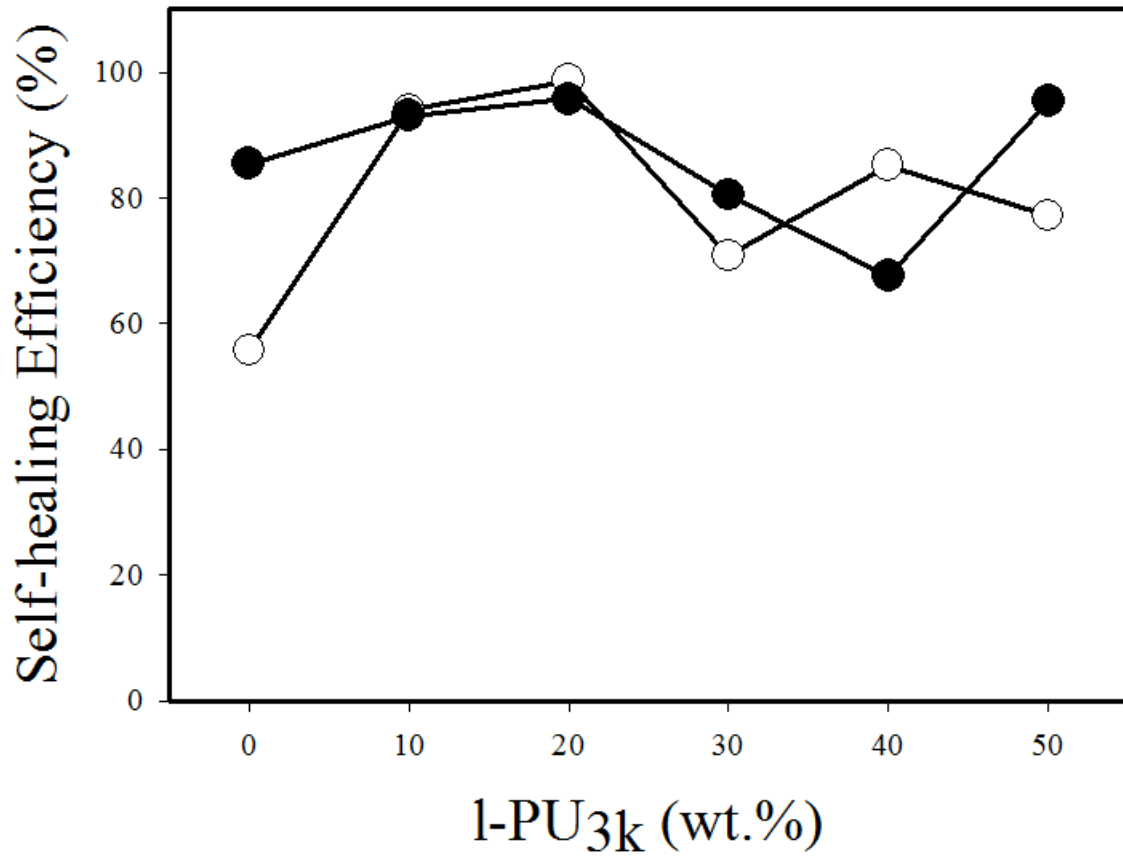


**Figure 4-7.** Self-healing efficiency vs l-PCL wt. % content. The damage type is puncture.  $\eta_1$ :  $\circ$ ,  $\eta_2$ :  $\bullet$ .

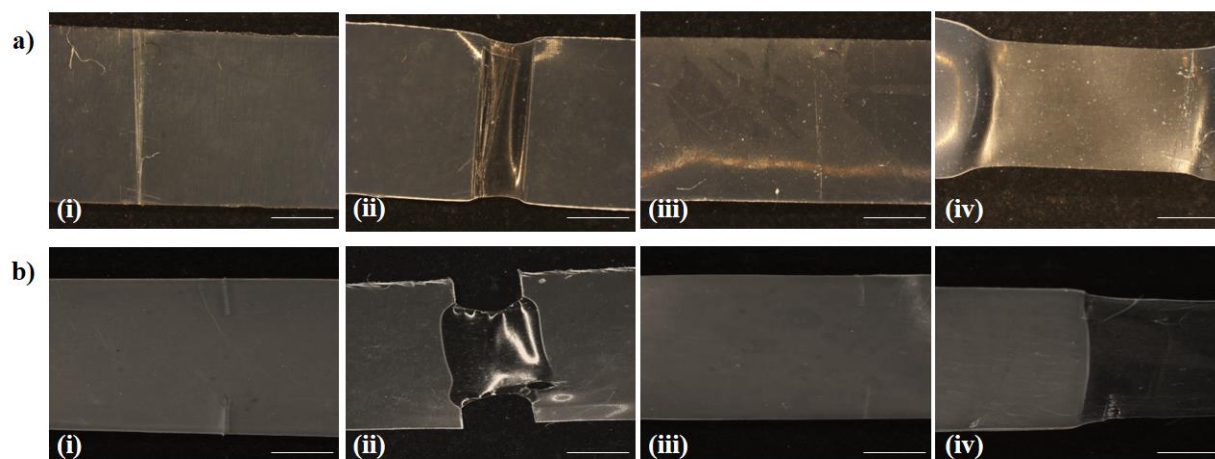


**Figure 4-8.** Optical microscope images of **a)** a hot compacted 80:20 sample showing **(i)** the virgin state, **(ii)** scratch (on both sides) damaged and stretched (~40% strain) state at RT (~22 °C), **(iii)** heated (90 °C) and healed state, and **(iv)** re-stretched state (~100% strain) after being cooled back to RT; **b)** a hot compacted 80:20 sample showing **(i)** the virgin state, **(ii)** double-edge notched and stretched (~40% strain) state at RT (~22 °C), **(iii)** heated (90 °C) and healed state, and **(iv)** re-stretched state (~100% strain) after being cooled back to RT. The scale bar is 0.5 mm.

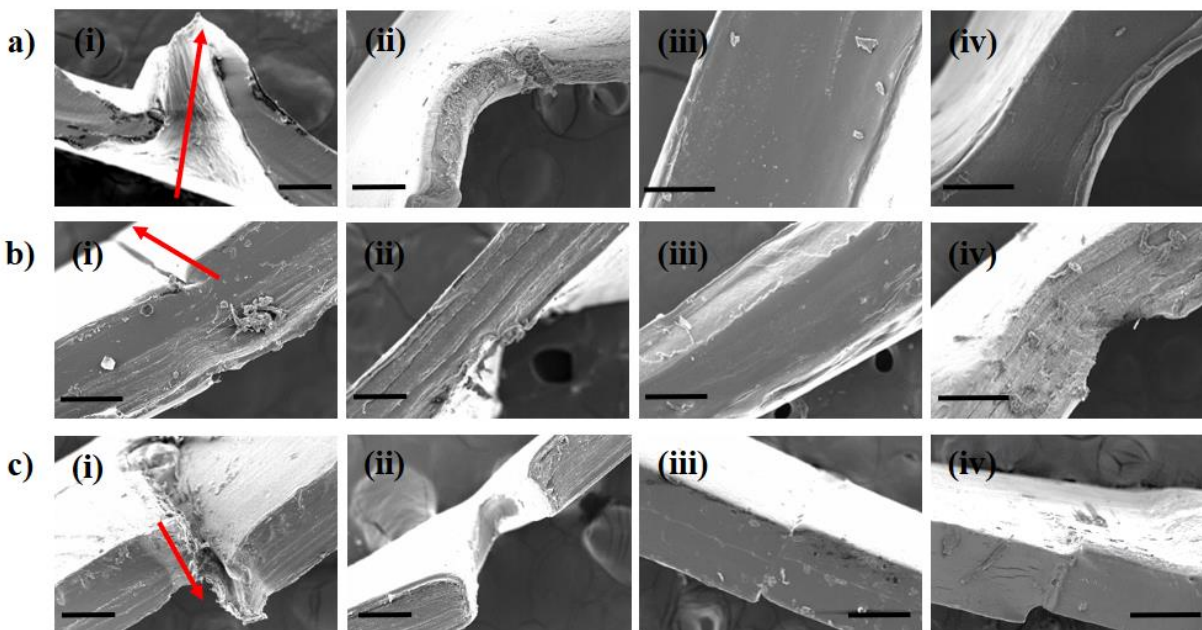


**Figure 4-9.** a) SEM imaging cross-sectional views of a) a puncture damaged 80:20 sample, b) a scratch damaged 80:20 sample, and c) a notch damaged 80:20 sample for (i) the damaged state, (ii) the damaged state upon 40% strain, (iii) the healed state, and (iv) the healed state upon 100% strain. The scale bar is 100  $\mu\text{m}$ . The red arrows indicate the damages accordingly.

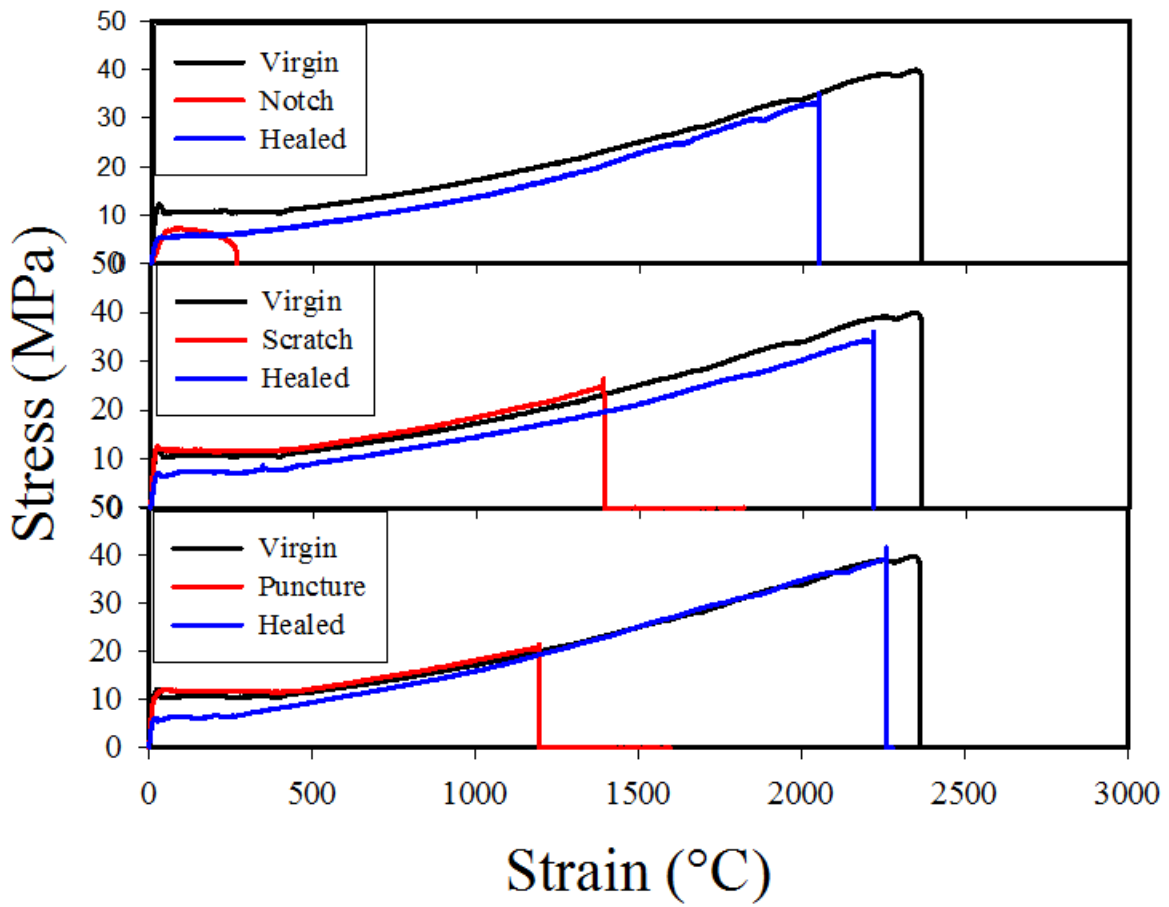


**Figure 4-10.** Stress vs strain curves for the virgin state, damaged state, and healed state of a hot compacted 80:20 sample under application of different types of damages: puncture (bottom), scratch (middle), and notch (upper), respectively.

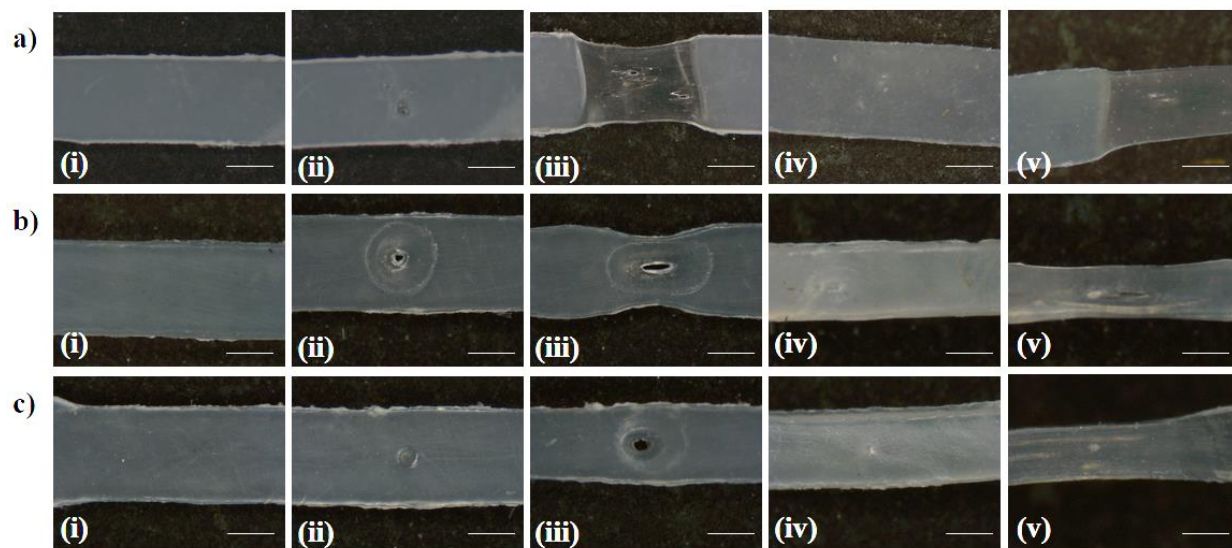


**Figure 4-11.** Optical microscope images of **a)** an isotropic 60:40, **b)** an oriented 60:40 whose stretching direction is perpendicular to original fiber orientation ( $90^\circ$ ), and **c)** an oriented 60:40 whose stretching direction is parallel with original fiber orientation ( $0^\circ$ ), respectively, showing **(i)** the virgin state, **(ii)** puncture damaged state, **(iii)** stretched ( $\sim 40\%$  strain) state at RT ( $\sim 22^\circ\text{C}$ ), **(iv)** heated ( $90^\circ\text{C}$ ) and healed state, and **(v)** re-stretched state ( $\sim 100\%$  strain) after cooled back to RT. The scale bar is 0.5 mm. The loading direction and film long axis direction are both horizontal.



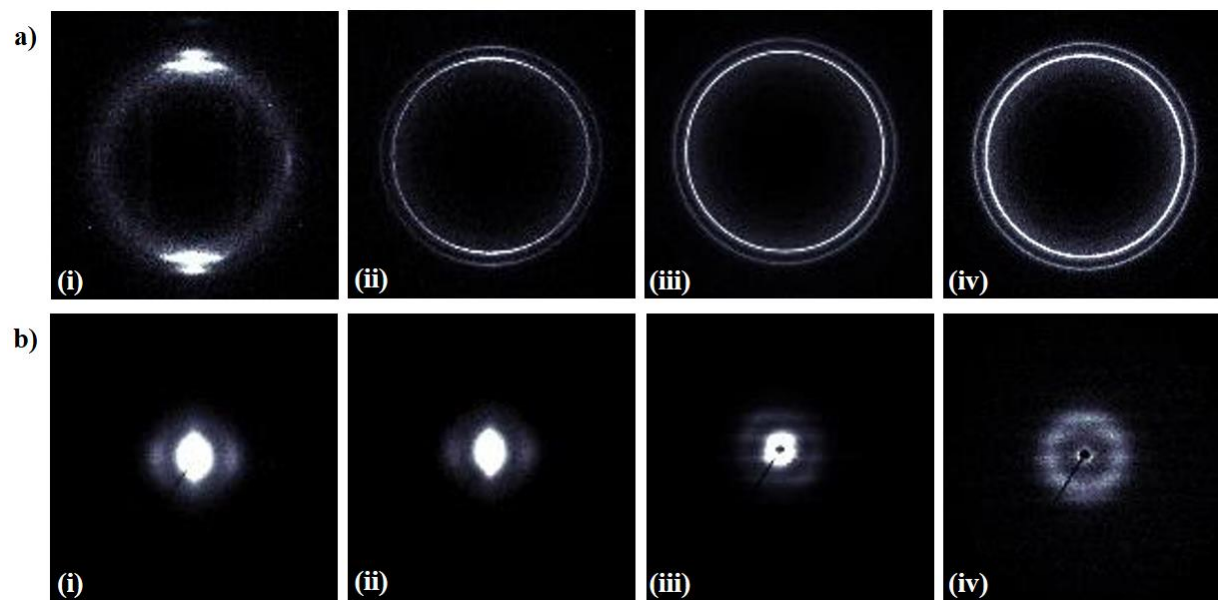


**Figure 4-12.** **a)** 2D WAXS patterns and **b)** SAXS patterns of **(i)** an oriented, electrospun 60:40, **(ii)** an oriented, hot compacted 60:40, **(iii)** an isotropic, electrospun 60:40, and **(iv)** an isotropic, hot compacted 60:40. The X-ray wavelength ( $\lambda$ ) is 1.5405 Å.

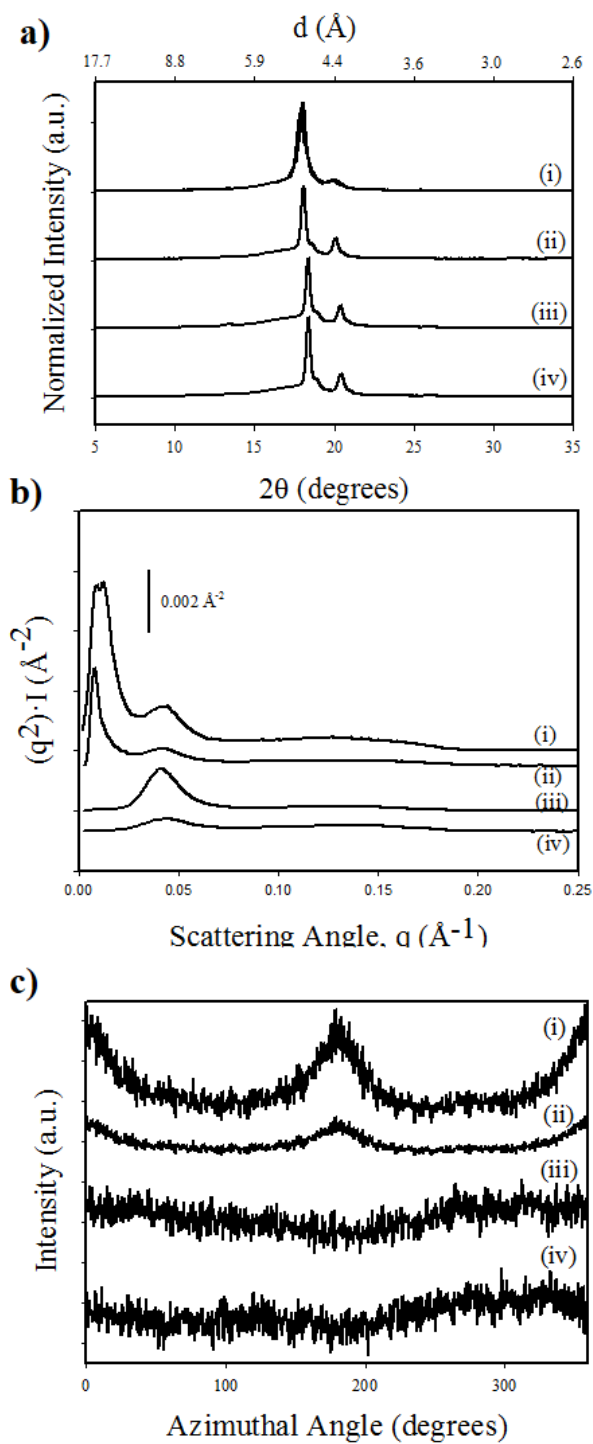


**Figure 4-13.** a) WAXS, b) SAXS, and c) azimuthal profiles ( $0$  and  $180^\circ$  = meridional) of (i) an oriented, electrospun 60:40, (ii) an oriented, hot compacted 60:40, (iii) an isotropic, electrospun 60:40, and (iv) an isotropic, hot compacted 60:40. The X-ray wavelength ( $\lambda$ ) is  $1.5405 \text{\AA}$ .

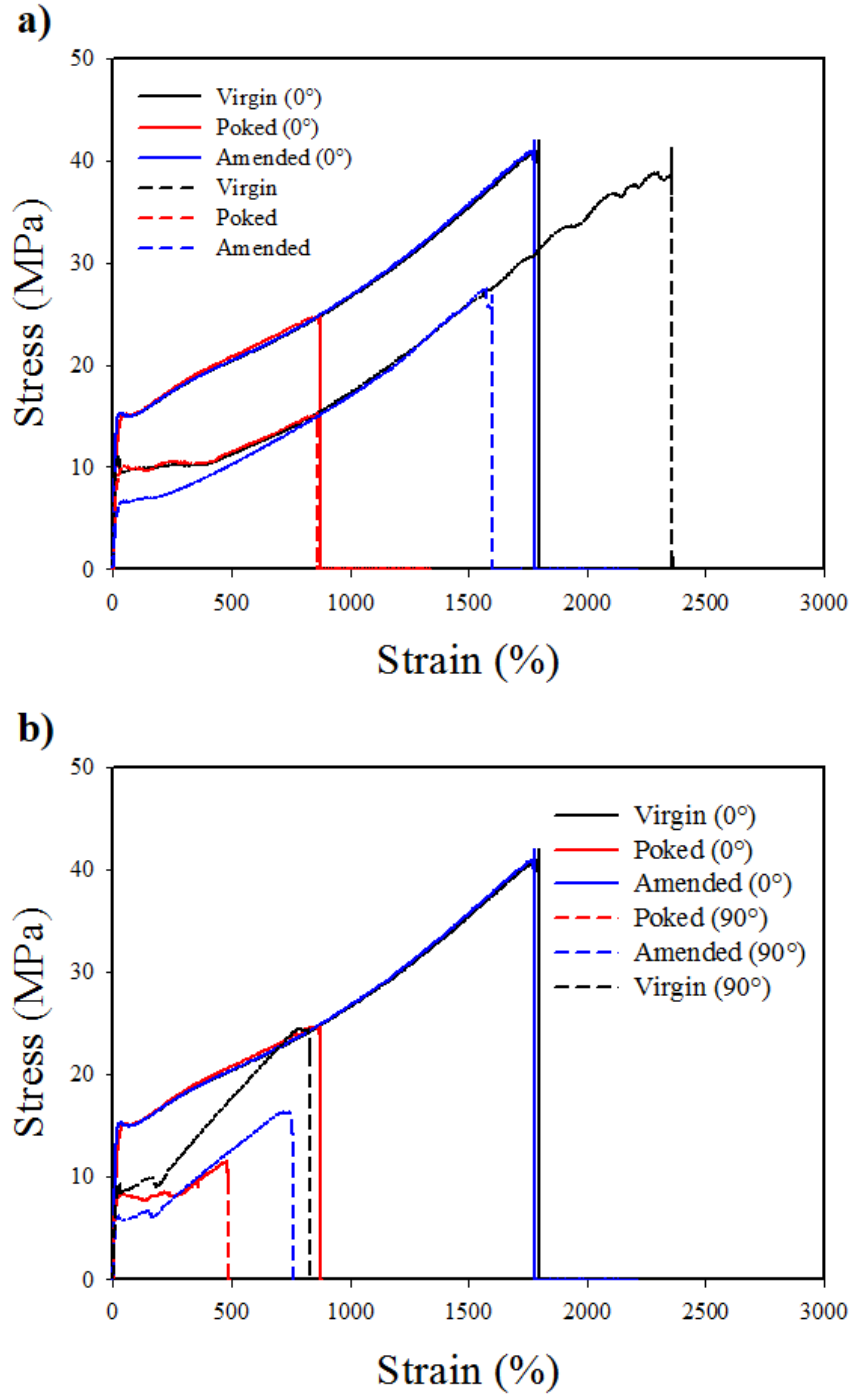


**Figure 4-14.** Stress vs strain curves for **a)** oriented 60:40 and isotropic 60:40 in comparison for the virgin, puncture damaged and healed states and for **b)** the virgin, puncture damaged and healed states of the sample whose stretching direction is parallel with fiber orientation (0°) and the sample whose stretching direction is perpendicular to fiber orientation (90°).

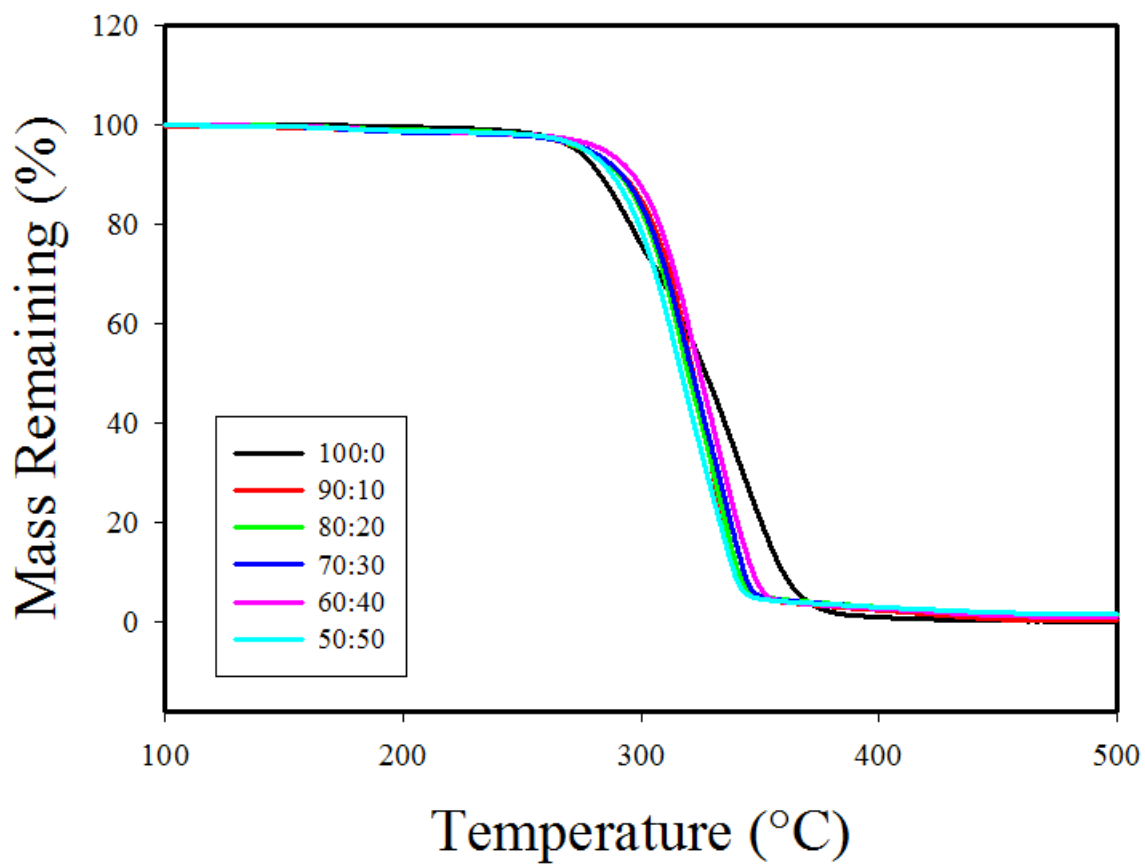


**Figure 4-15.** Thermogravimetric analysis (TGA) graph of electrospun fiber mats: 100:0 (black), 90:10 (red), 80:20 (green), 70:30 (blue), 60:40 (pink), and 50:50(F) (cyan).

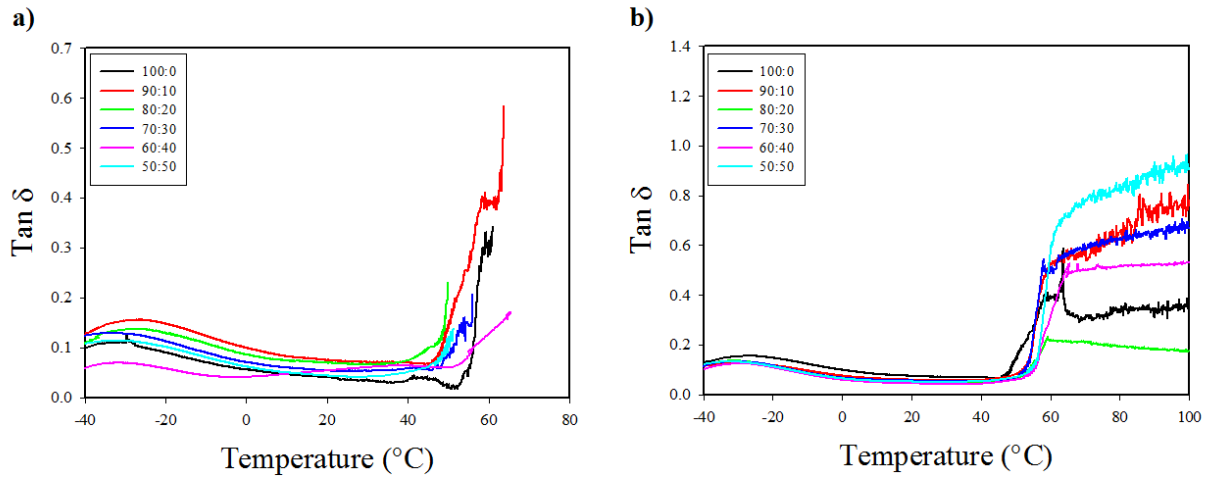


**Figure 4-16.**  $\tan \delta$  vs temperatures for **a)** electrospun fiber mats and **b)** hot compacted fiber mats, respectively: 100:0 (black), 90:10 (red), 80:20 (green), 70:30 (blue), 60:40 (pink), and 50:50 (cyan).

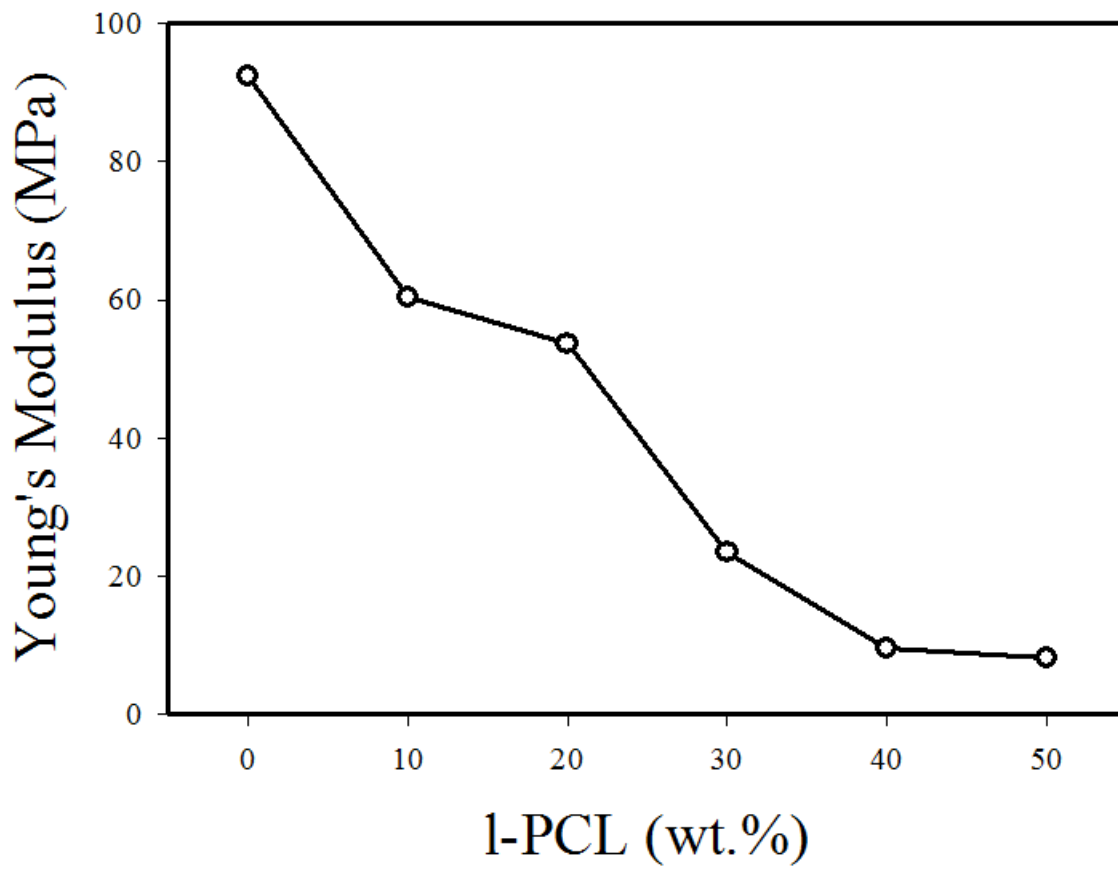


**Figure 4-17.** Young's Modulus (RT) vs 1-PCL wt. % content. Damage type is puncture.

## **Chapter 5: Design and Fabrication of Self-reversible Actuators via Electrospinning: Influence of Micro-geometry and Molecular Anisotropy**

### **5.1 Synopsis**

In recent years, thermal-responsive reversible actuation of polymer networks has attracted significant attention of researchers and technologists, alike, due to distinctive attributes of large actuation stroke and mechanical softness when compared to alternative approaches. However, the functional requirement of a constant externally applied load largely limits broader application of such actuation in robotics, biomedical engineering, and optical devices. In this chapter, a simple but adaptable approach involving electrospinning is developed to prepare a self-reversible bilayer actuator combining a two-way shape memory polymer (2W-SMP) and a thermoplastic elastomer, wherein the 2W-SMP exhibits temperature-triggering reversibility in shape changing under application of inherent stress from the elastomer. More specifically, micro-geometry and molecular anisotropy of such bilayer can be easily introduced and manipulated by varying several electrospinning parameters, ultimately yielding distinct actuation behavior. Excitingly, four representative actuators, including bending, flattening, twisting, and untwisting actuator, have been developed through creative manipulation of both micro-geometry and molecular anisotropy. The results show that all actuators revealed free-standing and reversible actuation upon heating/cooling cycles. A 131% increase in curvature from  $4.62 \text{ mm}^{-1}$  is achieved for bending actuator upon second heating at greater than  $50 \text{ }^\circ\text{C}$  while a 28% decrease in pitch length from 0.85 mm for twisting actuator upon second heating at greater than  $50 \text{ }^\circ\text{C}$ . More surprisingly, both flattening and untwisting actuator are capable of changing their programmed shapes to completely

flat state upon actuation, what we term as a “flattening actuator”. Cyclic tests demonstrate no significant deterioration of actuation for these actuators over multiple cycles.

## 5.2 Introduction

Demand has arisen rapidly for smart materials with the need emerging to develop and understand new functional products that are essentially composed of shape memory polymers (SMPs).<sup>1-4</sup> Such polymers possess the capacity to change their macroscopic configuration in response to environmental alteration (e.g. temperature),<sup>5,6</sup> attracting much interest of study both academically and industrially.<sup>7-10</sup> The shape memory (SM) effects in polymers can take two quite distinct forms: one-way shape memory (1WSM) and two-way shape memory (2WSM), the latter allowing temperature-triggered reversible actuation so long as a constant stress “bias” is applied to the material.<sup>11,12</sup> As a result, the applicability of 2W-SMPs for their use as reversible actuators has been reported, with authors attributing such reversible character, particularly and normally, to elongation upon cooling and contraction upon heating. However, an obvious hurdle that impedes broader application for these materials is the intrinsic requirement of externally applied force bias. We asked, can this bias be made *internal* to the material? In addition, applying external stress sometimes can be rather difficult especially when the dimensions of actuators are really small.<sup>13</sup> Therefore, a permanently applied external stress imposes a huge limitation for complex shape changing, and methods to attain free-standing reversible actuation are desired for a wide range of applications. To date, from a materials processing and fabrication point of view, two typical approaches have been developed and extensively used to tackle the aforementioned challenge: a molecular approach and a geometric approach.



In the former approach, the key to success is to ensure that skeleton-determining function and actuation function, on the molecular level, are well separated and sometimes interchangeable. Behl *et al* elaborated an ingenious method to make a free-standing, bidirectionally reversible polymer actuator in which one crystallizable domain with lower  $T_m$  is responsible for actuation while the other crystallizable domain with higher  $T_m$  determines the skeleton of actuator.<sup>14</sup> This skeleton provides a type of template – and associated macroscopic shape – for the crystallization of the second phase. A downside of this method is that two well spread melting transitions are necessary for quality two-way actuation. Along this line, instead of coupling two crystallizable domains with distinct  $T_m$ 's, Behl *et al* discovered that a single semicrystalline polymer network can carry both skeleton-determining- and actuation function as it provides a very broad melting transition span.<sup>15</sup> In this case, such broad melting transition allows the subdivision of the crystallites into two groups, one having a  $T_m$  closer to the lower end of bulk melting transition, thus serving as actuation domain, and the other revealing a  $T_m$  more towards the higher side so as to control the shape-shifting. Similar to the latter approach, Zhou *et al* reported on free-standing reversible behavior of an end-linked poly(octylene adipate) within which, at any partial molten state, both chemical network and crystalline skeleton can topographically constrain the polymer chains to direct the recrystallization process.<sup>16</sup> However, one major limitation for all methods involving partial melting is ultimate relaxation of yet-unmelted, constraint chains due to annealing at temperatures associated to partial melting. Moreover, this mechanism was extended to a poly( $\epsilon$ -caprolactone) (PCL) system comprising dual network architectures, which were achieved by further crosslinking the prior partially crosslinked polymer in a highly stretched state.<sup>17</sup> Here, the balancing of elastic stress of the

original, load-bearing portion with entropic stress of the lately formed portion resulted in an internal stress-induced crystallization upon cooling, finally contributing to reversible two-way actuation. It is noted that the actual actuation achieved in this approach might lack of consistency from batch to batch due to no precise control over relative degree of the first crosslinking to that of the second.

The second general approach involves creative geometric approaches. It has been pursued mostly through a laminate composite theory in which a geometric bias is established by combining two layers, one being a strained 2W-SMP with featuring excellent shape fixing and recovery, while, the other being a stress-free elastomer that provides the needed stress field for 2WSM behavior of SMP layer to occur. Chen et al designed and studied a shape memory polyurethane (SMPU) composite exhibiting 2WSM effect without the presence of external load.<sup>18,19</sup> More specifically, such a laminated composite was prepared by adhering a pre-strained PHA-based shape memory polyurethane to a fully relaxed elastic polyurethane (EPU), to finally yield a bilayer geometry featuring a metastable “state-of-ease”. This bilayer demonstrated the ability to bend towards SMPU upon heating and recover upon cooling reversibly at temperatures in the span from 25 °C to 60 °C. In the meantime, a polymeric laminate, in which a resin plate was attached to a carbon fiber-reinforced polymer plate with instant glue, was developed by Tamagawa to achieve free-standing reversible actuation.<sup>20</sup> Nonetheless, the methods involving use of adhesive of any kind have significant limitation in terms of manufacturing scalability and mechanical durability, not to mention the challenge of meeting dimensional requirements for glue to be applied properly. Another representative geometric approach for self-reversible actuation – from our own group – is based on the form of a bimorph wherein a preprogrammed

crosslinked poly(cyclooctene) (PCO) strip was embedded in an acrylate-based polymeric matrix, which can provide restoring stress on PCO core once photo-polymerized and cured completely.<sup>21,22</sup> Although this approach proved quite successful, we realized a couple significant drawbacks, including that SMP rips off from the matrix after several cycles due to absence of strong bonding in between SMP, that actuation performance deeply depends on both fabrication and integration of SMP in terms of local thicknesses, and also that there is a minimum thickness threshold for one layer relative to the other in order to present noticeable actuation, indicative of little possibility for small actuators.

To overcome the disadvantages of approaches above, we proposed a simple but more adaptable strategy of developing miniature, self-reversible actuators via a sequential electrospinning technique.<sup>23,24</sup> Here, electrospinning is a fabrication process of applying electric force to draw continuous fibers with diameters in the range from nanometers to micrometers. The often-untapped benefit of electrospinning is that the molecular anisotropy introduced in high spinning speeds can improve the recovery force of SMP to an extreme extent along the direction of fiber axis.<sup>25-27</sup> Consequently, increasing the difference between elastic stress of the matrix and entropic stress of SMP can greatly contribute to amplifying the two-way actuation. Besides, electrospinning offers superior convenience for producing desirable micro-geometry, specifically, a bilayer geometry in this work, through programmed, sequential deposition of each component. We postulate that strong bonding could be achieved at the interface between two layers due to the entanglement of fibers and short-range adhesion promoted through diffusion of “wet” fibers as they deposit. For polymer composition, we selected a latent crosslinkable PCL-based polyurethane (x-PU), developed elsewhere in this dissertation, with a low  $T_m$  acting as the shape fixing phase, and a thermoplastic polyurethane (Pellethane® 5863-80A) with a high  $T_m$  serving as the stress

restoring phase. On the one hand, in view of our prior work, it is well demonstrated that the x-PU allows not only formation of delicate fibers through facile solvent processing, but also latent crosslinking to network which enables good 2WSM behavior.<sup>28</sup> Moreover, our preliminary study proves the capability of this particular Pellethane to construct fine fibers via ordinary electrospinning process. Our fabrication approach was first to create the first layer by electrospinning a certain amount of x-PU containing thermal initiator at a high collector rotation speed to engender fiber and molecular orientation. Next, a second layer was formed on top of the first by electrospinning the same amount of Pellethane at comparatively low collector rotation speed to yield an unoriented elastomeric fibrous layer. For comparison, we also prepared samples in which the x-PU was unoriented while the Pellethane was oriented, expecting that this sample change would bring about distinct actuation behavior. We next cured the electrospun composites thermally through hot compaction while a metal spacer was used to control thickness as well as to prevent relaxation (shrinkage) particularly along the direction of fiber axis. Finally, rectangle specimens were cut from the electrospun bilayer sheets at different angles between the fiber orientation and the specimen long axis. This was to enable more complex self-reversible actuations, such as twisting. Microstructural, thermal, mechanical, and shape memory properties were characterized, to aid in better understanding the mechanisms for various actuation phenomena. Last but not least, we demonstrated four principal actuations visually, including bending, flattening, twisting and untwisting actuator, by videotaping the bench experiments, following which both qualitative and quantitative analyses were performed.

## **5.3 Experimental**

### **5.3.1 Materials**

The latent crosslinkable PCL-based polyurethane (x-PU,  $M_{n,PCL}$  of 3,000 g/mol) was synthesized by condensation polymerization method described in our previous work.<sup>28</sup> The thermoplastic polyurethane (Pellethane® 5863-80A) was received from Lubrizol and used as is. Dilauroyl peroxide (DLP, Luperox® LP, 97%) and *N, N*-Dimethylformamide (DMF, anhydrous, 99.8%) were purchased from Sigma-Aldrich. Chloroform and tetrahydrofuran (THF) were purchased from Fisher Scientific.

### 5.3.2 Preparation of Electrospun Bilayers

As a preparation for electrospinning process, 2.0 g x-PU and 61.9 mg (~3 wt. %) DLP were dissolved in a mixture of 8.0 mL chloroform and 4.0 mL DMF, while, 2.0 g Pellethane in a mixture of 12.0 mL THF and 8.0 mL DMF (Table 5-1). Both solutions were kept at 37 °C with constant stirring until dissolution completion.

A schematic showing the fabrication process for electrospun bilayers is presented in Scheme 5-1. As a representative example, we specify the fabrication of Bilayer01 here. This process simply takes two steps using a custom electrospinning set-up that has been reportedly utilized (Scheme 5-1):<sup>29</sup> in step 1, the x-PU solution was ejected through the 22 Gauge needle at a flow rate of 1.5 mL/h for 6 h with the needle being held at a potential of 16.0 kV, during which the tip-to-collector distance was set at 10 cm and the rotation speed of a 57.1 mm collecting mandrel was maintained at 400 rpm while the drum was held at a potential of 0.5 kV; in step 2, the x-PU solution, which was supplying the ejecting needle, was substituted by the Pellethane solution. Henceforth, the rotation rate was boosted up to 2,000 rpm and the higher potential was decreased from 16.0 kV to 14.0 kV, all employed for the duration of the 10-h electrospinning process, while all other conditions remained

unchanged (Table 5-2). The resulting fibrous web was finally vacuum-dried at room temperature for 2 d, revealing the structure of a bilayer with an approximate x-PU-to-Pellethane w/w ratio of 50:50. In contrast to Bilayer01, Bilayer02 was generated the way where the x-PU solution was electrospun under a rotation speed of 2,000 rpm while the Pellethane solution at 400 rpm. All other parameters were kept comparable to Bilayer01. Note that the fiber orientation introduced at high rotation speed always aligns in the direction in which the collecting mandrel rotates; i.e., in the “hoop” or circumferential direction.

The dried electrospun bilayers (i.e. Bilayer01 and Bilayer02) were then cured thermally by the following method. A rectangle sample was first cut and sandwiched between two mold release agent (Pol-Ease®2300, Polytek) coated, polished stainless steel sheets separated by a 0.30 mm thick stainless steel spacer, which lay atop the perimeter of the sample, acting as “clamps and anchors” to prevent fiber relaxation and contraction. The sample was held at 90 °C under a pressure of 1,000 psi for 2 h to achieve complete curing. The resulting specimen was finally taken out of the mold and the edges squeezed by the spacer were cut away after the specimen was cooled to room temperature.

To visualize and compare structural geometry of electrospun bilayers before and after thermal curing, scanning electron microscopy (SEM) was conducted using a JEOL JSM-5600 microscope under an accelerating voltage of 5 kV. Both cured bilayers were gold-sputtered for 60 s prior to imaging. Also, to study and ascertain molecular orientation, wide angle X-ray scattering (WAXS) analysis was performed using a Rigaku S-MAX3000 for both bilayers before and after thermal curing. A Rigaku MicroMax-002+ generator was operated under an accelerating voltage of 45 kV and a current of 0.88 mA to yield a collimated beam of Cu *K $\alpha$*  X-rays with a wavelength of 1.5405

Å. Scattering patterns were collected (see below) for 30 min. The sample-detector distance was fixed at 120.7 mm, yielding scattering angles  $3^\circ < 2\theta < 40^\circ$ . WAXS images were obtained and analyzed using a FujiFilm FLA7000 reader (with Fujifilm image plates CR HR-V) and SAXSgui software v2.03.04.

### 5.3.3 Thermal, Dynamic Mechanical, and Shape Memory Analysis

A TA Instruments Q500 was used for the thermogravimetric analysis (TGA) of both bilayers so as to estimate the actual composition of each. A small amount (5-10 mg) of sample was loaded and heated from 25 °C to 600 °C at a rate of 10 °C/min in an atmosphere of nitrogen. Mass percentage for each component in the bilayer was determined using the following equations:

$$w_{Pellethane}^{TGA}(\%) = \frac{\Delta M_{Pellethane}}{\Delta M_{Pellethane}^{Neat}} \times 100 \quad (1)$$

$$w_{x-PU}^{TGA}(\%) = 100 - w_{Pellethane}^{TGA} \quad (2)$$

Here,  $w_{Pellethane}^{TGA}$  is the TGA-based weight percentage of Pellethane in the bilayer,  $w_{x-PU}^{TGA}$  is the TGA-based weight percentage of x-PU in the bilayer,  $\Delta M_{Pellethane}$  is the mass loss (percentage of characteristic stage) of Pellethane in the bilayer, and  $\Delta M_{Pellethane}^{Neat}$  is the mass loss of neat Pellethane.

In the meantime, differential scanning calorimetry (DSC) was employed for the same purpose and then comparison with TGA. Samples weighing approximately 5 mg was first heated to 160 °C at 10 °C/min and cooled to -60 °C at 10 °C/min. Subsequently, a second heating was executed at 10 °C/min to 160 °C. The glass transition temperature ( $T_g$ , the step of heat flow), melting transition temperature ( $T_m$ , the peak of the endotherm), and the

enthalpy of melting ( $\Delta H$ , area beneath endothermic peak) were recorded, respectively, on the basis of second heating curve (to minimize the effects of thermal history). The composition for each component was presumably calculated using the equations below

$$w_{x-PU}^{DSC}(\%) = \frac{\Delta H_{x-PU}}{\Delta H_{x-PU}^{Neat}} \times 100 \quad (3)$$

$$w_{Pellethane}^{DSC}(\%) = 100 - w_{x-PU}^{DSC} \quad (4)$$

where  $w_{x-PU}^{DSC}$  is the DSC-based weight percentage of x-PU in the bilayer,  $w_{Pellethane}^{DSC}$  is the DSC-based weight percentage of Pellethane in the bilayer,  $\Delta H_{x-PU}$  is the melting enthalpy of x-PU portion in the bilayer, and  $\Delta H_{x-PU}^{Neat}$  is the melting enthalpy of neat x-PU, which is 51.76 J/g. We recognize that this is a rough estimation due to the assumption that x-PU would crystallize identically regardless of the presence of Pellethane phase.

A TA Instruments Q800 Dynamic Mechanical Analyzer (DMA) was adopted to explore the thermomechanical properties and also to ensure success of crosslinking x-PU in both bilayers. Note that neat crosslinked x-PU and neat Pellethane were examined for comparison purpose. In the multi-frequency controlled-strain mode each sample was equilibrated at -60 °C, held isothermal for 10 min, and heated continuously up to 160 °C at 3 °C/min. An oscillating amplitude of ca. 20  $\mu$ m, a preload force of 0.001 N, and a force track of 125% were utilized. Rectangle shaped samples with an approximate length-to-width ratio of 4:1 were used for testing.

To study 2WSM behavior of the two cured bilayers under externally stress-free conditions, dog bone shaped sample (ASTM D63 Type IV, scaled down by a factor of 4) were tested using DMA in controlled force mode in the following procedures: each specimen was (1) heated at a rate of 2 °C/min to 80 °C without applying external force except a preloading force of 0.001 N, (2) then



cooled to  $-20\text{ }^{\circ}\text{C}$  at  $2\text{ }^{\circ}\text{C}/\text{min}$ , and (3) reheated to the initial elevated temperature at  $2\text{ }^{\circ}\text{C}/\text{min}$ . The lengths were recorded as a function of temperatures while these steps were performed three times in succession. This investigation merely serves as a rough prediction to free-standing reversible actuation of both cured bilayers since that DMA only measures tensile displacement at various temperatures while both bilayers actuate laterally instead of uniaxially. Moreover, the effect of heating/cooling rate on thermal hysteresis was beyond the scope of this work.

### **5.3.4 Fabrication and Characterization of Actuators**

The fabrication method for each of four principle actuators is described as follows. First, the bending and the twisting actuators were prepared from the cured Bilayer01, and with the geometry shown in Scheme 5-2 and in Scheme 5-3, respectively. The major difference between these two actuators is how they were sectioned from the bulk bilayer sheet in terms of molecular and fibrous anisotropy. For the bending actuator, a rectangle strip was cut from the bulk sheet to have dimensions of  $0.88\text{ mm} \times 0.69\text{ mm} \times 0.20\text{ mm}$  (x-PU layer of  $0.09\text{ mm}$  and Pellethane layer of  $0.11\text{ mm}$ , image analysis of SEM image by ImageJ software, number of measurements: 50) with its longitudinal direction aligning with fiber orientation. In contrast, for the twisting actuator, a  $2.56\text{ mm} \times 0.48\text{ mm} \times 0.23\text{ mm}$  (x-PU layer of  $0.12\text{ mm}$  and Pellethane layer of  $0.11\text{ mm}$ ) rectangle, whose length is  $45^{\circ}$  to fiber orientation, was cut. Note that upon cutting we observed the strip to curl naturally to some extent towards Pellethane side, which we attributed to elastic recovery of oriented Pellethane fibers. On the other hand, the cured Bilayer02, in which x-PU layer was prepared to be oriented and the Pellethane layer was prepared to be unoriented, was utilized to make the flattening actuator and the untwisting actuator, as specified in Scheme 5-4 and in Scheme 5-5, respectively. The flattening actuator was sectioned the same way as was the

bending actuator while the untwisting actuator followed how the twisting actuator was developed. For actuator geometry, the dimensions were measured, correspondingly, to be  $1.71 \text{ mm} \times 0.88 \text{ mm} \times 0.07 \text{ mm}$  for flattening actuator and  $3.27 \text{ mm} \times 0.41 \text{ mm} \times 0.07 \text{ mm}$ , both revealing a Pellethane layer of  $0.03 \text{ mm}$  and a x-PU layer of  $0.04 \text{ mm}$ . The flattening actuator tended, upon cutting, to curl inherently towards the Pellethane side, which we attribute to the same cause as the bending actuator. However, the untwisting actuator had no obvious curling tendency in the first place.

To investigate and demonstrate the free-standing reversible actuation of all the actuators stated above, two water baths stabilized on a laboratory bench, one with a steady temperature of  $58 \text{ }^\circ\text{C}$ , which is well above the  $T_m$  of x-PU but below that of Pellethane, and the other at ca.  $0 \text{ }^\circ\text{C}$  which would adequately allow full crystallization of x-PU. Next, each actuator was heated in the hot water bath for 5-10 s, leading to a shape change, and then submerged in cold water bath for 5-10 s for shape reversal. During this sequence of steps (termed “actuation cycle”) no external stress was applied and pictures were taken to record the shape evolution. Such an actuation cycle was completed several times in succession to examine the quality of reversibility. To quantify the magnitude of actuation for both bending and flattening actuator, curvatures ( $\mathcal{K}$ ) at the initial, actuated, and reset state during the first and the second cycle were determined from photographs taken at each of these states. The curvature was calculated from the radius obtained by using ImageJ (the actual length was calibrated using the ruler in the photograph and pixels in the photograph was employed to measure curvature). Likewise, helical radius ( $\mathcal{R}$ ) along with helical pitch ( $\mathcal{P}$ , the spacing of one complete helix turn) were measured using the image analysis described at each of the three aforementioned states during the first and the second cycle for the twisting and untwisting actuators, respectively. Moreover, video was recorded for several self-reversible

actuation cycles for each individual actuator. Finally, hypothesized mechanisms for bending and flattening actuation phenomenon were postulated and will be discussed below.

## **5.4 Results and Discussion**

### **5.4.1 Preparation of Electrospun Bilayers**

In this work, we creatively have taken advantage of electrospinning technique to prepare small, soft bilayers with micro-geometry and molecular anisotropy, both playing profound roles in achieving fully free-standing reversible actuation. As previously described, two representative electrospun bilayers, Bilayer01 and Bilayer02 which exhibited different distributions of molecular anisotropy throughout layers, were fabricated via our custom electrospinning strategy. The surface morphology and cross-sectional structure for Bilayer01 and Bilayer02 were studied using SEM, as compiled in Figure 5-1. In particular, as for Bilayer01, Figure 5-1(a) and (b) reveals that fibrous structure of Pellethane before and after thermal curing, revealing that Pellethane preserved a fibrous structure after heat was applied, though relaxed slightly (in orientation) from the initial highly tensioned state. In contrast, the randomly oriented x-PU fibers (Figure 5-1(c)) turned into a crosslinked, solid film (Figure 5-1(d)) when heated above  $T_m$ . Given that the orientation of Pellethane fibers was not so obvious according to SEM imaging, WAXS analysis was conducted to better understand molecular orientation for the Bilayer01 sample. In Figure 5-2(a), an isotropic diffraction pattern was found for the uncured sample, indicating a lack of orientation for the crystalline. We speculate that it was due to the fact that, in this scenario, the oriented Pellethane fibers comprised little crystallinity so that the highly crystalline x-PU fibers, possessing no principal orientation, dictated the WAXS pattern predominately.

Interestingly, though, we observed that the azimuthal spread of the pattern divided into two bands which were close to the meridional (horizontal) axis after crosslinking, as the principal orientation of the Pellethane fibers is supposedly along such axis (Figure 5-2(c)). This change in WAXS pattern was attributed to be the root of rearrangement of the x-PU chains into the alignment in the equatorial (vertical) axis while the oriented Pellethane fibers were imposing compressive stress. This finding is in good agreement with previous observation by SEM investigation and is clearly shown via the azimuthal scans shown in Figure 5-3, where uncured Bilayer01 sample rendered no noticeable peaks. Intensity maxima (and thus indication of orientation) grew dramatically at  $0^\circ$  and  $180^\circ$  corresponding to the meridional axis once thermal curing was completed. Furthermore, the cross-sectional view of cured Bilayer01 sample (Figure 5-1(e)) lend a strong support to our speculation on the peculiar structure of a bilayer as a result of thermal curing, which was composed of the x-PU layer (right side) and the Pellethane layer (left side) along with tightly bonded interfaces in between. This is particularly germane to our actuator design, which requires coordination of moduli mismatch between the two contacting layers to achieve highly robust self-reversibility for the actuators without requiring use of adhesive or other special treatments.<sup>30-32</sup> The latter would increase manufacturing cost and complicate production procedures.

Along this line, the similar analysis was performed on the Bilayer02 samples. As expected, molecular anisotropy of the x-PU fibers prior to crosslinking was readily apparent, as shown in Figure 5-1(i). Interestingly, fiber orientation was well maintained during thermal crosslinking, yielding preservation of molecular anisotropy from the original state, as shown in Figure 5-1(j). This is consistent with WAXS observations: Figure 5-2(b) indicates strong orientation in the

meridional axis due to the highly crystalline x-PU fibers, and such orientation was lost to some degree because of the melting and relaxing of x-PU fibers during cure (Figure 5-2(d)). The associated azimuthal scanning profiles showed, for the uncured sample, two large, broad peaks at 90° and 270° which correspond to the equatorial axis, and that the intensity of these peaks were vastly reduced for the cured sample, both supportive of the statement above (Figure 5-3). Note that the molecular orientation of Bilayer02 was exactly 90° off comparing to that of Bilayer01, which helps to explain the difference in orientation axis between the two bilayers. Unlike Bilayer01, the as-spun Pellethane fibers in Bilayer02 appear to be quite isotropic and also in a very loose form (Figure 5-1(g)) because low rotation speed of collecting mandrel that was implemented during electrospinning process. More surprisingly, the loosely distributed Pellethane fibers became stretched upon the thermal crosslinking step as the outcome of balancing its elastic recovery with the tension from the aligned x-PU fibers (Figure 5-1(h)). The particular structure of fiber-film bilayer was evident with its cross-section imaged in Figure 5-1(f).

#### **5.4.2 Thermal, Dynamic Mechanical, and Shape Memory Analysis**

The results of the thermal characterization experiments are shown in Figure 5-4 and 5-5. Figure 5-4 shows the thermal degradation profiles for the bilayers and their neat constituents, as determined using TGA. Neat Pellethane has a characteristic of a two-stage degradation behavior, with the first stage occurring between ca. 300 °C and 350 °C along with a mass loss of ca. 20% while approximately 70% mass was lost in the second stage extending to over 400 °C. In contrast, neat x-PU features a degradation of one single, continuous step, and with barely no remaining mass left after that. Even though the degradation profiles of the two neat polymers have some overlap, the prominent difference allowed us to roughly assess the actual composition of the bilayer samples using eqn. (1)

and (2). Hence, Bilayer01 and Bilayer02 were found to consist of 45.6 and 60.4 wt. % x-PU, respectively (Table 5-3). For a similar and comparative purpose, DSC experiments were conducted on the same samples. As such, DSC heat flow profiles as a function of temperature are shown in Figure 5-3 (complete profiles are available in Figure 5-6), for the cured bilayers and constituent polymers. It was found that neat Pellethane has a  $T_g$  at ca. -15 °C and a  $T_m$  at ca. 140 °C while neat x-PU possesses a  $T_m$  at ca. 46 °C only. Therefore, both Bilayer01 and Bilayer02 “inherited” three thermal transitions from the two pure polymers despite variation in magnitude of the step change or endothermic peaks. The melting enthalpy of x-PU in each bilayer was adopted to calculate its corresponding weight content, based on that of neat x-PU, using Eqn. (3) and (4). As a result, 49.1 and 59.3 wt. % x-PU were incorporated in Bilayer01 and Bilayer02, respectively, roughly consistent with the estimation by TGA analysis. Broadly speaking, the actual composition was not significantly different from the prescribed composition of 50 wt. % x-PU in bilayer, indicating reasonably good processing reliability and also as an important guidance for interpretation of actuation phenomena.

To determine linear viscoelastic mechanical properties and their temperature dependences, DMA experiments were conducted. The tensile storage modulus ( $E'$  measured at  $f=1$  Hz) is plotted for the investigated temperature range for the two bilayers and two neat polymers (Figure 5-7). We realize that there exists the asymmetry in both geometry and modulus for either of bilayer, which implies no direct correlation between such tensile data and actual actuation behavior. Nevertheless, it was observed that the  $T_g$  of Pellethane and  $T_m$  of x-PU, which are represented by drastic drops in storage modulus, matched with what has been determined by DSC experiments. However, it proved very

difficult to determine the  $T_m$  of Pellethane by looking for its corresponding modulus decrease, primarily because of the occurrence of lateral actuation here (the sample was contracting *during* the DMA experiment). Note that all  $T_m$ 's detected by DMA might appear to be slightly higher than those by DSC since that a small oscillating force and a low heating/cooling rate were applied in DMA tests.<sup>33-35</sup> Besides, the traces in Figure 5-7 indicate that the storage modulus over the -55 °C to 50 °C temperature range in an order of neat x-PU > Bilayer02 > Bilayer01 > neat Pellethane. This order agrees with prior composition evaluation by thermal characterization experiments, given the fact that Bilayer01 contains less of more crystalline x-PU as compared to Bilayer02. Furthermore, both cured bilayers revealed a storage modulus smaller than 100 MPa at temperatures in the 0 – 50 °C span so as to be considered as soft materials in terms of their potential application for biomedical devices.<sup>36</sup>

Moving on to characterization of actuation behavior, here constrained to in-plane deformations constrained in a DMA fixture. Figure 5-8(a) and (b) show the tensile two-way actuation under stress-free condition for the cured Bilayer01 and cured Bilayer02, respectively. The two-way actuation cycles for both bilayers were only evaluated qualitatively, here, for the reason that DMA analysis of shape memory is limited to uniaxial displacement and cannot be used to quantify the lateral bending/curling intrinsic to the new materials. Surprisingly, both bilayer samples underwent *compressive* 2WSM effect featuring the cooling-induced contraction and heating-induced extension, which is quite the opposite of conventional 2WSM behavior. Considering the presence of thermal hysteresis, neither the contraction nor the extension was due to normal thermal expansion effects. Also, by testing each neat polymer (i.e. Pellethane and crosslinked x-PU) individually, the crosslinked semicrystalline x-PU certainly contributed to this reversible behavior

while the Pellethane was solely providing an internal compressive stress to the x-PU (Figure 5-9). We postulate that the crystallization of x-PU under a compressive stress gave rise to additional contraction that was reversed upon heating through  $T_m$ , with a thermal hysteresis of approximately 28 °C when a heating rate of 3 °C/min was used.<sup>37</sup> In addition to that, molecular anisotropy played a critical role in this special reversible shape memory effect and that will be discussed specifically later in this chapter. Concerning the quality of 2WSM in compression, moderate mechanical “creep” in uniaxial length was seen for either bilayer. This “drawback” was attributed primarily to the lightly crosslinked elastomer, Pellethane, which contributed similar “creep” in strain through several cool-heat cycles with absence of external force except a preloading force of 0.001 N (Figure 5-9(a)). However, we realized that the small preloading force was still a nontrivial factor impacting the sample while actual use of the free-standing actuators would feature no external force. Thus the “creep” might not be significant as it is during testing by DMA. In a similar manner, because DMA confines the motion of the bilayers only along uniaxial direction, the actuation of x-PU, which changes its shape much more dramatically, might drive the Pellethane through elastic domain into plastic domain, wherein Pellethane deformed irreversibly to some extent.

### 5.4.3 Self-reversible Actuators

The demonstration of various self-reversible actuators was done by taking snapshots and videos of bench work in hot/cold water, followed by image analysis to quantify each actuation. Based on the cured Bilayer01, the bending actuator and twisting actuator were designed and made accordingly using the method described earlier in this article. The results for these actuators are summarized in Figures 10 and 11. In particular, the two-way actuation of bending actuator was captured at its initial, actuated, and reset states, as indicated in Figure 5-10(a). This actuator, which intrinsically curled (as cut) towards the



Pellethane side with a curvature ( $\mathcal{K}$ ) of  $3.16 \text{ mm}^{-1}$ , curled intensely in the same direction upon first heating-induced actuation, yielding an enclosed cylinder shape with a  $\mathcal{K}$  of  $10.41 \text{ mm}^{-1}$ . (We considered coating one side a distinct color, but the actuators are very thin and some of them are translucent this was not helpful.) The bending actuator was then cooled in a cold-water bath set at  $0 \text{ }^\circ\text{C}$  and – importantly – responded by significantly uncurling to a film with curvature,  $\mathcal{K} = 4.62 \text{ mm}^{-1}$ . We reasoned that the change in curvature during the first actuation cycle was impacted by thermal-mechanical processing history, as the sample was not thermally treated after processing before this test. This note applies to all remaining actuators in this work. Beyond this first cycle, the actuation/resetting procedures were repeated immediately, revealing that  $\mathcal{K} = 10.66 \text{ mm}^{-1}$  on heating and  $\mathcal{K} = 4.69 \text{ mm}^{-1}$  on cooling. Henceforth, it was evident that reversible bending actuation was achieved with good repeatability. More cycles were followed and quantified here (Figure 5-10(b)), but not recorded in the video. However, by inspection, no significant variation in curvatures for the hot and cold steps (relative to earlier iterations) was noticed. Furthermore, the associated video for entire reversible actuation is available in Video 5-1, where super-rapid, highly repeatable free-standing reversible actuation was observed. Similarly, the actuation of twisting actuator was recorded step by step as shown in Figure 5-11(a). This actuator was initially in a form of helix with a helical radius ( $\mathcal{R}$ ) of  $0.22 \text{ mm}$  and a spiral pitch ( $\mathcal{P}$ ) of  $1.56 \text{ mm}$ , turning to a more twisted helix that has a  $\mathcal{R}$  of  $0.15 \text{ mm}$  and a  $\mathcal{P}$  of  $0.60 \text{ mm}$  once heated through x-PU's  $T_m$  to  $55 \text{ }^\circ\text{C}$ . Upon cooling to  $0 \text{ }^\circ\text{C}$ , the actuation un-curled and lengthened through pitch extension. In particular, the radius and pitches reversed their actuation direction to dimensions of  $0.17 \text{ mm}$  and  $0.85 \text{ mm}$ , respectively. The same behavior ( $\mathcal{R}$  increased from  $0.15 \text{ mm}$  at  $55 \text{ }^\circ\text{C}$  to  $0.17 \text{ mm}$  at  $0 \text{ }^\circ\text{C}$  while  $\mathcal{P}$  increased from

0.61 mm at 55 °C to 0.85 mm at 0 °C) was observed during the second cycle, indicating high repeatability with almost no shape memory being lost. A further visual demonstration can be found in Video 5-2.

As stated previously, the flattening actuator and untwisting actuator were built upon the cured Bilayer02. It is important that the nature of the state of stress of the oriented x-PU causes flattening instead of curling. In contrast to the bending actuator, the flattening actuator has an inherent curling trend towards the Pellethane side, which was changed into a completely flat shape when shape recovery of x-PU and elastic recovery of Pellethane were equilibrated explicitly upon heating (Figure 5-12(a)). Upon heating to 58 °C, the sample flattened, with  $\mathcal{K}$  decreasing from 2.77 mm<sup>-1</sup> (room temperature, as cut) to ca. 0 mm<sup>-1</sup> (basically flat state), indicating a significant actuation from the largely curled state to the flat state upon a single thermal trigger. Upon cooling, the flattened sample returned to its curled state. The duration of a couple reversible actuation cycles was documented in Video 5-3. Last but not least, the two-way reversible actuation of untwisting actuator was investigated and reported in Figure 5-13. Unlike the flattening actuator, this actuator was nearly flat before activated for the first time, which could be due to the deviation of molecular anisotropy distribution across the whole bulk sheet. Then, identical heat/cool program was run for several times and the first two of them were quantified by measuring the corresponding  $\mathcal{R}$  and  $\mathcal{P}$  at various states. The results indicated that the sample coiled up upon the first cooling to have a  $\mathcal{R}$  of 0.29 mm and a  $\mathcal{P}$  of 0.99 mm, then untwisting and returning back to utterly flat and untwisted shape upon the second heating, and forming the spiral shape again upon second heating. This unprecedented stress-free reversible actuation

was videotaped to better reveal how fast the shape actuation and shape resetting were attained (Video 5-4).

In light of related literatures, we recognized that solutions to the large deflection of a thin plate or laminate can be used to generally describe the actuation behavior of our actuators based on a structure of bilayer, using the equation in the following:  $EI = Ebh^3/12$ , where  $EI$  stands for bending rigidity,  $E$  for Young's modulus,  $h$  for thickness, and  $b$  for width.<sup>38-40</sup> Therefore, in order to optimize the actuation performance for each actuator, these parameters must be tuned in coordination appropriately as they have great influence in either the x-PU layer or the Pellethane layer. However, the exploration of performance optimization was beyond the scope of the present work.

#### **5.4.5 Actuation Mechanism**

An actuation mechanism for the bending actuator is hypothesized and illustrated in Scheme 5-6. Prior to the first heating-induced actuation, the highly oriented Pellethane fibers are represented by the straight blue lines, pointing in the longitudinal axis of rectangle sample. Here, I describe the development of internal stresses and associated orientations during bilayer manufacturing and then during actuation cycle testing. Following electrospinning, the Pellethane fibers have a profound tendency to contract via elastic recovery after releasing from the collecting drum, which leads to shrinking along the principal fiber axis. However, the crosslinked semicrystalline x-PU layer resists such tendency of the Pellethane leading to mechanical equilibrium between the two layers, with each in a state of stress. In particular, the Pellethane contraction applies a compressive stress to the x-PU layer (and constituent fibers), which results in the formation of x-PU crystallites

that align width-wise as highlighted in red when the bilayer is being cured at a prescribed elevated temperature. This hypothesis was firmly supported by the observation in SEM and WAXS studies (Figure 5-1, Figure 5-2(a) and (c)). Upon heating to a temperature  $T_{m,x-PU} < T < T_{m,Pellethane}$ , the x-PU crystallites melt fully and become absolutely amorphous. It is known that in amorphous state polymer chains typically take much more space than in the crystalline state where they are packed closely in a high order. From a macroscopic viewpoint, the x-PU layer elongates dramatically in the direction of the Pellethane fiber axis due to the melting event, while the Pellethane fibers are not affected except the minor thermal expansion. Consequently, the bending actuator curls significantly towards the Pellethane side. In the following cooling step, the x-PU crystallites are re-established with a principal orientation which is perpendicular to the fiber axis of Pellethane, as before heat-triggered actuation. We postulate that this hypothesized mechanism applies to the actuation of twisting actuator.

Along similar lines, Scheme 5-7 elucidates the potential mechanism for the flattening actuator. In this actuator design, the molecular anisotropy of x-PU was intentionally introduced through the process of electrospinning, aligning along the longitudinal direction of specimen. On the contrary, the Pellethane fibers were processed to be unoriented, but still exhibit a nontrivial shrinking tendency in all directions, including the direction of x-PU's molecular orientation. Upon heating beyond the x-PU melting transition, the oriented x-PU phase melts and contracts in the direction of original orientation. Here, two main factors are probably in play, which engender such contraction of x-PU: (1) volumetric considerations discussed above; (2) compressive stress from the Pellethane fibers. Due to the permanent, covalent crosslinks, the x-PU crystallites are formed again in the original orientation, upon cooling below  $T_m$  of x-PU, in accordance with the

permanent shape of x-PU. Likewise, the actuation of untwisting actuator can be interpreted on this basis. However, note that we have no other direct evidence, thus far, to back our hypothesized mechanisms beyond the results obtained in SEM and WAXS experiments (Figure 5-1, Figure 5-2(b) and (d)). We recommend development and experimental validation of a theoretical model of the type applied previously by H. Qi and coworkers<sup>21,22</sup> to test these ideas.

## 5.5 Conclusions

Soft, stimulus-responsive, self-reversible actuation is quite advantageous in applications where use of external constraints or stress is largely restricted. In this paper, a novel, convenient fabrication process for thermal-triggering free-standing actuators via electrospinning process was developed. The model actuators consist of a covalently crosslinked, semicrystalline polyurethane with a lower  $T_m$  and a thermoplastic elastomeric polyurethane with a higher  $T_m$ . Micro-geometry and molecular anisotropy were implemented to investigate their influence on the resulting actuation behavior of various designs. Actuation characterization was done for multiple cycles in succession along with microstructural, thermal, dynamic mechanical, and shape memory analysis, to thoroughly understand the science behind. The results showed that different actuations were achieved under completely no externally stress-free environment in effect of micro-geometry and molecular orientation, including bending, twisting, flattening, and untwisting actuation. Two simple actuation mechanisms corresponding to specific design were presented to explain the specific actuation phenomenon as well as the origin of distinct actuations.

## 5.6 References

1. Maitland, D. J.; Metzger, M. F.; Schumann, D.; Lee, A.; Wilson, T. S.: Photothermal Properties of Shape Memory Polymer Micro-actuators for Treating Stroke. *Laser. Surg. Med.* **2002**, 30, 1 – 11.
2. Hu, J.; Chen, S.: A Review of Actively Moving Polymers in Textile Applications. *J. Mater. Chem.* **2010**, 20, 3346 – 3355.
3. Serrano, M. C.; Carbajal, L.; Ameer, G. A.: Novel Biodegradable Shape-memory Elastomers with Drug-releasing Capabilities. *Adv. Mater.* **2011**, 23, 2211 – 2215.
4. Ebara, M.; Uto, K.; Idota, N.; Hoffman, J. M.; Aoyagi, T.: Shape-memory Surface with Dynamically Tunable Nano-geometry Activated by Body Heat. *Adv. Mater.* **2012**, 24, 273 – 278.
5. Ge, Q.; Luo, X.; Rodriguez, E. D.; Zhang, X.; Mather, P. T.; Dunn, M. L.; Qi, H. J.: Thermomechanical Behavior of Shape Memory Elastomeric Composites. *J. Mech. Phys. Solids* **2012**, 60, 67 – 83.
6. Diani, J.; Gilormini, P.; Frédy, C.; Rousseau, I.: Predicting Thermal Shape Memory of Crosslinked Polymer Networks from Linear Viscoelasticity. *Int. J. Solids Struct.* **2012**, 49, 793 – 799.
7. Liu, C.; Qin, H.; Mather, P. T.: Review of Progress in Shape-memory Polymers. *J. Mater. Chem.* **2007**, 17, 1543 – 1558.
8. Mather, P. T.; Luo, X.; Rousseau, I. A.: Shape Memory Polymer Research. *Annu. Rev. Mater. Res.* **2009**, 39, 445 – 471.
9. Behl, M.; Razaq, M. Y.; Lendlein, A.: Multifunctional Shape-memory Polymers. *Adv. Mater.* **2010**, 22, 3388 – 3410.

10. Xie, T.: Recent Advances in Polymer Shape Memory. *Polymer* **2011**, 52, 4985 – 5000.
11. Stuart, M. A. C.; Huck, W. T. S.; Genzer, J.; Müller, M.; Ober, C.; Stamm, M.; Sukhorukov, G. B.; Szleifer, I.; Tsukruk, V. V.; Urban, M.; Winik, F.; Zauscher, S.; Luzinov, I.; Minko, S.: Emerging Applications of Stimuli-responsive Polymer Materials. *Nat. Mater.* **2010**, 9, 101 – 113.
12. Hong, S. J.; Yu, W.; Youk, J. H.: Two-way Shape Memory Behavior of Shape Memory Polyurethanes with a Bias Load. *Smart Mater. Struct.* **2010**, 19, 035022.
13. Imai, S.: Operating Methods for Two-way Behavior Shape Memory Polymer Actuators without Using External Stress. *IEEJ Trans.* **2014**, 9, 90 – 96.
14. Behl, M.; Kratz, K.; Zotzmann, J.; Nöchel, U.; Lendlein, A.: Reversible Bidirectional Shape-memory Polymers. *Adv. Mater.* **2013**, 25, 4466 – 4469.
15. Behl, M.; Kratz, K.; Noechel, U.; Sauter, T.; Lendlein, A.: Temperature-memory Polymer Actuators. *Proc. Natl. Acad. Sci. U.S.A.* **2013**, 110, 12555 – 12559.
16. Zhou, J.; Turner, S. A.; Brosnan, S. M.; Li, Q.; Carrilo, J. Y.; Nykypanchuk, D.; Gang, O.; Ashby, V. S.; Dobrynin, A. V.; Sheiko, S. S.: Shapeshifting: Reversible Shape Memory in Semicrystalline Elastomers. *Macromolecules* **2014**, 47, 1768 – 1776.
17. Meng, Y.; Jiang, J.; Anthamatten, M.: Shape Actuation via Internal Stress-induced Crystallization of Dual-cure Networks. *ACS Macro Lett.* **2015**, 4, 115 – 118.
18. Chen, S.; Hu, J.; Zhuo, H.; Zhu, Y.: Two-way Shape Memory Effect in Polymer Laminates. *Mater. Lett.* **2008**, 62, 4088 – 4090.
19. Chen, S.; Hu, J.; Zhuo, H.: Properties and Mechanism of Two-way Shape Memory Polyurethane Composites. *Compos. Sci. Technol.* **2010**, 70, 1437 – 1443.

20. Tamagawa, H.: Thermo-responsive Two-way Shape Changeable Polymeric Laminate. *Mater. Lett.* **2010**, 64, 749 – 751.
21. Westbrook, K. K.; Mather, P. T.; Parakh, V.; Dunn, M. L.; Ge, Q.; Lee, B. M.; Qi, H. J.: Two-way Reversible Shape Memory Effects in A Free-standing Polymer Composite. *Smart Mater. Struct.* **2011**, 20, 065010.
22. Ge, Q.; Westbrook, K. K.; Mather, P. T.; Dunn, M. L.; Qi, H. J.: Thermomechanical Behavior of A Two-way Shape Memory Composite Actuator. *Smart Mater. Struct.* **2013**, 22, 055009.
23. Huang, Z.; Zhang, Y.; Kotaki, M.; Ramakrishana, S.: A Review on Polymer Nanofibers by Electrospinning and Their Applications in Nanocomposites. *Compos. Sci. Technol.* **2003**, 63, 2223 – 2253.
24. Greiner, A.; Wendroff, J. H.: Electrospinning: A Fascinating Method for the Preparation of Ultrathin Fibers. *Angew. Chem. Int. Ed.* **2007**, 46, 5670 – 5703.
25. Ji, F.; Zhu, Y.; Hu, J.; Liu, Y.; Yeung, L.; Ye, G.: Smart Polymer Fibers with Shape Memory Effect. *Smart Mater. Struct.* **2006**, 15, 1547 – 1554.
26. Meng, Q.; Hu, J.: A Review of Shape Memory Polymer Composites and Blends. *Compos. Part A* **2009**, 40, 1661 – 1672.
27. Tseng, L.; Mather, P. T.; Henderson, J. H.: Shape-memory-actuated Change in Scaffold Fiber Alignment Directs Stem Cell Morphology. *Acta Biomater.* **2013**, 9, 8790 – 8801.
28. Kuang, W.; Mather, P. T.: A Latent Crosslinkable PCL-based Polyurethane: Synthesis, Shape Memory, and Degradation. *J. Mater. Res.* **2017**, xx, xxx – xxx.



29. Luo, X.; Mather, P. T.: Preparation and Characterization of Shape Memory Elastomeric Composites. *Macromolecules* **2009**, *42*, 7251 – 7253.
30. Ji, M.; Jiang, N.; Chang, J.; Sun, J.: Near-infrared Light-driven, Highly Efficient Bilayer Actuators Based on Polydopamine-modified Reduced Graphene Oxide. *Adv. Funct. Mater.* **2014**, *24*, 5412 – 5419.
31. Su, J.; Harrison, J. S.; St. Clair, T. L.: Polymer-polymer Bilayer Actuator. US Pat., 6 545 391 B1, 2003.
32. Liu, J.; Wang, Z.; Xie, X.; Cheng, H.; Zhao, Y.; Qu, L.: A Rationally-designed Synergetic Polypyrrole/graphene Bilayer Actuator. *J. Mater. Chem.* **2012**, *22*, 4015 – 4020.
33. Chung, T.; Romo-Uribe, A.; Mather, P. T.: Two-way Reversible Shape Memory in A Semicrystalline Network. *Macromolecules* **2008**, *41*, 184 – 192.
34. Nishi, T.; Wang, T. T.: Melting Point Depression and Kinetic Effects of Cooling on Crystallization in Poly(vinylidene fluoride)-Poly(methyl methacrylate) Mixtures. *Macromolecules* **1975**, *8*, 909 – 915.
35. Haas, T. W.; Maxwell, B.: Effects of Shear Stress on the Crystallization of Linear Polyethylene and Polybutene-1. *Polym. Eng. Sci.* **1969**, *9*, 225 – 241.
36. Ramakrishana, S.; Mayer, J.; Wintermantel, E.; Leong, K. W.: Biomedical Applications of Polymer-composite Materials: A Review. *Compos. Sci. Technol.* **2001**, *61*, 1189 – 1224.
37. Baker, R. M.; Henderson, J. H.; Mather, P. T.: Shape Memory Poly( $\epsilon$ -caprolactone)-*co*-Poly(ethylene glycol) Foams with Body Temperature Triggering and Two-way Actuation. *J. Mater. Chem. B* **2013**, *1*, 4916 – 4920.

38. Xue, Y.; Jairazbhoy, V. A.; Niu, X.; Qu, J.: Large Deflection of Thin Plates under Certain Mixed Boundary Conditions – Cylindrical Bending. *J. Electron. Packag.* **2003**, 125, 53 – 58.
39. Wang, S.; Karmakar, D.; Soares, C. G.: *Maritime Technology and Engineering*; Taylor & Francis Group: London, 2015.
40. Altenbach, H.; Altenbach, J.; Kissing, W.: *Mechanics of Composite Structural Elements*; Springer: Berlin, Heidelberg, 2004.

**Table 5-1.** Solution Preparation for Electrospinning

Sample	Mass (g)	Chloroform (mL)	THF (mL)	DMF (mL)	DLP (wt. %)
x-PU	2.0	8.0	-	4.0	3.0
Pellethane	2.0	-	12.0	8.0	0.0

**Table 5-2.** Fabrication of Bilayers via Electrospinning

Sample	x-PU				Pellethane			
	Ejection Rate (mL/h)	Rotating Speed (rpm)	Ti m (h)	Voltage (kV)	Ejection Rate (mL/h)	Rotating Speed (rpm)	Ti m (h)	Voltage (kV)
Bilayer01 <sup>a</sup>	1.5	400	6	16.0	1.5	2000	10	14.0
Bilayer02 <sup>b</sup>	1.5	2000	6	16.0	1.5	400	10	14.0

<sup>a</sup> Pellethane is anticipated to be oriented.

<sup>b</sup> x-PU is anticipated to be oriented.

**Table 5-3.** Composition Evaluation

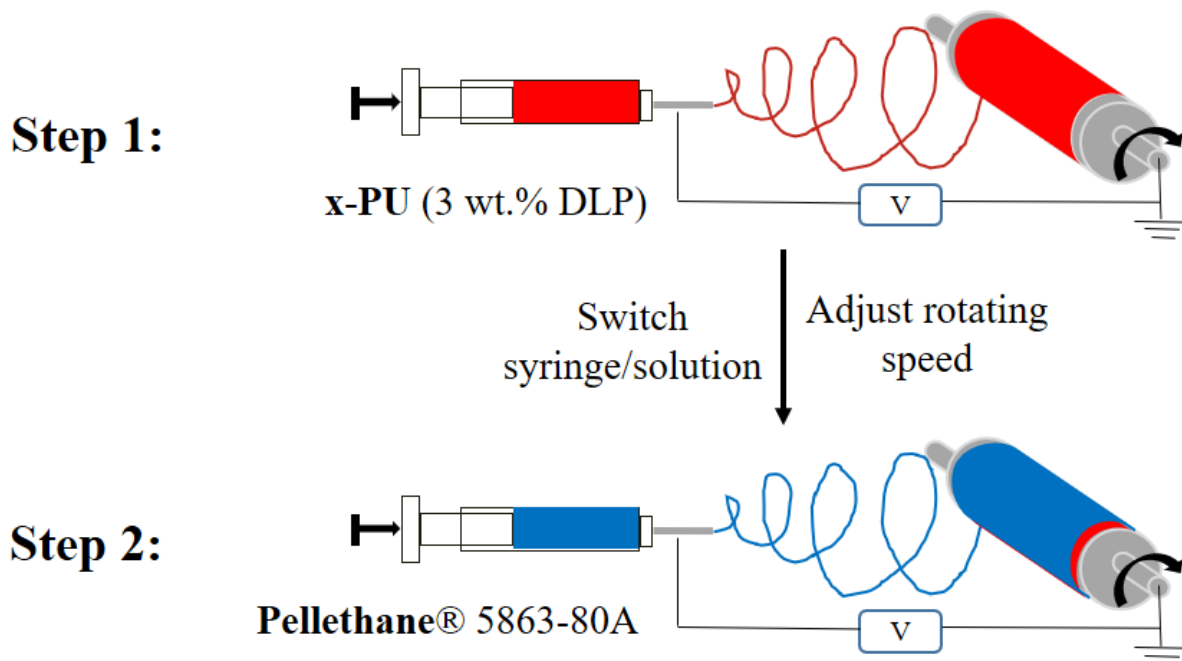
Sample	$W_{x-PU}^{TGA}$ (wt. %) <sup>a</sup>	$W_{Pellethane}^{TGA}$ (wt. %) <sup>a</sup>	$W_{x-PU}^{DSC}$ (wt. %) <sup>b</sup>	$W_{Pellethane}^{DSC}$ (wt. %) <sup>b</sup>
Bilayer01	45.6	54.4	49.1	50.9
Bilayer02	60.4	39.6	59.3	40.7

<sup>a</sup> Calculated based on characteristic decomposition steps from TGA profiles.

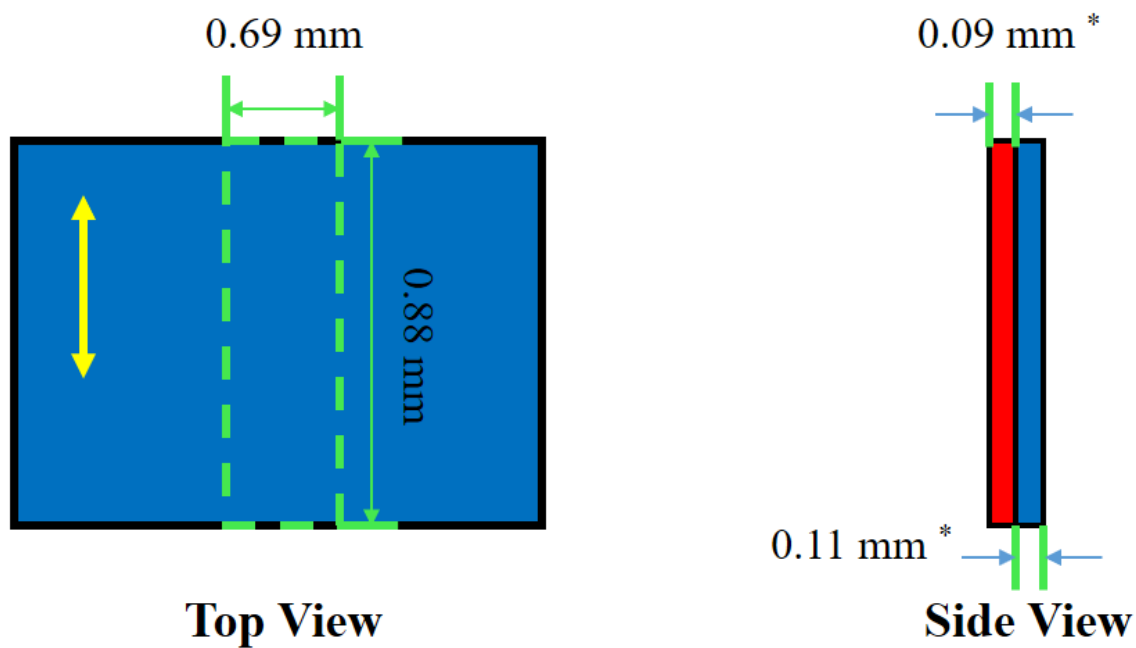
<sup>b</sup> Calculated from crystallinity of x-PU portion relative to that of neat x-PU ( $\Delta H_{m,x-PU}^{Neat} = 51.76$  J/g).

**Table 5-4.** Thermal Characteristics of Cured Fibrous Bilayers

Sample	$T_g$ (°C)	$T_m$ (°C)	$\Delta H_m$ (J/g)	$T_c$ (°C)
Bilayer01	-21.4	44.1	25.4	14.0
Bilayer02	-25.0	45.7	30.7	17.6

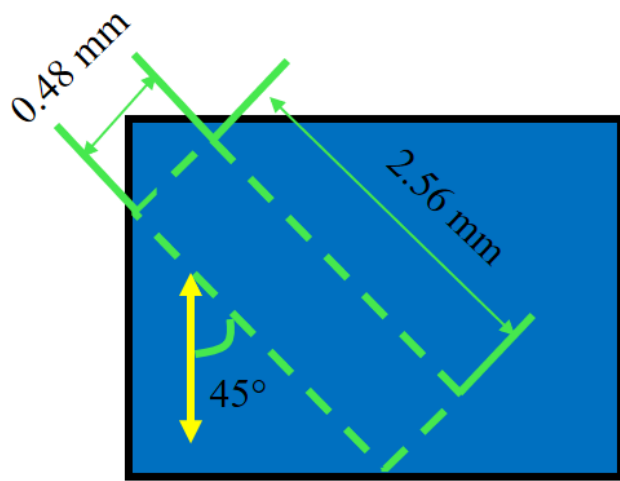


**Scheme 5-1.** A two-step approach of fabricating bilayers via electrospinning. Step 1: x-PU (red) is first spun into one layer; Step 2: x-PU was substituted by Pellethane (blue) that forms the other layer. Rotating speed of collecting mandrel is adjusted to create molecular and geometric anisotropy when switching solutions.

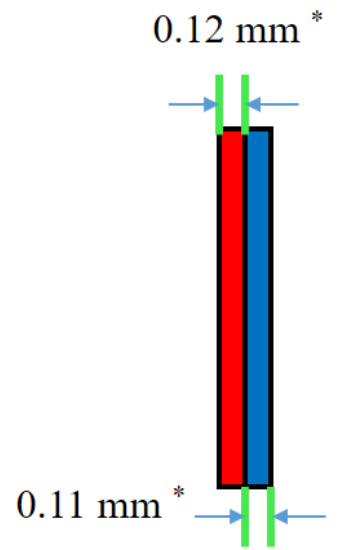


**Scheme 5-2.** Geometry of bending actuator from cured Bilayer01. Yellow arrow indicates the fiber orientation introduced during electrospinning. The x-PU layer in red while the Pellethane layer in blue. \* The average thickness of each layer was measured based on SEM image using ImageJ.



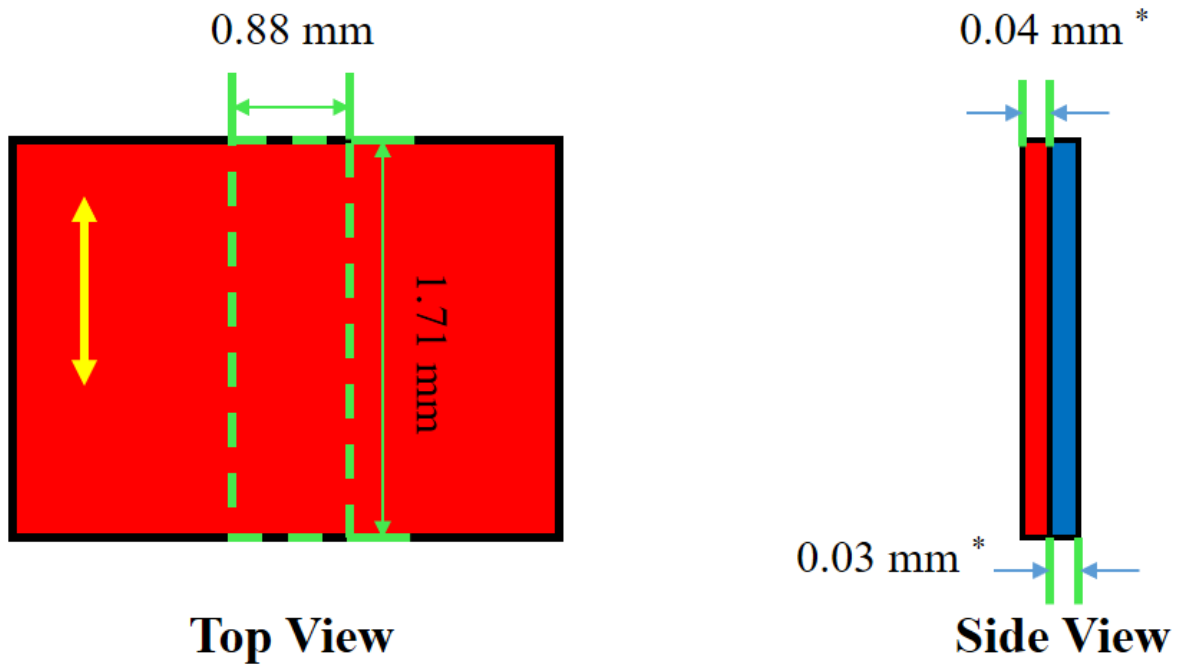


**Top View**

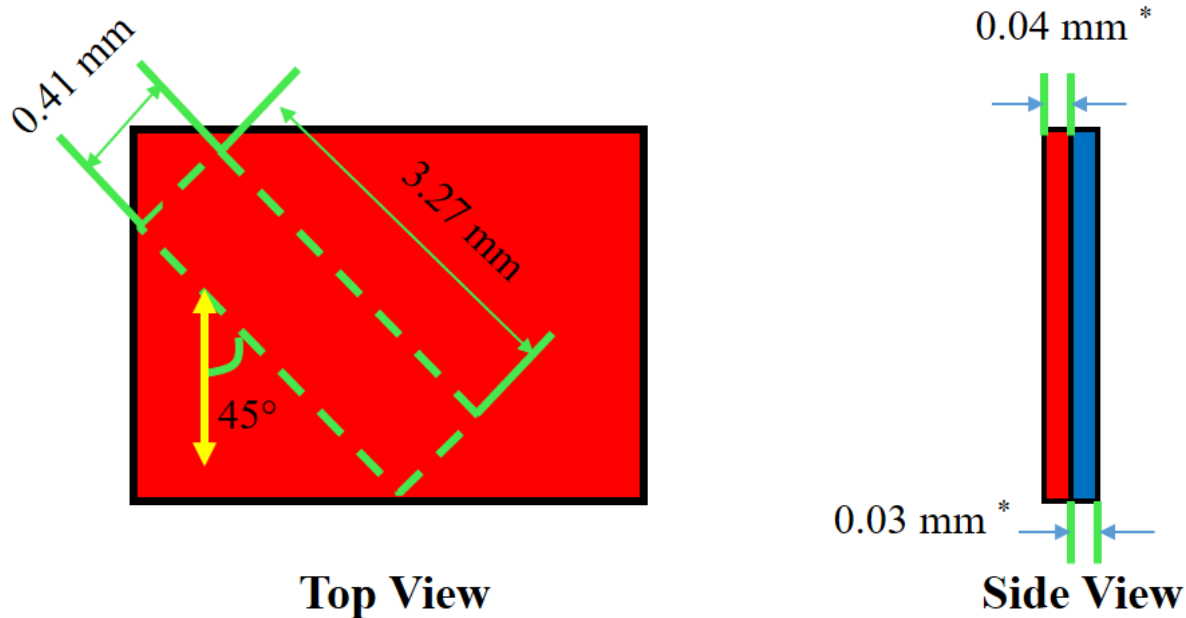


**Side View**

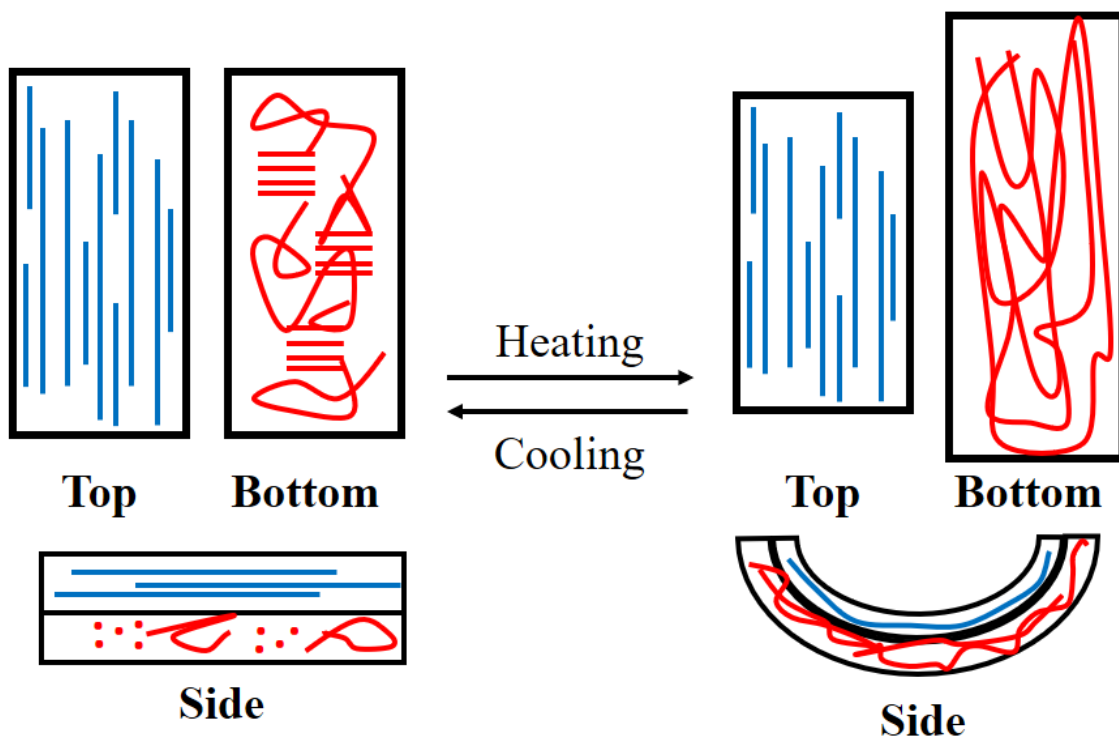
**Scheme 5-3.** Geometry of twisting actuator from cured Bilayer01. Yellow arrow indicates the fiber orientation introduced during electrospinning. The x-PU layer in red while the Pellethane layer in blue. \* The average thickness of each layer was measured based on SEM image using ImageJ.



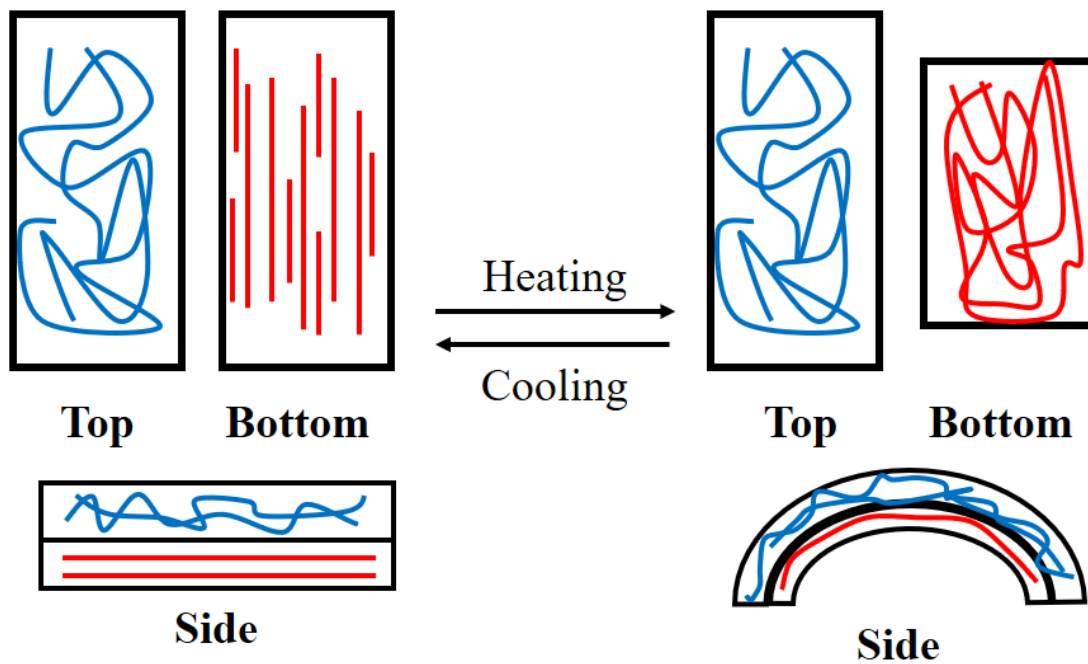
**Scheme 5-4.** Geometry of flattening actuator from cured Bilayer02. Yellow arrow indicates the fiber orientation introduced during electrospinning. The x-PU layer in red while the Pellethane layer in blue. \* The average thickness of each layer was measured based on SEM image using ImageJ.



**Scheme 5-5.** Geometry of untwisting actuator from cured Bilayer02. Yellow arrow indicates the fiber orientation introduced during electrospinning. The x-PU layer in red while the Pellethane layer in blue. \* The average thickness of each layer was measured based on SEM image using ImageJ.



**Scheme 5-6.** Hypothetic actuation mechanism of bending actuator prepared from cured Bilayer01. The x-PU chains are in red while the Pellethane in blue. Originally, highly oriented Pellethane fibers are imposing compressive stress onto x-PU chains some of which formed crystallites align in cross-wise direction. Upon heating above  $T_m$  of x-PU but not high enough to relax Pellethane fibers, x-PU crystallites melt and become amorphous domain which occupies more space than in its fully crystallized state. Consequently, the actuator bends towards Pellethane side. Upon cooling, the shape transformation is reversed due to recrystallization process.



**Scheme 5-7.** Hypothetic actuation mechanism of flattening actuator prepared from cured Bilayer02. The x-PU chains are in red while the Pellethane in blue. Originally, x-PU fibers are highly oriented so that corresponding crystallites align along the direction of fiber axis. Meanwhile, Pellethane fibers are randomly distributed and applying a certain amount of compressive stress onto x-PU, yielding a naturally curled bilayer towards Pellethane side. Upon heating above  $T_m$  of x-PU but not high enough to relax Pellethane fibers, x-PU crystallites melt and contract to lower entropic energy. Consequently, the actuator becomes flat upon heating and the shape transformation is reversed due to recrystallization process upon cooling.

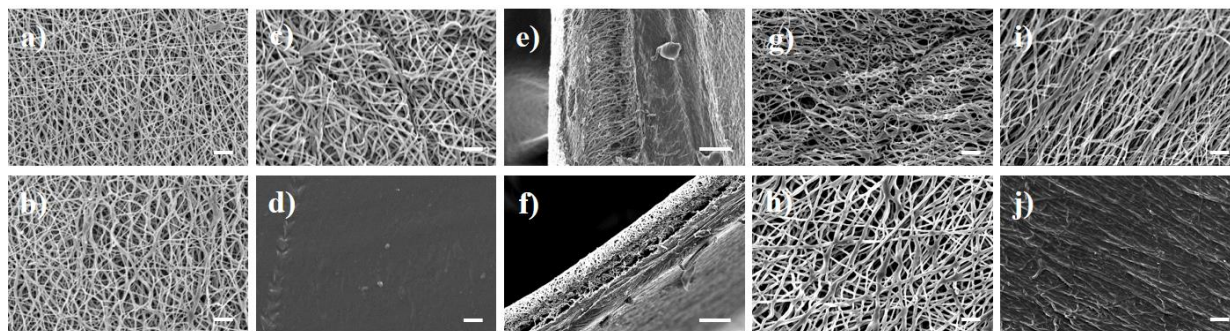


**Figure 5-1.** Scanning electron microscope (SEM) images of Bilayer01: Pellethane side **a)** before curing and **b)** after curing, x-PU side **c)** before curing and **d)** after curing, and **e)** cross-sectional view of cured sample; of Bilayer02: Pellethane side **g)** before curing and **h)** after curing, x-PU side **i)** before curing and **j)** after curing, and **f)** cross-sectional view of cured sample. Scale bar = 10  $\mu\text{m}$  in **a)**, **b)**, **c)**, **d)**, **g)**, **h)**, **i)** and **j)**; 50  $\mu\text{m}$  in **e)** and **f)**.

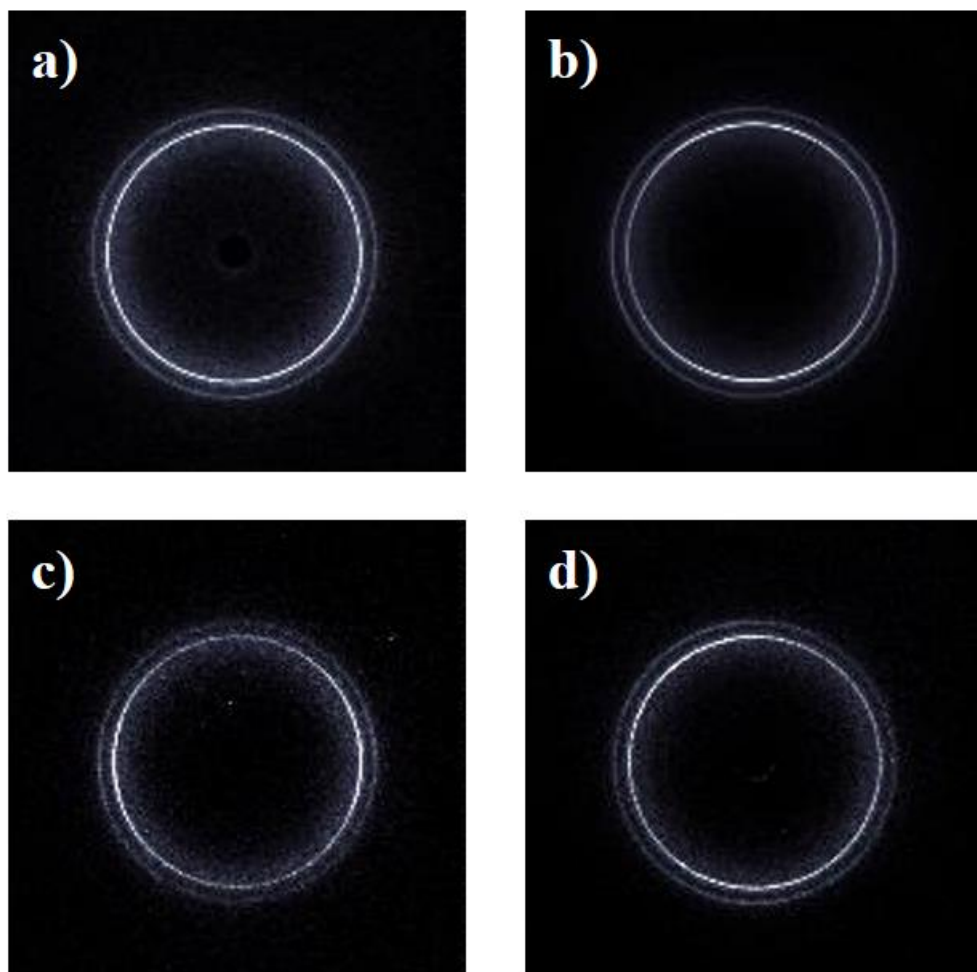


**Figure 5-2.** 2D WAXS patterns of bilayers before and after thermal curing: **a)** uncured Bilayer01, **b)** uncured Bilayer02, **c)** cured Bilayer01, and **d)** cured Bilayer02. The X-ray wavelength ( $\lambda$ ) is 1.5405 Å. Both the principle orientation of fiber axis and strip's long axis are horizontal.

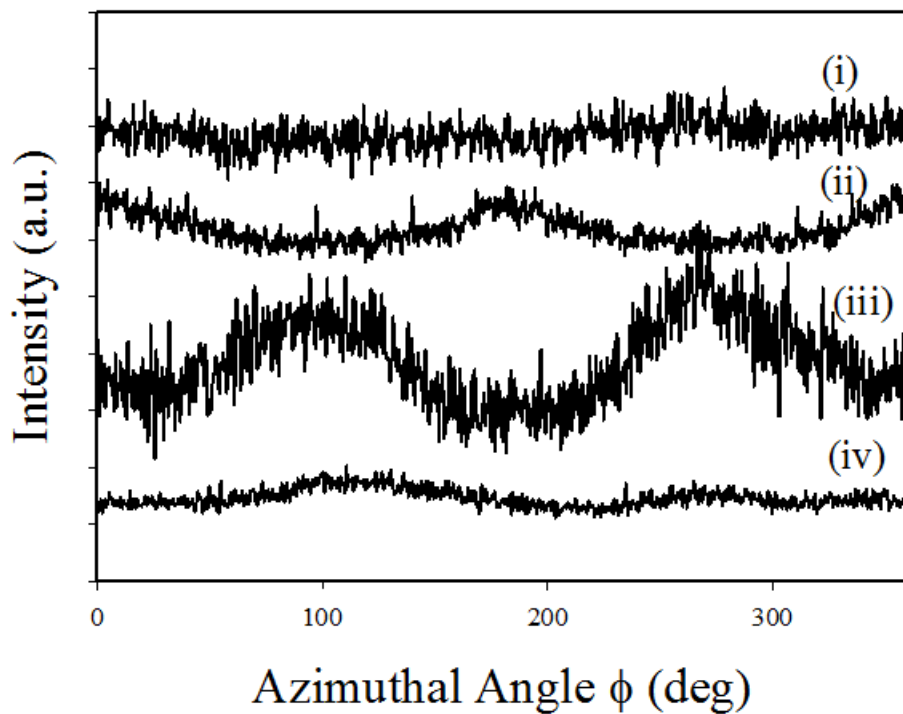


**Figure 5-3.** Azimuthal scanning profiles for bilayers before and after thermal curing: (i) uncured Bilayer01, (ii) cured Bilayer01, (iii) uncured Bilayer02, and (iv) cured Bilayer02. The X-ray wavelength ( $\lambda$ ) is 1.5405 Å.



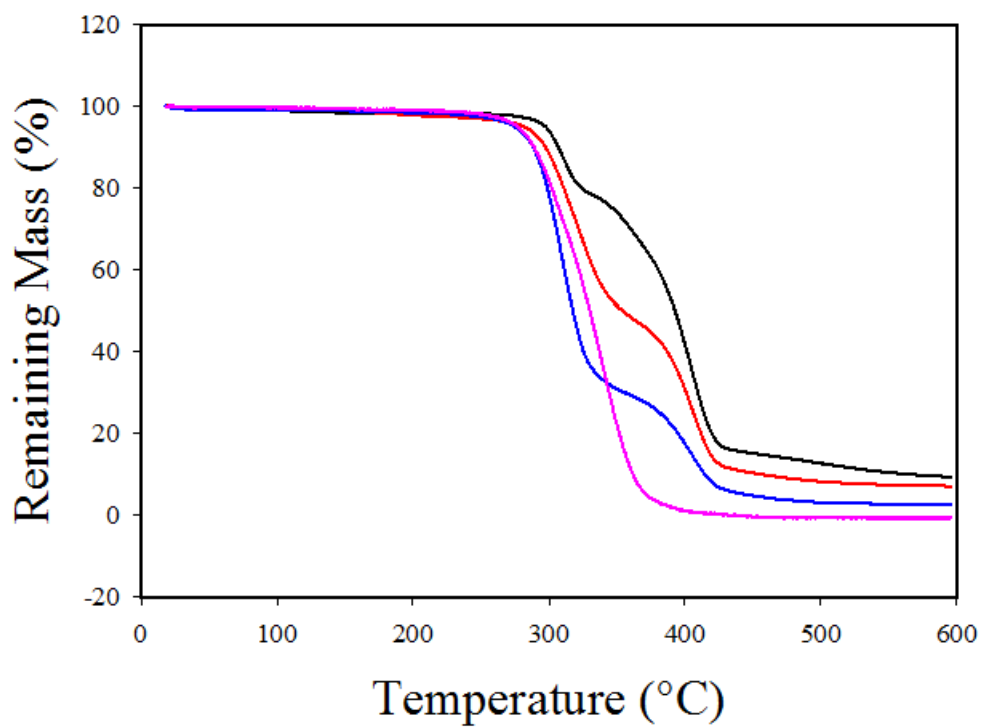


**Figure 5-4.** Thermogravimetric analysis (TGA) profiles of neat Pellethane (black), Bilayer01 (red), Bilayer02 (blue), and neat x-PU (pink). Heating rate of 10 °C/min.

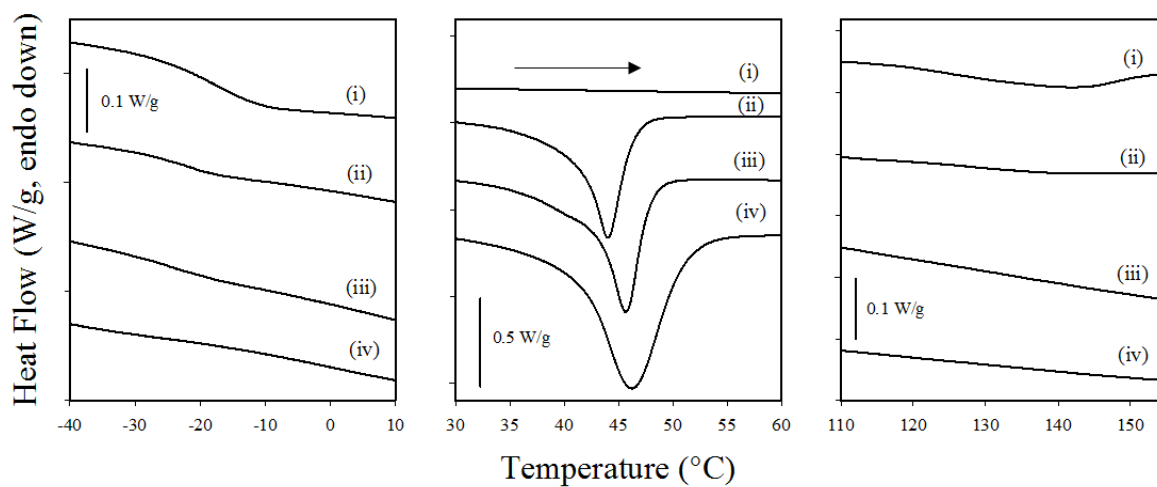


**Figure 5-5.** Differential Scanning Calorimetry (DSC) analysis graph of cured bilayers and substituent polymers: (i) neat Pellethane, (ii) cured Bilayer01, (iii) cured Bilayer02, and (iv) cured x-PU. The second heating was recorded at a rate of 10 °C/min.

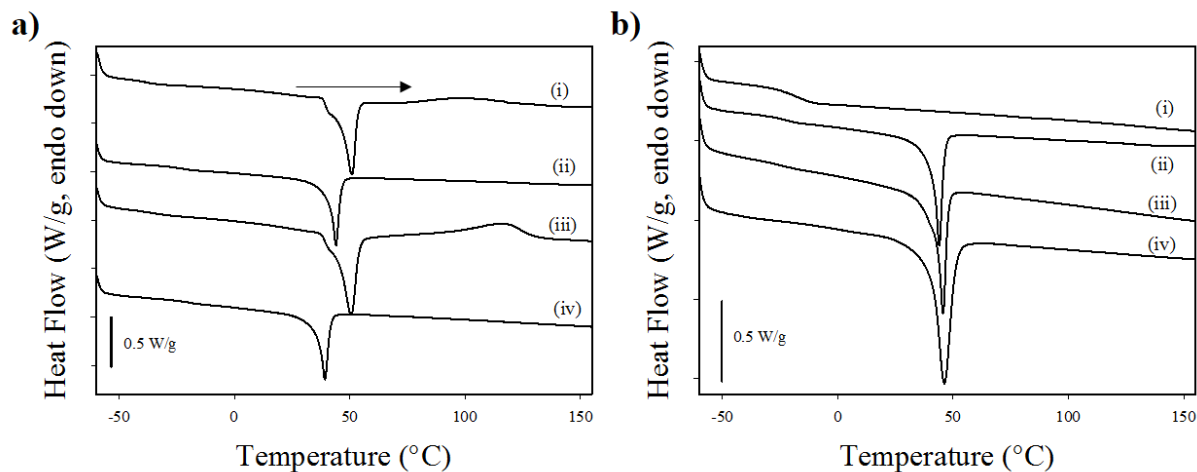


**Figure 5-6.** Differential Scanning Calorimetry (DSC) analysis graph of **a)** uncured electrospun bilayers: (i) first heating and (ii) second heating of Bilayer01, and, (iii) first heating and (iv) second heating of Bilayer02; and of **b)** cured bilayers and substituent polymers: (i) neat Pellethane, (ii) Bilayer01, (iii) Bilayer02, and (iv) neat x-PU. Heating rate is 10 °C/min.

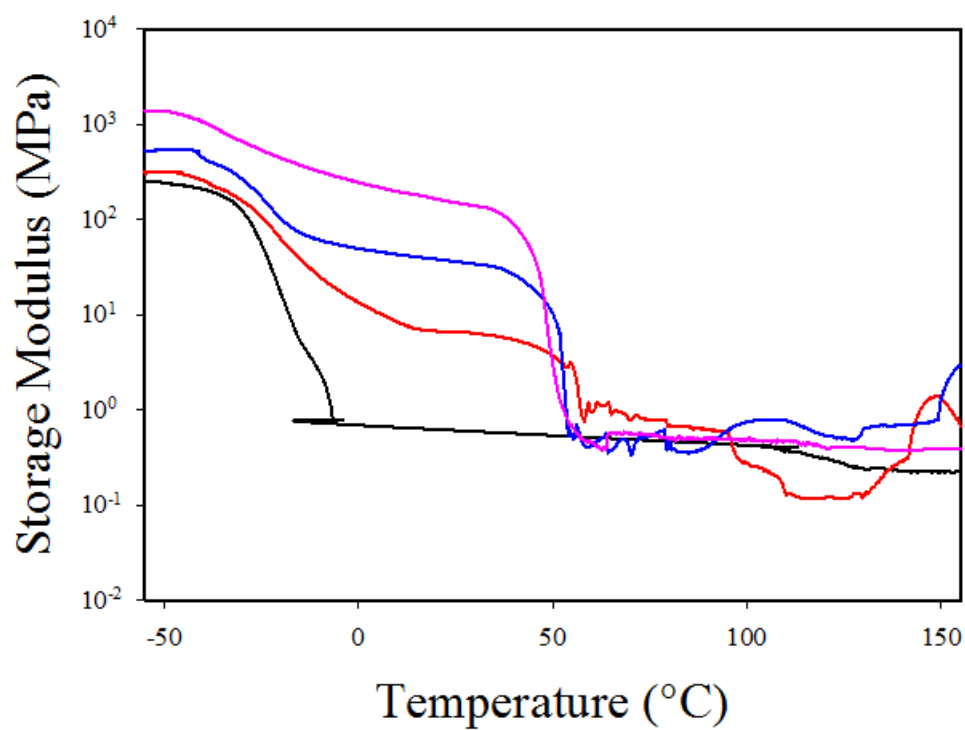


**Figure 5-7.** Tensile storage modulus ( $E'$ ) vs temperatures for cured bilayers and substituent polymers: neat Pellethane (black), Bilayer01 (red), Bilayer02 (blue), and neat x-PU (pink).  $E'$  was recorded at a heating rate of 3  $^{\circ}\text{C}/\text{min}$  with frequency of 1 Hz.

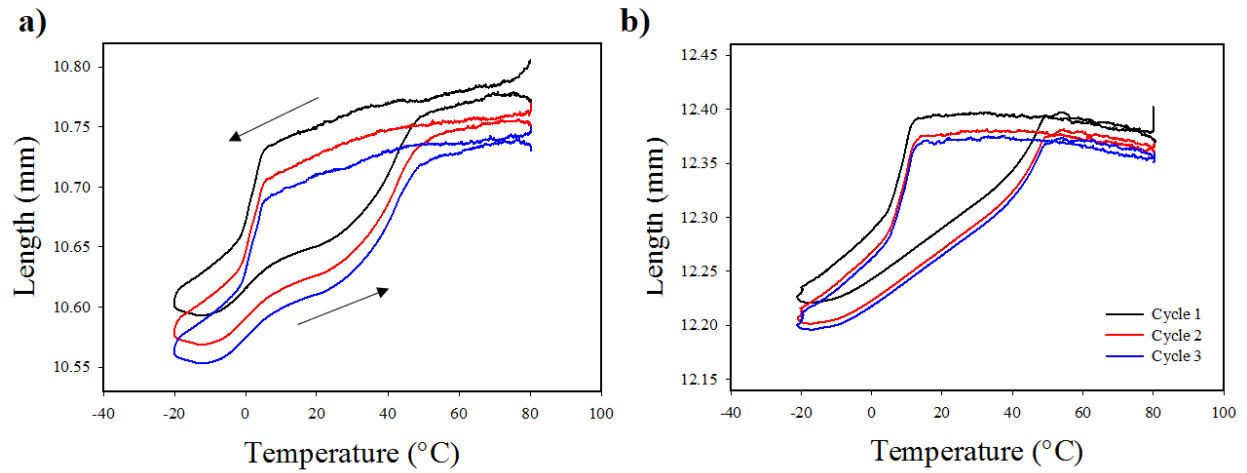


**Figure 5-8.** Tensile two-way actuation under stress-free condition for **a)** Bilayer01 and **b)** Bilayer02, both cured thermally. The samples were heated to 80 °C without applying external stress except preloading force of 0.001 N, following which alternate cooling and heating process was adopted at a rate of 2 °C/min.

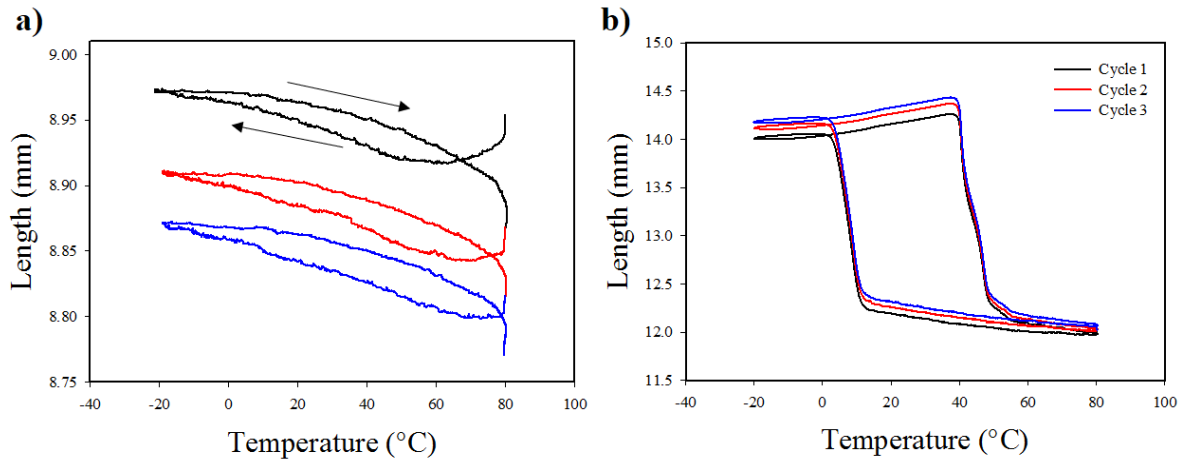
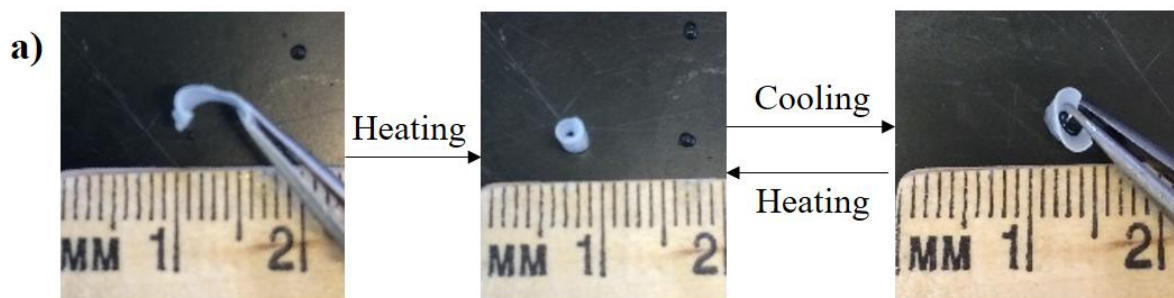


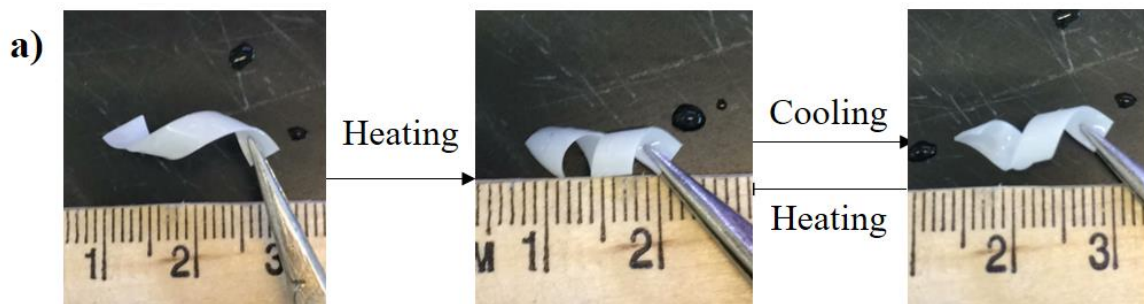
**Figure 5-9. a)** Tensile two-way actuation under stress-free condition for neat Pellethane. The samples were heated to 80 °C without applying external stress except preloading force of 0.001 N, following which alternate cooling and heating process was adopted at a rate of 2 °C/min; **b)** two-way shape memory cycles for crosslinked x-PU under 220 kPa. The sample was deformed under each constant stress at 80 °C, followed by cooling and heating steps (2 °C/min).



b)

Quantity *	Initial (mm <sup>-1</sup> )	1 <sup>st</sup> Heating (mm <sup>-1</sup> )	1 <sup>st</sup> Cooling (mm <sup>-1</sup> )	2 <sup>nd</sup> Heating (mm <sup>-1</sup> )	2 <sup>nd</sup> Cooling (mm <sup>-1</sup> )	3 <sup>rd</sup> Heating (mm <sup>-1</sup> )	3 <sup>rd</sup> Cooling (mm <sup>-1</sup> )
$\mathcal{K}$	3.16	10.41	4.62	10.66	4.69	10.69	4.71

**Figure 5-10. a)** Snapshots of two-way actuation of bending actuator. The sample changed from a bent shape to a more bent/curled shape by heating in a  $\sim 58$  °C water bath. Then its shape recovered by cooling in a  $\sim 0$  °C water-ice bath. The reversible actuation can be repeated by alternate heating and cooling; **b)** Quantification of reversible two-way actuation of bending actuator. Curvature ( $\mathcal{K}$ ) was calculated from Radius which was directly measured using ImageJ.

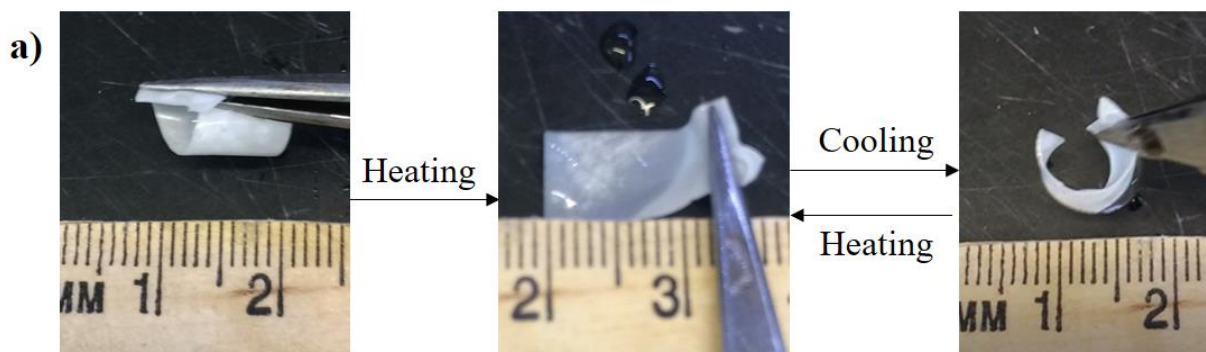


b)

Quantity *	Initial (mm)	1 <sup>st</sup> Heating (mm)	1 <sup>st</sup> Cooling (mm)	2 <sup>nd</sup> Heating (mm)	2 <sup>nd</sup> Cooling (mm)	3 <sup>rd</sup> Heating (mm)	3 <sup>rd</sup> Cooling (mm)
$\mathcal{R}$	0.22	0.15	0.17	0.15	0.17	0.15	0.17
$\mathcal{P}$	1.56	0.60	0.85	0.61	0.85	0.63	0.84

**Figure 5-11. a)** Snapshots of two-way actuation of twisting actuator. The sample changed from a twisted shape to a more twisted shape by heating in a  $\sim 55$  °C water bath. Then its shape recovered by cooling in a  $\sim 0$  °C water-ice bath. The reversible actuation can be repeated by alternate heating and cooling; **b)** Quantification of reversible two-way actuation of twisting actuator. Spiral radius ( $\mathcal{R}$ ) and spiral pitch (center-to-center spacing,  $\mathcal{P}$ ) were estimated using ImageJ.

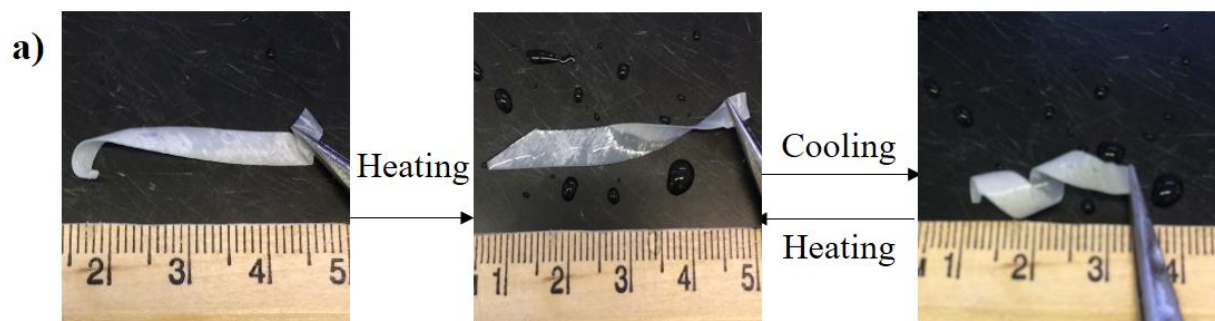




b)

Quantity *	Initial (mm <sup>-1</sup> )	1 <sup>st</sup> Heating (mm <sup>-1</sup> )	1 <sup>st</sup> Cooling (mm <sup>-1</sup> )	2 <sup>nd</sup> Heating (mm <sup>-1</sup> )	2 <sup>nd</sup> Cooling (mm <sup>-1</sup> )	3 <sup>rd</sup> Heating (mm <sup>-1</sup> )	3 <sup>rd</sup> Cooling (mm <sup>-1</sup> )
$\mathcal{K}$	2.77	~0	2.35	~0	2.35	~0	2.33

**Figure 5-12. a)** Snapshots of two-way actuation of flattening actuator. The sample changed from a curled shape to a flat shape by heating in a ~58 °C water bath. Then its shape recovered by cooling in a ~0 °C water-ice bath. The reversible actuation can be repeated by alternate heating and cooling; **b)** Quantification of reversible two-way actuation of flattening actuator. Curvature ( $\mathcal{K}$ ) was calculated from Radius which was directly measured using ImageJ.



**b)**

Quantity *	Initial (mm)	1 <sup>st</sup> Heating (mm)	1 <sup>st</sup> Cooling (mm)	2 <sup>nd</sup> Heating (mm)	2 <sup>nd</sup> Cooling (mm)	3 <sup>rd</sup> Heating (mm)	3 <sup>rd</sup> Cooling (mm)
$\mathcal{R}$	$\infty$	$\infty$	0.29	$\infty$	0.30	$\infty$	0.32
$\mathcal{P}$	$\infty$	$\infty$	0.99	$\infty$	0.97	$\infty$	0.97

**Figure 5-13. a)** Snapshots of two-way actuation of untwisting actuator. The sample changed from a twisted shape to a flat shape by heating in a  $\sim 55^\circ\text{C}$  water bath. Then its shape recovered by cooling in a  $\sim 0^\circ\text{C}$  water-ice bath. The reversible actuation can be repeated by alternate heating and cooling; **b)** Quantification of reversible two-way actuation of untwisting actuator. Spiral radius ( $\mathcal{R}$ ) and spiral pitch (center-to-center spacing,  $\mathcal{P}$ ) were estimated using ImageJ.

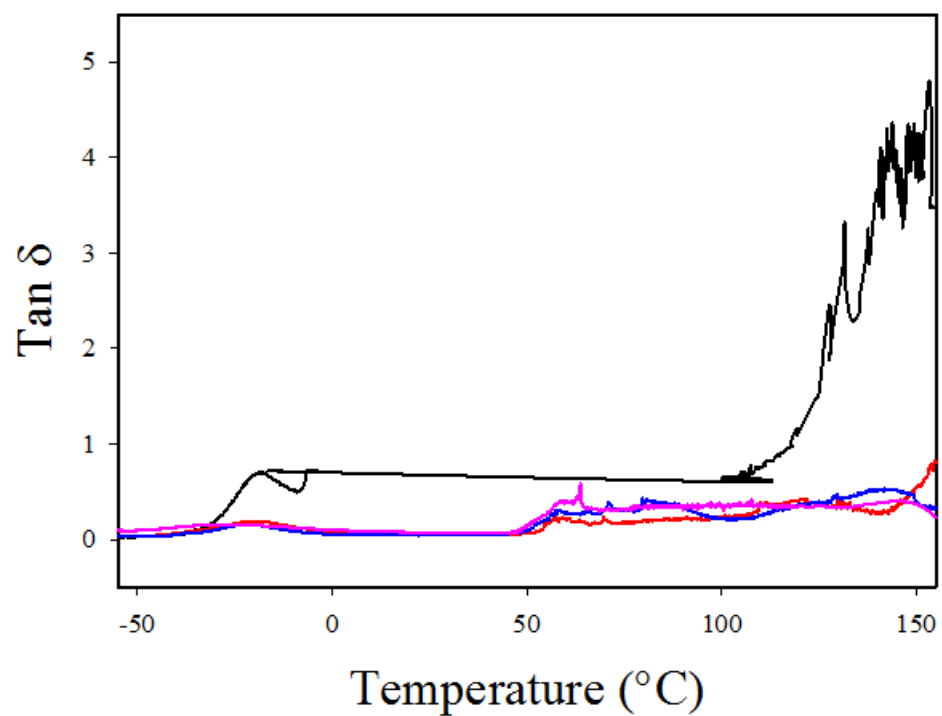


**Figure 5-14.** Tan  $\delta$  vs temperatures for cured bilayers and substituent polymers: neat Pellethane (black), Bilayer01 (red), Bilayer02 (blue), and neat x-PU (pink).

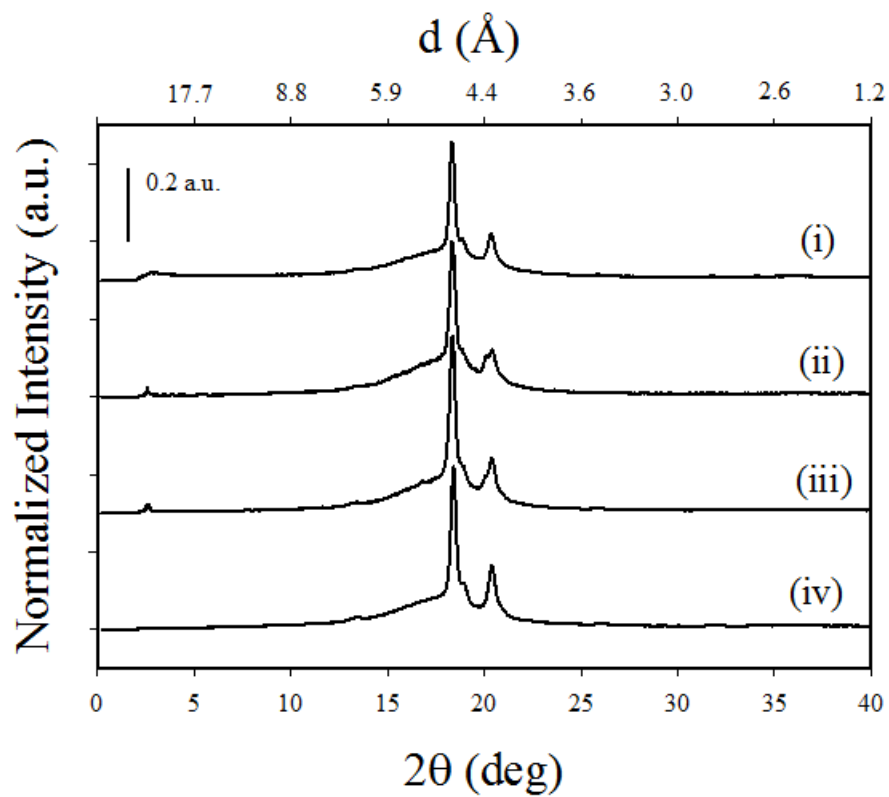


**Figure 5-15.** 2D WAXS profiles of bilayers before and after thermal curing: (i) uncured Bilayer01, (ii) uncured Bilayer02, (iii) cured Bilayer01, and (iv) cured Bilayer02. The X-ray wavelength ( $\lambda$ ) is 1.5405 Å.

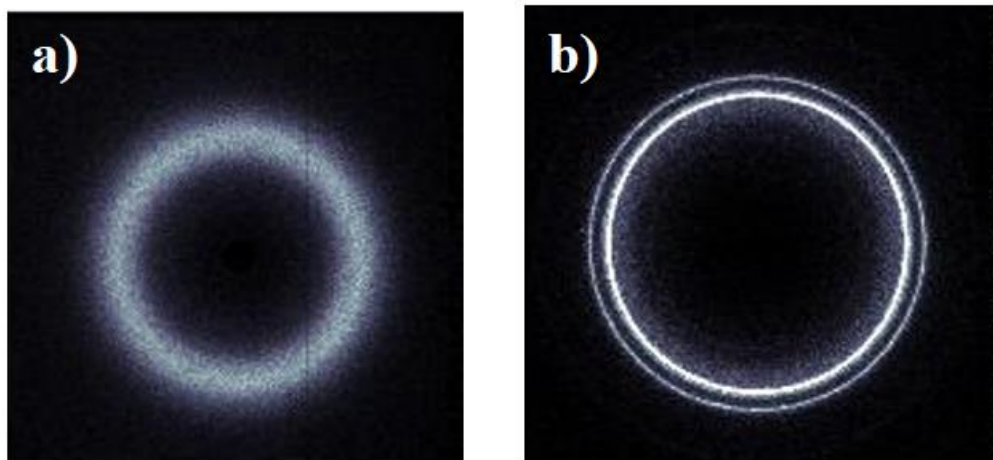


**Figure 5-16.** 2D WAXS patterns of bilayers before and after thermal curing: **a)** neat Pellethane and **b)** neat x-PU. The X-ray wavelength ( $\lambda$ ) is 1.5405 Å.

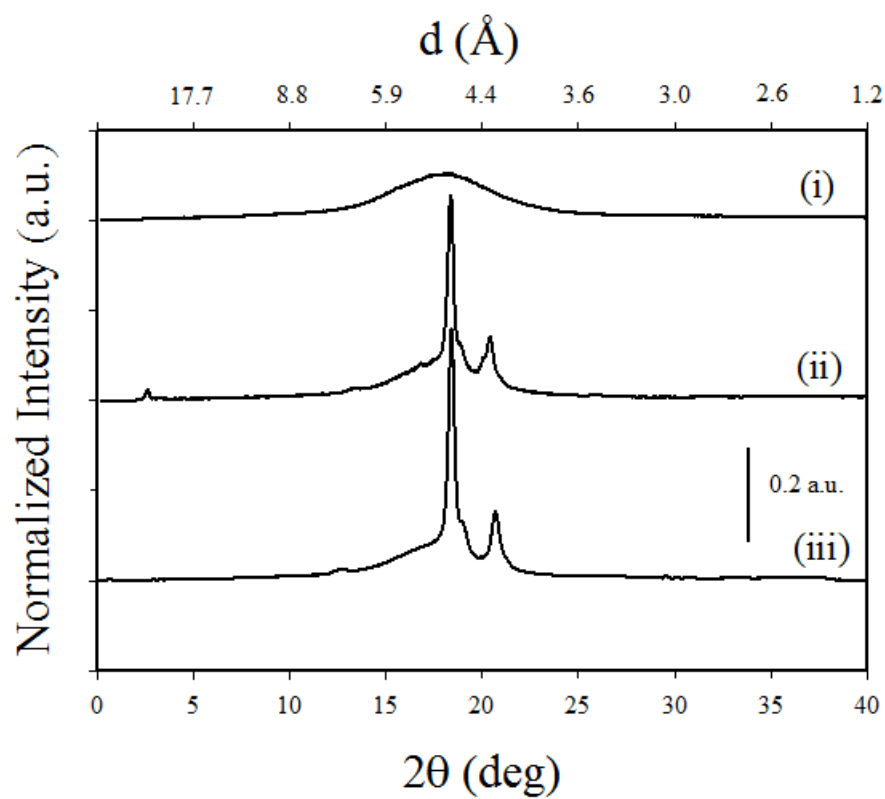
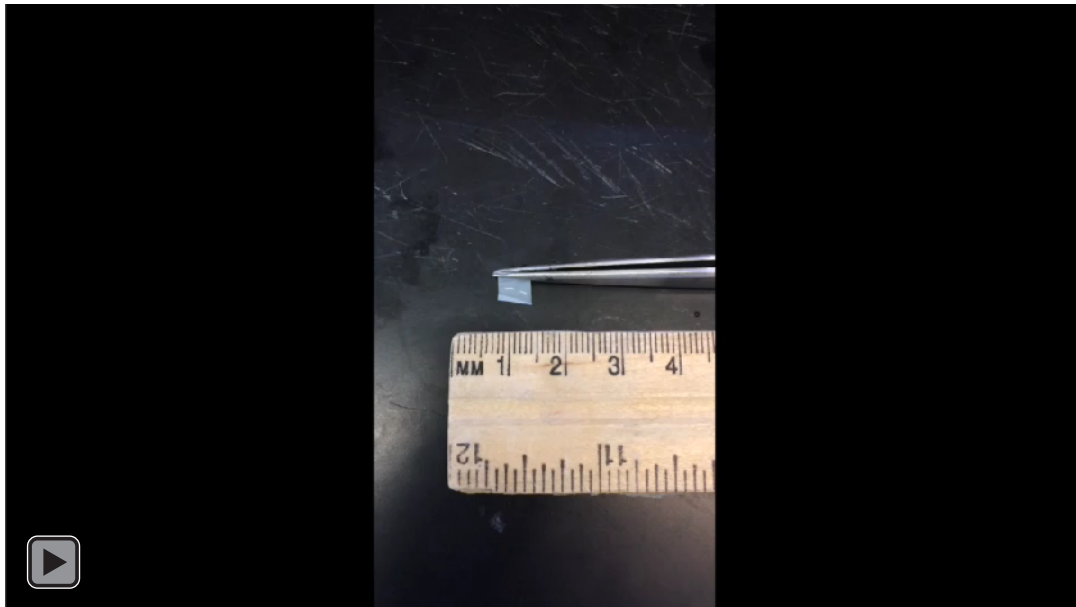
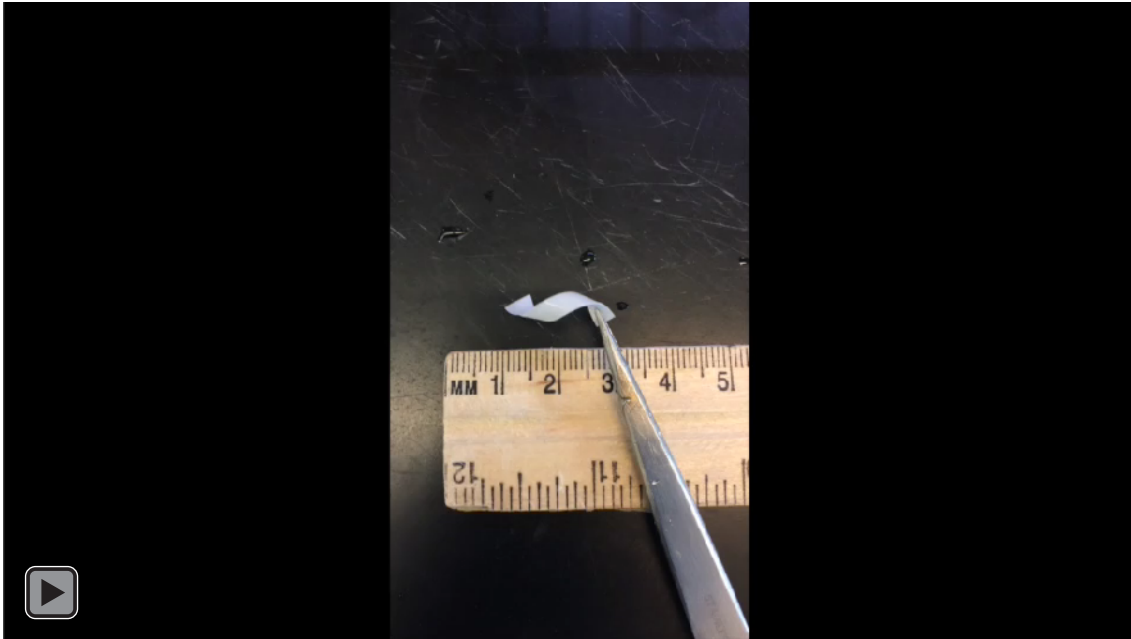


**Figure 5-17.** 2D WAXS profiles of (i) neat Pellethane, (ii) cured Bilayer01, and (iii) cured x-PU. The X-ray wavelength ( $\lambda$ ) is 1.5405 Å.

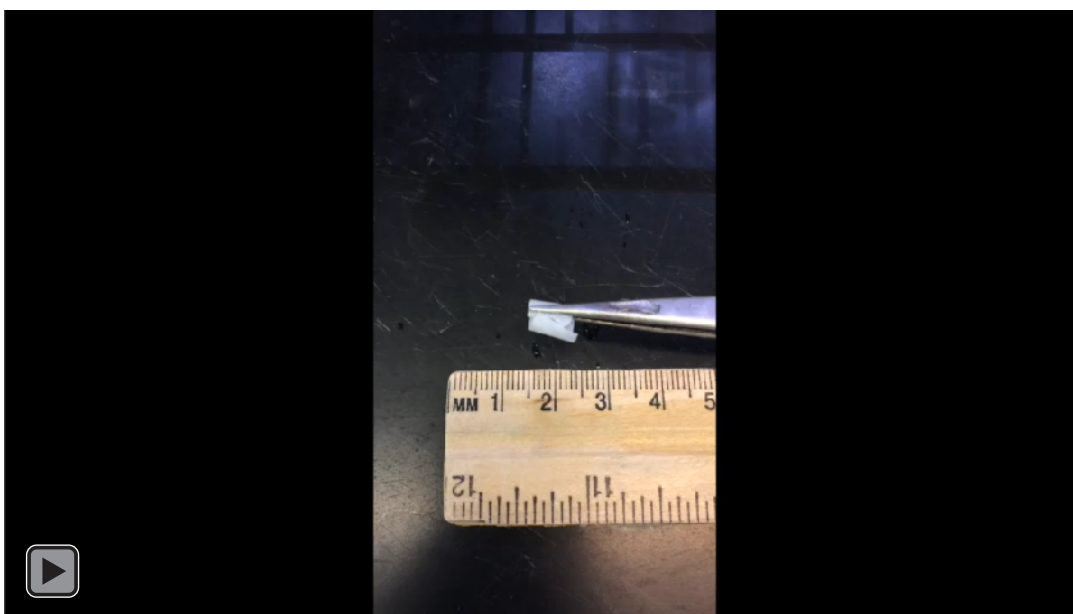


**Video 5-1.** Self-reversible two-way actuation of bending actuator. The sample was actuated at  $\sim 58$  °C above  $T_m$  of x-PU, turning to a more bent shape towards Pellethane side as Pellethane fibers were exerting compressive stress onto x-PU. Then the initial shape was recovered by cooling at  $\sim 0$  °C. Such free standing reversible actuation can be repeated by alternate heating and cooling.

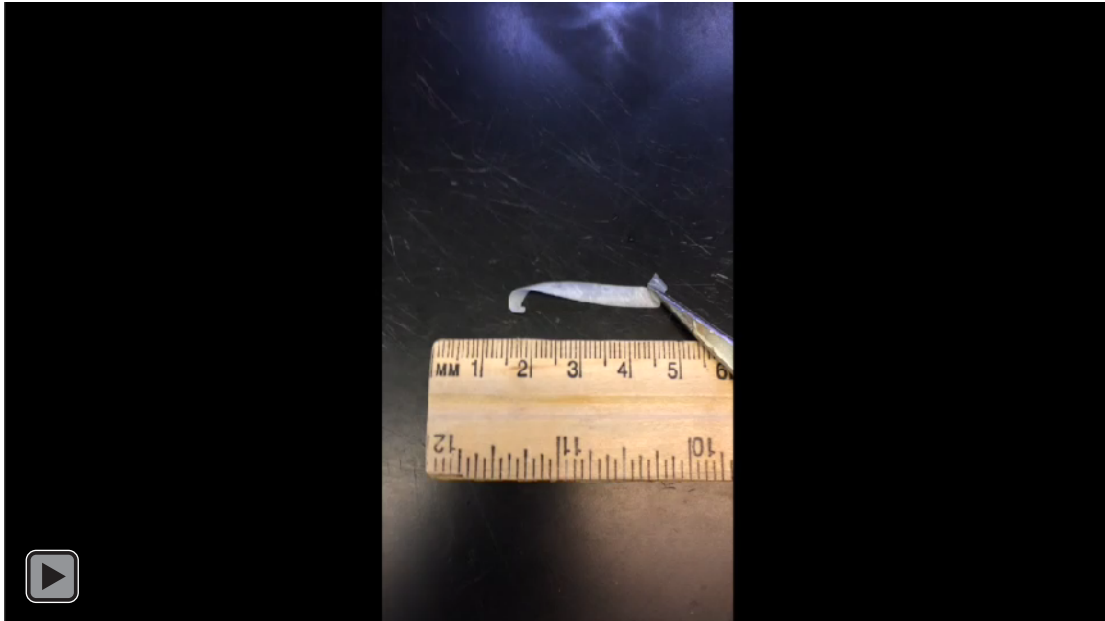


**Video 5-2.** Self-reversible two-way actuation of twisting actuator. The sample was actuated at  $\sim 55$  °C above  $T_m$  of x-PU, turning to a more twisted, spiral shape with Pellethane side being inside as Pellethane fibers were exerting compressive stress onto x-PU. Then the initial shape was recovered by cooling at  $\sim 0$  °C. Such free standing reversible actuation can be repeated by alternate heating and cooling.





**Video 5-3.** Self-reversible two-way actuation of flattening actuator. The sample was actuated at  $\sim 58$  °C above  $T_m$  of x-PU, turning to a completely flat shape as oriented x-PU contracted extensively. Then the initial shape was recovered by cooling at  $\sim 0$  °C. Such free standing reversible actuation can be repeated by alternate heating and cooling.



**Video 5-4.** Self-reversible two-way actuation of untwisting actuator. The sample was actuated at  $\sim 55\text{ }^{\circ}\text{C}$  above  $T_m$  of x-PU, turning to a flat shape as oriented x-PU contracted extensively. Then the initial shape was recovered by cooling at  $\sim 0\text{ }^{\circ}\text{C}$ . Such free standing reversible actuation can be repeated by alternate heating and cooling.

## **Chapter 6: Conclusions and Future Work**

### **6.1 Overall Summary**

In my research, I designed, synthesized, and fabricated several thermomechanically active polymer networks based on latent crosslinking of semicrystalline polymers, as presented in previous chapters of this dissertation. The fundamental understandings of tuning shape memory effects, especially two-way reversible shape memory (2WSM), were explored to provide general guideline for future applications. A novel, latent-crosslinkable, electrospinnable, biodegradable polyurethane was developed and the processing–thermal curing relationships in its molecular, thermal, and shape memory properties were investigated systematically. A blend system, which exhibited the shape memory assisted self-healing (SMASH) effect, and a bilayer system, which revealed the free-standing reversible actuation upon temperature triggering, were realized and studied where both relied on the electrospinning technique and the unsaturated polyurethane. The following are the conclusions and recommended studies for future directions for the work discussed in some of the previous chapters.

### **6.2 Latent-crosslinkable PCL-based Polyurethane**

#### **6.2.1 Conclusions**

Chapter 3 focused on the development of a novel, versatile thermoplastic polyurethanes containing unsaturation using a biodegradable soft segment, polycaprolactone-diol (PCL-diol), and a small functional diol with pendant allyl group, 3,4-dihydroxy-1-butene (DHB), using a one-pot synthesis technique. The molecular and thermal properties of these materials were

investigated by GPC, DSC and  $^1\text{H}$  NMR initially, and PCL<sub>3k</sub>-TPU was picked out for further study due to a suitable melting temperature that would allow favorable shape fixing. In this work, PCL<sub>3k</sub>-TPU was successfully processed into films, by solvent casting and fiber mats, by electrospinning, respectively. Dilauroyl peroxide (DLP) was used as a thermal initiator to crosslink films and electrospun mat samples covalently via compression molding process. SEM images indicate successful formation of fiber at a scale of nanometers, and a unique structure containing partially melted fibers and homogeneously distributed phase. Analysis with a DMA illustrated that crosslinked PCL<sub>3k</sub>-TPUs, either in a form of film or spun mat, exhibited outstanding one-way and two-way shape memory behavior, both with decent shape fixing and recovery. Furthermore, the critical stresses were estimated, indicating that crosslinked PCL<sub>3k</sub>-TPUs needed no or very little stress for crystallization-induced elongation to take place. Last but not the least, enzymatic degradation study suggests that the processing of samples resulted in quite different microstructures, playing a significant role in degradation behavior. It is also found that our PCL<sub>3k</sub>-TPUs undergoes bulk degradation in a two-step way that the degradation progressed faster in the first a few days than after. Considering the easy processability, exceptional reversible actuation, and predictable biodegradability, we envision that this material can be utilized in mechanical and medical applications including reversible actuators, sensors, and stents.

### 6.2.2 Future Work

In light of the work specified in Chapter 2, there are a few things that can be done to tune thermomechanical properties of PCL<sub>3k</sub>-TPU in order to fulfill certain requirement for various purposes. Firstly, molecular weight of soft segments in this material correlates quite directly to the overall  $T_m$  given the results of PCL<sub>2k</sub>-TPU shown in Chapter 3. Either increasing or decreasing molecular weight could lead to extending of  $T_m$  limits towards the higher temperature end or lower

temperature end (up to a limit), respectively. However, the resulting polyurethane could turn from solid to liquid when molecular weight of soft segments was so small that  $T_m$  gets below room temperature. Also, crystallinity would decrease extensively with molecular weight, resulting in a serious decline in mechanical strength and shape memory capability of the material. On the other side, it could be not so beneficial if molecular weight went too high, because crosslink density would decrease as the crosslinking sites would be separated by one or more huge soft segments in each single polymer chain. Secondly, the alteration of crosslinker concentration could essentially shift the melting point as well as affect the mechanical stability of the material in the cured state. Thirdly, one of the most important impact of our work is that the PCL<sub>3k</sub>-TPU can serve as an important design paradigm, wherein the soft segment, here PCL, can be replaced by other biodegradable segment so as to achieve distinct physical, chemical, or biological properties ultimately. For instance, the well-known “stealth” effect accounts for the overwhelming use of poly(ethylene glycol) (PEG) in biomedical applications due to the excellent hydrophilicity of PEG, especially as the coating for drug delivery, that allows enhancement of water solubility in the body.<sup>1</sup> So, based on our model polymer, a latent-crosslinkable PEG-based polyurethane can be developed for some biodegradable drug-delivery vehicle with featuring shape memory. A previous study reported from our group involving a PCL network with chemically incorporated PEG-based peptide exhibited biocompatibility.<sup>2</sup> Thus, another idea would be to add bioactive factors or peptides to the PCL<sub>3k</sub>-TPU to increase the biological activity if it proves necessary. The main bioactive materials include bioactive ceramics, bioactive glasses, and bioactive glass-ceramics.<sup>3-5</sup>

Currently, many soft polymeric materials have been widely used in applications such as tissue engineering scaffolds,<sup>6,7</sup> graft stents,<sup>8,9</sup> etc. due to their enhanced mechanical properties and biocompatibility. Although, to our best knowledge, there doesn't exist a design or device on the

market thus far requiring all the features that the PCL<sub>3k</sub>-TPU equips, we envision that such scaffolds and stents can be developed using this material. In particular, one important aspect of being good scaffolds and stents is the evolution of mechanical strength during biodegradation.<sup>10-</sup>

<sup>13</sup> As presented in Chapter 3, the biodegradability of PCL<sub>3k</sub>-TPU has been reported with the presence of some lipase at a certain concentration. However, the mechanical strength as a function of degradation time was not investigated yet. The extension of the present work should help us to better estimate the potential of the material to be used as scaffolds or stents and also improve our basic understanding of the degradation mechanism from a different angle. To be applicable for *in vivo* implantation, further experiments on cytocompatibility needed. As far as we know, it was reported that cytotoxicity tests were performed on human endothelial cells for several catalysts commonly used in the synthesis of polymers for biomedical use, including tetramethylbutanediamine (TMBDA), 1-4 diazo (2,2,2) octane (DABCO), dibutyl-tin-dilaurate (DBTDL), and stannous octane (SnOct).<sup>14</sup> The extent of cytotoxicity at a concentration of 2 wt. % was in the following order: DABCO < TMBDA < SnOct < DBTDL. It is clear that DBTDL exhibited the highest cytotoxicity given that specific dose. Therefore, it becomes necessary to probe the optimal concentration of the Tin-based catalysts used for synthesis of the PCL<sub>3k</sub>-TPU, at which concentration most cells would remain alive/active and the key mechanical properties of the material would not be compromised significantly in the meanwhile. The previous work suggested a range of catalyst concentrations from 0.01 wt. % to 0.5 wt. %. Then the polymers generated at each catalyst concentration would be examined separately using MTT or related cell assay, while ordinary thermal and mechanical characterization would be done correspondingly for comparison purpose. We expect that the catalyst concentration below 0.05 wt. % may result in a cell viability greater than 70%.

Recently, it has become attractive to develop new methods to synthesize reversible networks crosslinked with dynamic covalent linkage as the resulted networks would enable particular autonomous behavior on a molecular basis like self-healing. One outstanding advance of making such reversible networks is the improvement in the either processing or adjusting ability in practical use, owing to the fact that a dynamic linkage can make the material resettable, but without requiring to destruction of the whole molecular structure, after covalent crosslinking. Promisingly, our synthesized PCL<sub>3k</sub>-TPU can be modified and tailored through a proper method of using some dynamically reversible linkages, in order to broaden the range of application in the reality. We realized that the thermally-induced Diels-Alder (DA) reaction, a [4 + 2] cycloaddition of a diene and a dienophile, is of extraordinary interest for the future work (Scheme 6-1).<sup>15</sup> More specifically, pendent furfuryl groups (PFu) could be incorporated through a thermally-induced thiol-ene radical addition reaction which takes advantage of the carbon-carbon double bonds pendent to the backbone of PCL<sub>3k</sub>-TPU. The DA linkages would form, allowing covalent crosslinking of the material in the presence of a maleimide-bearing crosslinker. Then, the cleavage of such linkages could be triggered by heating to moderate or elevated temperatures at which retro-DA reaction is favored. Thus, the modified PCL<sub>3k</sub>-TPU is anticipated to be thermally dynamic and reconfigurable to its “permanent” shapes. We envision that this could be fairly useful in applications where 2WSM effect is needed with both permanent and temporary shapes being reprogrammable to a certain extent. Besides utilizing covalent or physical crosslinking alone to achieve 2WSM effect, a combination thereof may make something unexpected but more astonishing to happen in the end. A PCL-POSS chemical/physical double network was previously elaborated by a former member of our research group, exhibiting two rubbery plateaus separated well from each other.<sup>16</sup> Unfortunately, an apparent downside is the use of a tetrathiol crosslinker through thiol-ene click

chemistry which inherently impedes the processability as discussed already in Chapter 3. However, this finding can guide exploration of future directions for continuation of our present work if of special interest is the development of a triple shape memory polymer with the ability to reset its permanent shape.

Considering the excellent ability to process and the ease to chemically crosslinking post-synthesis, we imagine that the PCL<sub>3k</sub>-TPU would have a great potential in the field of 3D printing. 3D printing has gained a great deal of public attention, in comparison to traditional manufacturing, for production of complex biomedical devices such as implants, scaffolds for tissue engineering, diagnostic platforms and drug delivery systems.<sup>17</sup> The simplified schematic setup of a polymer jetting 3D printer with separate support and build material channels, where each layer is planarized and cured by UV exposure immediately after its deposition, is shown in Figure 6-1 for presentation purpose.<sup>18</sup> However, it is known that the state of the art 3D printing techniques are severely limited by printable material and also subject to several disadvantages like mechanical stiffness and low resolution. To overcome these main limitations, there are two printing routes that seem more reasonable with our material as opposed to other solid free form fabrication technologies. Given that the PCL<sub>3k</sub>-TPU was cured effectively by a thermal treatment in the present work, one way to go is the so-called indirect 3D printing in which a negative mold is first printed and then the final polymer is cast within it. Certainly, the mold material should have an extremely high softening temperature along with good thermal and solvent resistance, and also have some feature that we can use for demolding once the positive shape was formed and finalized. As a result, we could easily make any desirable shape out of the crosslinkable polyurethane using this method and then crosslink it thermally as what has been done in Chapter 3, when a proper mold material is identified. Another approach would include photo-crosslinking instead of thermal crosslinking in order to



prevent the original constructs from being sabotaged during curing step. However, a few technical hurdles must be addressed to begin with. It is evident that continuous UV exposure would generate a significant amount of heat which could melt the semicrystalline material to eventually lose the shape programmed initially, a phenomenon also referred to as shape recovery. A proper strategy of photo-crosslinking is necessarily required in this regard. It may be a good idea to alternate UV exposure (on and off) to avoid accumulating too much heat that would trigger shape recovery. However, such an approach may be difficult to implement at an industrial scale. Moreover, another primary concern is the net efficiency for photo-crosslinking of an opaque polymer. It is obvious that, in that sense, the polymer chains at the surface would have a relatively higher degree of crosslinking as compared with those closer to the geometric center due to some kind of shielding effect of the surface molecules on the transmittance of UV light. Even though we don't have a good solution to this yet, perhaps creation of high porosity through porogen-leaching may help.<sup>19,20</sup> If a certain number of interconnected pores were created across the entire construct, the crosslinking difference between the surface and inside should be minimized as possible. Note that, to attain high degree of crosslinking, it could be equally important to pick a suitable photo-crosslinker which is able to distribute evenly rather than to aggregate together. Therefore, it is worth to try suspending porogens among the material and leaching it without affecting the material to yield numerous pores which may likely result in a global uniformly crosslinked network.

## **6.3 Self-reversible Actuators**

### **6.3.1 Conclusions**

Chapter 5 explains explicitly the advantage of soft, stimulus-responsive, self-reversible actuation in applications where use of external constraints or stress is largely restricted. In this chapter, a

novel, convenient fabrication process for thermal-triggering free-standing actuators via electrospinning process was developed. The model actuators consist of a covalently crosslinked, semicrystalline polyurethane with a lower  $T_m$  and a thermoplastic elastomeric polyurethane with a higher  $T_m$ . Micro-geometry and molecular anisotropy were implemented to investigate their influence on the resulting actuation behavior of various designs. Actuation characterization was done for multiple cycles in succession along with microstructural, thermal, dynamic mechanical, and shape memory analysis, to thoroughly understand underlying mechanisms. The results showed that different actuations were achieved without application of an external stress and with variations of micro-geometry and molecular orientation. Such variations afforded a variety of reversible actuation phenomena, including bending, twisting, flattening, and untwisting actuation. Two simple actuation mechanisms corresponding to specific design were presented to explain the specific actuation phenomenon as well as the origin of distinct actuations. We envision that this approach, considering necessary modification and optimization, can be used in biomedical and/or mechanical applications such as micro-robotics, biomedical devices and artificial muscles, shape changing substrates, among others.

### **6.3.2 Future Work**

In the current study, we recognized that solutions to the large deflection of a thin plate or laminate can be used to generally describe the actuation behavior of our actuators specified in Chapter 5, which were based on a structure of bilayer, using the equation in the following:  $EI = Ebh^3/12$ , where  $EI$  stands for bending rigidity,  $E$  for Young's modulus,  $h$  for thickness, and  $b$  for width. Therefore, in order to optimize the actuation performance for each actuator, these parameters must be tuned in coordination appropriately as they have great influence for either layer. Since the thickness of each layer is proportional to the corresponding ejection time during electrospinning,

a gradient of ejection times for each component would be used to develop a composition gradient for the final bilayer ranging from 10:90 to 90:10 w/w at a fixed increment of 10 wt. %. The other parameter (i.e. width) in that equation remains unaltered. Then a profile of actuation performance as a function of thickness would be obtained for us to further understand the actuation behavior and to find out the optimized fabrication parameters for optimal actuation performance.

In Chapter 5, all the actuators revealed a contractile 2WSM effect, regardless the design and geometry. Based on our knowledge of common 2WSM materials, we speculated that 2WSM behavior in tension should exhibit a significantly larger actuation magnitude than that in compression. So, it would be fantastic if we could find an elastomeric material that exerts tensile stress onto the SMP, and also if the final actuator can reprogram both actuated (upon heating) and reset shape (upon cooling) to varying degrees even after completion of crosslinking. McMullin et al introduced a family of biodegradable thermoplastic elastomers (TPEs) containing POSS as a physical crosslink (Scheme 6-2), demonstrating not only a dependence of thermal and mechanical properties on the POSS content but also a high elasticity with greater than 70% recovery.<sup>21</sup> More importantly, this material is absolutely electrospinnable, and its equilibrium shapes can be changed by melting and subsequent recrystallizing the POSS segments. Hence, the future plan was illustrated in Scheme 6-3. In particular, we can dual-spin the x-PU containing an amount of crosslinker and the TPE (here the POSS-based, reconfigurable TPE) at the same time, or to make bilayers like what has been done in Chapter 5. During electrospinning, there should be no need for introducing any molecular anisotropy. Hot compaction would be conducted to chemically crosslink the x-PU. Subsequently, the sample would be heated to ca. 15 °C above  $T_m$  of the POSS, then stretched uniaxially to a large extent, and finally cooled down to a low temperature below all  $T_c$ 's while the external stress is maintained. At this point, if POSS content was enough to hold the

TPE's new permanent state, the TPE should apply tensile stress to the covalently crosslinked x-PU whose permanent shape is unchangeable unless chemical bonds were broken. Note that small recovery after unloading would be acceptable as entropic recovery of x-PU and elasticity of TPE may need to reach a new stress equilibrium. Therefore, an easy design could be a free-standing uniaxial actuator that may be capable of adjusting its reversible actuation magnitude upon resetting the "permanent" state of TPE component. Moreover, making a tri-layer that has one component sandwiched by the other can provide a better geometrical symmetry to avoid any bias generated during thermal curing.

During the exploration of twisting or untwisting actuation in self-reversible actuator development, further designs were inspired as well. Today it has been of increasing interest to develop helical fibers that resemble plant tendrils at the nanoscale due to potential applications in fields such as nanoscale sensors, filtration materials, and oil sorbents.<sup>22-24</sup> In this regard, Wu et al invented an enlightening approach for the fabrication of the helical nanofibers with polyurethane and poly(*m*-phenylene isophthalamide) by the co-electrospinning system with an offset-centered core-shell spinneret (Figure 6-2).<sup>25</sup> Applying this idea to our case, we could use exactly the same co-electrospinning setup but feed the core-syringe and the shell-syringe with the x-PU and the Pellethane, respectively. The biggest advantage of doing so is that the Pellethane sheath can perfectly confine the flow of the melted x-PU and thus maintain the integrity of the fibrous structure during thermal curing. High rotating speed of the collecting drum could be adopted in order to create molecular orientation. Then the helical fibers would be heated to crosslink under the condition that physical restriction is in place to prevent the stress relaxation of the Pellethane shell, assumed that any pre-existed molecular anisotropy would be erased by rearrangement of

polymer chains. By switching Pellethane with the aforementioned TPE, we can develop a helical self-reversible actuator at the nanoscale, and with the ability to adjust the helical pitch and radius.

In the context of resettable 2WSM effect, another idea was inspired on a dual-electrospinning basis. Previously, a poly(tetrahydrofuran)-based polyurethane incorporating backbone carrying unsaturation (x-THF) was synthesized and then crosslinked with peroxide to form networks which exhibited promising 2WSM effect. Besides, Meng et al demonstrated a single-phase, self-reversible actuator through internal stress-induced crystallization of dual-cure networks (Figure 6-3), which provided good guidance on a potential direction for the present work.<sup>26</sup> So, a dual-cure network consisting of the x-PU and x-THF could be engendered, using dual-electrospinning process, to achieve triple shape memory as well as resettable 2WSM effect as the  $T_m$ 's of the two polymers are separated sufficiently. There will be two approaches as described below: one is to crosslink the two polymers with the same crosslinker simultaneously and then to program each temporary shape one by one; the other is to use different crosslinkers, which require different activation temperatures for effective crosslinking, to crosslink the two polymers separately so that one polymer can be crosslinked in a strained state at a temperature after the other has already been cured fully at another temperature. In addition, thanks to the dual-electrospinning technique, a functionally graded shape memory composite would be possible by adjusting the ejection rate for each polymer during the electrospinning process, theoretically similar to what a former group member has accomplished.<sup>27</sup> We envision that this functionally graded, self-reversible actuator, if worked out well, can offer great potential for material-based temperature actuators as well as in applications where controlled shape actuation is on demand.

## 6.4 References

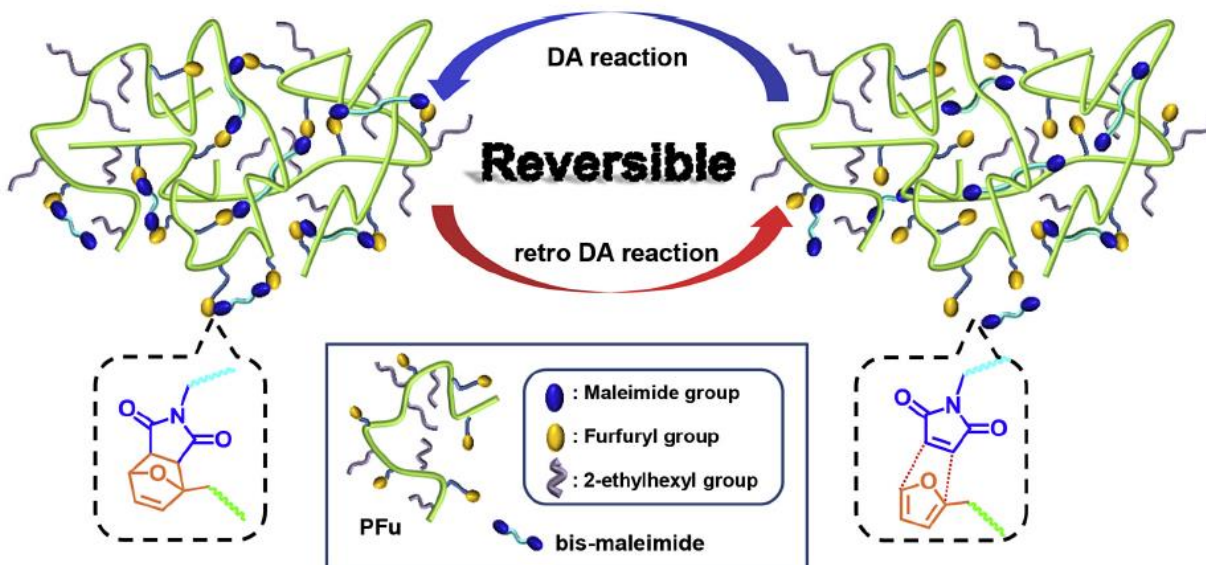
1. Knop, K.; Hoogenboom, R.; Fischer, D.; Schubert, U. S.: Poly(ethylene glycol) in Drug Delivery: Pros and Cons as Well as Potential Alternatives. *Angew. Chem. Int. Ed.* **2010**, 49, 6288 – 6308.
2. Xu, X.; Davis, K. A.; Yang, P.; Gu, X.; Henderson, J. H.; Mather, P. T.: Shape Memory RGD-containing Networks: Synthesis, Characterization, and Application in Cell Culture. *Macromol. Symp.* **2011**, 309-310, 162 – 172.
3. Jarcho, M.; Kay, J. F.; Gumaer, K. I.; Doremus, R. H.; Drobeck, H. P.: Tissue, Cellular and Subcellular Events at A Bone-ceramic Hydroxylapatite Interface. *J. Bioeng.* **1977**, 1, 79 – 92.
4. Jarcho, M.: Calcium Phosphate Ceramics as Hard Tissue Prosthetics. *Clin. Orthop. Relat. Res.* **1981**, 157, 259 – 278.
5. Hench, L. L.; Splinter, R. J.; Allen, W.; Greenlee, T.: Bonding Mechanisms at the Interface of Ceramic Prosthetic Materials. *J. Biomed. Mater. Res.* **1971**, 5, 117 – 141.
6. Holzwarth, J. M.; Ma, P. X.: Biomimetic Nanofibrous Scaffolds for Bone Tissue Engineering. *Biomaterials* **2011**, 32, 9622 – 9629.
7. Agrawal, C.; Ray, R. B.: Biodegradable Polymeric Scaffolds for Musculoskeletal Tissue Engineering. *J. Biomed. Mater. Res.* **2001**, 55, 141 – 150.
8. Mani, G.; Feldman, M. D.; Patel, D.; Agrawal, C. M.: Coronary Stents: A Materials Perspective. *Biomaterials* **2007**, 28, 1689 – 1710.
9. Hind, P.; Hong, J.; Lam-Tsai, Y.; Gress, F.: A Comprehensive Review of Esophageal Stents. *Gastroenterol. Hepatol.* **2012**, 8, 526 – 534.

10. Middleton, J. C.; Tipton, A. J.: Synthetic Biodegradable Polymers as Orthopedic Devices. *Biomaterials* **2000**, 21, 2335 – 2346.
11. Maurus, P. B.; Kaeding, C. C.: Bioabsorbable Implant Material Review. *Oper. Tech. Spots Med.* **2004**, 12, 158 – 160.
12. Yaszemski, M. J.; Payne, R. G.; Hayes, W. C.; Langer, R. S.; Aufdemorte, T. B.; Mikos, A. G.: The Ingrowth of New Bone Tissue and Initial Mechanical Properties of A Degrading Polymeric Composite Scaffold. *Tissue Eng.* **2007**, 1, 41 – 52.
13. Chu, C. C.: Hydrolytic Degradation of Polyglycolic Acid: Tensile Strength and Crystallinity Study. *J. Appl. Polym. Sci.* **1981**, 26, 1727 – 1734.
14. Tanzi, M. C.; Verderio, P.; Lampugnani, M. G.; Resnati, M.; Dejana, E.; Sturani, E.: Cytotoxicity of Some Catalysts Commonly Used in the Synthesis of Copolymers for Biomedical Use. *J. Mater. Sci. Mater. Med.* **1994**, 5, 393 – 396.
15. Jung, S.; Liu, J.; Hong, S.; Arunbabu, D.; Noh, S.; Oh, J.: A New Reactive Polymethacrylate Bearing Pendent Furfuryl Groups: Synthesis, Thermoreversible Reactions, and Self-Healing. *Polymer* **2017**, 109, 58 – 65.
16. Lee, K. M.; Knight, P. T.; Chung, T.; Mather, P. T.: Polycaprolactone-POSS Chemical/Physical Double Networks. *Macromolecules* **2008**, 41, 4730 – 4738.
17. Chia, H. N.; Wu, B. M.: Recent Advances in 3D Printing of Biomaterials. *J. Biol. Eng.* **2015**, 9, 4.
18. Hofmann, M.: 3D Printing Gets A Boost and Opportunities with Polymer Materials. *ACS Macro Lett.* **2014**, 3, 382 – 386.

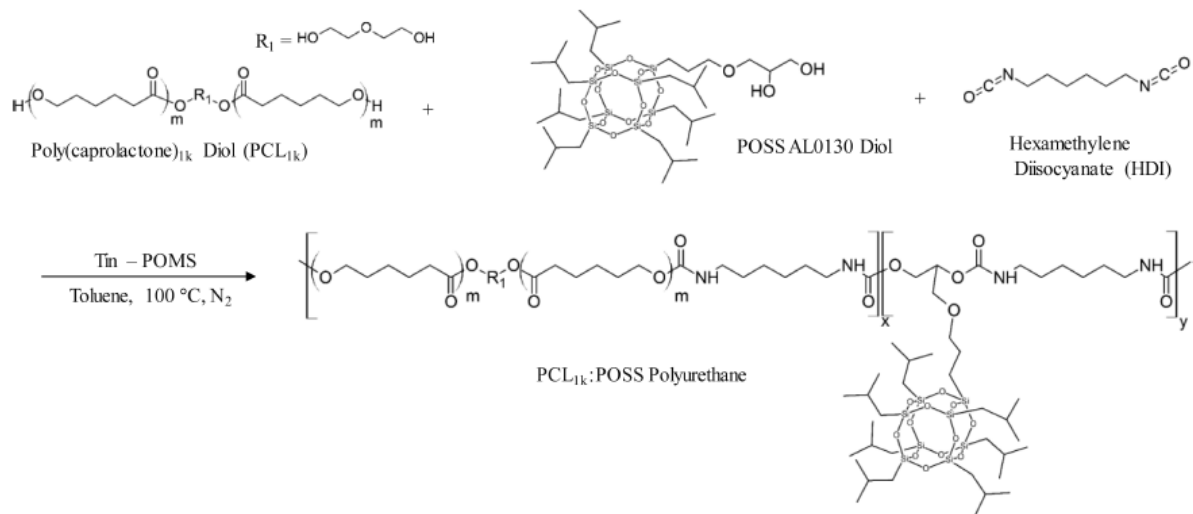
19. Tran, R. T.; Naseri, E.; Kolasnikov, A.; Bai, X.; Yang, J.: A New Generation of Sodium Chloride Porogen for Tissue Engineering. *Biotechnol. Appl. Biochem.* **2011**, 58, 335 – 344.
20. Johnson, T.; Bahrapourian, R.; Patel, A.; Mequanint, K.: Fabrication of Highly Porous Tissue-engineering Scaffolds Using Selective Spherical Porogens. *Biomed. Mater. Eng.* **2010**, 20, 107 – 118.
21. McMullin, E.; Rebar, H. T.; Mather, P. T.: Biodegradable Thermoplastic Elastomers Incorporating POSS: Synthesis, Microstructure, and Mechanical Properties. *Macromolecules* **2016**, 49, 3769 – 3779.
22. Yan, Y.; Yu, Z.; Huang, Y. W.; Yuan, W. X.; Wei, Z. X.: Helical Polyaniline Nanofibers Induced by Chiral Dopants by A Polymerization Process. *Adv. Mater.* **2007**, 19, 3353 – 3357.
23. Gao, Y.; Hao, J.; Wu, J.; Zhang, X.; Hu, J.; Ju, Y.: Supramolecular Helical Nanofibers Assembled from A Pyridinium-functionalized Methyl Glycyrrhetate Amphiphile. *Nanoscale* **2015**, 7, 13568 – 13575.
24. Lee, C. C.; Grenier, C.; Meijier, E. W.; Schenning, A. P. H. J.: Preparation and Characterization of Helical Self-assembled Nanofibers. *Chem. Soc. Rev.* **2009**, 38, 671 – 683.
25. Wu, H.; Zheng, Y.; Zeng, Y.: Fabrication of Helical Nanofibers via Co-electrospinning. *Ind. Eng. Chem. Res.* **2015**, 54, 987 – 993.
26. Meng, Y.; Jiang, J.; Anthamatten, M.: Shape Actuation via Internal Stress-induced Crystallization of Dual-cure Networks. *ACS Macro Lett.* **2015**, 4, 115 – 118.



27. DiOrio, A. M.; Luo, X.; Lee, K. M.; Mather, P. T.: A Functionally Graded Shape Memory Polymer. *Soft Matter* **2011**, 7, 68 – 74.

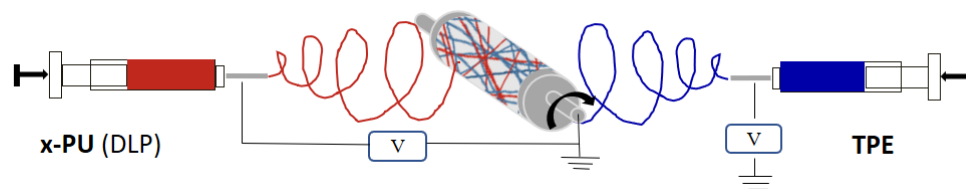


**Scheme 6-1.** Thermoreversible DA/retro-DA reactions of dynamically-crosslinked networks prepared from a reactive mixture containing PFu having pendent furfuryl groups and a bismaleimide model crosslinker. (Adapted with permission from Jung, S.; Liu, J.; Hong, S.; Arunbabu, D.; Noh, S.; Oh, J.: A New Reactive Polymethacrylate Bearing Pendent Furfuryl Groups: Synthesis, Thermoreversible Reactions, and Self-Healing. *Polymer* **2017**, *109*, 58 – 65.).

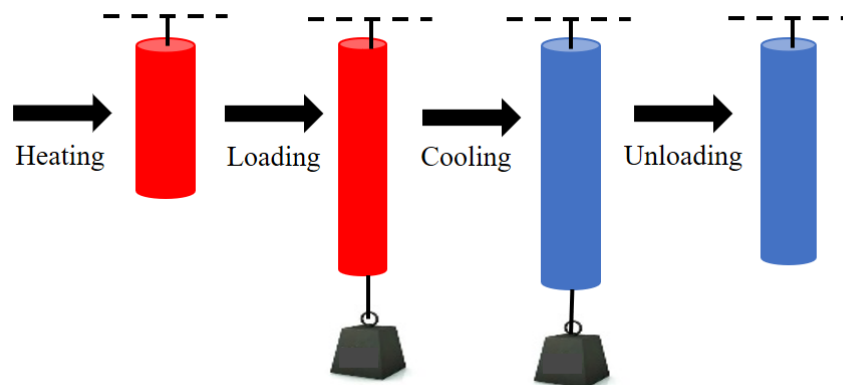


**Scheme 6-2.** Example schematic of a POSS-incorporating polyurethane synthesis. (Adapted with permission from McMullin, E.; Rebar, H. T.; Mather, P. T.: Biodegradable Thermoplastic Elastomers Incorporating POSS: Synthesis, Microstructure, and Mechanical Properties. *Macromolecules* **2016**, *49*, 3769 – 3779.).

**Step 1:**



**Step 2:**



**Scheme 6-3.** Example schematic of fabrication process for the free-standing actuators which may exhibit reversible two-way actuation in tension. First is to dual-spin the x-PU containing an amount of crosslinker and the TPE at the same time. Hot compaction would be conducted to chemically crosslink the x-PU. Subsequently, the sample would be heated to ca. 15 °C above  $T_m$  of the POSS, then stretched uniaxially to a large extent, and finally cooled down to a low temperature below all  $T_c$ 's while the external stress is maintained.

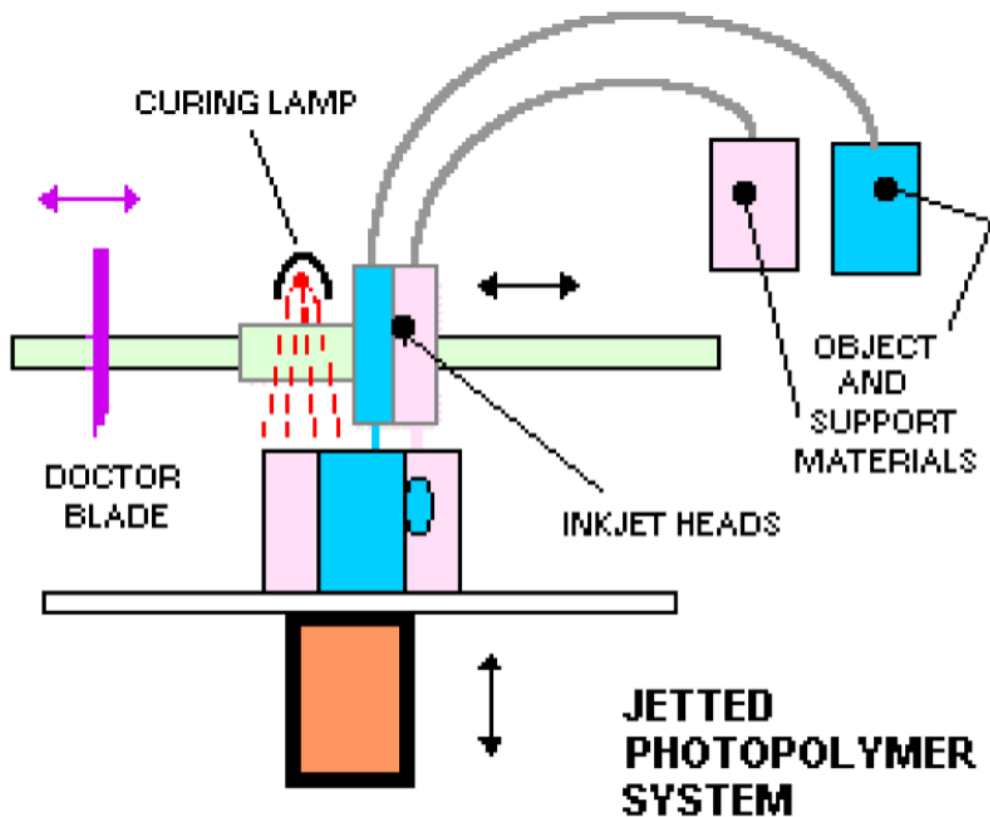


**Figure 6-1.** Simplified presentation of a polymer jetting 3D printer with separate support and build material channels; where each layer is planarized and cured by UV exposure immediately after its deposition. (Adapted with permission from Hofmann, M.: 3D Printing Gets A Boost and Opportunities with Polymer Materials. *ACS Macro Lett.* **2014**, *3*, 382 – 386.).

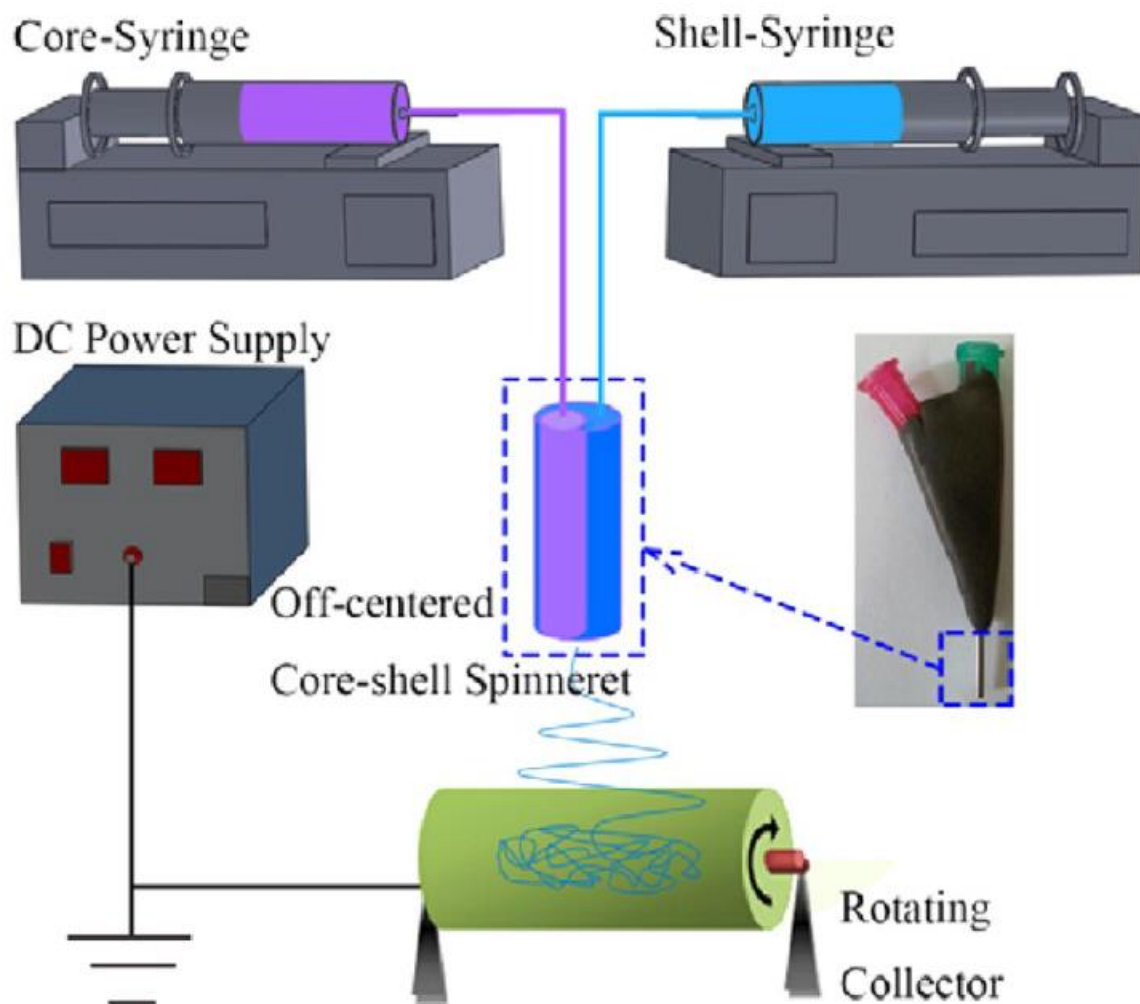


**Figure 6-2.** Schematic of off-centered co-electrospinning system. (Adapted with permission from Wu, H.; Zheng, Y.; Zeng, Y.: Fabrication of Helical Nanofibers via Co-electrospinning. *Ind. Eng. Chem. Res.* **2015**, *54*, 987 – 993.).

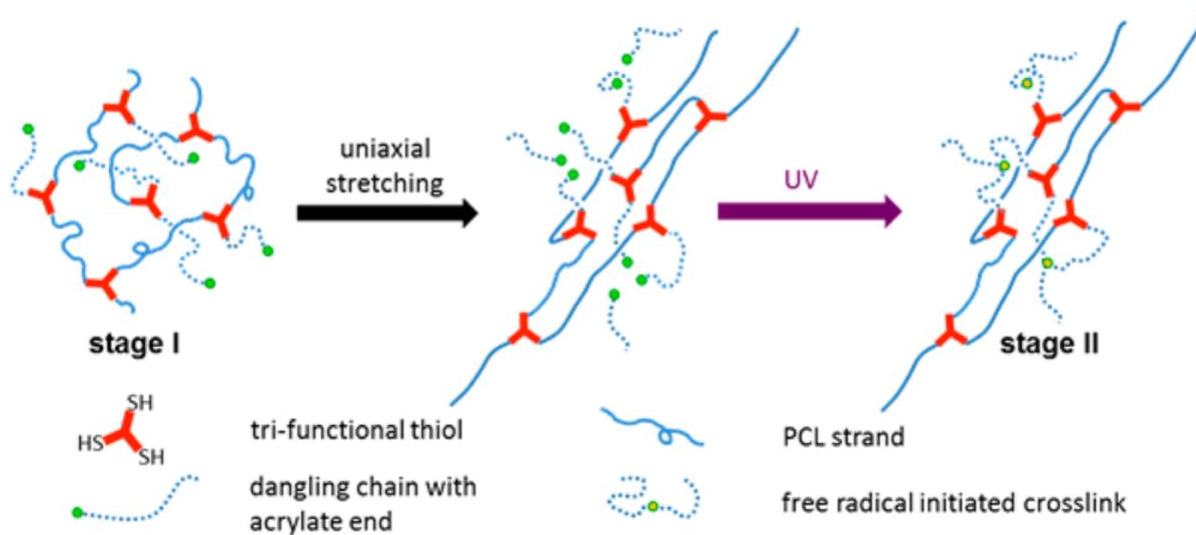


**Figure 6-3.** Cartoon showing preparation of dual-cure network stress-free actuators. (Adapted with permission from Meng, Y.; Jiang, J.; Anthamatten, M.: Shape Actuation via Internal Stress-induced Crystallization of Dual-cure Networks. *ACS Macro Lett.* **2015**, *4*, 115 – 118.).

## Appendix

### A1. Poly(tetrahydrofuran)-based Polyurethane

#### A1.1. POSS-incorporating PU

Motivation: Seeking to achieve reversible actuation in the 20 – 40 °C, a different approach was proposed to use a multiblock polymer architecture consisting of two blocks in which the “soft” block is the crystalline switching block with relatively low melting transitions, the “hard” block with a higher thermal transition ( $T_g$  or  $T_m$ ), and the two are linked together by a linker molecule.<sup>1,2</sup> In such approach, the primary synthetic variables include: the composition and molecular weight (MW) of each block, the weight percentage of the hard block, and the total MW of the multiblock copolymer. It is recognized that the composition and MW of each block will impact their melting points. This is particularly important for the soft block since that will regulate the actuation and recovery temperatures, which need to be near ambient temperature. Consequently, both the composition and MW of the soft block will be varied. Initially, we will hold fixed the value of the hard block’s MW at 30% and quickly “freeze” the design of the hard block when a synthesis approach and melting temperature value for that block are satisfied. A third block or modification to the linker molecule can be introduced to enable the polymers to be dispersed in a waterborne suspension if that process is deemed useful in the future. However, development of that polymer chemistry is beyond the scope of the proposed work.

Methods: Based on our knowledge and experience with the known polymer chemistry that might meet the requirements, poly(tetrahydrofuran)-diol (pTHF) with a nominal  $M_n$  of 2,900 g/mol, TMP diolisobutyl POSS (POSS), and hexamethylene diisocyanate (HDI) were chosen via step-



growth polymerization for such chemistry (Scheme A1.1.1). In order to attain good crosslink density and high total MW, two synthesis strategies were developed in the following: the one-step reaction and the two-step, end-capping reaction, the former featuring a one-pots synthesis in Toluene at 90 °C for 10 h, using the Tin POSS catalyst (Hybrid Plastics®). In the latter strategy, a prepolymer, supposedly with relatively low MW, is first produced from pTHF and HDI only for varying times under a mild reaction condition (70 °C), and then POSS is added to continue the reaction for an extended time (8 h), but at a higher temperature (90 °C), to form the final polyurethane architecture. The pTHF:POSS:HDI feed ratio, mass of catalysts used, or a combination thereof was varied for optimization purpose. The prepolymer reaction time, for the second route exclusively, was varied to understand the dependence on final MW. Note that the cage-like structure in POSS, here, acts as a physical crosslink.<sup>3</sup> Last but not the least, thermal, dynamic mechanical, and shape memory experiments were carried out to characterize the material. Note that the samples, which were prepared for the experiments mentioned above, were all annealed by heating to and being held at 130 °C for 1 h, then cooling slowly to and being held at 50 °C for 1 h, and further cooling to -20 °C, for the purpose of maximizing the POSS crystallization.

Preliminary Results: A summary of all the synthesis attempts was shown in Table A1.1.1. The results of DSC tests were posted in Figure A1.1.1, revealing two individual melting transitions on heating which represented the melting of pTHF and that of POSS, respectively. The storage modulus was plotted for two representative samples prepared, correspondingly, by the two synthesis routes, as shown in Figure A1.1.2. The one-way and two-way shape memory cycles for the PU1:2:3C1.5N5 sample were shown in Figure A1.1.3 and A1.1.4, respectively. It was evident that the polyurethane synthesized without the prepolymer step exhibited good, repeatable 1WSM except the training cycle (first cycle) while the 2WSM behavior was promising but showing

moderate “creep” in strain, which requires further improvement in order to be useful in practical application.

### **A1.2. Saturated PU, Acylation, and Crosslinking**

Motivation: Solid polymer electrolytes have attracted worldwide interest as potential replacement for solvent electrolytes that largely limit the thermal stability, energy density, and safety of commercial secondary lithium cells.<sup>4,5</sup> Poly(tetrahydrofuran) (pTHF) came up as an excellent candidate who resembles poly(ethylene oxide) (PEO) and improves the ionic conductivity of lithium batteries when doped with alkali salts.<sup>6,7</sup> However, neither pTHF nor PEO could provide the room temperature ionic conductivity sufficient for battery applications and also have operating temperatures high enough to maintain the solid form of polymer electrolytes. Moreover, we hypothesized that nanofibers with principal molecular orientation would have a positive influence on ionic conductivity since the interlaying of fibers generates large surface area facilitating high electrolyte uptake and easy transport of ions.<sup>8</sup> We realized that it is necessary to improve thermal stability of the material to boost the operating temperature up to high values by crosslinking the material to become a thermoset. Concerning that, Theron et al elaborated a brilliant way to modify, crosslink and reactively electrospin a thermoplastic medical polyurethane for vascular graft application, wherein acylation of urethane linkage resulted in pendent allyl groups actively available for covalent crosslinking.<sup>9</sup> On the other hand, it was reported that peroxide can crosslink saturated polymer upon hydrogen adsorption.<sup>10</sup> It seems possible to achieve successful crosslinking of high MW pTHF without need of acylation. Therefore, our approach is to develop a high MW pTHF that allows acylation to create allyl crosslinking sites as well as formation of fine nanofibers. Subsequent tuning and improving will be a must to tackle the ultimate goal, but that was beyond the scope of this dissertation.

Methods: A simple and effect step-growth polymerization was performed based on pTHF-diol and HDI or a different diisocyanate (Scheme A1.2.1). Some microstructural and thermal characterization were done as preliminary studies for this work. The acylation procedures using 4-pentenoyl chloride were specified in Scheme A1.2.2. The acylated samples were demonstrated by taking photos of physical appearance, and NMR analysis was utilized to assess success of crosslinking. In terms of the polymers that were not treated by acylation processing, HDI-N4 was used to mix with diauroyl peroxide (DLP, Luperox<sup>TM</sup>, Sigma-Aldrich), which likely has a better affinity with polyurethane DCP, through solvent casting in order for covalent crosslinking. The curing time, crosslinker concentration, or a combination thereof was varied to understand the optimal curing condition for this method. Gel fraction measurements were conducted to quantitatively evaluate the extent of crosslinking, which was followed by related mechanical and shape memory analysis. On the other side, for electrospinning process, 1 g un-acylated polymer was fully dissolved in a solvent mixture comprising 12 mL THF and 8 mL DMF, the ejecting needle was held at a potential of 12 kV, the tip-to-collector distance with 10 cm, the rotation rate of a 57.1 mm collecting drum was maintained at 1000 rpm while the drum was held at a potential of 0.5 kV and a flow rate of polymer solution supplying the 22 Gauge needle was 2.0 mL/h, all employed over the 10-hour process.

Preliminary Results: The synthesis results were compiled in Table A1.2.1. The thermal properties of all synthesized polymers were presented in Figure A1.2.1, showing that the  $T_m$ 's spread over the 18 – 24 °C range. The HDI-N2 and HDI-N4 were chosen for further analysis as well as acylation processing due to their relatively high MWs. The pictures showing acylated HDI-N2 and HDI-N4 were available in Figure A1.2.2. Furthermore, NMR spectra for these two samples were shown in Figure A1.2.3, revealing very unremarkable characteristic peaks for the allyl

function groups, perhaps, due to not-so-successful acylation processing. To investigate peroxide crosslinking of saturated polymers, the curing studies on HDI-N4 were concluded in Table A1.2.2. DMA was employed to investigate the thermomechanical properties of the HDI-N4 samples at various states: uncured, cured with 1.0 wt. % DLP for 1 h, and cured with 1.0 wt. % DLP for 1.5 h, respectively, as indicated in Figure A1.2.4. It was observed that both cured samples showed a rubbery plateau in modulus after melting transition as compared to the uncured. Also, it seems that the rubbery plateau would be extended towards the higher temperature end in some degree when crosslinker concentration was increased and higher gel fraction values were obtained. In addition, 1WSM and 2WSM cycles for both D1T1.0 and D1T1.5 were plotted in Figure A1.2.5 and A1.2.6, respectively, suggesting promising shape memory properties but with severe “creep” in strain most likely due to low degree of crosslinking. In the end, the unacylated HDI-N4 was processed into a fibrous web, both sides of which were imaged using SEM, as shown in Figure A1.2.7.

### **A1.3. Backbone-carrying Unsaturation**

Motivation: Previously, to make pTHF networks that can show good 2WSM effect, we tried to acylate the high MW pTHF and then crosslink it thermally with the presence of thermal initiator, or crosslink the high MW pTHF directly. Neither approaches turned out to be completely successful for the reasons stated above. A kind of chemically more active crosslinking site is required to be incorporated through a modification method featuring a higher conversion rate. In view of prior experience and our knowledge of polymer chemistry, *cis*-2-butene-1,4-diol (BeD),<sup>11-13</sup> a small molecule that possesses a backbone-carrying carbon-carbon double bond which allows covalent crosslinking, is chosen to insert into the old chemical formula.

Methods: BeD, pTHF-diol, and HDI were polymerized together in the presence of 1 wt. % Tin POMS catalyst through a one-port reaction process where toluene was the solvent and inert reaction atmosphere was applied during the 12-h course (Scheme A1.3.1). The dried product was cast, with 1 wt. % DLP, into a film which was then crosslinked by compression molding. Thermal, dynamic mechanical, and shape memory analysis were carried out to characterize the material at different crosslinking states.

Preliminary Results: The DSC profiles were recorded in Figure A1.3.1 for the crosslinkable pTHF-based PU before and after curing, respectively. A nice rubbery plateau was found only for the cured sample, as indicative of decent crosslinking (Figure A1.3.2). The 2WSM behavior of the cured sample was showcased in Figure A1.3.3, suggesting a temperature-regulating reversibility with improved mechanical stability in comparison to the predecessors of the material.

## **A2. PCL-diols and PCL-based PUs Bearing Unsaturation in Backbone**

Motivation: Continuing on the work done to develop crosslinkable polyurethane, there exists a different approach to incorporate the unsaturation by making unsaturated polyolefin instead of adding a small, unsaturated diol. However, there may be several pros and cons for this idea: first of all, it would be easier to control distribution of the crosslinking sites when only the polyolefin bearing the unsaturation and the linker are needed for the reaction; higher chances would be expected to achieve high total molecular weight if the stoichiometry was involved for two reagents other than three; nonetheless, crosslink density would be negatively affected when the molecular weight of the polyolefin got too high. Poly( $\epsilon$ -caprolactone) (PCL) is an aliphatic linear polyester, biodegradable and biocompatible polymer which is FDA approved and widely used in pharmaceutical products and wound dressings.<sup>14</sup> It can be synthesized by either ring-opening

polymerization of  $\epsilon$ -caprolactone or by free radical ring-opening polymerization of 2-methylene-1,3-dioxepane.<sup>15</sup> More importantly, its melting point that falls in the range closely near room temperature may enable broader applications than the pTHF, and its good solubility makes it a great processing-wise. Thus, on one hand, we propose to synthesize a family of crosslinkable PCL-diols (x-PCL) with varying MW via ring-opening polymerization of  $\epsilon$ -caprolactone (CL) using BeD as the initiator. The x-PCL is next polymerized with HDI to form a polyurethane architecture bearing C=C unsaturation in the backbone, allowing chemical crosslinking through addition of DLP. On the other hand, a segmented polyurethane architecture is developed following the method discussed previously regarding the preparation of crosslinkable pTHF-based PU for comparison purpose. The ideas conceived here may be particularly useful in applications where a backbone-carrying unsaturation is desired versus pendent allyl groups as detailed in Chapter 3.

Methods: To fabricate the x-PCL, BeD and CL were added at a mole ratio of 1:30 into 100 mL distilled toluene and then incubated at 100 °C for 24 h under nitrogen atmosphere (Scheme A2.1). The resulting polymers were precipitated in cold hexanes and subject to 3-d vacuum drying prior to further use or processing. In the meantime, a pure PCL was prepared as a control. Along the line, the x-PCL obtained from last step was reacted with HDI at a feed mole rate of 1:1, using Tin POMS catalyst for the duration of the 24-h polymerization, to build up high molecular weights (Scheme A2.2). The crosslinkable PCL-based PU was then mixed with 1 wt. % DLP through solvent casting, following which thermal curing was performed by compression molding at 90 °C for 2 h. As an alternative method, PCL-diol with a  $M_n$  of 2 or 3 kDa, BeD, and HDI were added at a feed mole ratio of 1:1:2, simultaneously, in 100 mL distilled toluene at 100 °C for 12 h under nitrogen environment, as illustrated in Scheme A2.3. Molecular, thermal, mechanical, and shape memory characterization were conducted to understand the materials produced by each route as

well as to compare the two routes. Select synthesis batch was chosen for electrospinning (a solvent mixture of 10 mL CHCl<sub>3</sub> and 2 mL DMF; time was 8 h; voltage was 16 kV) to see if the material can be processed into a fibrous web at the micro- or nano-scale. However, thermal crosslinking of fibrous web is beyond the scope of the present study.

Preliminary Results: For the former, two-step method, a summary of synthesis results was included in Table A2.1. In addition to that a few photos were taken to visually demonstrate the physical appearance of some representative samples obtained as described above (Figure A2.1). Thermogravimetric analysis was done using TGA as shown in Figure A2.2. Figure A2.3 revealed a  $T_m$  of the synthesized x-PCLs in the 41 – 55 °C range. The chemical composition for a representative x-PCL sample was analyzed and confirmed with successful incorporation of C=C, as shown in Figure A2.4. After HDI added for continued polymerization, the synthesis results were summarized in Table A2.2. Note that melting point was reduced significantly while the x-PCL became corresponding x-PCL-based PU due to the incorporation of HDI which impeded crystallization of PCL phase. The thermal features upon second heating were studied selectively for the x-PCL-TPU N3, N5, and N6 sample, as found in Figure A2.5. Furthermore, the NMR spectra of x-PCL-TPU N5 and N6 were provided, respectively in Figure A2.6a and b, to especially verify the incorporation of C=C unsaturation. Particularly, for x-PCL-TPU N5, three attempts were made to create fibrous mats using electrospinning technique at varying ejecting rate of polymer solutions which were 1.0 mL/h, 1.5 mL/h and 2.0 mL/h, and, corresponding results were shown individually in Figure A2.7. The x-PCL-TPU N5 crosslinked by 1 wt. % DLP was tested using DMA, revealing a decent rubbery plateau after occurrence of melting transition (Figure A2.8). Switching gear to the latter, one-step method, we can find related synthesis results in Table A2.3. The chemistry of the synthesized polymers was investigated using NMR analysis, which indicated

successful addition of C=C in the backbone of both PCL<sub>2k</sub>-based and PCL<sub>3k</sub>-based PUs as shown in Figure A2.9. The BeD-PCL<sub>2k</sub>-TPU N2 and BeD-PCL<sub>3k</sub>-TPU N1 were weighed 2 g separately, adding in a solvent mixture of 8 mL CHCl<sub>3</sub> and 2 mL DMF, and finally electrospinning at an ejecting rate of 1.5 mL/h under 16 kV for 10 h. Both resultant fibrous webs were imaged using SEM (Figure A2.10), showing that a lot of beads were generated and bonded with fibers during the 10-h electrospinning process. We attributed this to the relatively low molecular weight of the material.

### **A3. Uniaxially Self-reversible Actuator**

Motivation: Given the fact that we managed to develop a couple self-reversible actuators based on the x-PU and Pellethane, it is worth of giving a try on a design featuring uniaxial actuation. Also, the effect of molecular anisotropy on the uniaxial actuation performance is investigated to understand how to amplify the actuation magnitude the most. We speculate that this can offer a meaningful guidance on development of other actuator designs.

Methods: The x-PU containing 3 wt. % DLP was dual-spun with the Pellethane (5863-80A) to form a homogeneously distributed, interspersed fibrous mat made of these two polymers, as schematically shown in Scheme A3.1. The concentrations of x-PU and of Pellethane were 0.167 g/mL and 0.100 g/mL, respectively. A potential of 16 kV was held at the ejecting needle of the syringe supplying x-PU at 1 mL/h and a potential of 14 kV was held at the ejecting needle of the syringe supplying Pellethane at 1.7 mL/h while the collecting mandrel rotating at 400 rpm was grounded. After 10-h dual-electrospinning process, the fibrous web obtained was completely dried for 2 d prior to subsequent hot compaction, which lasted for 2 h at 90 °C under a compressive load of 1000 lb., using a hot press. Microstructural, thermal, dynamic mechanical, and shape memory



analysis were carried out to better evaluate the design and actual execution of fabrication. Speaking of influence of molecular anisotropy, two variables were considered: the rotation speed of the collecting mandrel and prestrain ahead of crosslinking. The spinning speed was altered from 400 rpm to 1000 while 0%, 50%, or 200% prestrain was utilized (i.e. sample 1: 400 rpm + 0% prestrain; sample 2: 1000 rpm + 0% prestrain; sample 3: 400 rpm + 50% prestrain; sample 4: 400 rpm + 200% prestrain). More specifically, the prestrain was introduced by stretching the as-spun samples using a custom manual stretcher, and then held at that strain throughout a 2-h curing step at 90 °C. Subsequently, the sample was unloaded from the manual stretcher and was post-cured for another 2 h at prescribed elevated temperature. At last, the uniaxial actuators prepared on different conditions were analyzed using DMA to explore the stress-free 2WSM behavior.

Preliminary Results: Figure A3.1 showed the physical appearance of the fibrous web fabricated by dual-electrospinning x-PU and Pellethane before and after thermal curing. It was evident that continuous, fine fibers were formed and these fibers turned to solid film upon heating. The DSC profiles of the fibrous web prior to and after hot compaction were plotted in Figure A3.2. The regular DMA testing was done on the crosslinked sample as revealed in Figure A3.3. Then, a tensile two-way reversible actuation under varying external forces was conducted, using DMA in the controlled force mode, to record the strain, stress, and temperature as a function of time (Figure A3.4). A tensile stress of ca. 0.8 MPa was exerted on the sample for the first two cycles and that stress was next removed for the following two cycles. It was observed that, for the two cycles in the beginning, the sample behaved the way typical 2WSM polymers do, while, more interestingly, the two-way reversible actuation was still realized, largely reduced in amplitude though, after external load was removed. We reasoned this phenomenon as an enlightening indicator of free-standing reversible actuation regulated by ambient temperature variation. Figure A3.5 showed the

uniaxial two-way actuation of all four samples, which were specified in the methods section, under externally stress-free condition. It was clearly observed that all sample revealed recognizable 2WSM effect to varying degrees except sample 1 which was prepared using rotation speed at 400 rpm without any prestraining. Among the samples tested in this experiment, sample 2 rendered the most promising 2WSM behavior in terms of actuation magnitude. Thus, we postulated that the electrospinning process has a more profound influence on molecular anisotropy as well as actuation performance than mechanical prestraining does. However, further studies such as WAXS experimentation are required to support this hypothesis and to then understand the mechanism.

#### A4. References

1. Bae, Y. H.; Huh, K. M.; Kim, Y.; Park, K.: Biodegradable Amphiphilic Multiblock Copolymers and Their Implications for Biomedical Applications. *J. Control. Release* **2000**, 64, 3 – 13.
2. Li, G.; Wang, L.; Ni, H.; Pittman Jr., C. U.: Polyhedral Oligomeric Silsesquioxane (POSS) Polymers and Copolymers: A Review. *J. Inorg. Organomet. Polym.* **2001**, 11, 123 – 154.
3. Wu, J.; Mather, P. T.: POSS Polymers: Physical Properties and Biomaterials Applications. *J. Macromol. Sci. C: Polym. Rev.* **2009**, 49, 25 – 63.
4. Tarascon, J. M.; Armand, M.: Issues and Challenges Facing Rechargeable Lithium Batteries. *Nature* **2001**, 414, 359 – 367.
5. Agrawal, R. C.; Pandey, G. P.: Solid Polymer Electrolytes: Materials Designing and All-solid-state Battery Applications: An Overview. *J. Phys. D: Appl. Phys.* **2008**, 41, 223001.
6. Alamgir, M.; Moulton, R. D.; Abraham, K. M.: Li<sup>+</sup>-conductive Polymer Electrolytes Derived from Poly(1,3-dioxolane) and Polytetrahydrofuran. *Electrochim. Acta* **1991**, 36, 773 – 782.
7. Akbulut, O.; Taniguchi, I.; Kumar, S.; Shao-Horn, Y.; Mayes, A. M.: Conductivity Hysteresis in Polymer Electrolytes Incorporating Poly(tetrahydrofuran). *Electrochim. Acta* **2007**, 52, 1983 – 1989.
8. Raghavan, P.; Zhao, X.; Kim, J.; Manuel, J.; Chauhan, G. S.; Ahn, J.; Nah, C.: Ionic Conductivity and Electrochemical Properties of Nanocomposite Polymer Electrolytes Based on Electrospun Poly(vinylidene fluoride-co-hexafluoropropylene) with Nano-sized Ceramic Fillers. *Electrochim. Acta* **2008**, 54, 228 – 234.

9. Theron, J. P.; Knoetze, J. H.; Sanderson, R. D.; Hunter, R.; Mequanint, K.; Franz, T.; Zilla, P.; Bezuidenhout, D.: Modification, Crosslinking and Reactive Electrospinning of A Thermoplastic Medical Polyurethane for Vascular Graft Applications. *Acta Biomater.* **2010**, 6, 2434 – 2447.
10. Loan, L. D.: Peroxide Crosslinking Reactions of Polymers. *Pure Appl. Chem.* **1972**, 30, 173 – 180.
11. Murakami, H.; Mastui, Y.; Ozawa, F.; Yoshifuji, M.: Cyclodehydration of *cis*-2-Butene-1,4-diol with Active Methylene Compounds Catalyzed by A Diphosphinidencyclobutene-coordinated Palladium Complex. *J. Organomet. Chem.* **2006**, 691, 3151 – 3156.
12. Son, N. T.; Jáky, M.; Simándi, L.: Kinetics and Mechanism of the Permanganate Oxidation of *cis*-2-Butene-1,4-diol. *Inorg. Nucl. Chem. Lett.* **1976**, 12, 291 – 296.
13. Musolino, M. G.; Cutrupi, C. M. S.; Donato, A.; Pietropaolo, D.; Pietropaolo, R.: *cis*-2-Butene-1,4-diol as Probe for Studying Isomerization versus Hydrogenation and Hydrogenolysis Reactions. *Appl. Catal., A* **2003**, 243, 333 – 346.
14. Ng, K. W.; Hutmacher, D. W.; Chantz, J.; Ng, C. S.; Too, H.; Lim, T. C.; Phan, T. T.; Teoh, S. H.: Evaluation of Ultrathin Poly( $\epsilon$ -caprolactone) Films for Tissue-engineered Skin. *Tissue Eng.* **2001**, 7, 441 – 455.
15. Pitt, C. G.: Poly- $\epsilon$ -caprolactone and Its Copolymers. *Drugs Pharm. Sci.* **1990**, 45, 71 – 120.

**Table A1.1.1.** Summary of Polyurethane Syntheses

Sample	Yield (Mass %)	pTHF:POSS:HDI actual ratio	Molecular Weight (M <sub>n</sub> , kDa)	PDI
PU1:2:3C3R3N1*	26.3%	2.05:1.00:2.57	718	1.33
PU1:2:3C3R2N2	36.4%	1.06:1.00:1.93	62	1.21
PU1:2:3C3R2N4	26.5%	0.75:1.00:1.69	78	1.48
PU1:2:3C1.5N5	46.5%	0.70:1.00:1.67	172	1.45
PU1:1:2C3N7	77.8%	1.44:1.00:2.81	118	1.66

\* Nomenclature: **PU** stands for polyurethane, **1:2:3** for the pTHF:POSS:HDI actual ratio determined by NMR analysis, **C3** for 3 mg catalyst used in the reaction, **R3** for 3 h reaction time for making the prepolymer, and **N1** for the very first batch of synthesis.

**Table A1.2.1.** Synthesis Results of High MW pTHF-based PUs

	Feed mole ratio (pTHF:HDI)	Yield (Mass %)	Molecular weight ( $M_n$ , kDa)	PDI	$T_m$ (°C) <sup>a</sup>	$\Delta H_m$ (J/g)
HDI-N1*	1:1	81.7	35.1	2.70	24.1	31.55
HDI-N2	1:1	74.2	102	1.74	20.6	27.64
HDI-N3	1:1	81.6	38.0	1.56	22.1	28.10
HDI-N4	1:1	82.3	219	1.61	21.7	29.97
TDI-N1	1:1	63.9	58.3	3.22	16.8	30.74

\* Nomenclature: **HDI (TDI)** for hexamethylene diisocyanate (toluene 2,4-diisocyanate), **N1** for batch 1.

<sup>a</sup>  $T_m$ 's are values at peaks by DSC (heating at 10°C/min).

**Table A1.2.2.** Synthesis Results of High MW pTHF-based PUs

	DLP Concentration (wt. %)	Curing time (h)	Curing temperature (°C)	Gel fraction (%) <sup>a</sup>
D1T1.0 *	1.0	1.0	90	34.6
D1T1.5	1.0	1.5	90	42.1
D1T2.0	1.0	2.0	90	39.8
D2T1.5	2.0	1.5	90	46.6
D2T2.0	2.0	2.0	90	51.7

\* Nomenclature: **D1** for 1 wt.% DLP, **T1.0** for 1 hour for curing time.

<sup>a</sup> Solvent extraction in THF (average from **three** tests).

**Table A2.1.** Synthesis Results of Crosslinkable PCL-diols

	Feed mole ratio <sup>a</sup> (BeD:CL)	Yield (Mass %)	Molecular weight (M <sub>n</sub> , kDa)	PDI	T <sub>m</sub> (°C) <sup>b</sup>	ΔH <sub>m</sub> (J/g)
PCL control	0:1	22.6	5.39	1.10	52.7	64.92
x-PCL N6*	1:30	39.0	6.60	1.10	55.7	67.95
x-PCL N7	1:30	99.4	5.58	1.03	49.9	64.46
x-PCL N8	1:20	94.6	3.56	1.08	52.7	66.83
x-PCL N10	1:20	94.5	2.71	1.11	41.2	72.53
x-PCL N11	1:20	97.7	4.97	1.30	48.2	61.82

\* Nomenclature: **BeD** for *cis*-2-Butene-1,4-diol, **PCL** for polycaprolactone, **N6** for attempt 6

<sup>a</sup> To estimate target degree of polymerization:  $DP=[M]/[I]$ , where [M] is concentration of monomers (CL), [I] is concentration of initiators (BD).

<sup>b</sup> T<sub>m</sub>'s are values at endothermic peaks by DSC (heating at 10°C/min)



**Table A2.2.** Synthesis Results of x-PCL-based Polyurethanes

	Yield (Mass %)	Molecular weight ( $M_n$ , kDa)	PDI	$T_m$ (°C) <sup>a</sup>	$\Delta H_m$ (J/g)
x-PCL-TPU N1 *	37.8	178	1.66	38.5	31.92
x-PCL-TPU N3 <sup>b</sup>	94.3	239	1.58	39.6	33.79
x-PCL-TPU N4	66.2	192	2.10	N/A <sup>c</sup>	N/A
x-PCL-TPU N5	75.8	59.7	1.23	42.3	42.13
x-PCL-TPU N6	72.8	49.7	1.24	44.3	4410

\* Nomenclature: **x-PCL** for crosslinkable polycaprolactone, **TPU** for thermoplastic polyurethane, **N1** for attempt 1.

<sup>a</sup>  $T_m$ 's are values at endothermic peaks by DSC (heating at 10°C/min)

<sup>b</sup> N1, N3, and N4 used x-PCL N8 as starting material; N5 and N6 originated from x-PCL N10

<sup>c</sup> N/A due to premature gelation

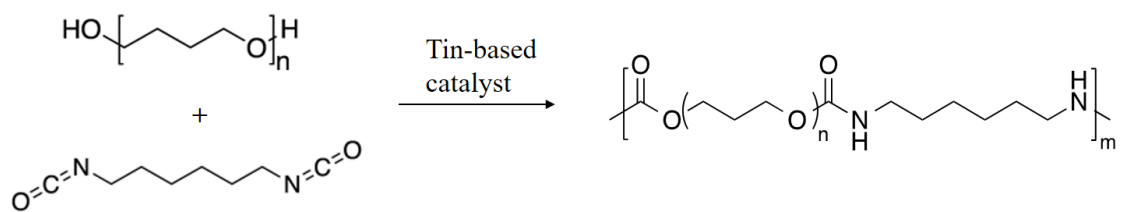
**Table A2.2.** Synthesis Results of BeD-PCL-TPUs

	Yield (Mass %)	Molecular weight ( $M_n$ , kDa)	PDI	$T_m$ (°C) <sup>a</sup>	$\Delta H_m$ (J/g)
BeD-PCL <sub>2k</sub> -TPU N1*	88.7	167	1.08	51.4	31.80
BeD-PCL <sub>2k</sub> -TPU N2	86.0	47.5	1.39	47.9	35.59
BeD-PCL <sub>2k</sub> -TPU N3	87.2	40.3	1.54	48.2	30.65
BeD-PCL <sub>3k</sub> -TPU N1	84.3	19.3	1.86	51.8	36.5
BeD-PCL <sub>3k</sub> -TPU N2	76.9	58.8	1.76	49.2	29.0

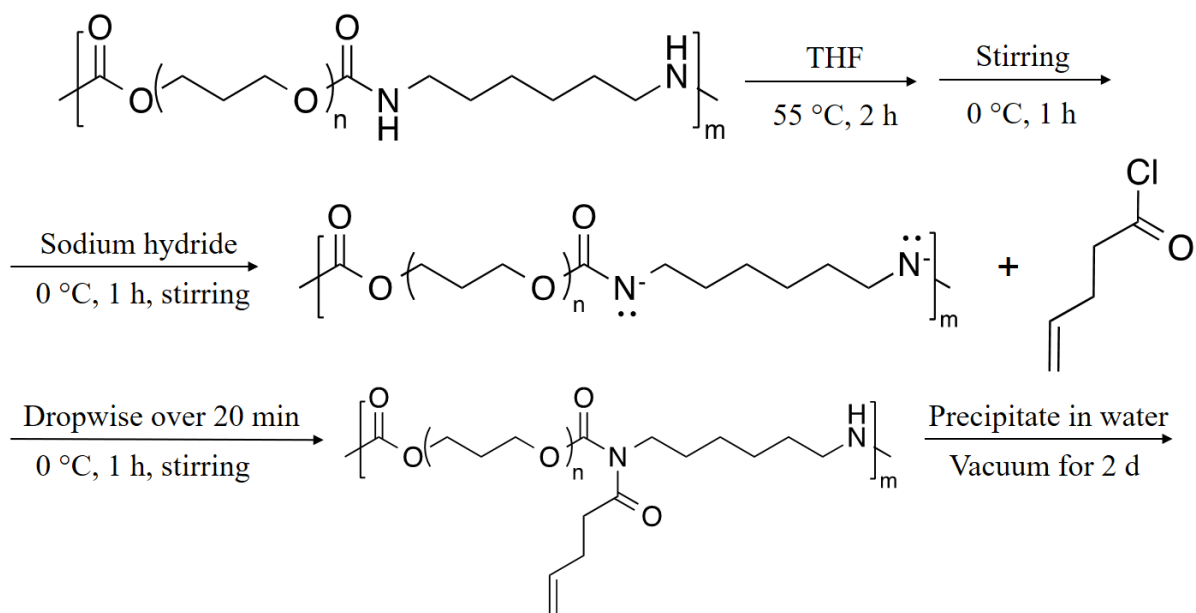
\* Nomenclature: **BeD** for *cis*-2-Butene-1,4-diol, **PCL<sub>xk</sub>** for polycaprolactone with nominal  $M_n$  of x kDa, **N1** for attempt 1.

<sup>a</sup>  $T_m$ 's are values at endothermic peaks by DSC (heating at 10°C/min)

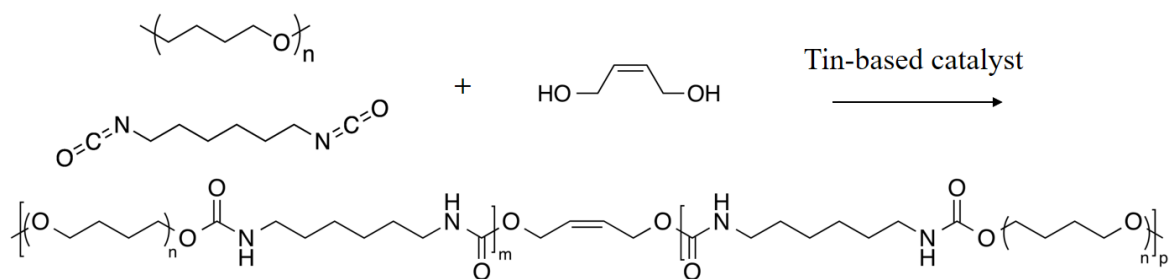




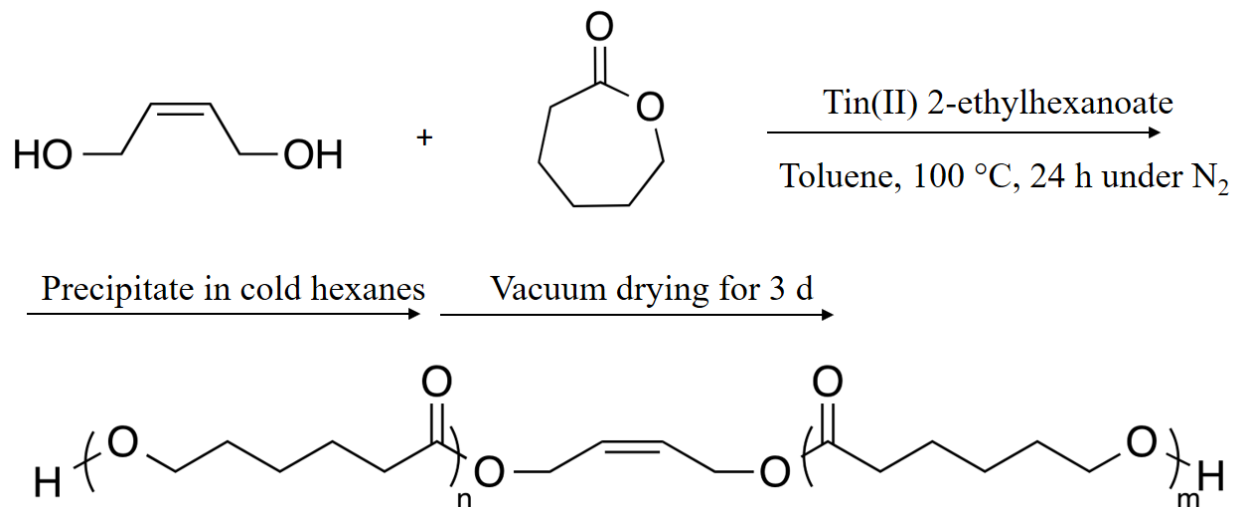
**Scheme A1.2.1.** Synthesis of high molecular weight pTHF-based polyurethane.



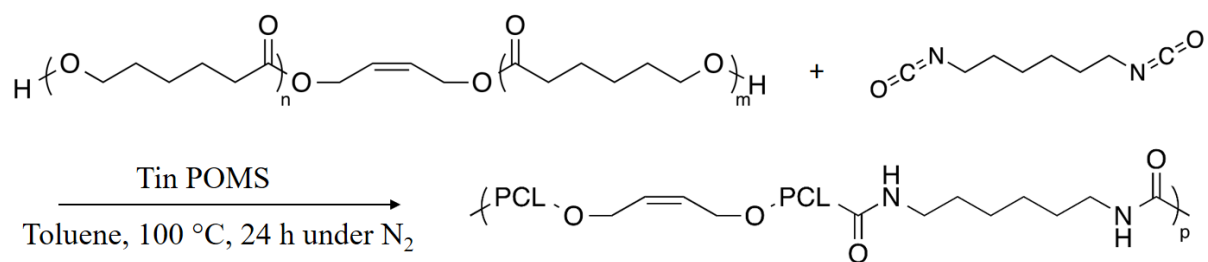
**Scheme A1.2.2.** Acylation of high molecular weight pTHF-based PU with 4-pentenoyl chloride.



**Scheme A1.3.1.** Synthesis of pTHF-based PU with backbone-carrying carbon-carbon double bonds, using pTHF-diol of 2.9 kDa, HDI, and *cis*-2-butene-1,4-diol, a small molecule having crosslinking sites.

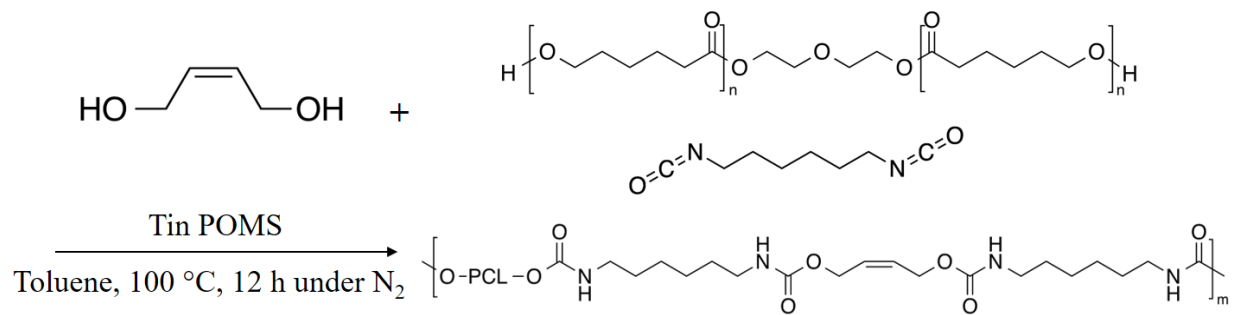


**Scheme A2.1.** Preparation of crosslinkable PCL-diol from  $\epsilon$ -caprolactone and *cis*-2-butene-1,4-diol (BeD) in effect of Tin(II) 2-ethylhexanoate.

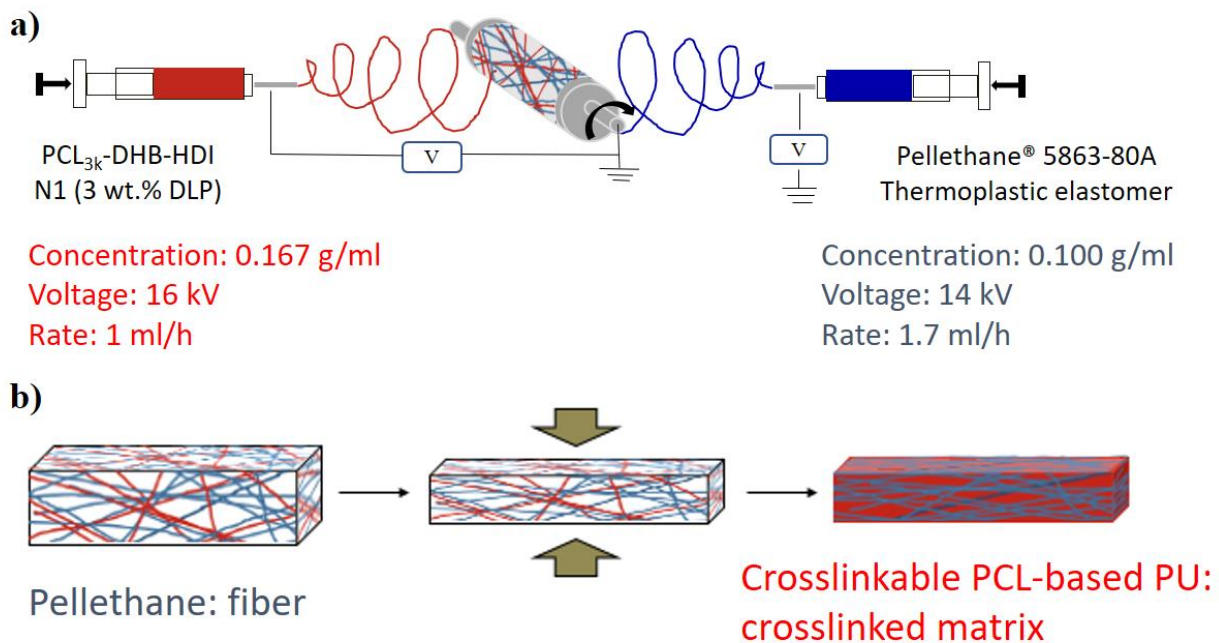


**Scheme A2.2.** Synthesis of crosslinkable PCL-based PU bearing unsaturation in the backbone using x-PCL and HDI.





**Scheme A2.3.** Synthesis of PCL-based PU with backbone-carrying carbon-carbon double bonds, using  $\epsilon$ -PCL, HDI, and *cis*-2-butene-1,4-diol, a small molecule having crosslinking sites.



**Scheme A3.1.** **a)** Schematic showing the dual-electrospinning of x-PU and Pellethane; **b)** Cartoon illustrating the thermal curing process of the spun fiber webs via hot compaction.

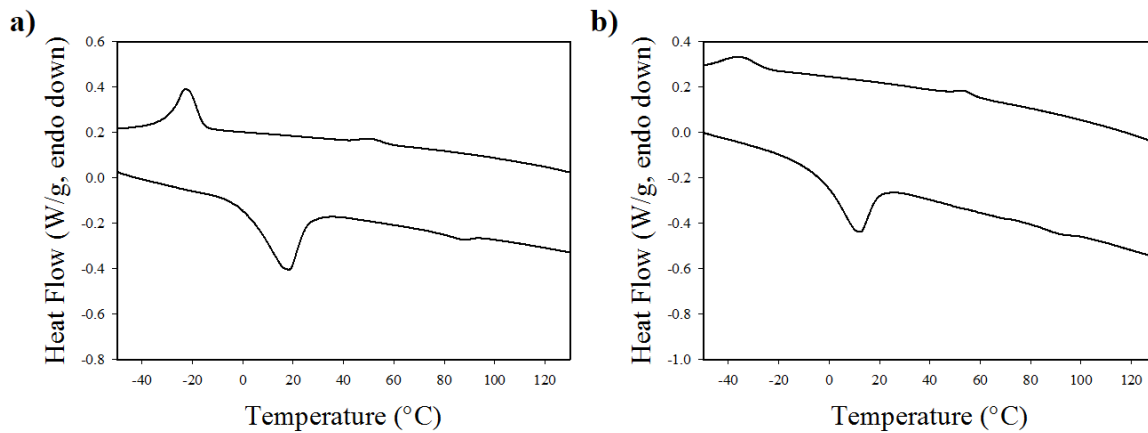


**Figure A1.1.1.** Differential Scanning Calorimetry (DSC) analysis graph of **a)** PU1:2:3C3R2N2 and **b)** PU1:2:3C1.5N5. Heating/cooling rate is 10 °C/min.

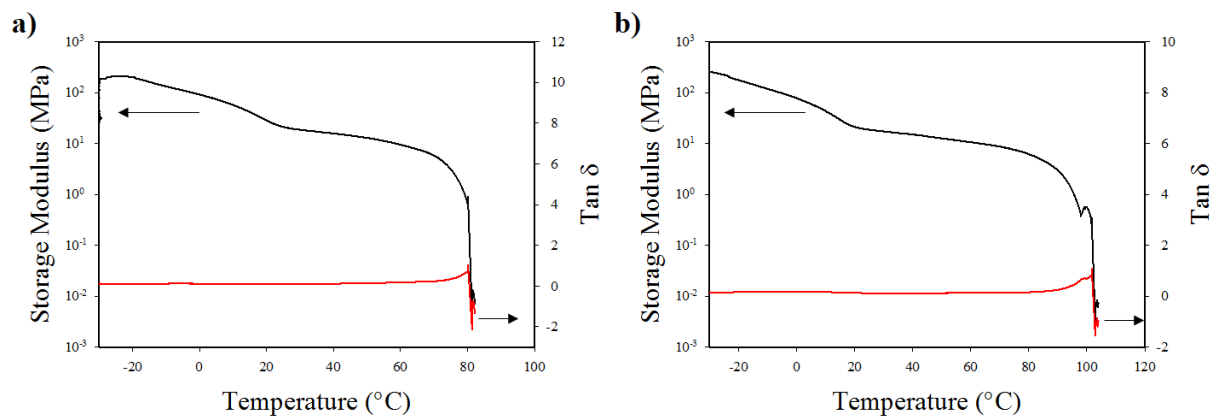


**Figure A1.1.2.** Storage modulus ( $E'$ ) profiles as a function of temperature for a) PU1:2:3C3R2N2 and b) PU1:2:3C1.5N5. The frequency is 1 Hz.

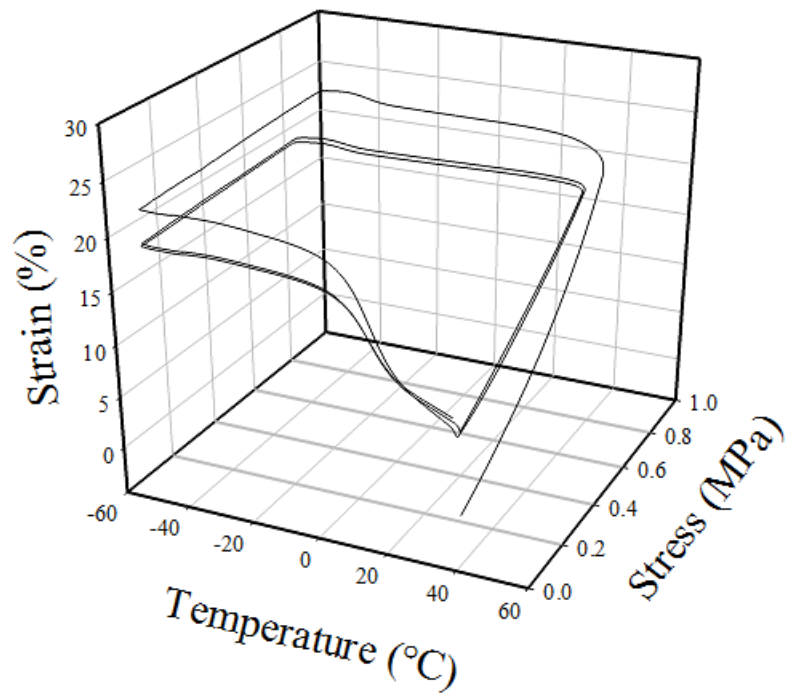


**Figure A1.1.3.** One-way shape memory cycle of PU1:2:3 C1.5N5. The sample was deformed to 20% strain at 40 °C. A temporary shape was fixed by cooling at a rate of 2 °C/min and unloading, and then the original shape was recovered by heating at 2 °C/min.

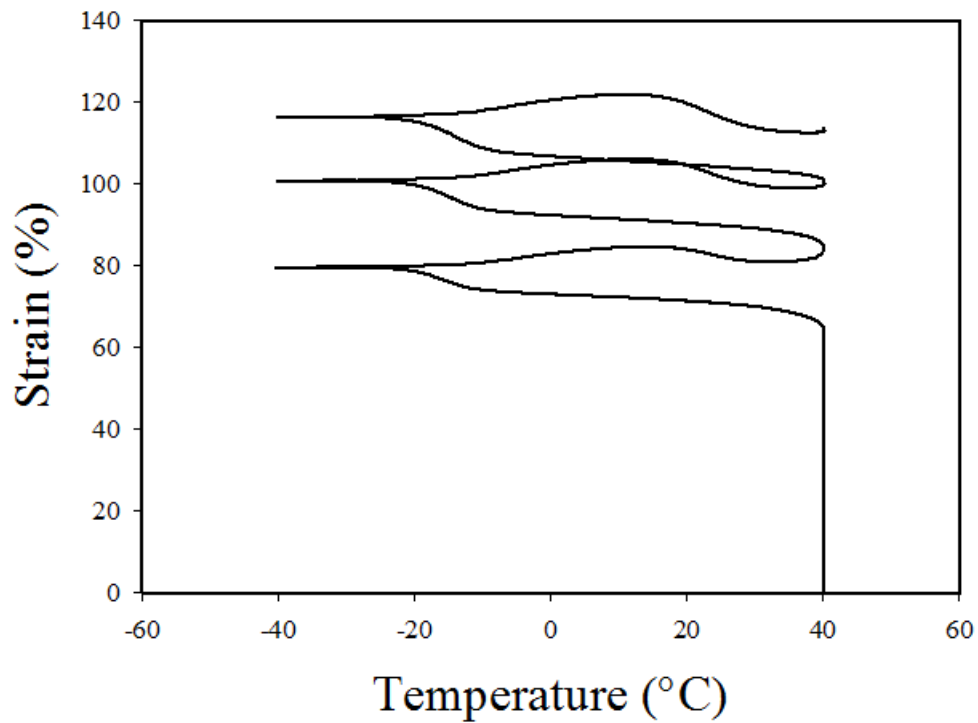


**Figure A1.1.4.** Two-way shape memory cycle of PU1:2:3C1.5N5 under application of an external stress of 0.65 MPa. The sample was stretched under high temperature (40 °C). The deformation step is followed by a cooling process at a rate of 2 °C/min, inducing an increase in strain. Then, the increased strain decreases by a heating process at a rate of 2 °C/min to 40 °C.

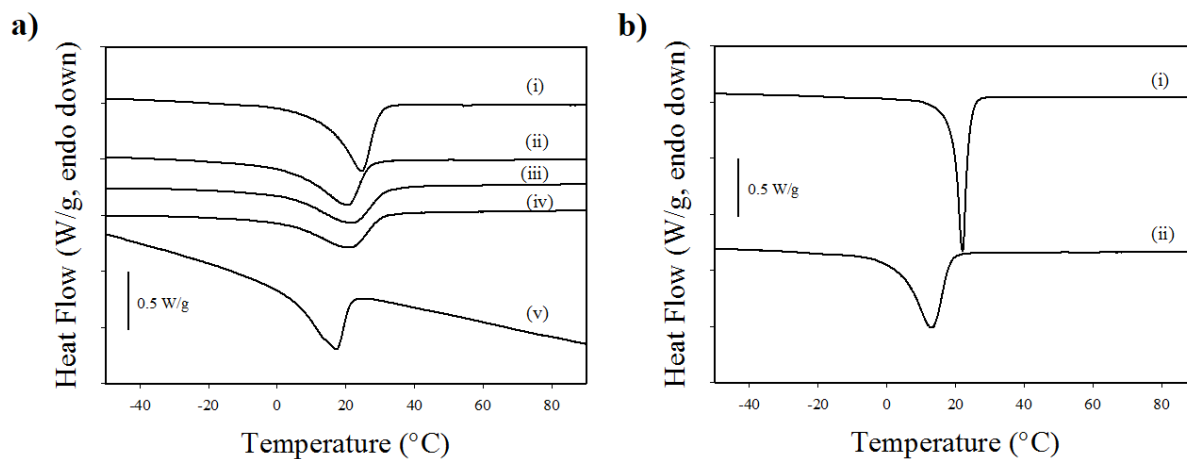


**Figure A1.2.1.** Differential Scanning Calorimetry (DSC) analysis graph of **a)** high MW pTHF-based PUs: (i) HDI-N1, (ii) HDI-N2, (iii) HDI-N3, (iv) HDI-N4, and (v) TDI-N1; of **b)** acylated HDI-N4: (i) before peroxide curing and (ii) after peroxide curing. Heating/cooling rate is 10 °C/min.



**Figure A1.2.2.** Pictures detailing the physical appearance of acylated **a)** HDI-N2 and **b)** HDI-N4.



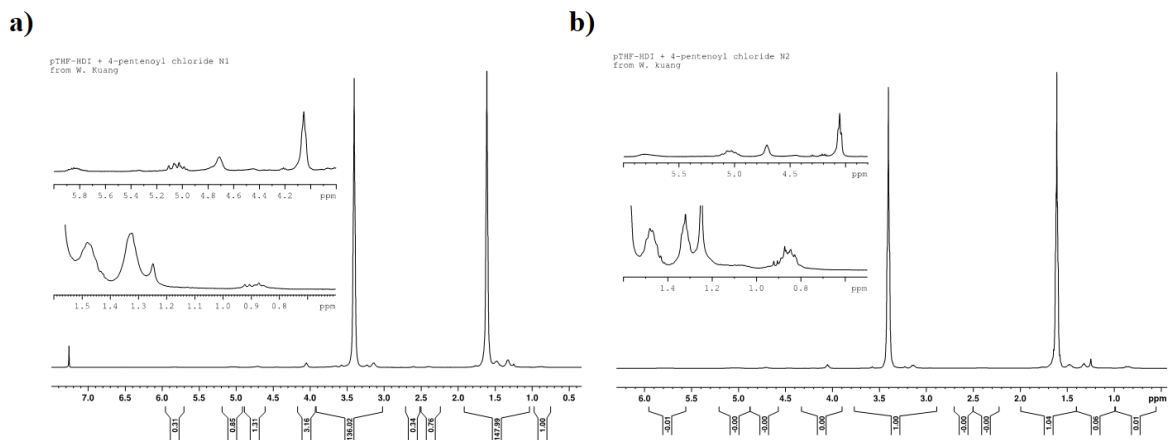


**Figure A1.2.3.** NMR spectra for **a)** acylated HDI-N2 and **b)** acylated HDI-N4.

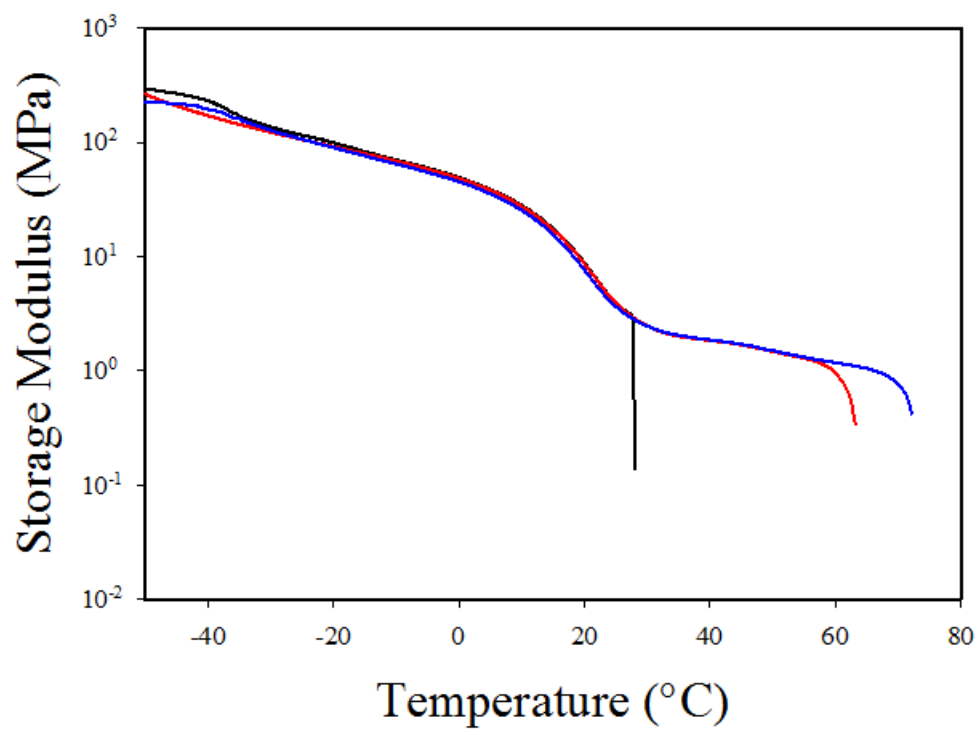


**Figure A1.2.4.** Storage modulus ( $E'$ ) profiles as a function of temperature for the HDI-N4 samples: uncured (black), D1T1.0 (red), and D1T1.5 (blue). The frequency is 1 Hz.

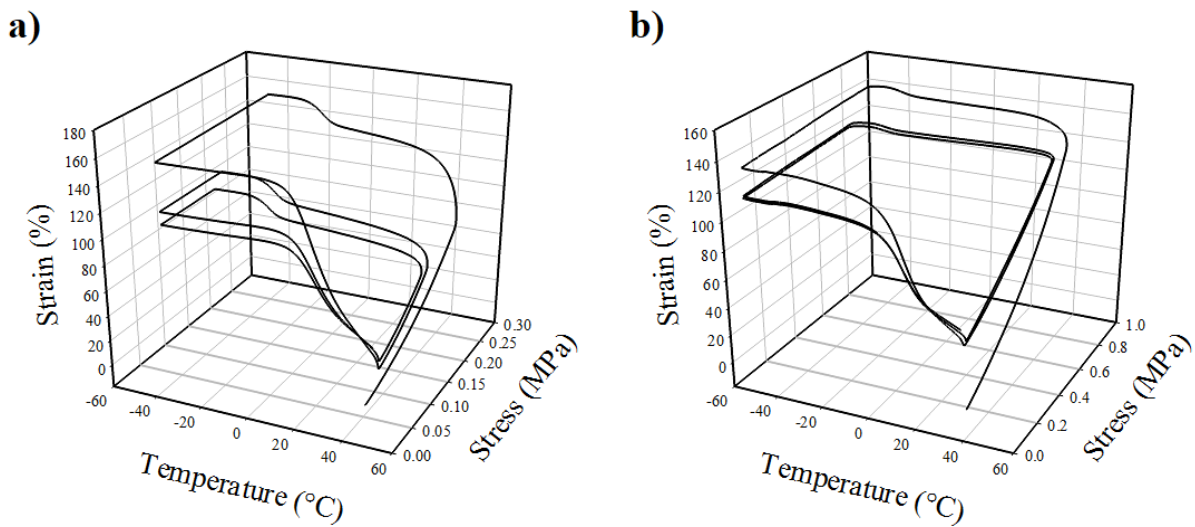


**Figure A.1.2.5.** One-way shape memory cycle of **a)** D1T1.0 and **b)** D1T1.5. The sample was deformed to 100% strain at 50 °C. A temporary shape was fixed by cooling at a rate of 2 °C/min and unloading, and then the original shape was recovered by heating at 2 °C/min.

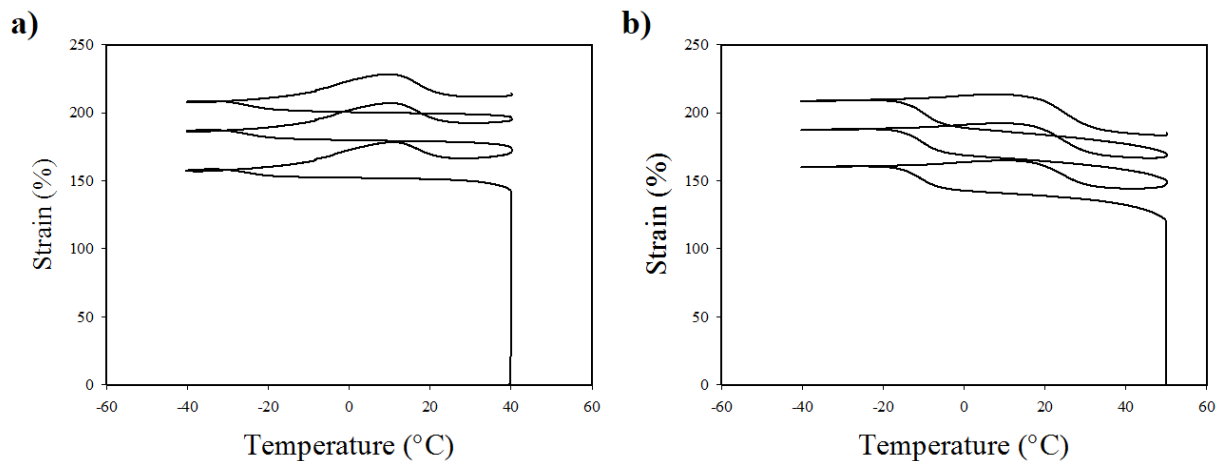


**Figure A1.2.6.** Two-way shape memory cycle of **a)** D1T1.0 and **b)** D1T1.5. The sample was stretched to ca. 150% strain at a high temperature. The deformation step is followed by a cooling process at a rate of 2 °C/min, inducing an increase in strain. Then, the increased strain decreases by a heating process at a rate of 2 °C/min.

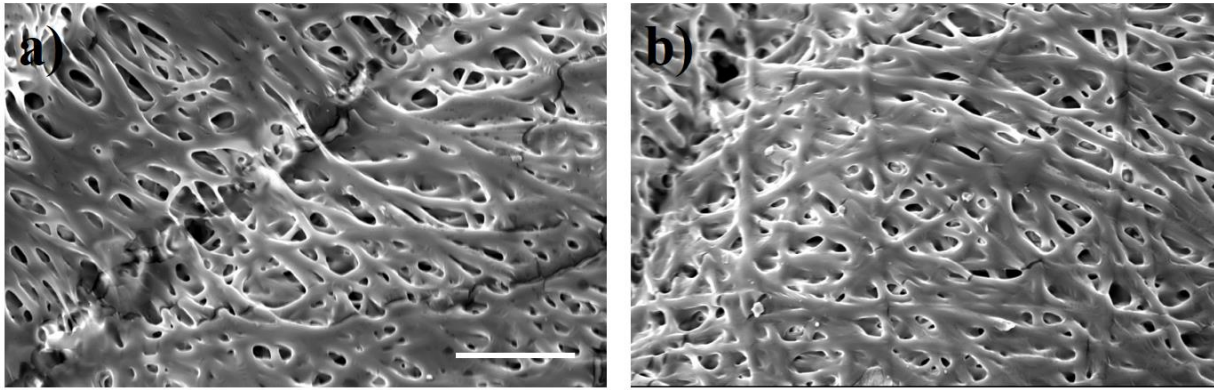


**Figure A1.2.7.** Scanning electron microscope (SEM) images of the electrospun HDI-N4 sample: **a)** top side and **b)** bottom side (in contact with the foil wrap). Scale bar = 50  $\mu\text{m}$ .

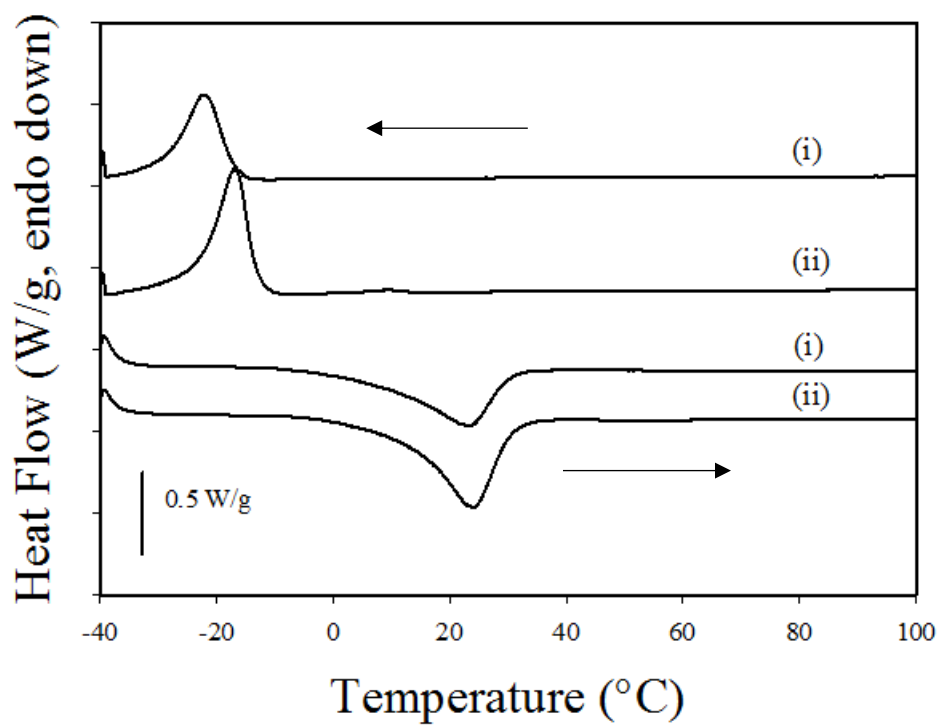


**Figure A1.3.1.** Differential Scanning Calorimetry (DSC) analysis graph of the crosslinkable pTHF-based PU: (i) before curing and (ii) after curing. Heating/cooling rate is 10 °C/min.

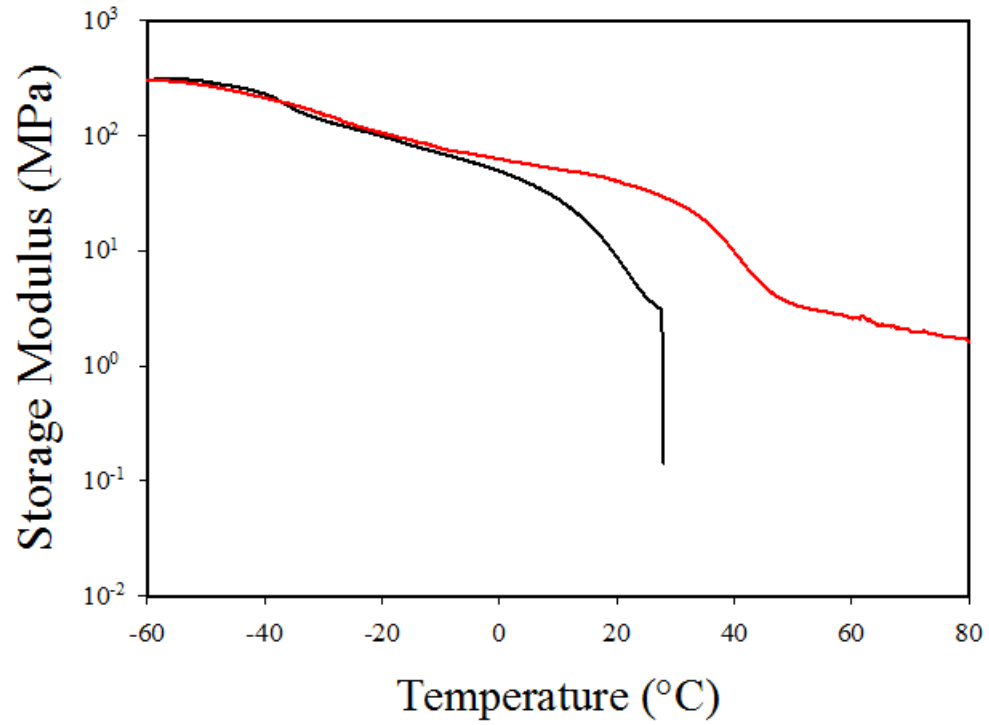


**Figure A1.3.2.** Storage modulus ( $E'$ ) profiles as a function of temperature for the crosslinkable pTHF-based PU: uncured (black) and cured with 1 wt. % DLP at 90 °C for 2 h (red). The frequency is 1 Hz.

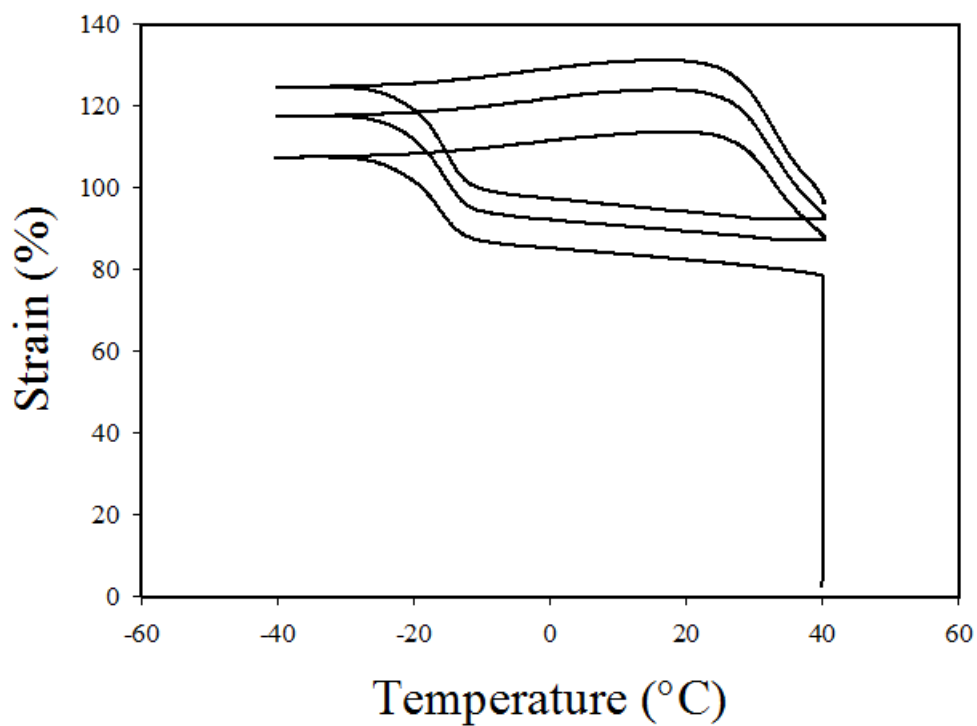


**Figure A1.3.3.** Two-way shape memory cycle of the cured pTHF-based PU. The sample was stretched to ca. 80% strain at a high temperature. The deformation step is followed by a cooling process at a rate of 2 °C/min, inducing an increase in strain. Then, the increased strain decreases by a heating process at a rate of 2 °C/min.



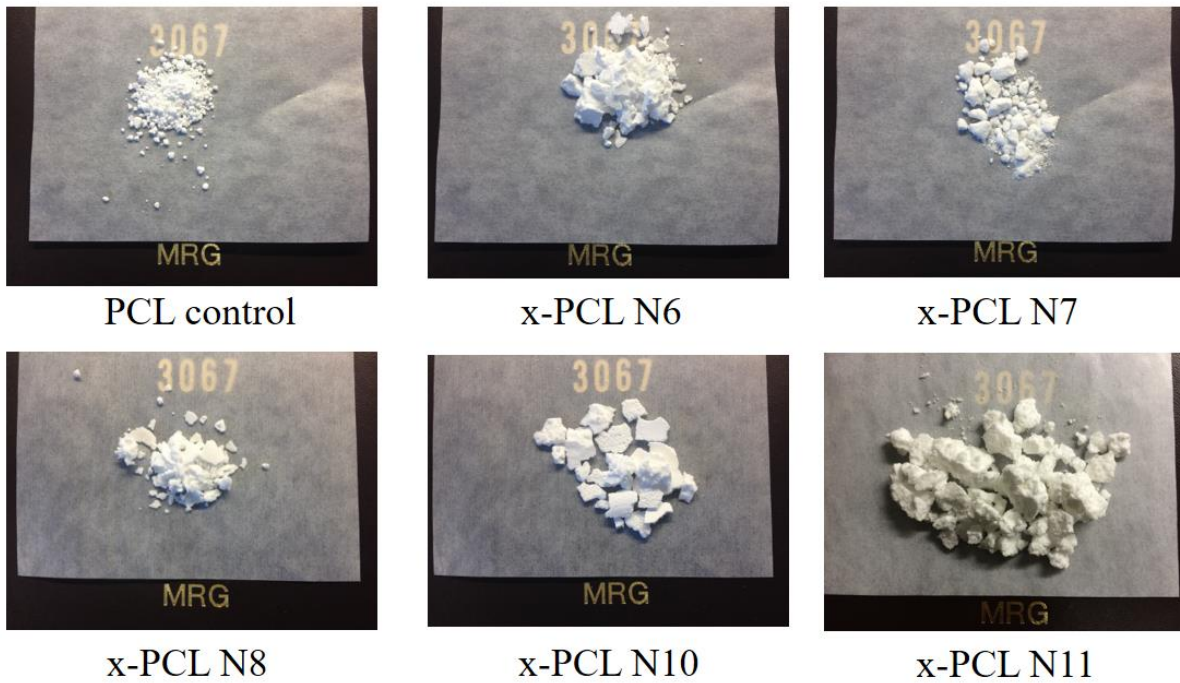


**Figure A2.1.** Pictures showing the physical appearance of synthesized x-PCLs and control PCL.

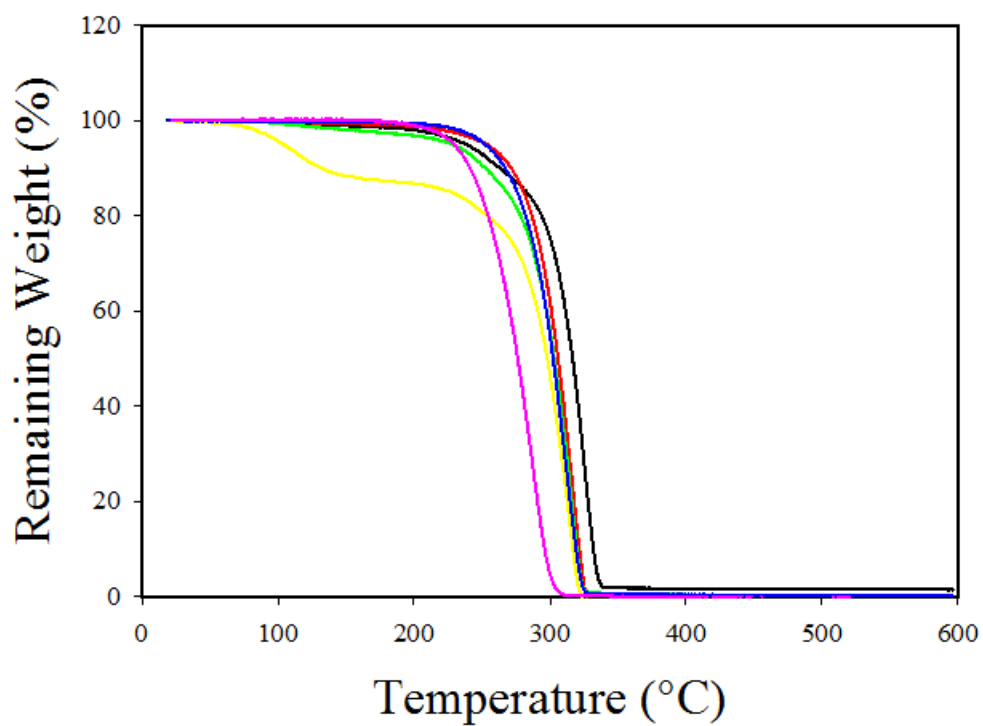


**Figure A2.2.** Thermogravimetric analysis (TGA) profiles of PCL control (black), x-PCL N6 (red), x-PCL N7 (green), x-PCL N8 (yellow), x-PCL N10 (blue), and x-PCL N11 (pink). Heating rate of 10 °C/min.

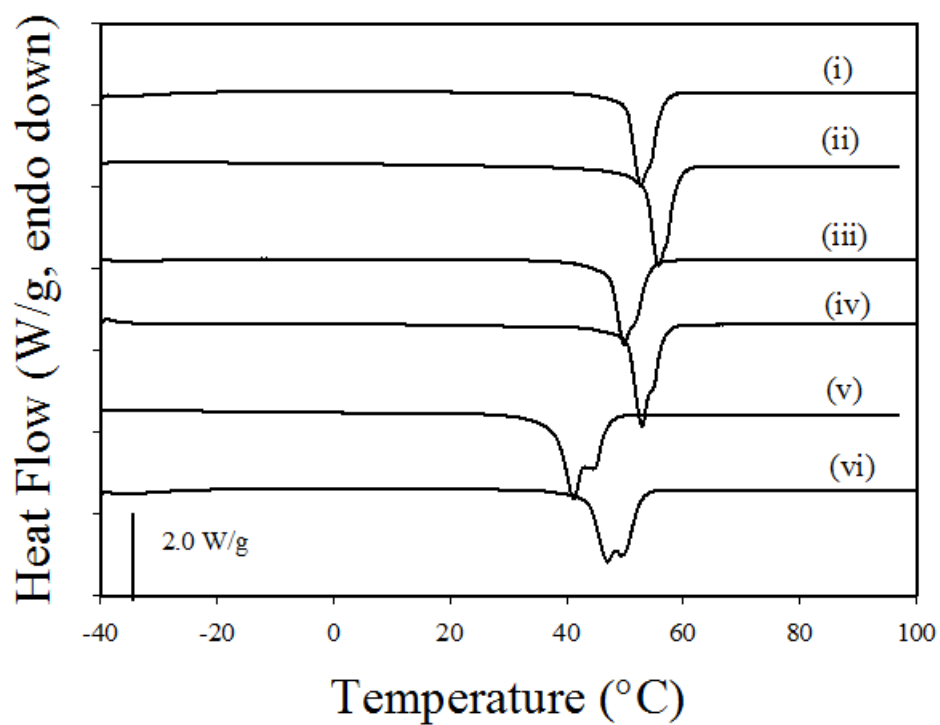


**Figure A2.3.** Differential Scanning Calorimetry (DSC) analysis graph of the x-PCLs: (i) control PCL, (ii) x-PCL N6, (iii) x-PCL N7, (iv) x-PCL N8, (v) x-PCL N10, and (vi) x-PCL N11. Heating rate is 10 °C/min.

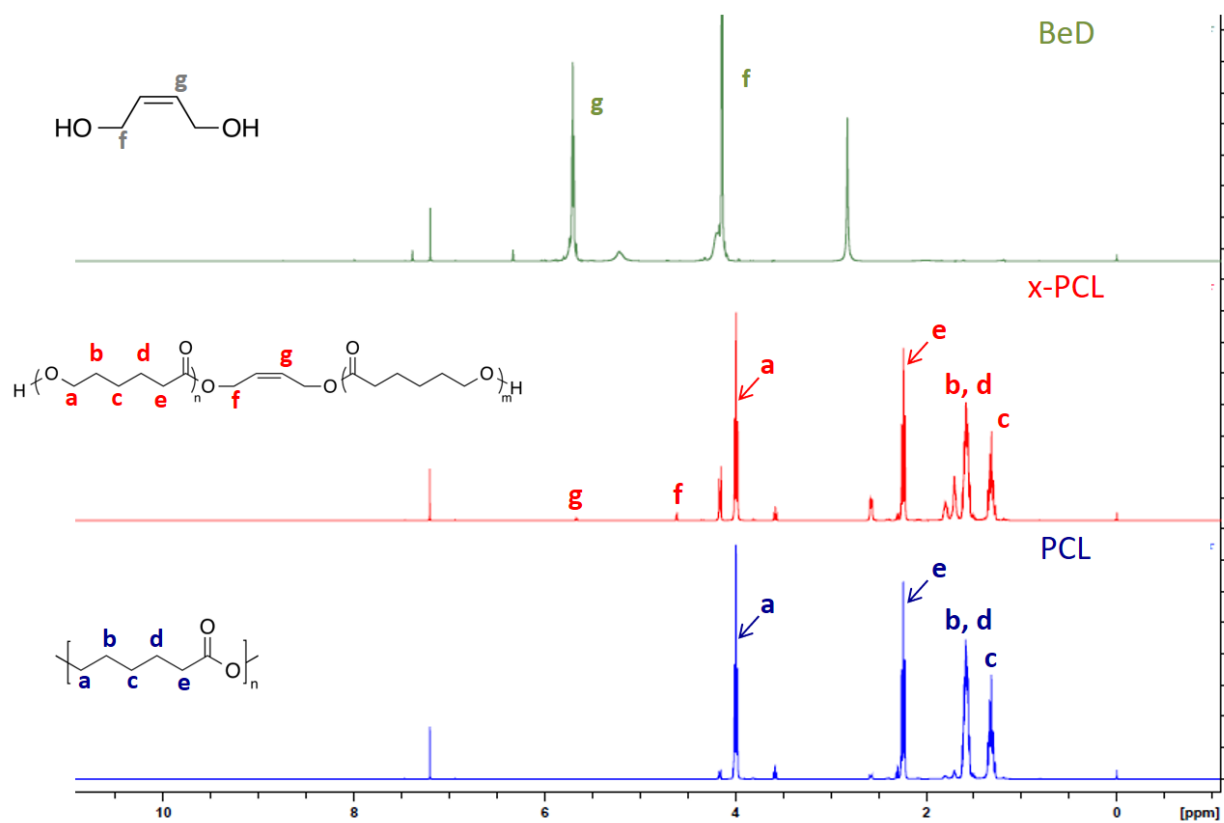


**Figure A2.4.** NMR analysis for pure BeD, control PCL, and a representative x-PCL. The characteristic peaks associated to the protons in the chemical structure are used to determine success of chemical synthesis.

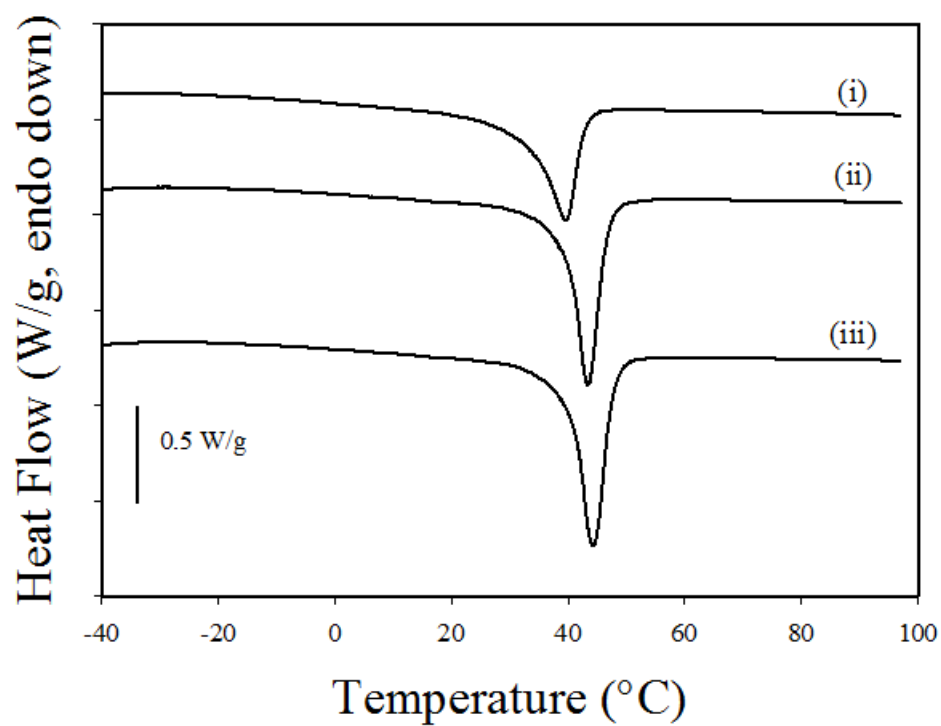


**Figure A2.5.** Differential Scanning Calorimetry (DSC) analysis graph of the x-PCL-based PUs: (i) x-PCL-TPU N3, (ii) x-PCL-TPU N5, and (iii) x-PCL-TPU N6. Heating rate is 10 °C/min.

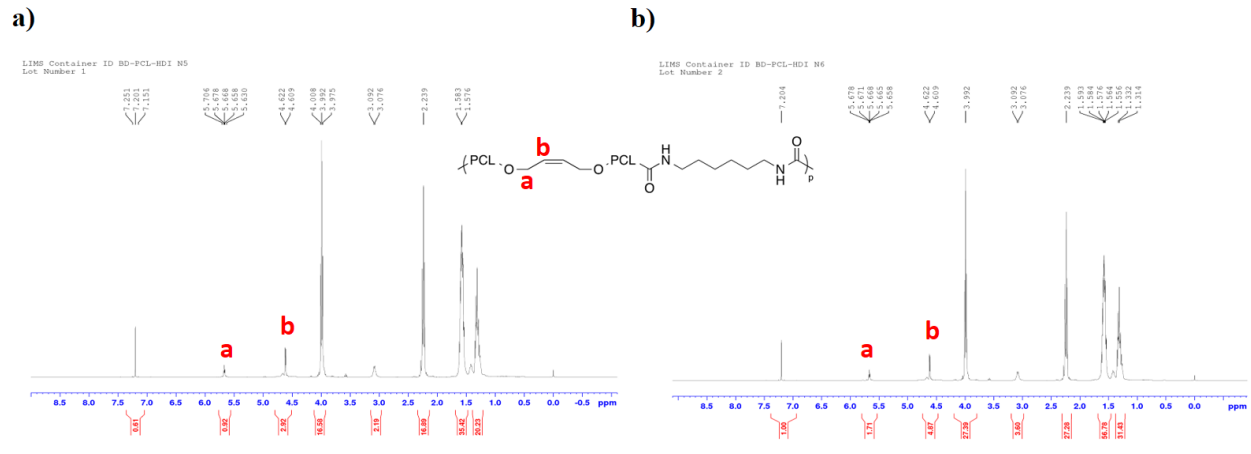


**Figure A2.6.** NMR analysis for **a)** x-PCL-TPU N5 and **b)** x-PCL-TPU N6.

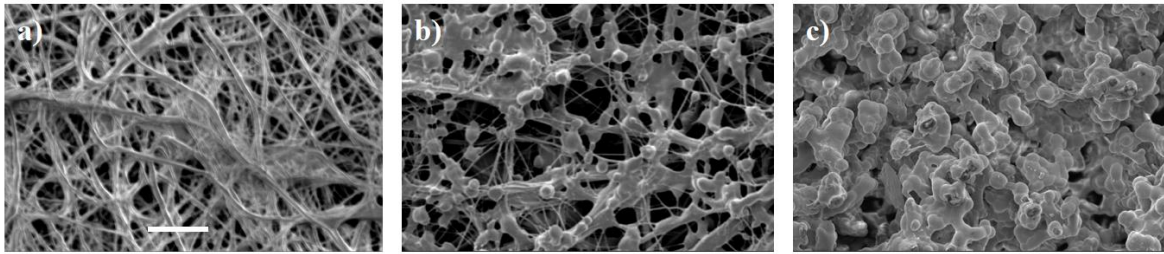


**Figure A2.7.** Scanning electron microscope (SEM) images of the electrospun x-PCL-TPU N5 sample generated at different ejecting rates: **a)** 1.0 mL/h, **b)** 1.5 mL/h, and **c)** 2.0 mL/h. Scale bar = 50  $\mu\text{m}$ .

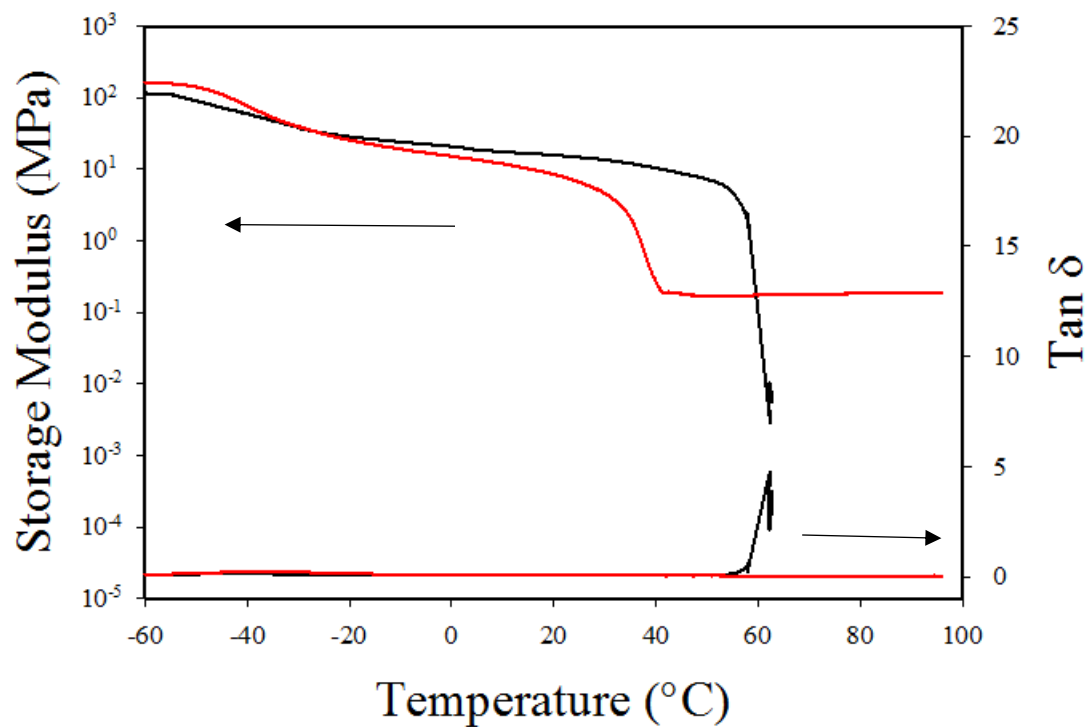


**Figure A2.8.** Storage modulus ( $E'$ ) profiles as a function of temperature for x-PCL-TPU: uncured (black) and cured with 1 wt. % DLP at 90 °C for 2 h (red). The frequency is 1 Hz.



a)

LIMS Container ID BeD-PCL2k-HD1 N2

b)

IMS Container ID BeD-PCL3k-HD1 N1

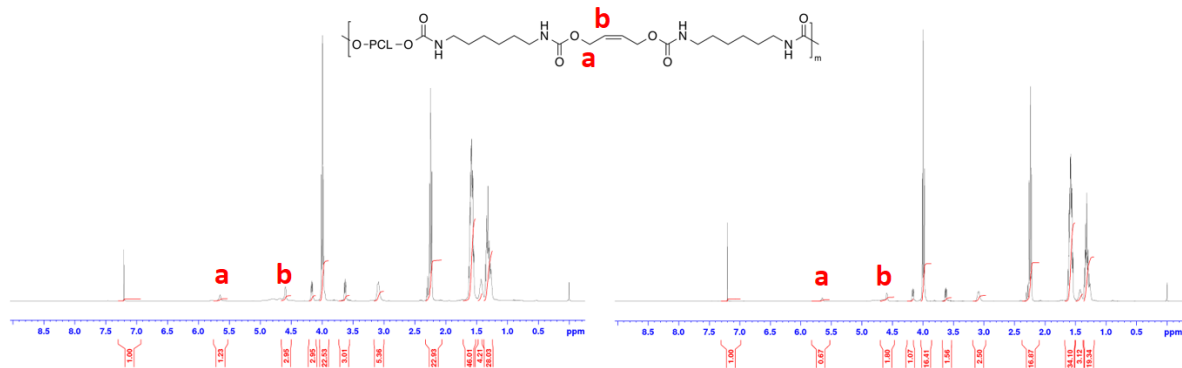


**Figure A2.9.** NMR analysis for a) BeD-PCL<sub>2k</sub>-TPU N2 and b) BeD-PCL<sub>3k</sub>-TPU N1.

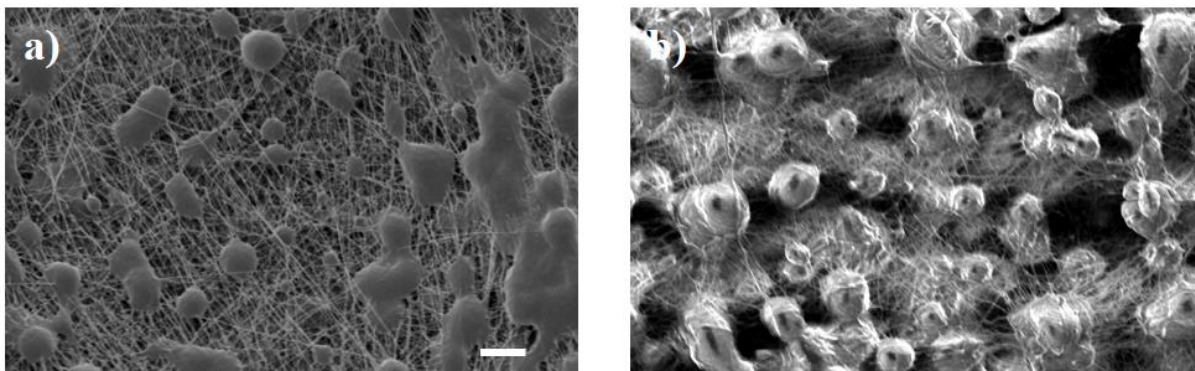


**Figure A2.10.** Scanning electron microscope (SEM) images of **a)** electrospun BeD-PCL<sub>2k</sub>-TPU N2 and **b)** electrospun BeD-PCL<sub>3k</sub>-TPU N1. Scale bar = 10  $\mu$ m.

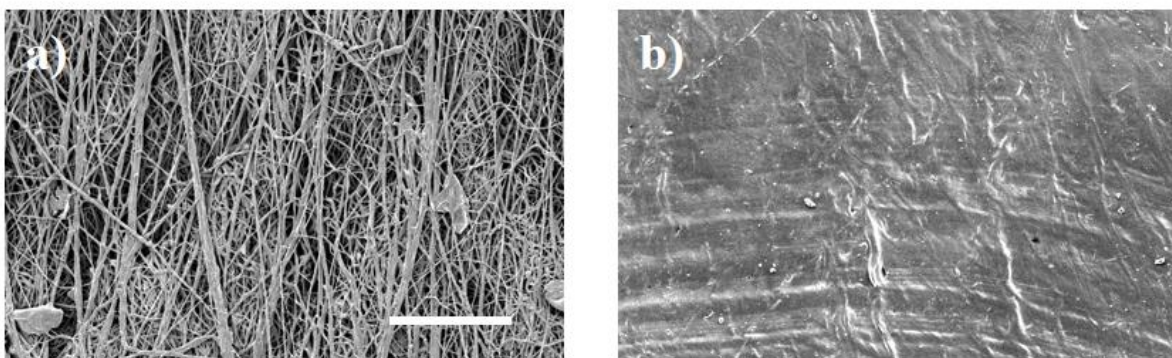


**Figure A3.1.** Scanning electron microscope (SEM) images of the dual-spun fibrous web made of x-PU and Pellethane **a)** before thermal curing and **b)** after thermal curing. Scale bar = 50  $\mu\text{m}$ .

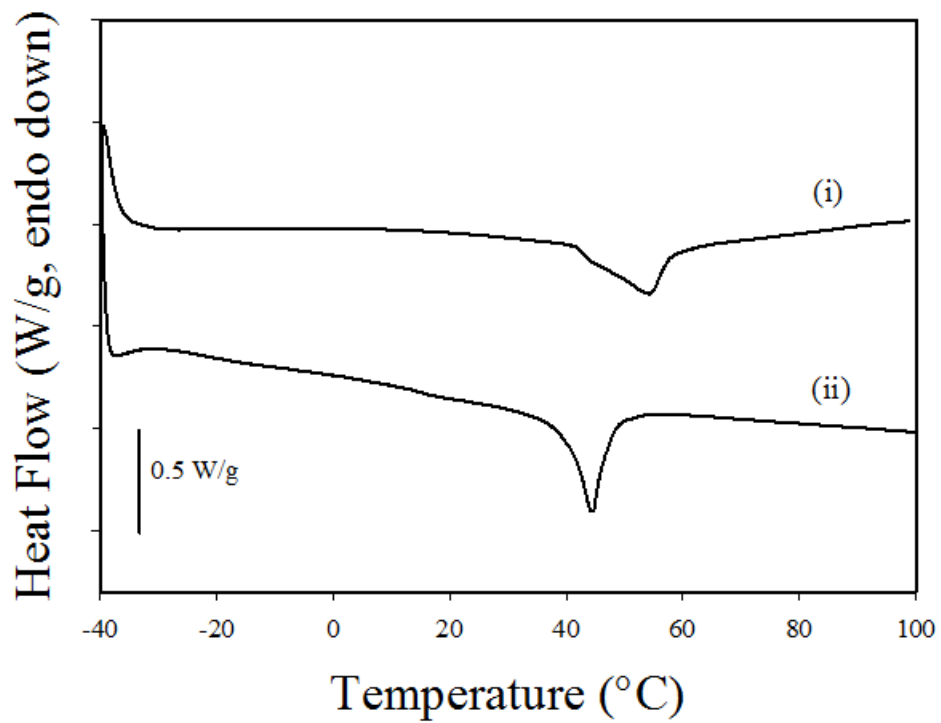


**Figure A3.2.** Differential Scanning Calorimetry (DSC) analysis graph of fibrous web (i) before and (ii) after hot compaction. Heating rate is 10 °C/min.

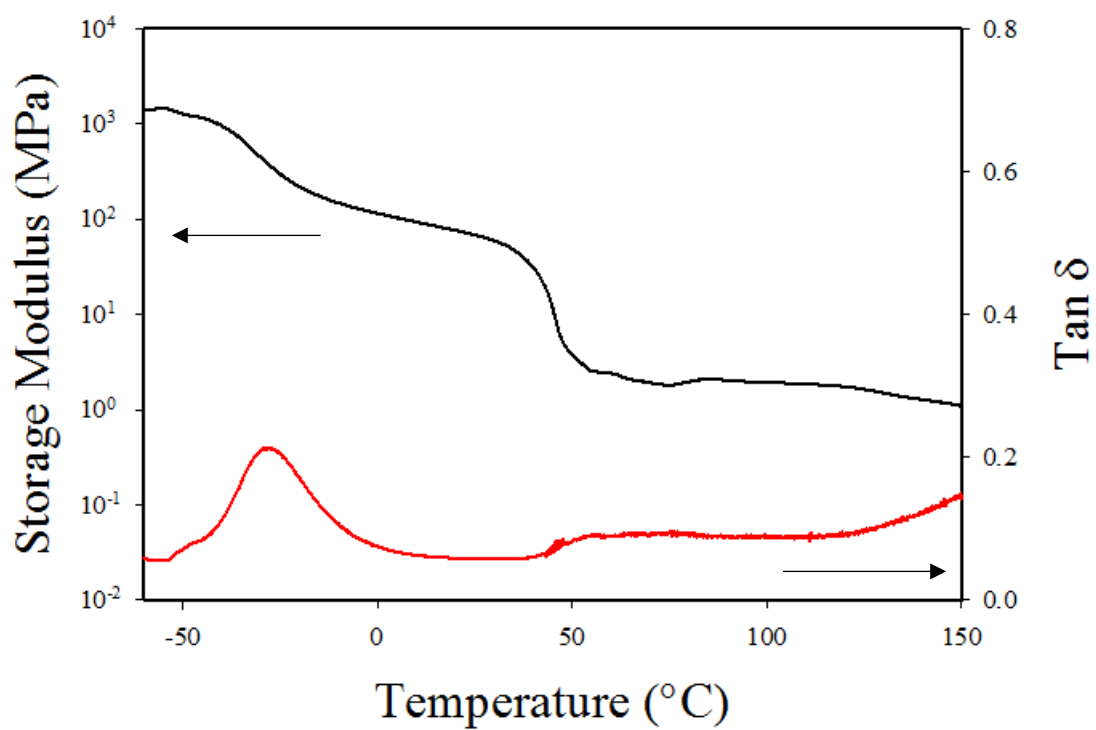


**Figure A3.3.** Storage modulus ( $E'$ ) profiles as a function of temperature for the crosslinked fibrous web. The frequency is 1 Hz.

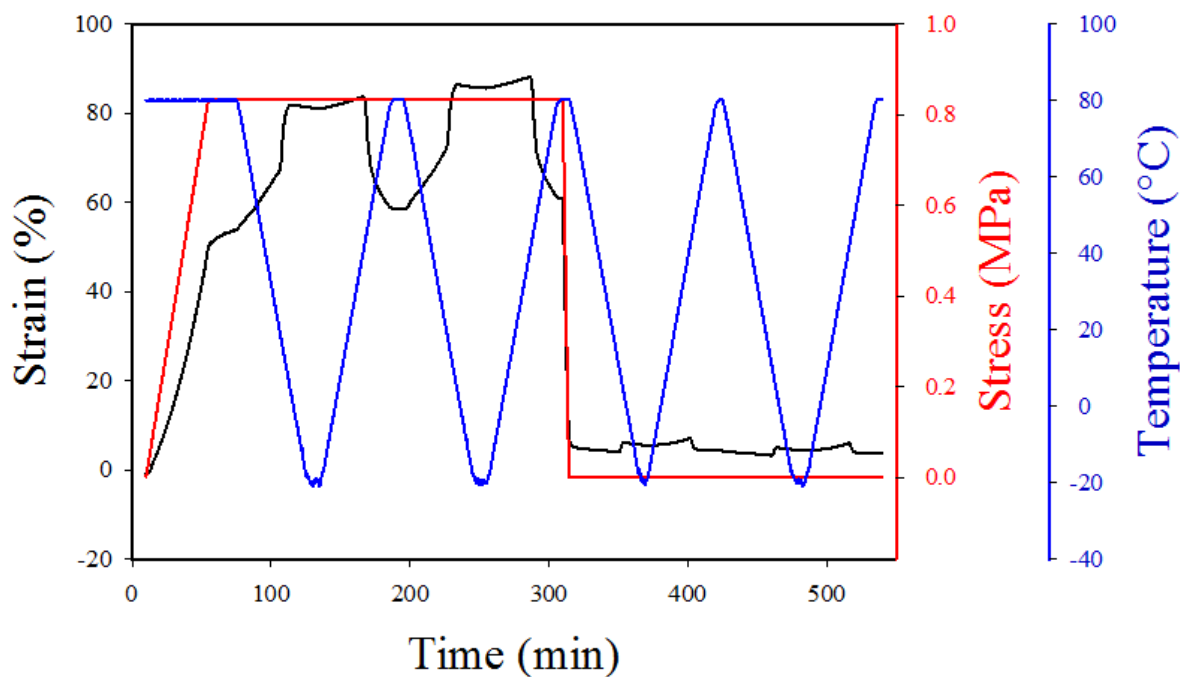


**Figure A3.4.** Tensile two-way shape memory testing of the crosslink fibrous web. The sample was deformed and kept at the stress corresponding to ca. 80% strain for the first two cycles, while no external stress was applied during the last two cycles, during all which alternate heating and cooling at 2 °C/min were employed.

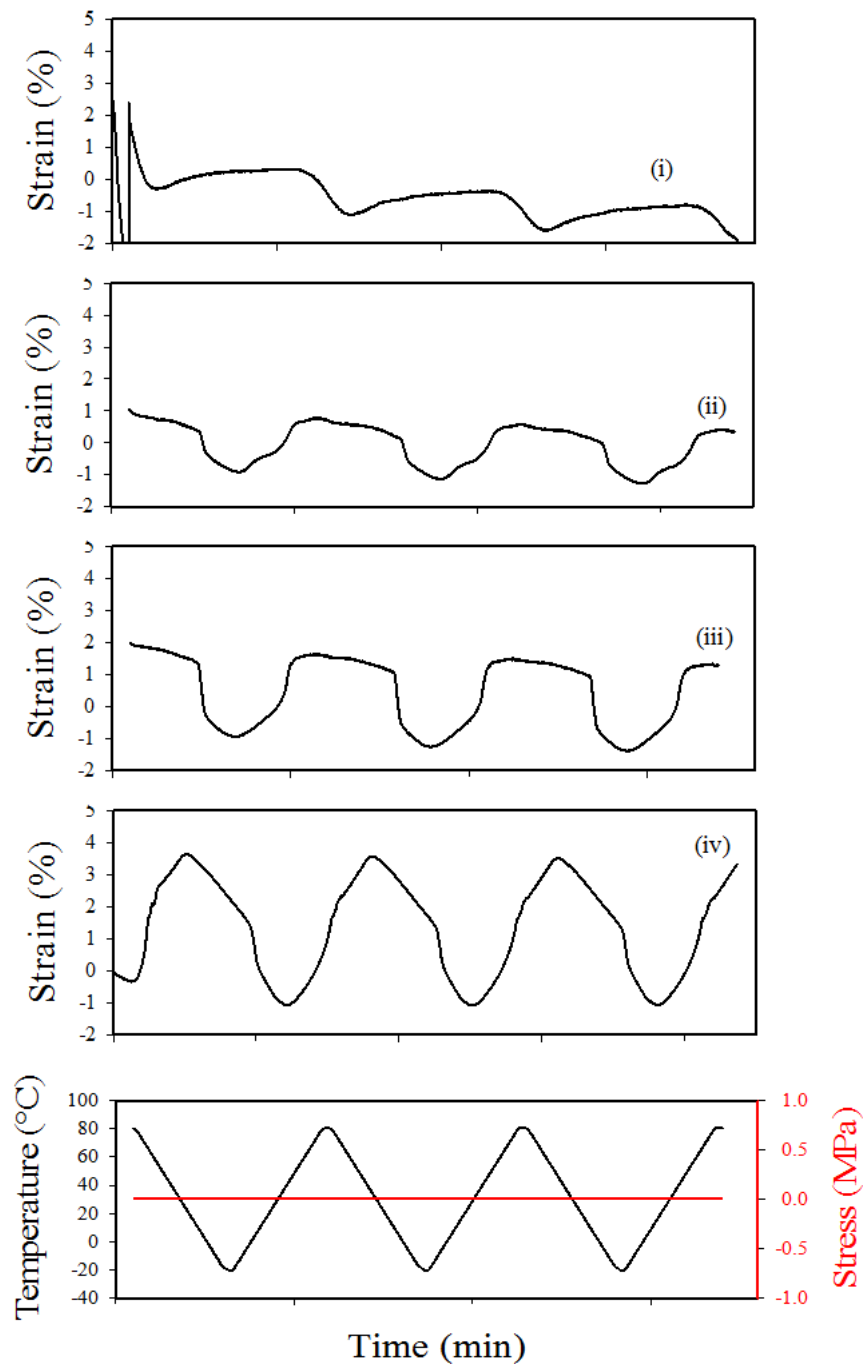


**Figure A3.5.** Tensile two-way shape memory cycles under externally stress-free condition: (i) sample 1 (400 rpm + 0% prestrain), (ii) sample 3 (400 rpm + 50% prestrain), (iii) sample 4 (400 rpm + 200% prestrain), and (iv) sample 2 (1000 rpm + 0% prestrain). All samples followed the temperature variation recorded in the bottom figure.

## VITA

**NAME OF AUTHOR:** Wenbin Kuang

**PLACE OF BIRTH:** Changsha, Hunan, China

**DATE of BIRTH:** December 1<sup>st</sup>, 1989

### EDUCATION:

B.S. in Bioengineering, Tianjin University, Tianjin, China (2012)

Ph.D. in Chemical Engineering, Syracuse University, Syracuse, NY (2017)

### PUBLICATIONS AND SELECTED PRESENTATIONS:

- Kuang, W.; Mather, P.T.: Design and Fabrication of Self-reversible Actuators via Electrospinning: Influence of Micro-geometry and Molecular Anisotropy. *In Preparation.*
- Kuang, W.; Mather, P. T.: Tuning of Reversible Actuation via ROMP-based Copolymerization of Semicrystalline Polymers. *In Preparation.*
- Kuang, W.; Schwartz, B.; Mather, P. T.: Electrospun Polyurethane Blends Exhibiting Shape Memory and Self-healing Properties. *In Preparation.*
- Kuang, W.; Mather, P. T.: A Latent Crosslinkable PCL-based Polyurethanes: Synthesis, Shape Memory, and Degradation. *In Preparation.*
- Lawton, M. I.; Tillman, K. R.; Mohammed, H. S.; Kuang, W.; Shipp, D. A.; Mather, P. T.: Anhydride-based Reconfigurable Shape Memory Elastomers. *ACS Macro Lett.* **2016**, *5*, 203 – 207.
- Kuang, W., Mather, P. T., “Crosslinkable, Electrospinnable, Biodegradable Polyurethane,” 2017 MRS Spring Meeting & Exhibit, Oral Presentation, Phoenix, AZ, April 21<sup>st</sup>, 2017.